FINAL REPORT FOR NIAC PHASE I

MAARSS

Magnet Architectures and Active Radiation Shielding Study
NASA Johnson Space Center
Houston, Texas
November 12, 2012

Principal Investigator:	Shayne C. Westover	- NASA Johnson Space Center
Co-Investigators:	Rainer B. Meinke, Ph.D	- Advanced Magnet Lab, Inc.
	Roberto Battiston, Professor	- University of Perugia and INFN
	William J. Burger, Ph.D.	- University of Perugia
	Steven Van Sciver, Ph.D.	- Florida State University
	Scott Washburn	- University of Colorado, Boulder
In Collaboration with:	Steve R. Blattnig, Ph.D.	- NASA Langley Research Center
	Ken Bollweg	- NASA Johnson Space Center
	Robert C. Singleterry, Ph.D.	- NASA Langley Research Center
	D. Scott Winter	- NASA Johnson Space Center

Contents

I. LIST OF FIGURES

II.   LIST OF TABLES

Magnet Architectures and Active Radiation Shielding Study

1. Objectives

Protecting humans from space radiation is a major hurdle for human exploration of the solar system and beyond. Like on Earth, large magnetic fields surrounding a spaceship would deflect charged particles away from the habitat region and reduce the radiation dose to acceptable limits. The objective of this study is to determine the feasibility of current state of the art (SOA) high temperature superconducting (HTS) magnets as a means to protect crew from space radiation exposure on long duration missions beyond Low Earth Orbit (LEO).   The study will look at architecture concepts to deflect high energy Galactic Cosmic Radiation (GCR) and Solar Proton Events (SPEs). Mass, power, and shielding efficiency will be considered and compared with current passive shielding capabilities. This report will walk the reader through several designs considered over the one year study and discuss the multiple parameters that should be evaluated for magnetic shielding. The study team eventually down-selects to a scalable light weight solenoid architecture that is launchable and then deployable using magnetic pressure to expand large diameter coils. Benefitting from the low temperature and high vacuum environment of deep space, existing high-temperature superconductors make such radiation shields realistic, near-term technical developments.

2. Concept Development

R. Meinke - Advanced Magnet Lab, Inc

The extended magnetic field of the earth constitutes an effective shield against ionizing radiation coming from the sun and intergalactic space. Surrounding a spaceship with large volumes of magnetic fields can accordingly protect the habitat of a spaceship and enable extended missions of human beings for the exploration of the solar system and in the far future of intergalactic space.

In order to design an effective radiation shield for a spaceship, the basic requirements imposed on the magnetic field have to be understood. It is an obvious requirement that the field direction of the magnetic field has to be oriented in such a direction that charged particles are bent away from the habitat. Since the Lorentz forces acting on moving charged particles are always perpendicular to the field direction as well as the velocity vector of the particles, various field configurations meet this requirement. However, in order to affect particles pointing in the direction of the habitat and to protect this area, the magnetic field has to be perpendicular to such particle directions.

The bending strength of a magnetic field on charged particles depends on the product of field strength, i.e., flux density measured in Tesla, and the path length of particles in the field. It is therefore equivalent to use shielding magnets with very large volumes filled with a relative low flux density or smaller field volumes, but filled with a high flux density. As long as the product of flux density and path length is the same, both approaches deliver the same bending strength. This offers two possibilities for efficient shielding, and deciding between them is an important step in the development of a feasible solution. The analysis performed under this contract identified clear advantages for large volumes and lower flux densities. As explained in more detail later, the existing experience with large magnets clearly shows that it is technologically simpler to build magnets with large volume and smaller flux density than the opposite approach. This is in particular the case for superconducting magnets. However, a novel concept of expandable superconducting coils is required.

Volume and flux density are not the only parameters that need to be considered in the realization of magnets for a practical radiation shield. Several other issues related to the realization of magnets with sufficiently large products of flux density and path length seen by the traversing particles, have to be taken into account. Large magnets in most cases have extended fringe magnetic fields, which also can intrude into the spaceship habitat, where flux densities of more than a few Gauss could lead to difficult or even unacceptable conditions. Furthermore, an effective radiation shield surrounding a spaceship will consist of a set of large magnets, and the forces acting between the individual magnets need to be considered. The forces acting between large magnets can reach levels of several 10^6 Newton, which would be difficult to counteract in particular for space applications, where heavy support structures are unwanted. Furthermore, a set of large magnets surrounding the spaceship can put significant pressure onto the spaceship habitat and pose unacceptable mechanical problems.

Many other issues in the realization of the magnetic radiation shield need to be considered and will be discussed below, but it is important to mention already that even the difficulties in manufacturing superconducting magnets with the necessary features and performance are an important parameter to decide on a concept. This is of particular importance since lightweight coils that can expand are necessary for the radiation space shield.

Finally, it needs to be pointed out that this project for obvious reasons only considers superconducting magnets. The flux density needed to bend particles with momenta in the range of 1 GeV/c or higher, requires flux densities in the Tesla range for coils of realistic dimensions. Substantial current levels, typically in the kA range, are necessary to produce such flux densities. The ohmic losses and related power requirements for normal conducting magnets operating at the required currents are impractical for space applications. Furthermore, normal conducting magnets typically contain large amounts of iron, which would make such magnets too heavy for space launch. Superconducting magnets on the contrary can produce the required flux densities without any iron enhancement by currents only, and coils similar to blimps become realistic. Additionally, superconducting magnets can operate in a persistent mode, i.e., no power supply is needed, once the coil has been excited to the operational current level.

The conceptual design study of an active radiation shield based on magnets performed under this project is furthermore assuming that lightweight, expandable superconducting magnets are technically feasible. Predicated on this approach, very large field volumes become feasible with lightweight magnets that fit into conventional launch systems. While the concept of expandable superconducting magnets seems counterintuitive, convincing arguments will be presented, which clearly indicate the feasibility of the assumed concept. A proof-of-principle experiment to demonstrate that superconducting coils can expand under the influence of Lorentz forces and remain operational is already in preparation while this report was written.

2.1.   Related Study for European Space Agency

The current NIAC Phase-1 project was predicated on work previously done for the university in Perugia, Italy. The shielding system analyzed during this project consisted of a set of superconducting double-helix (DH) coils, which surround a cylindrical spaceship habitat. The cross section of this baseline configuration is shown in Figure 2.1.; its key parameters are summarized in Table 2.1. As presented in this table, the complete shielding system consists of 12 DH coils, which each have a diameter of 2 m and a flux density in their aperture of 2 Tesla, yielding a total integrated field of about 4 Tesla*m.

A more detailed analysis of the assumed baseline system identified several shortcomings and technical difficulties, which raised the question, if other coil configurations would offer advantages over the assumed configuration. A list of key requirements and features was therefore compiled, see Table 2.2, which allows an objective comparison between various coil configurations for a shielding system.

Figure 2.1. Schematic cross-section layout of radiation shield, consisting of 12 double-helix coils surrounding a cylindrical inner habitat.
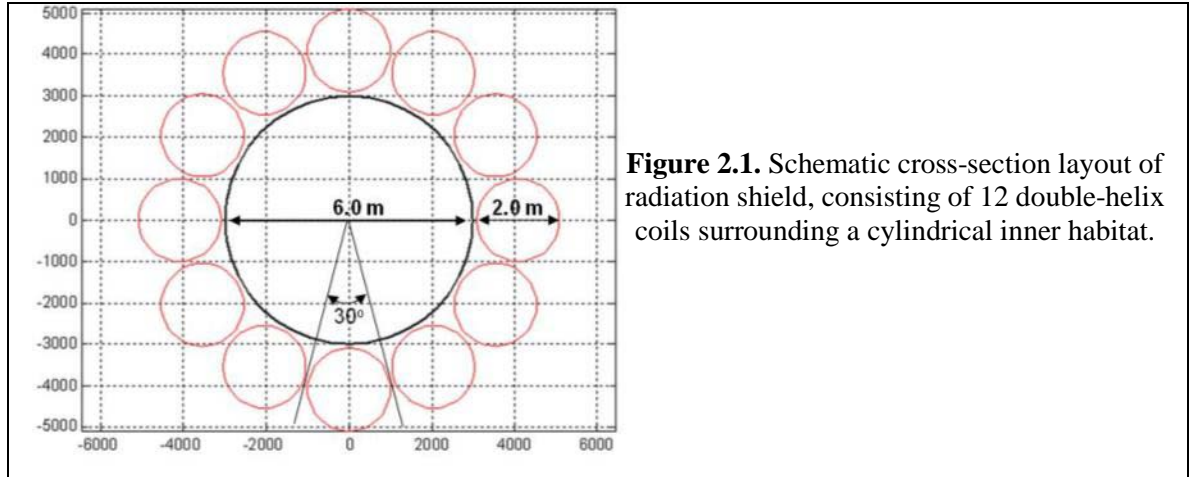
Table 2.1. Key parameters of double-helix baseline configuration

Parameter	Unit	Value
Habitat Length	m	10
Habitat Diameter	m	6
Base Coil Diameter	m	2
Number of Base Coils	N/A	12
Integral Bdl in Base Coil	Tesla*m	4

Table 2.2. Key parameters and features used for an objective comparison of magnetic shielding configurations

Rating Parameters:

- Shielding Efficiency
- Field in Habitat
- Mechanical Stability/Magnetic Pressure on Individual Coil
- Expandability
- Peak Field Enhancement
- Coil-to-Coil Forces
- Forces on Habitat
- Scalability to Higher Fields
- Quench Safety
- kA*meter of Required Conductor
- Ease of Construction

The original baseline system based on DH coils surrounding the habitat was further analyzed during this project and for completeness all results of the previous and the current analysis are presented below. A rather comprehensive set of other potential coil configurations are then analyzed during this study and graded based on the parameter set presented in Table 2.2.

2.1.1. Shielding Magnets Based on Double-helix Coil Configuration

Based on the radiation shield layout shown in Figure 2.1 the following parameter set for the individual DH coils has been developed (see Table 2.3). The transverse field generated by a DH coils increases with the tilt angle of the turns measured against the plane perpendicular to the coil axis. Equivalently this can be stated that the transverse field value increases with the modulation amplitude of the winding pattern. To achieve high field strength a relative large tilt angle of 65 degrees has been chosen for the DH base coil. Since the magnetic shielding should protect a habitat length of 10 m with a flux density of about 2 Tesla, the total coil length has to be 18 m. The resulting base coil is shown in Figure 2.2. Although this coil length sounds relatively large, the extra field in front and behind the 10-m long habitat will most likely improve the shielding against particles incoming from the front or rear and can be part of these shields.

Table 2.3. Main parameters of "Base Coil" for radiation shield.

Parameter	Unit	Value
Inner Diameter	m	2
Coil Length	m	18
Number of Layers	N/A	8
Number of Turns per Layer	N/A	275
Conductor Width	mm	50
Tilt Angle of Wdg.	deg	65
Operational Temperature	K	25
Operational Current	A	9000
Operational Margin	%	20
Nominal Central Field	T	2
Peak Field	T	2.4
Stored Energy	MJ	67.5
Magnetic Pressure	atm	16

The DH coil of the presented design consists of 8 conductor layers and requires a total conductor length of about 24,570 m. With the estimated weight of the YBCO tape conductor of 0.040 kg/m the total weight of each individual coil for the conductor only is about 985 kg.

The magnetic pressure of 16 atm, presented in Table 2.3, is an estimate based on the equation: $P_m = B^2/(2\mu_o)$, which is given by the radially outward directed Lorentz forces acting on the coil winding. If the coil is regarded as a balloon, this pressure is responsible for its inflation. This pressure, on the other hand, determines the average stress that has to be sustained by the coil winding support structure. In order to counteract an outward directed pressure, coils with cylindrical shape are advantageous in comparison to pie-shaped coils, which however could completely surround the habitat without any gaps between them. A system consisting of such pie-shaped coils has been considered, but was discarded due to very high peak fields inside of the coil winding and the difficulty of maintaining the pie-shaped coil cross section.

Figure 2.2. Isometric view of DH "Base Coil". For reasons of clarity only 2 of the 8 concentric conductor layers are shown.
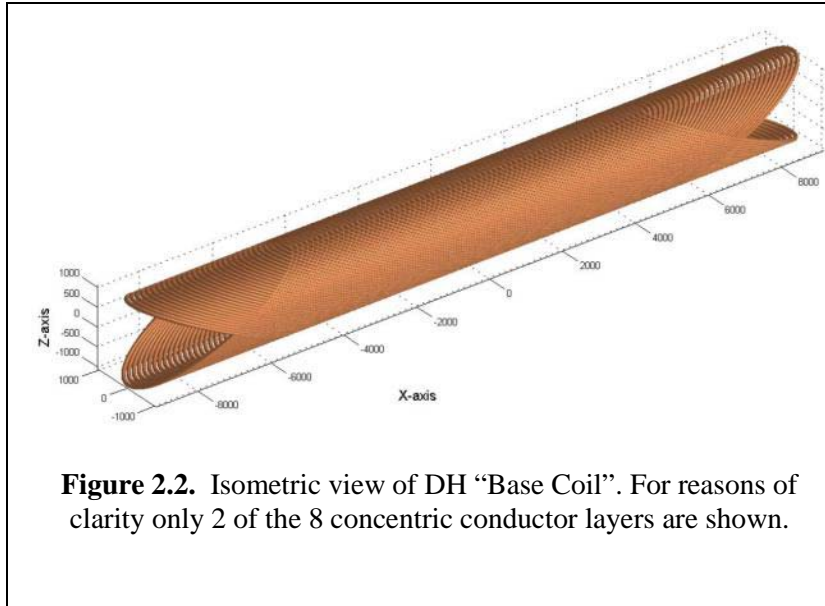
As shown in Figure 2.3 the dipole field inside of the DH aperture is about 2 Tesla in the central 10-m section of the coil. Beyond ± 5 m the field falls off, reaching 1 Tesla at about ± 7 m. The field within the perpendicular cross section of the coil in the central region is shown in Figure 2.4. As can be seen, the field is practically constant within one part of a thousand up to a radius of 0.9 m. Very close to the conductors the field strength increases. Such increase in flux density near the conductors is found in practically any potential coil configuration. The resulting peak field that is reached inside of the winding determines the operational margin of the coil.

Figure 2.3. Dipole field in DH "Base Coil" along its axis for the nominal current of 9000 A.
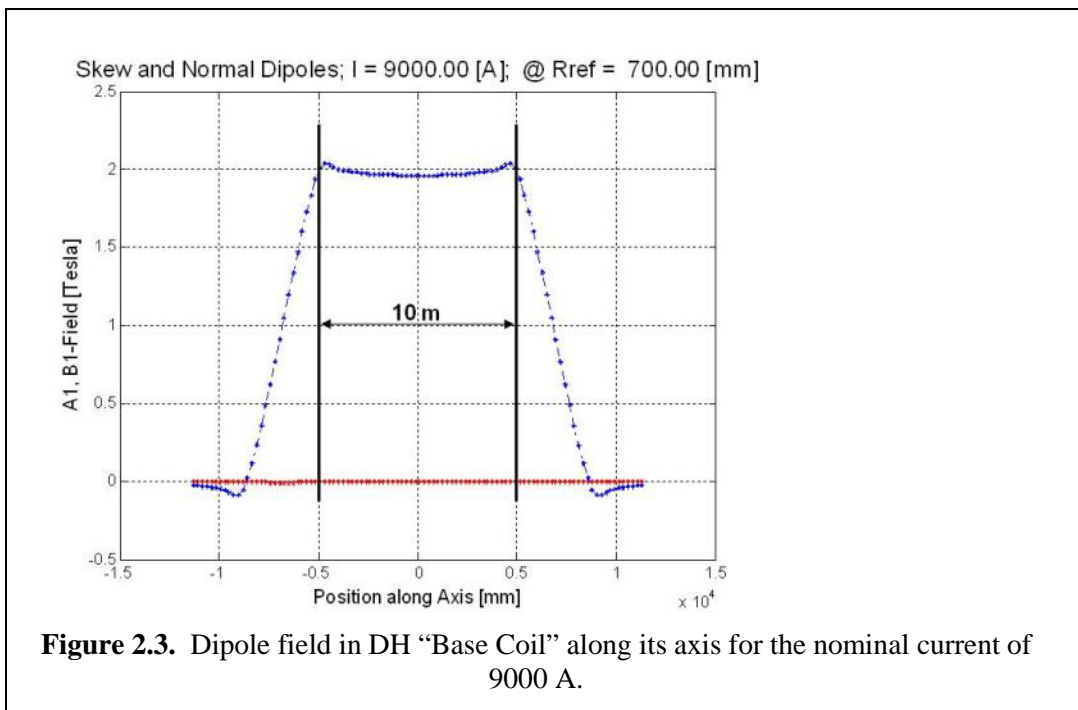
 The value of "field enhancement", i.e., the ratio between the peak field inside of the winding and the field found in the coil aperture, is an important parameter for the comparison of different coil configurations. Since the peak field determines the critical current of a superconducting coil, it is advantageous, if the field enhancement is as small as possible. For DH coils this ratio depends on the number of layers in the coil and decreases with increasing number of layers. This is one of the reasons why a relatively large number of layers, namely 8, are chosen for the design of the DH base coil. From the point of view of "expandability" and "coil manufacturing" the smallest number of layers (2) would be preferred, but the field enhancement in this case would be about 50 %.

The dependence of field enhancement near the conductors on the number of layers does not change, when several coils are arranged into the complete radiation shield (see Figure 2.1). However, as discussed later, flux sharing between adjacent coils leads to significant field enhancements and the operational margin of the coils has to be reconsidered in this context.

2.1.2. Forces Acting on Isolated DH Base Coil

For an understanding of the forces acting inside of a cylindrical DH Base coil the forces acting in an isolated coil have been determined and are presented below. The forces acting in axial direction are presented in Figure 2.5.
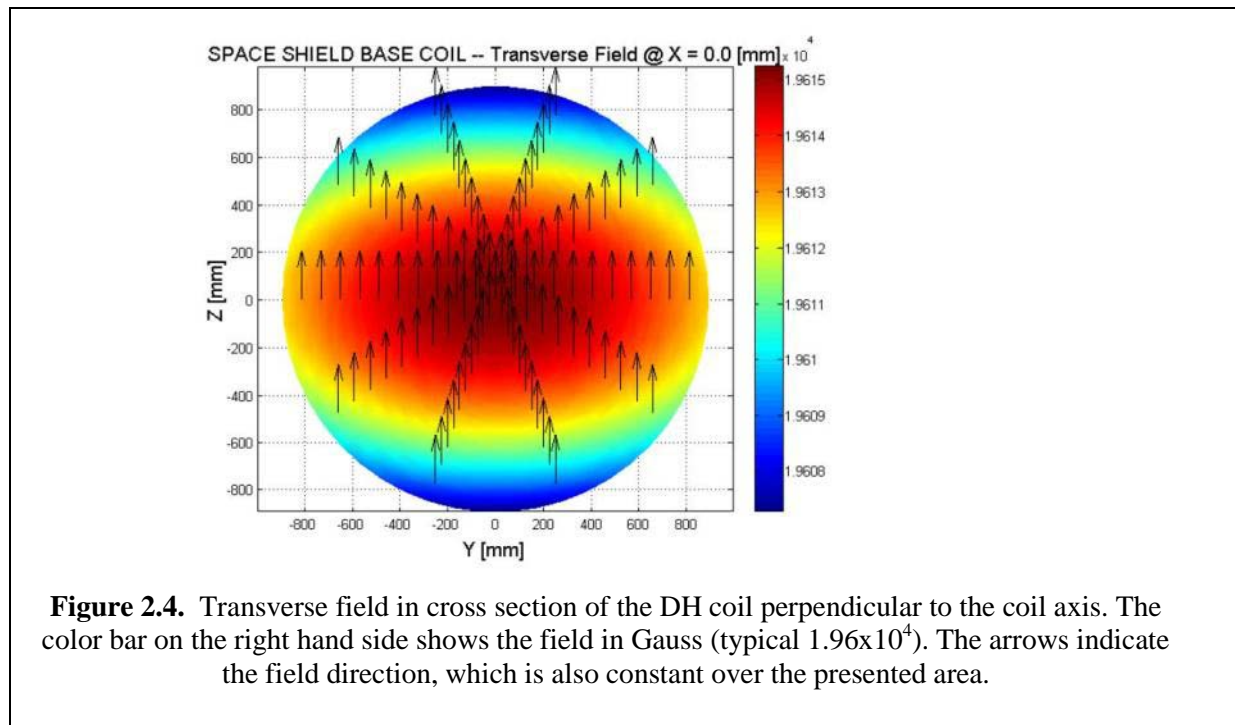
Figure 2.4. Transverse field in cross section of the DH coil perpendicular to the coil axis. The color bar on the right hand side shows the field in Gauss (typical 1.96×10^4). The arrows indicate the field direction, which is also constant over the presented area.

Figure 2.5. Axial forces versus azimuth angle for two consecutive layers versus azimuth angle integrated over the full length of the shielding coil.
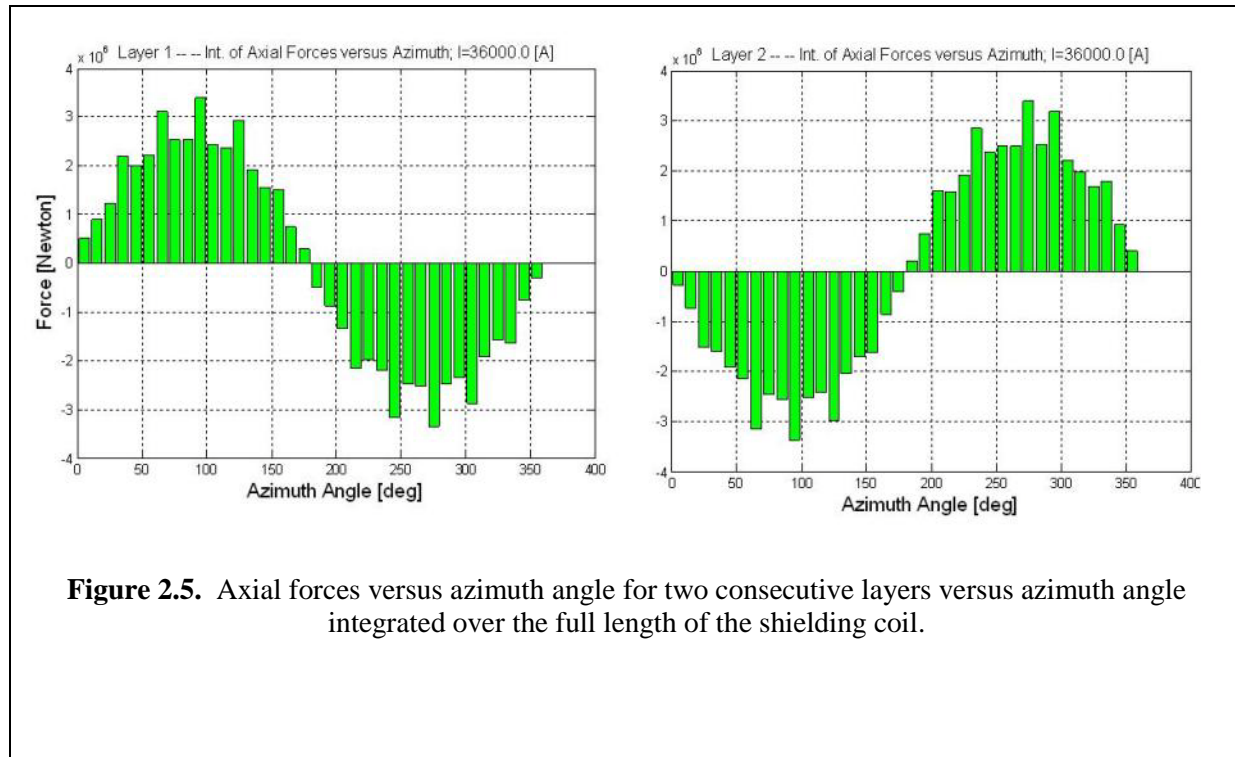
As can be seen from Figure 5 axial forces are present inside of the DH base coil. It is a unique feature of the DH coil configuration that these forces cancel for sets of two consecutive layers, but thereby lead to shear forces in the coil support structure, which need to be counteracted. The same conclusions can be drawn from Figure 2.6, which presents the axial forces per mm of conductor as a function of axial position and azimuth angle. In this case the forces are presented as a function of position on the surface of individual layers.

Figure 2.6. Axial forces acting on the conductor per mm of length as a function of axial position and azimuth angle per layer of the shielding coil.
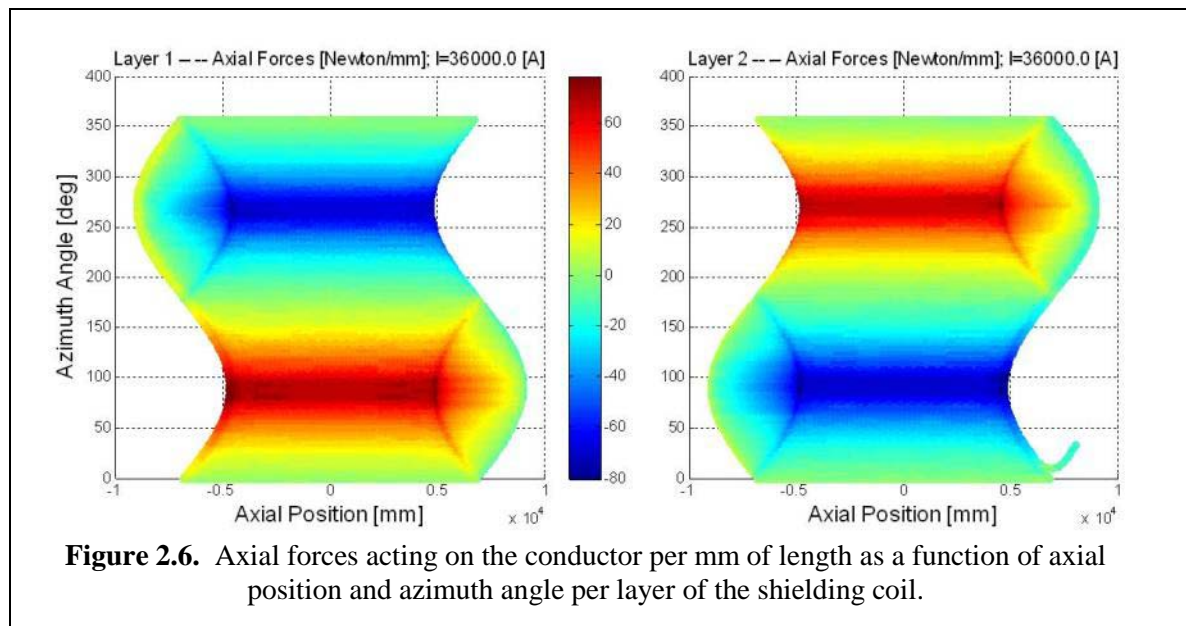
The transverse forces (shown in Figure 2.7) are calculated as

$$F_{Trans} = \sqrt{F_y{}^2 + F_z{}^2},$$

where F_y and F_z are the force components acting perpendicular to the coil axis (X-axis). For the stability of the coil support, these forces have to be transformed into radial and azimuthal components.

For a better understanding of the usefulness of magnetic pressure calculated as $P_m = B^2/(2\mu_o)$, we are considering a solenoid coil and compare the result with a numerical calculation of the radial pressure acting on the winding. In the numerical calculation the surface is subdivided in small rectangular bins, which extend in axial direction and along the circumference. The result of this calculation for the solenoid coil is shown in . As indicated in Figure 2.8, the peak pressure acting on the windings in the middle section of the solenoid is 15.98 atm. The simple estimate of the magnetic pressure, using the equation: $P_m = B^2/(2\mu_o)$, based on the solenoid field of 2 Tesla, yields 15.92 atm, a value in perfect agreement with the numerical calculation.

The field in DH coils, however, is in the transverse direction and the simple analytical equation used for the magnetic pressure calculation is not completely correct. For a more detailed understanding of the acting forces, we are considering a cross section through the DH coil and calculate the forces acting on each intersection of the conductor with this plane. The forces presented in Figure 2.9 are per conductor length of 1 cm.

Figure 2.7. Transverse forces versus axial position and azimuth angle per layer of the shielding coil.

Figure 2.8. Left: Radial pressure acting on the surface of a solenoidal coil in bins of axial length and azimuthal circumference versus axial position and azimuth angle. Right: Isometric view of the solenoid coil.

.

Figure 2.9. Left: Cross section through the innermost layer of the shielding coil. The colored dots indicate the locations, where the conductors of the DH coil are intersected. The arrows show the force direction; the arrow lengths are proportional to the acting force in Newton/cm. Right: Same plot for outer layer.

The field direction in Figure 2.9 is in the vertical direction of the plot. Both Figures show that all conductors for the isolated DH coil are pulled in such a way that the coil will seek an elliptical shape with the larger axis of the ellipse perpendicular to the field direction, as indicated in Figure 2.10.

Figure 2.10. Schematic diagram of expected shape change in coil with dipole geometry.
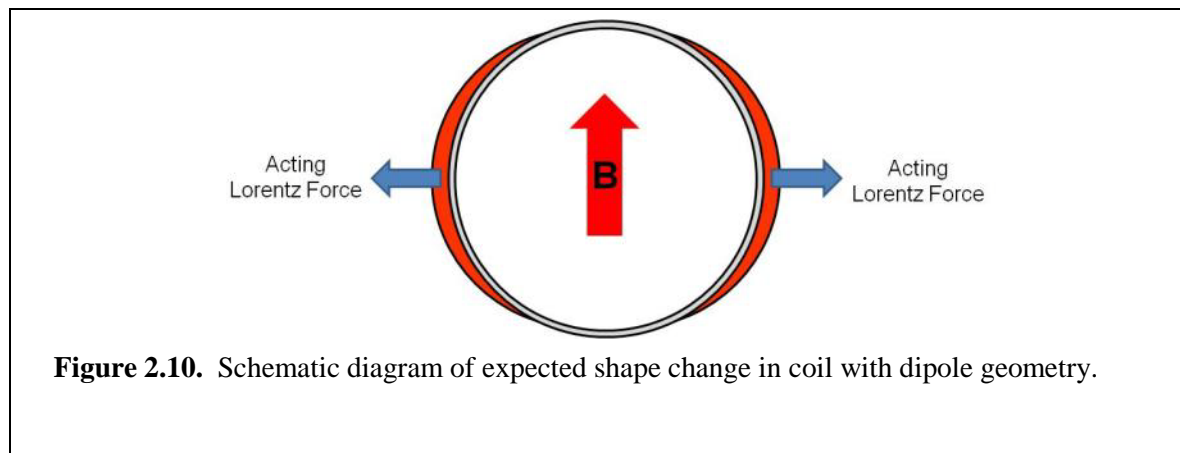
Integrating the calculated Lorentz forces over coil surface elements in axial and azimuthal direction, a radial and azimuthal pressure can be determined, which is presented in Figure 2.12. The decomposition of the Lorentz forces in radial and azimuthal directions is shown in Figure 2.11.
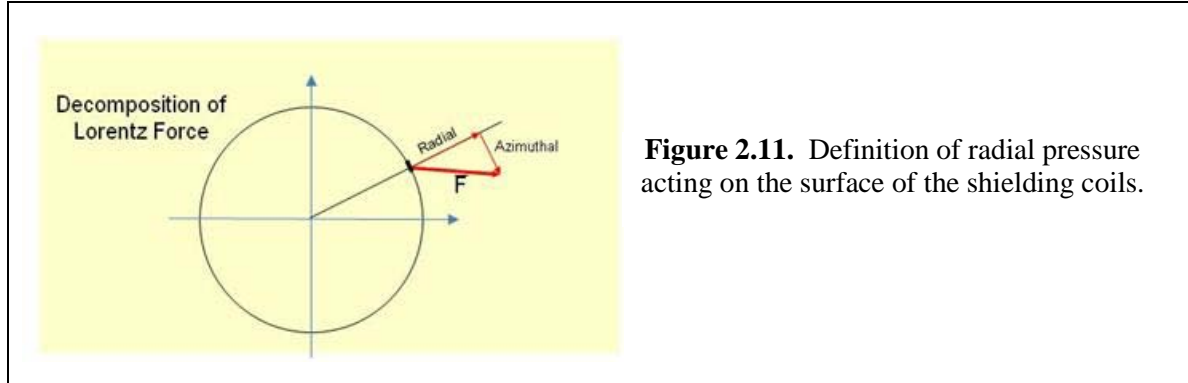
Figure 2.11. Definition of radial pressure acting on the surface of the shielding coils.
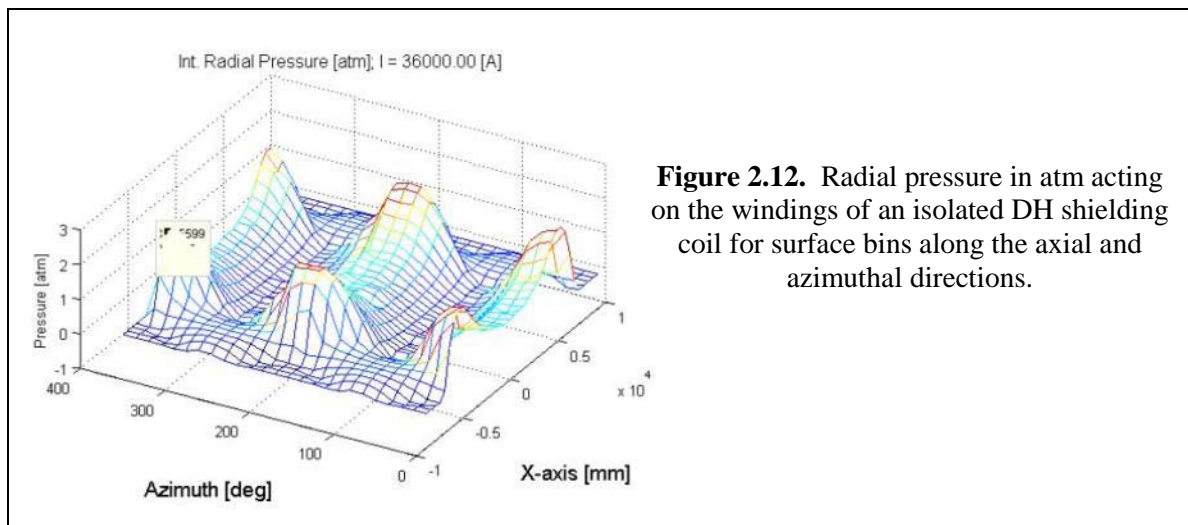
Figure 2.12. Radial pressure in atm acting on the windings of an isolated DH shielding coil for surface bins along the axial and azimuthal directions.

The pressure distribution presented in Figure 2.12 shows the maximum radial pressures on the coil surface near 0° and 180° as expected from the Lorentz force distributions presented in Figure 2.9. The pressure shows humps at these azimuthal positions towards the coil ends. This is in agreement with the peak fields in the coils at the same locations. It is important to point out that the maximum radial pressure is only 2.4 atm. This value is significantly smaller than the approximate magnetic pressures that were calculated from the transverse Lorentz forces. The discrepancy is due to the fact that a large part of the transverse Lorentz force is in the azimuthal direction. It is safe to assume that these azimuthal forces will be sustained within the support structure of the coil and will not lead to a shape change of the coil cross section.

2.1.3. Integrated Field along Diagonal through Coil Aperture

For radiation shielding calculations the value of the integrated field along the path of a charged particle is the relevant parameter. As expected from the uniform field inside of the DH coil, the integrated field is independent of the azimuthal direction as shown in Figure 2.13.
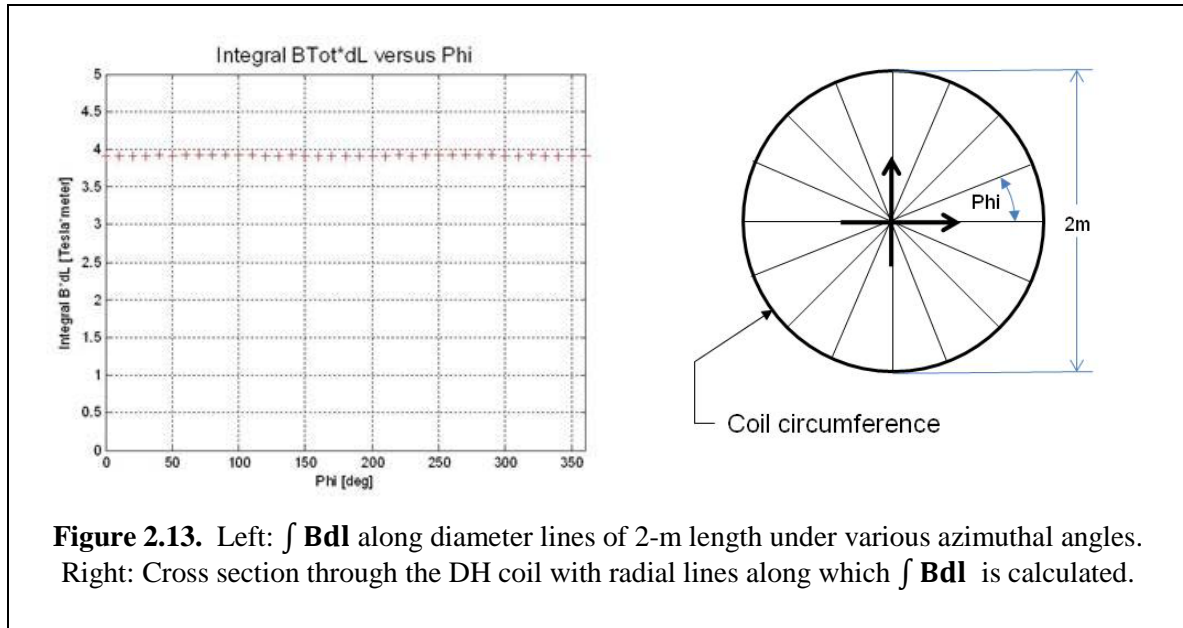
Figure 2.13. Left: ∫ **Bdl** along diameter lines of 2-m length under various azimuthal angles. Right: Cross section through the DH coil with radial lines along which ∫ **Bdl** is calculated.

2.1.4. Analysis of Complete Space Shield Configuration

As indicated in Figure 2.1 the spaceship habitat is surrounded by 12 DH coils, which are described above. An isometric view of the complete assembly is shown in Figure 2.14. The field distribution (flux density) throughout the whole cross section is shown in Figure 2.15. The magnetic field is highly concentrated to the ring of the shielding coils. Inside and outside of this ring the field is very small. The orientations of the individual coils are arranged in such a way that a continuous field direction between neighboring coils is introduced. One could say that the flux is channeled from coil to coil like in a Halbach array. The magnetic field, therefore, is not limited to the inside of the DH coils. In fact, a strong field enhancement is observed towards the conductor windings and between adjacent coils. This is due to the fact that unlike solenoid coils, dipoles have significant fields outside their aperture, where the flux returns, and for an arrangement of densely packed dipole coils flux sharing between neighboring coils leads to field enhancements.

For a quantitative analysis of the field enhancement caused by flux sharing, the field at key locations inside and outside of the DH coils has been determined. The results are shown in Figure 2.17. A comparison with Figure 2.16, which shows the flux density in the cross section of an isolated DH coil, a significant enhancement of flux density is observed. In fact, the flux density increases from 2 Tesla to 3.29 Tesla, constituting an increase by about 65%. The field in the gap between the coils actual is 4.18 Tesla, which is more than twice the flux density inside of the isolated DH base coil.

Figure 2.14. Isometric view of complete shielding coil assembly under two different viewing angles. For reasons of clarity only 2 layers with wide conductor spacing are shown. The other dimensions are very close to the actual design. The habitat cylinder with 6 m diameter is indicated as an open cylinder.
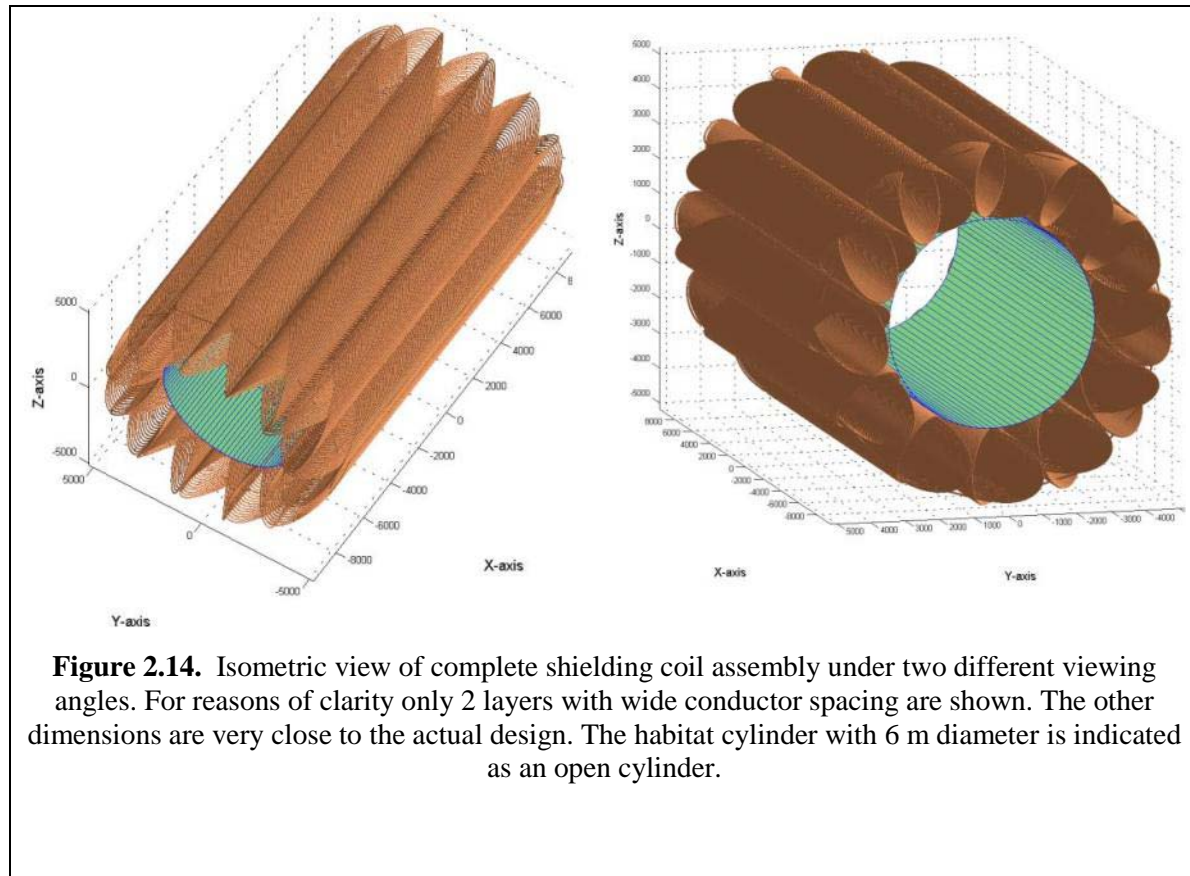
For the shielding efficiency of the DH coil array $\int \boldsymbol{Bdl}$ as a function of azimuth angle is the relevant parameter. The distribution of $\int \boldsymbol{Bdl}$ as a function of azimuth angle is shown in Figure 2.18. As can be seen in the figure, the integrated field through the whole diameter increases from the original design goal of 4 Tesla*m to values between 6.25 Tesla*m and slightly more than 7 Tesla*m. The original design goal for $\int \boldsymbol{Bdl}$ can therefore be met with a much lower operational current in the individual DH coils. On the other hand, the DH coils as designed could not function at the original operational current of 9000 A (see Table 2.3). The operational margin of the superconductor was based on a peak field of 2.4 Tesla, which is significantly exceeded in the array at 9000 A.

As pointed out, the flux density increase due to flux sharing between neighboring coils has important consequences on the design of the shield coil system. While the operational margin requirement, due to the increased field seen by the superconductor, could be solved with more layers in the coil or a lower operational temperature, severe limitations might arise from the forces acting between coils. The forces acting on the coils in the array arrangement are described below.
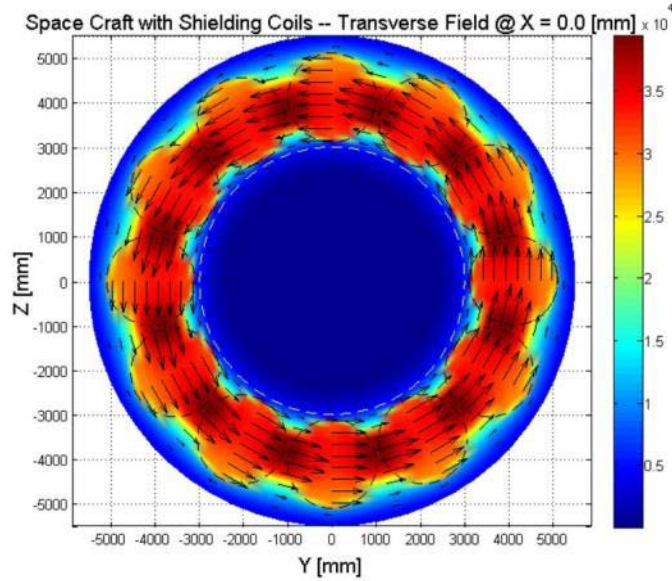
Figure 2.15. Flux density distribution in complete shielding coil assembly. The individual DH coils are indicated by circles. The color-coding represents the flux density at any point. The color bar gives the flux density in Gauss (see factor 10^4). The arrows indicate the field direction; the length of the arrows is proportional to the magnitude of the flux density.
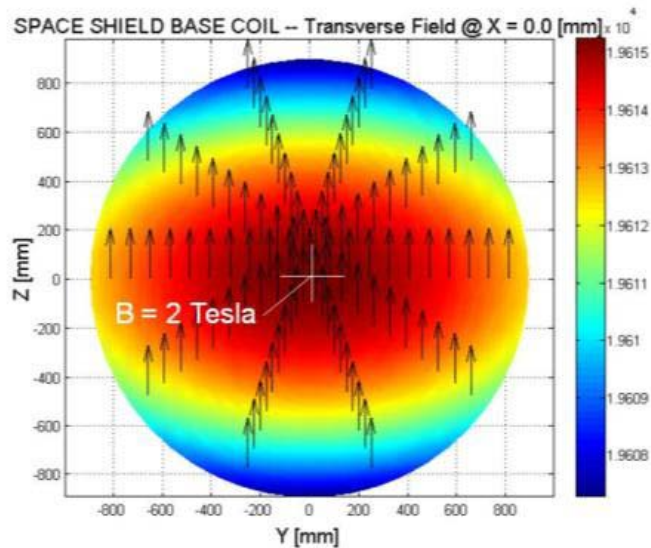
Figure 2.16. Flux density distribution in central cross section of isolated DH coil.

Figure 2.17. Left: Flux density determined in center of a DH coil that is part of the whole array. Color coding and arrows are the same as in Figure 2.16. Right: Flux density determined in the gap between two adjacent DH coils of the array.

Figure 2.18. Left: Shielding coil configuration in cross sectional view with an indication of diagonal lines for various azimuth angles Φ. Right: $\int \boldsymbol{Bdl}$ along diagonal lines as a function of azimuth angle Φ.

The resulting, attractive force acting between the two DH coil is 7.1 MN. The force is calculated by considering small conductor elements of one coil and calculating the Lorentz force acting on this element, given the field generated by the other coil. The force therefore gives the integral force acting between the two 18-m long DH coils. To get an intuitive understanding of this force, one can consider that 1 kg acting on a surface produces a weight force of about 10 Newton. 7 MN are therefore needed to counteract a mass of about 700 tons. Given the fact that the peak field in the DH coils occurs near the coil ends, the acting force is not uniformly distributed over the length of the coils.
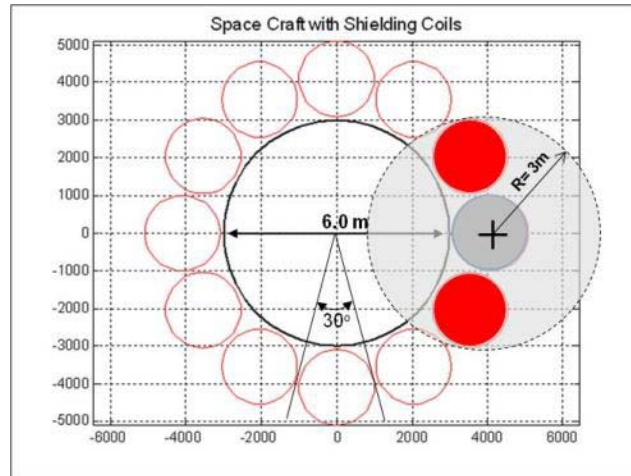
Figure 2.20. Scenario of shielding array with missing coil (indicated in gray). Forces acting on the two neighboring coils are determined.
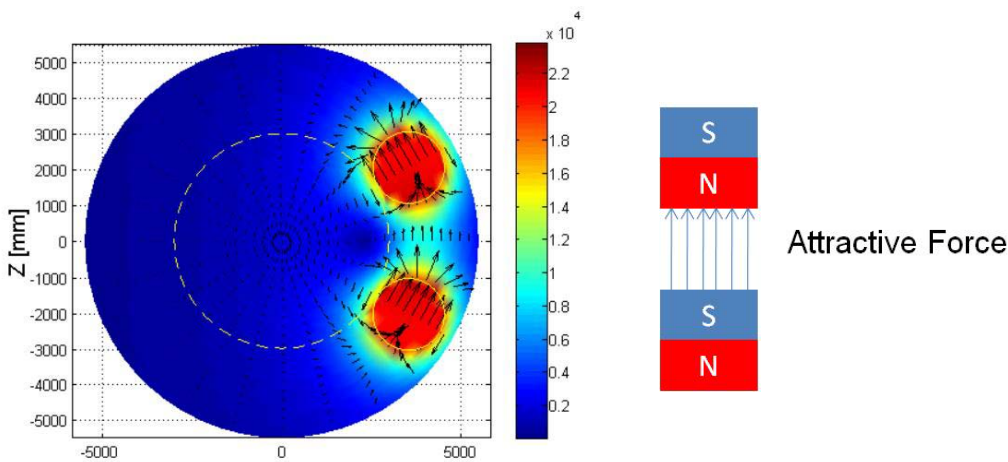
Figure 2.21. Left: Flux density distribution of 2 DH coils of the shielding configuration with the coil between them missing. The color coding and arrows are the same as in previous Figures. Right: Simplified model to show that the force between the two coils is attractive, since the field lines emerging from the lower coil/magnet enter the upper one.

For completeness we have also determined the force acting between two isolated DH coils. The resulting flux density distribution is shown in Figure 2.22. The resulting force of this configuration is 51.5 MN. As before this force can be visualized as due to a weight of about 500 tons.

Figure 2.22. Left: Flux density distribution of 2 neighboring DH coils of the shielding configuration. The color-coding and arrows are the same as in previous Figures. Right: Simplified model to show that the force between the two coils is attractive, since the field lines emerging from the lower coil/magnet enter the upper one.
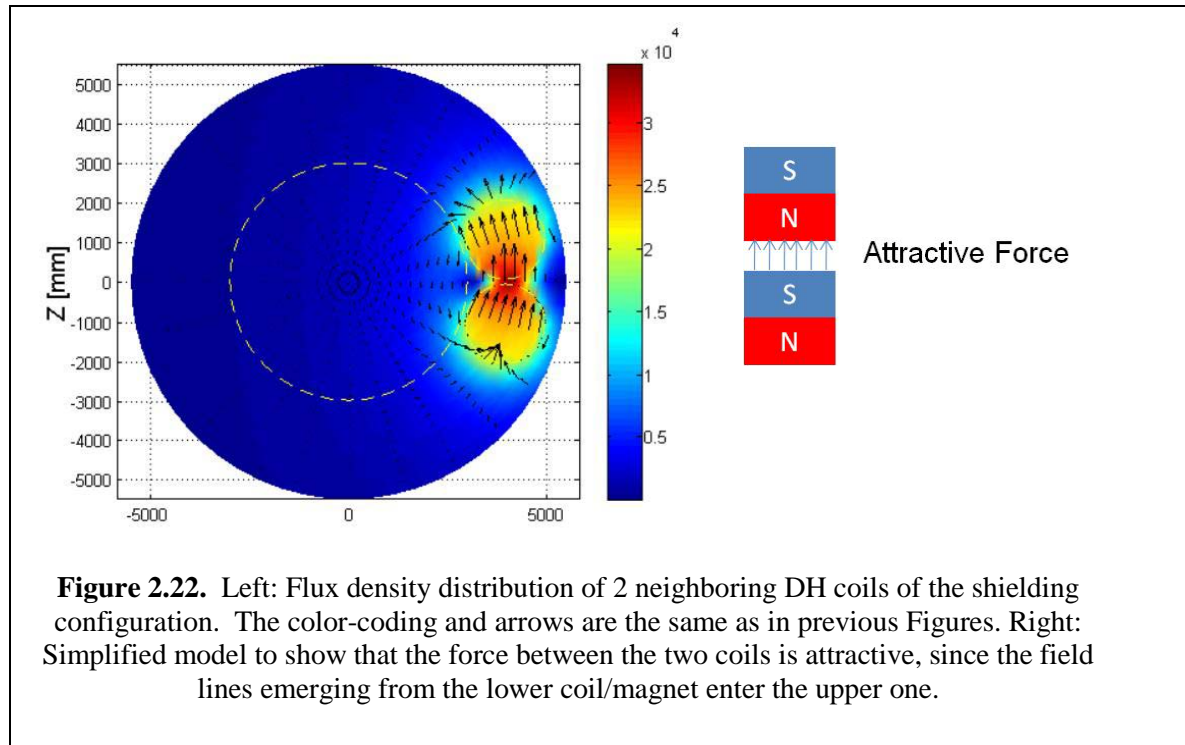
Give the large forces acting on the DH coils in the array configuration, it is important to calculate the force acting on any coil when it is part of the complete assembly. This scenario is shown in Figure 2.23 with an inward directed force of 28.0 MN results. Total force of all 12 coils acting radially onto the surface of the cylindrical habitat area is therefore about 336 MN. Given the total surface area of the habitat cylinder of $A = \pi * 6m * 18m = 340\ m^2$, the acting force on average produces a pressure of about 10 atm. Again it has to be pointed out that this pressure is not totally uniform, but would be stronger towards the ends of the DH coils and weaker towards the middle. Furthermore in the configuration, schematically shown in Figure 2.23, the DH coil cylinders touch the habitat region only over a small part of its circumference and some extra support structure is required to distribute the acting force.

As pointed out before, the presented design with an operational current of 9000 A is much stronger than the original design goal, which requested an $\int Bdl$ of 4Tesla*m instead of the much higher value present in the array. Given the large forces acting in the array under these conditions, it is necessary to determine the forces for the field configuration that is limited to the requested $\int Bdl$ of 4Tesla*m.
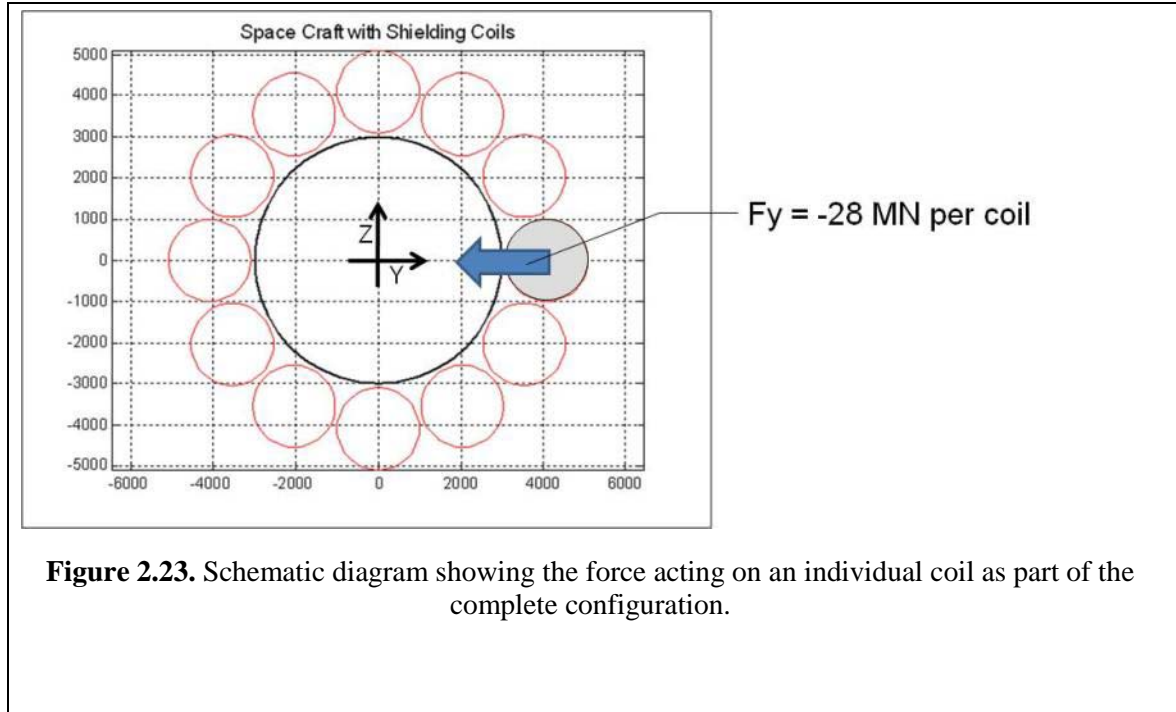
Figure 2.23. Schematic diagram showing the force acting on an individual coil as part of the complete configuration.

In order to achieve the requested field strength, the current in the array can be reduced to about 61% of its design value of 9,000 amp for the 8-layer coil.

The resulting flux density distribution in the cross section of the array is presented in Figure 2.24. As can be seen, the flux density in the center of each coil is reduced to 2 Tesla and the field in the gap between two coils is 2.5 Tesla. This configuration is therefore also in reasonable agreement with the peak field requirement that determines the operational margin of the coils.

Figure 2.24. Flux density distribution for the reduced field in the complete shielding coil assembly.
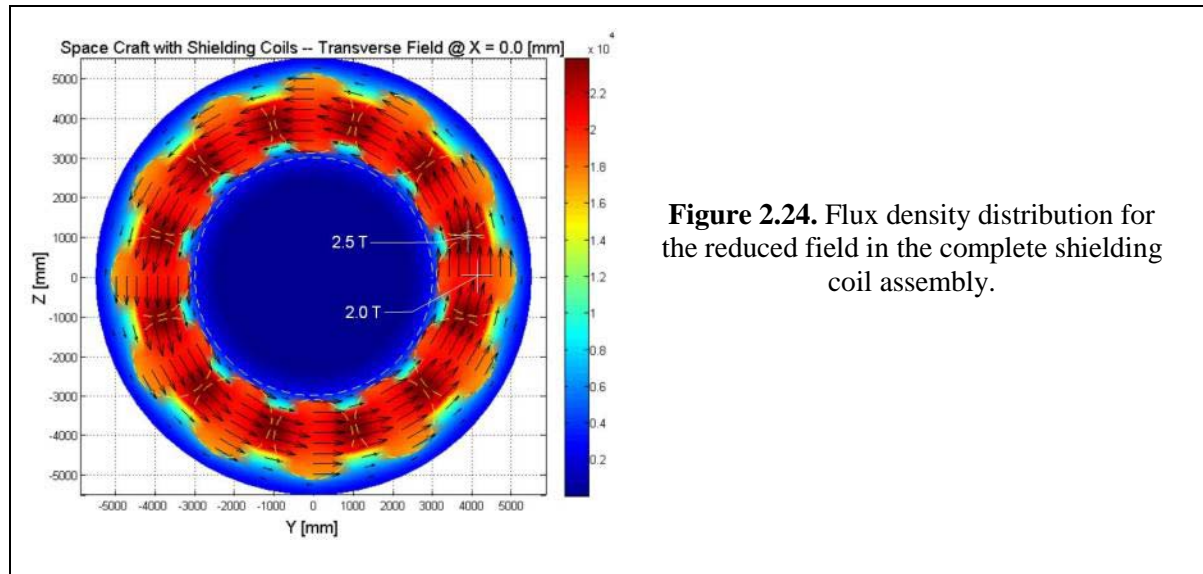
The resulting $\int \boldsymbol{Bdl}$ distribution is shown in Figure 2.25 and shows an average value of 4 Tesla*m.

Figure 2.25. $\int \boldsymbol{Bdl}$ along diagonal lines as a function of azimuth angle Φ.
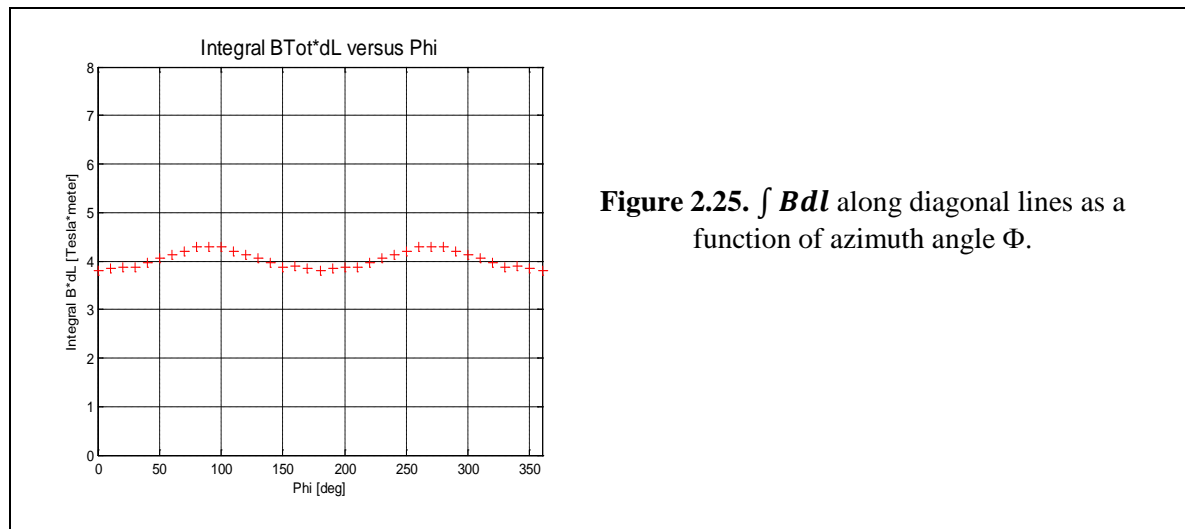
The total attractive force acting between two isolated DH coils, as analyzed in Figure 2.22 is reduced to 18.9 MN (from 51 MN); the total attractive force between two coils with the one missing between them is reduced to 2.6 MN (from 7.1 MN). Finally, the force acting on any coil in the complete shielding array configuration is reduced to 10.3 MN (from -28 MN). The resulting average pressure acting on the surface of the habitat cylinder is reduced to 3.6 atm from the original 10 atm.

Although, the presented shielding coil configuration, which consists of 12 DH coils has some positive features, several concerns for the realization of such a system exist. DH coils consisting of 8 concentric layers would be rather stiff, and it seems impossible to produce coils of this design that are flexible enough to be expandable. Additionally, such large forces would require significant structure to manage

the loads and require a very large launch mass. It seems therefore necessary to analyze other coil configurations.

2.2.   Other Configurations Evaluated

The shielding array concept based on DH coils identified several issues that need to be overcome in the realization of such a system. Two main technical difficulties in this concept are the large forces acting on the spaceship habitat and the flexibility of multi-layer coil configuration. The stiffness of a multi-layer coil would make it very difficult to offer the required flexibility that will be needed for coils that quasi inflate or expand under the effect of the acting magnetic pressure. Both of these issues would even become more pronounced, if one considers a shielding array with higher field strength or coils with larger dimensions. For these reasons magnetic shielding array configurations based on coils with a smaller number of layers and also those based on coils other than DH have been analyzed. Due to the limited scope of the current project these configurations could not be fully optimized, and not all parameters that might be important for the final realization of the concepts have yet been determined. However, the performed analysis shows clear advantages and disadvantages of the concepts considered. The summary table based on the performed concept study of multiple concepts constitutes a major achievement of this Phase-1 NIAC project and can serve as a valuable base for future studies.

2.2.1. Toroids with Radial Field Direction

Some toroidal coils offer the unique advantage that the magnetic flux can be fully contained in the aperture of the coil and the outside fringe magnetic field is insignificant. It seems therefore attractive to surround the spaceship habitat with a set of toroidal coils. Such coil configurations can be developed out of DH coils in the following way. A two-layer DH coil is generated as shown in Figure 2.26, with a coil diameter of about 2 m. As shown in the figure, the windings are oriented in such a way that the field is in the X-Y plane. Based on the fact that a two-layer DH coil is being used, only a transverse magnetic field is presented and the axial field, which still exists in each single layer, is practically completely canceled. The DH coil is then bent in the X-Y plane, as shown in Figure 2.27 to form a complete toroid, which can fit around the spaceship habitat of 6-m diameter. The length of the generated DH has been chosen accordingly. By bending each of the two layers individually, the tilted coil ends of the DH fit exactly together, when bent to a circle without leaving any gap between the two ends (compare Figure 2.27).

Based on the field direction in the straight DH coil, the field direction of the final toroid is in radial direction. The resulting field direction can be seen in Figure 2.28, which shows a cross section through the toroidal coil. The plane of the cross section is shown on the left hand side of the figure; the flux density and the field direction are shown on the right of Figure 2.28. As can be seen from the color-coding in the cross section and the color bar, the flux density is about 2 Tesla. However, it is important to point out that the external field of the toroid, as generated here, is not zero on the outside. Due to the fact that the flux inside of the straight DH coil is perpendicular to the coil axis, the flux clearly extends to the outside of the aperture.
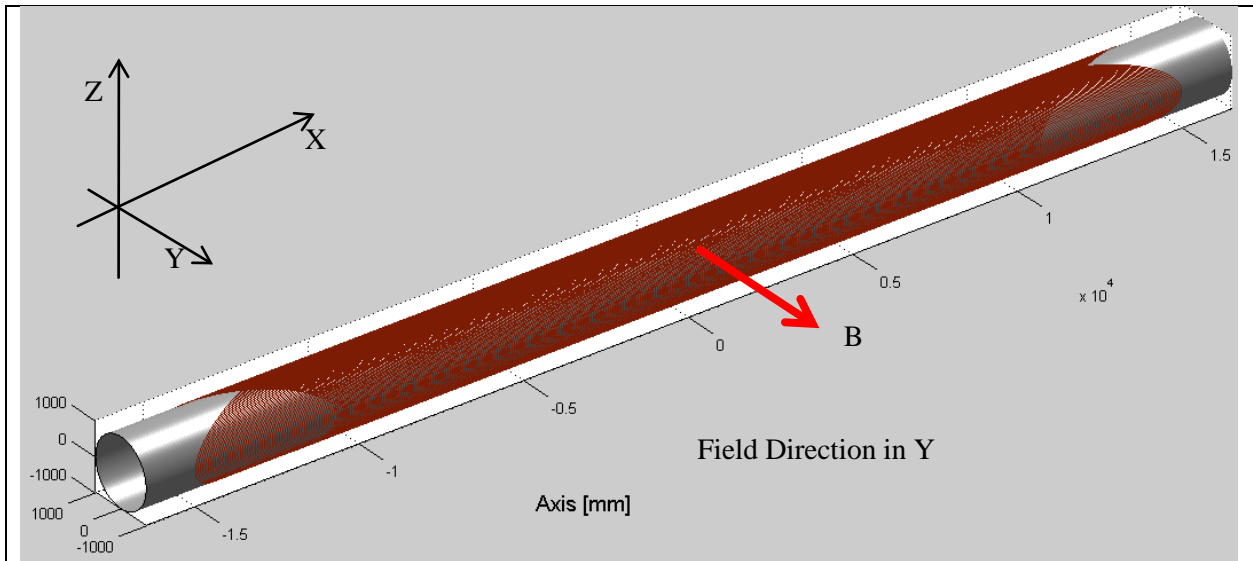
Figure 2.26. DH coil consisting of two concentric layers. The windings are oriented to generate a field perpendicular to the coil axis in the direction of the Y-axis. The axial field components are canceled.
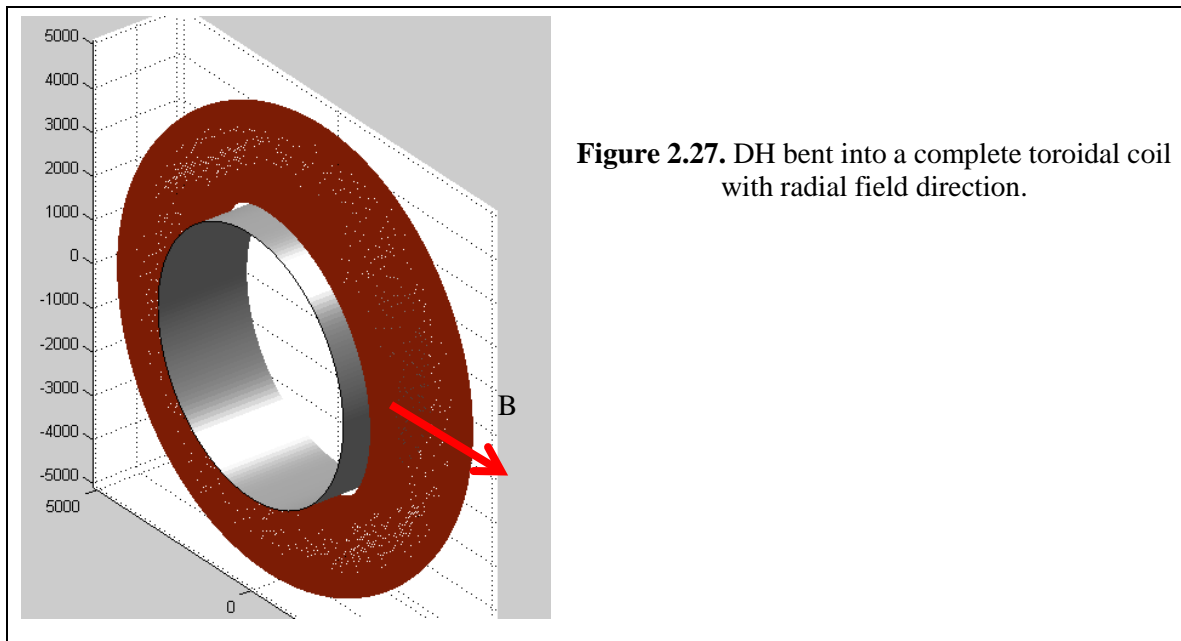
Figure 2.27. DH bent into a complete toroidal coil with radial field direction.
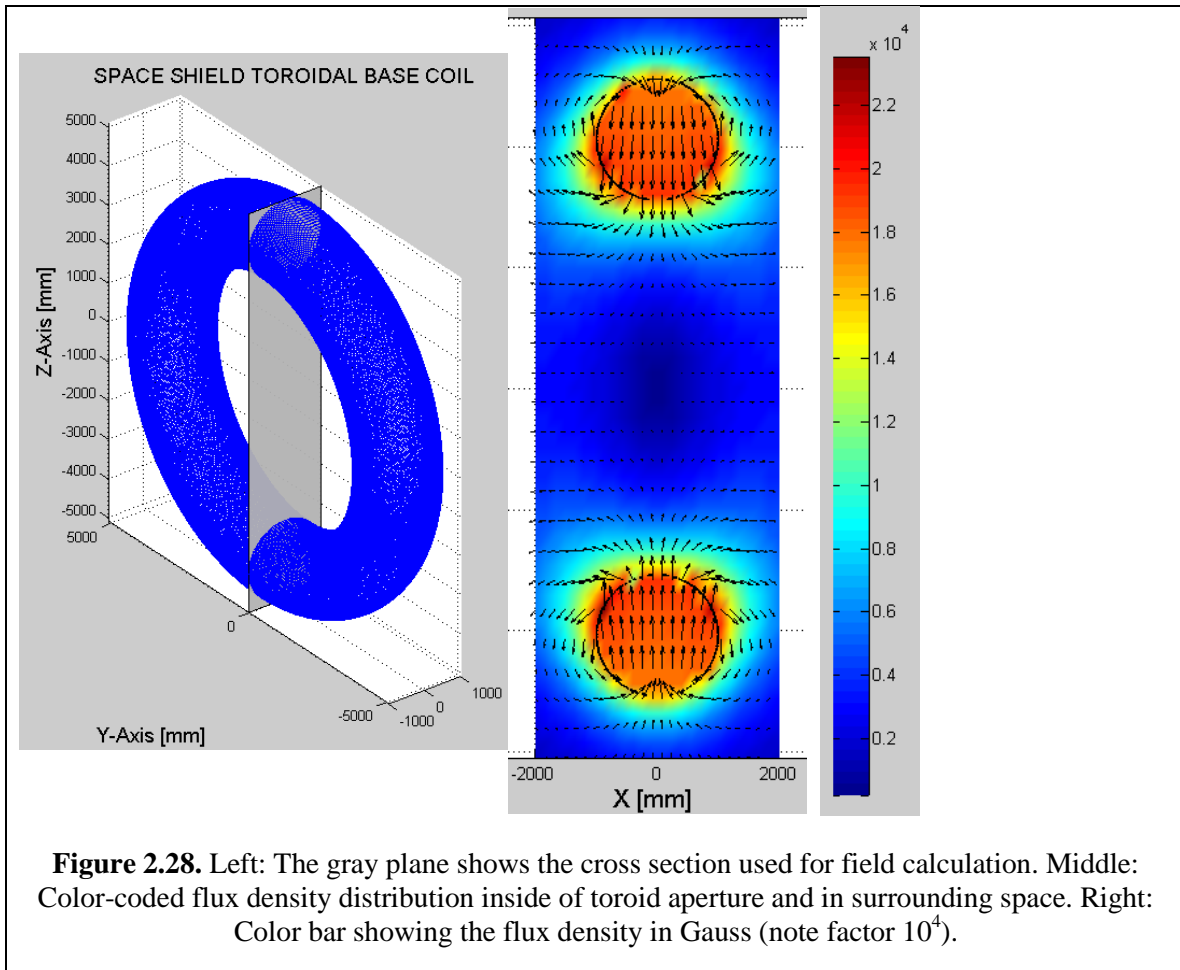
Figure 2.28. Left: The gray plane shows the cross section used for field calculation. Middle: Color-coded flux density distribution inside of toroid aperture and in surrounding space. Right: Color bar showing the flux density in Gauss (note factor 10^4).

Several of such toroidal coils can be stacked up along the length of the spaceship habitat to supply shielding over the full length. A cross section through the resulting array consisting of 5 individual toroids is shown in Figure 2.29. The distance in axial direction between two of the toroids is 500 mm. The current direction in all coils is in the same direction, and as can be seen from Figure 2.29, a significant field enhancement is found between adjacent coils. Based on the fact that the flux from two coils that are adjacent to each other, are in the same direction, the coils will repel each other. Furthermore, some of the flux from a given coil will close itself by passing through the two neighboring coils on both sides, and therefore reduce the flux inside of these apertures. Since the toroid at the end of the system only has a neighboring coil on one side, the flux density in the end toroids is higher than inside of those in the middle (compare Figure 2.29).

The field inside of the spaceship habitat has been analyzed by calculating the flux density in a plane perpendicular to the spaceship axis. Such a plane, intercepting a toroidal coil, is indicated in Figure 2.30. Due to the fact that the field distribution is symmetric in all directions on this plane, the field is calculated along a single straight line, which goes through the center of the toroid. The central 6 m of this line are inside of the habitat; the adjacent 2 m on both sides are inside of the toroidal coil. As can be seen in Figure 2.31, the flux density is rather small in the central part of the spaceship habitat with a

central value of about 42 Gauss only. However, the flux density is rising towards the wall of the habitat (in all radial directions) reaching values of about 1 Tesla.
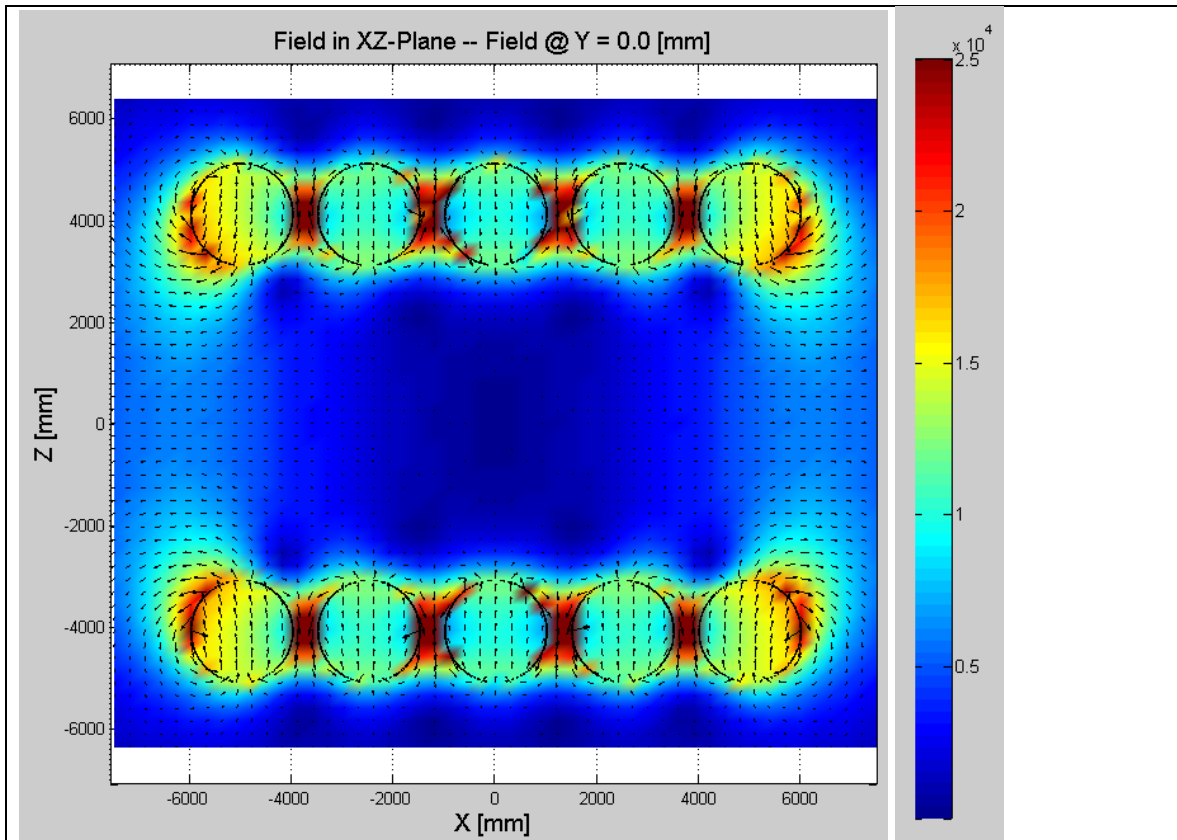
Figure 2.29. Flux density distribution of 5-toroid array with 500-mm gap between adjacent coils.

It is obvious from this analysis that the presented array has significant shortcomings. The neighboring coils reduce the flux density inside of the coil apertures; there are strong fields between adjacent coils, pushing them apart, and the field in the habitat rises in radial direction towards the cylindrical wall of the habitat. It has been tried to improve these shortcomings by increasing the distance between adjacent toroids. The corresponding figures are shown below.

Figure 2.32 shows the flux density in an axial cross section of the whole array for a spacing of 1000 mm between individual toroids. The corresponding flux density in the habitat is shown in Figure 2.33, but for a plane that is located between two toroids (compare Figure 2.34). The field inside of the toroid apertures is increased due to the fact that less flux from neighboring coils is present. The field in the habitat is even lower in the center, but rises even more than for the 500 mm spacing towards the habitat cylinder wall.
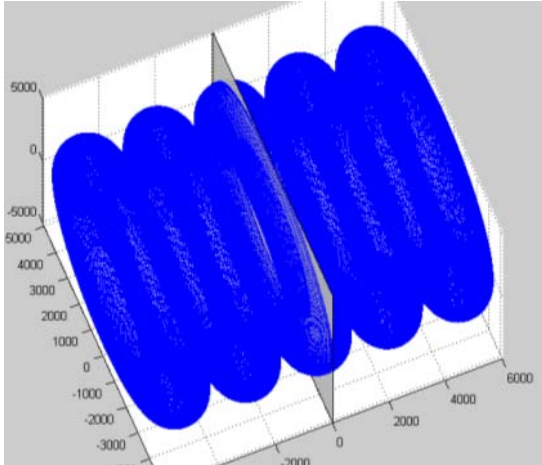
Figure 2.30. Plane through an individual toroid coil, perpendicular to spaceship habitat axis. Gap between toroids is 500 mm.
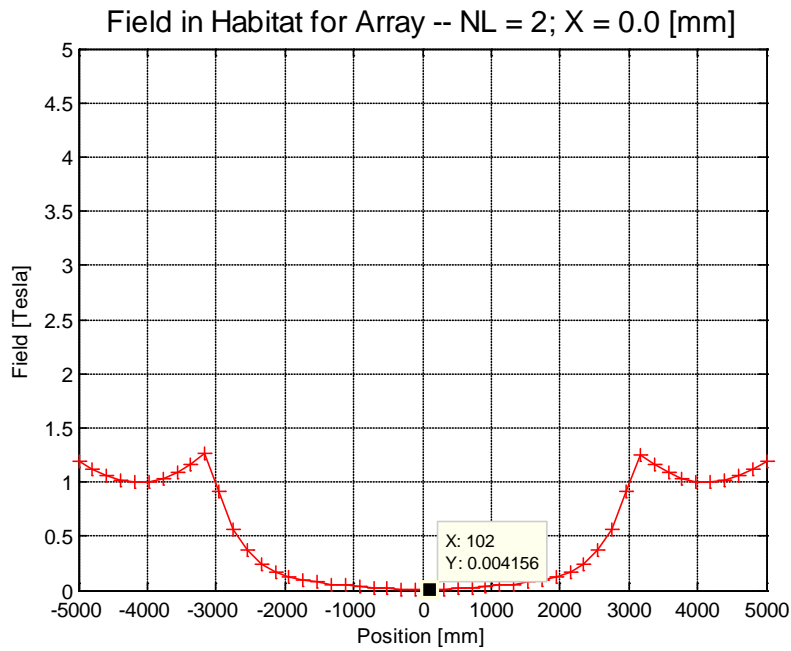
Figure 2.31. Flux density on the plane indicated in the previous Figure showing a field of about 1 Tesla in the coil aperture and a field of about 42 Gauss in the spaceship habitat. Toroid spacing is 500 mm.
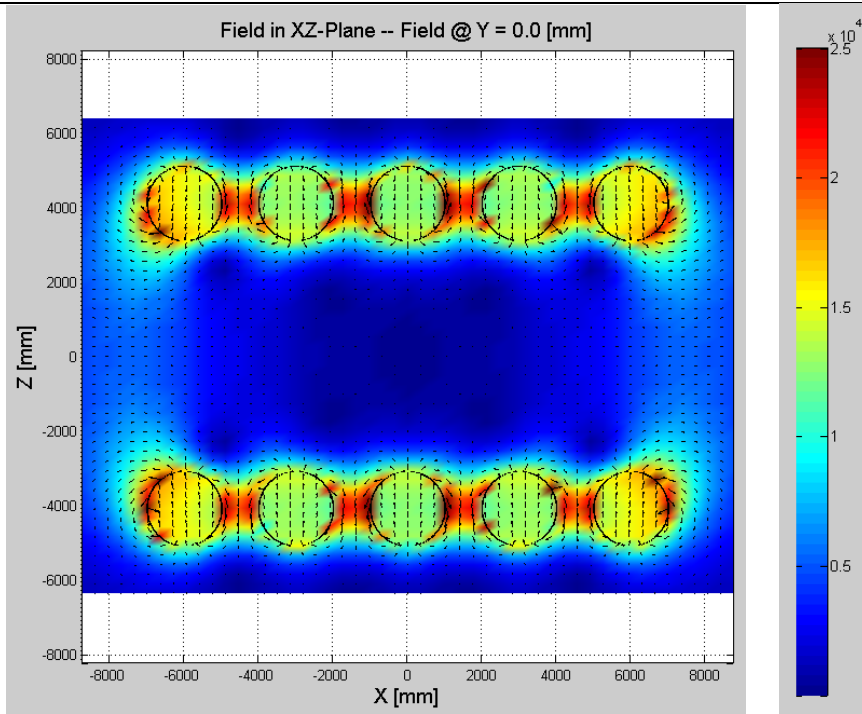
Figure 2.32: Flux density distribution of 5-toroid array with 1000-mm gap between adjacent coils.
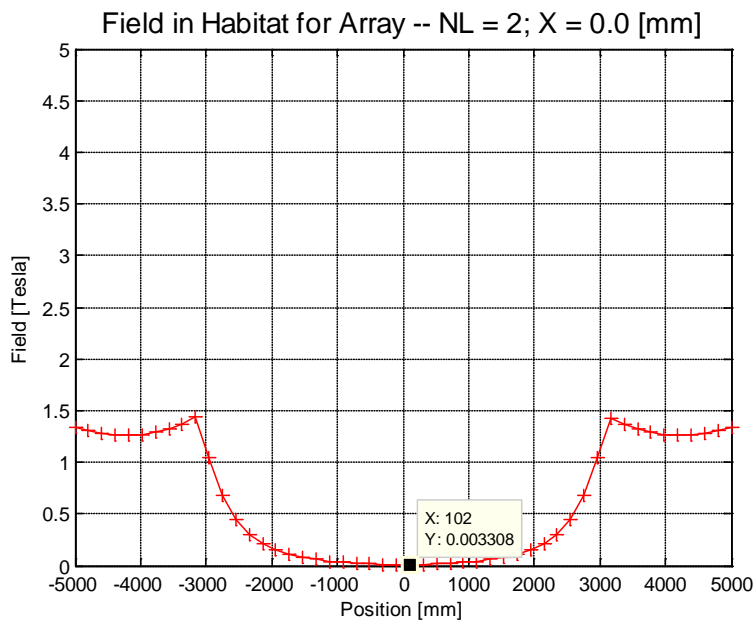
Figure 2.33. Flux density on the plane as indicated in Figure 2.30 for a toroid spacing of 1000 mm.

Figure 2.34. Plane indicating the position, where the field in the habitat is determined. Gap between adjacent toroids is 1000 mm

Figure 2.35. Field in the habitat on the plane indicated in Figure 2.34.
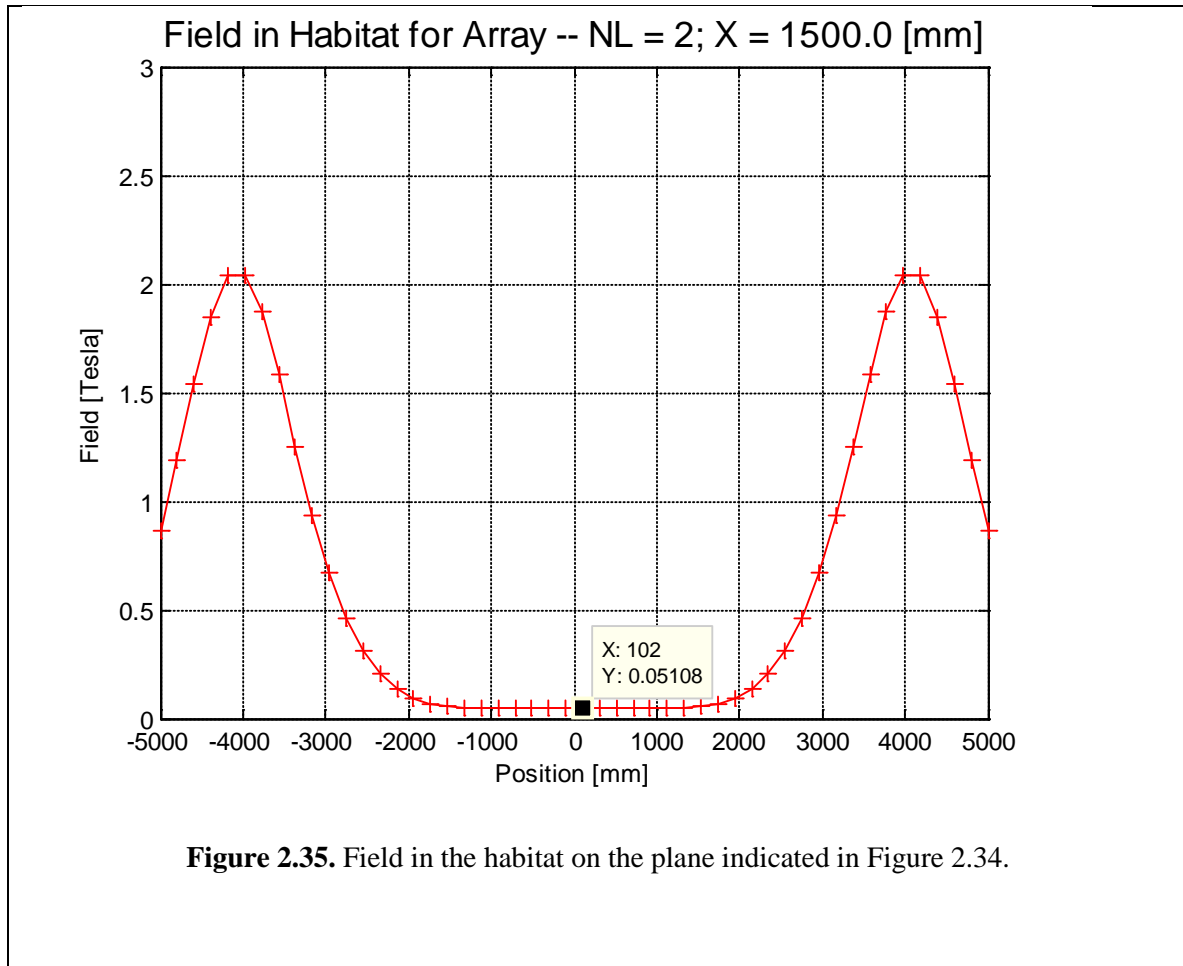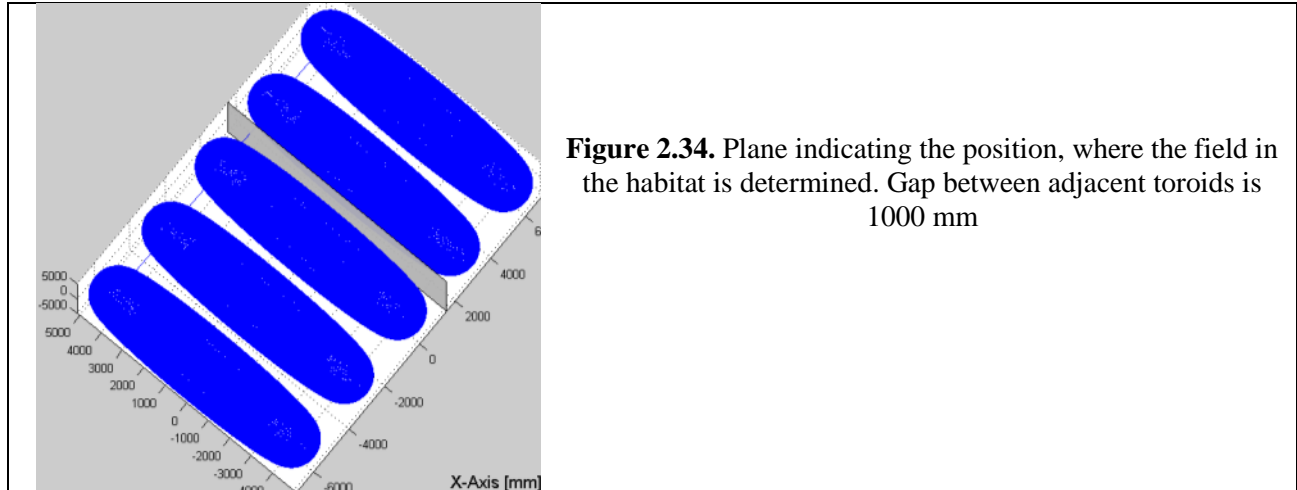
For completeness we are still showing the fields and flux densities for a toroid spacing of 2000 mm. The large gap would have the advantage that a large axial length can be covered with a small number of

individual coils and as shown before there is a significant flux density between adjacent toroids despite the gap between them. Additionally, as shown later, a larger spacing reduces the repulsive forces acting between toroids. The flux density in the whole axial cross section of the shielding array consisting of 5 toroids is shown in Figure 2.36. However, with the spacing of 2000 mm the flux density between two adjacent toroids is now reduced to only about 0.8 Tesla; the field inside of the toroid apertures is still less than the 2 Tesla, which were present in the straight DH coils. The corresponding flux densities inside of the habitat for the 2000 mm spacing are presented in Figure 2.38 and Figure 2.40, the planes used for these calculations are in Figure 2.37 and Figure 2.39.

Figure 2.36. Flux density distribution of 5-toroid array with 2000-mm gap between adjacent coils.
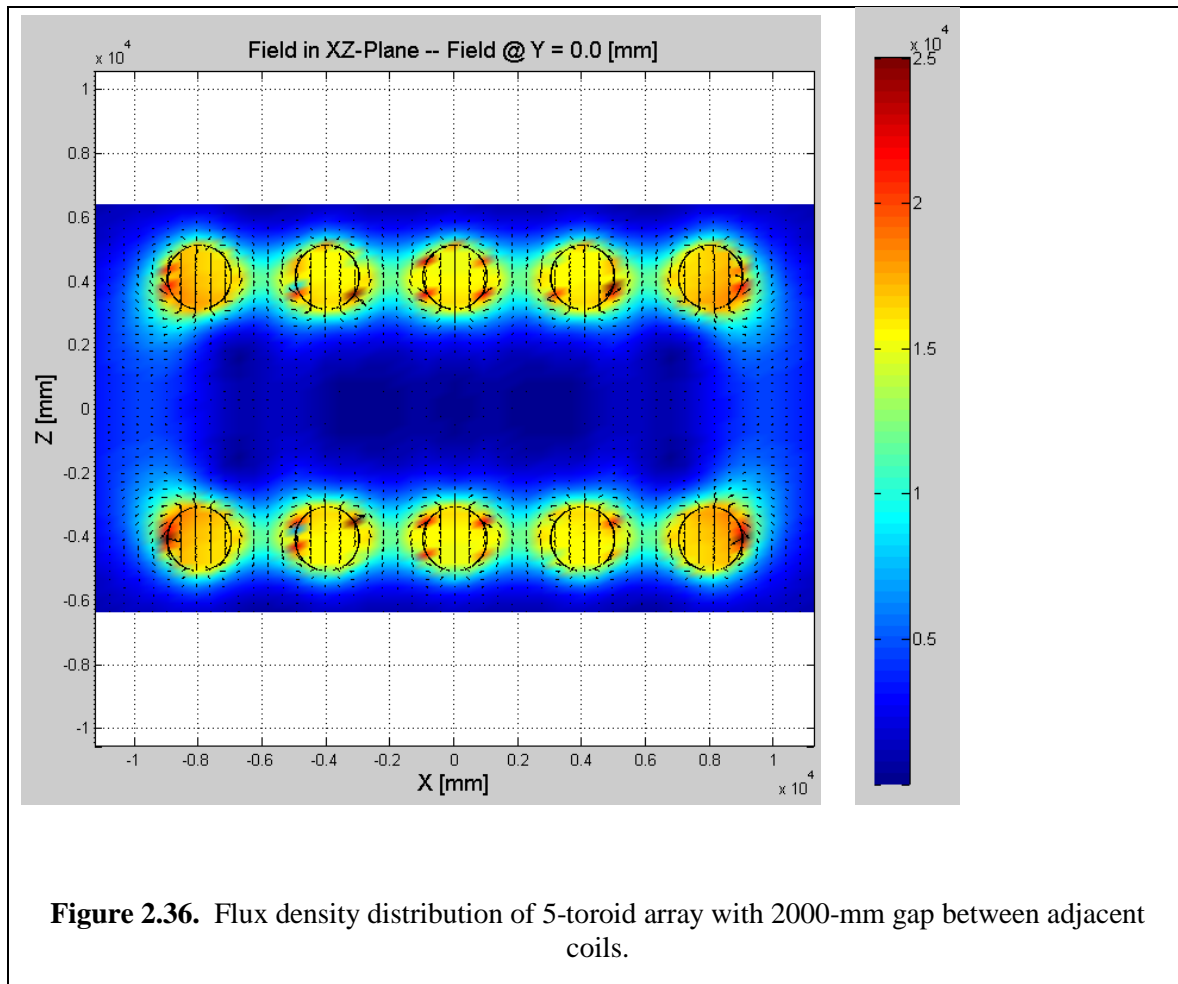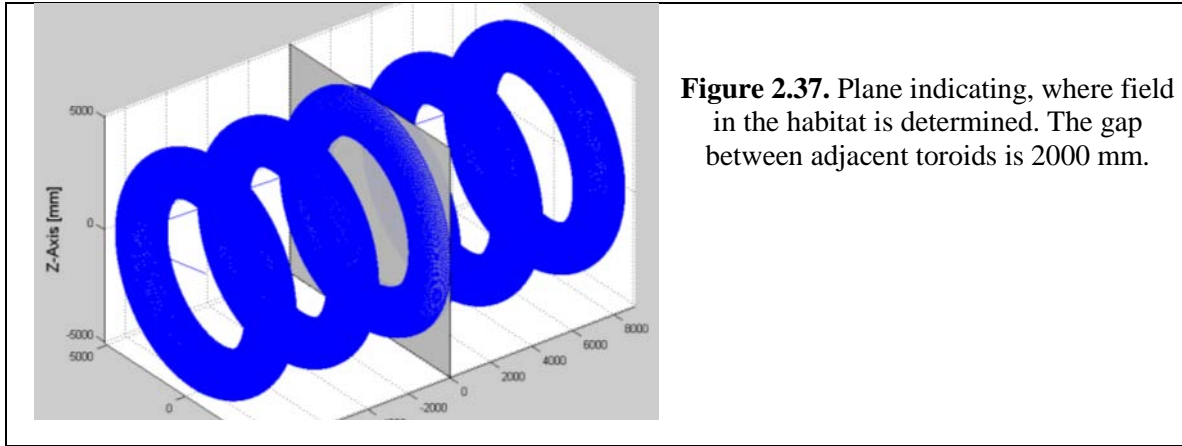
Figure 2.37. Plane indicating, where field in the habitat is determined. The gap between adjacent toroids is 2000 mm.
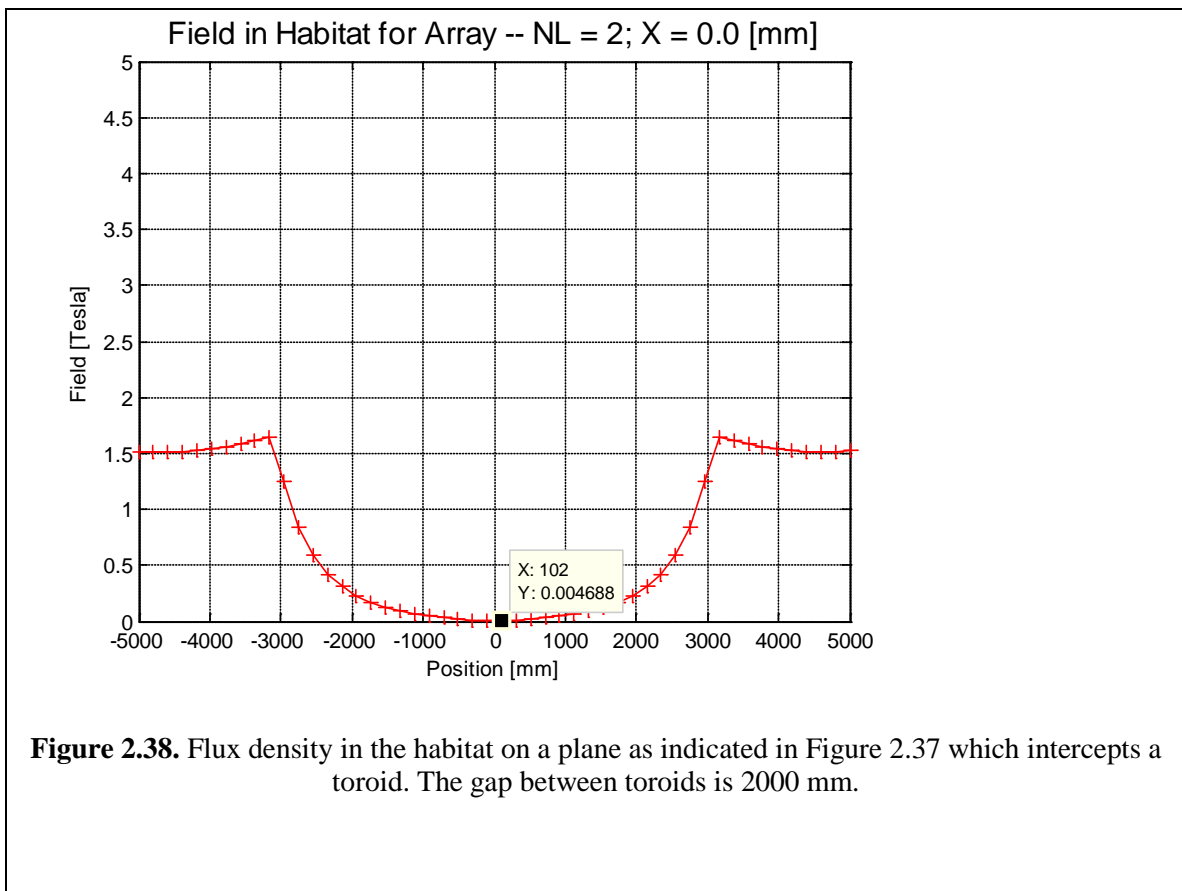
Figure 2.38. Flux density in the habitat on a plane as indicated in Figure 2.37 which intercepts a toroid. The gap between toroids is 2000 mm.

Figure 2.39. Plane indicating, where field in the habitat is determined. The gap between adjacent toroids is 2000 mm.

Figure 2.40. Flux density in the habitat on a plane as indicated in Figure 2.39, which is located in the middle between two toroids. The gap between toroids is 2000 mm.
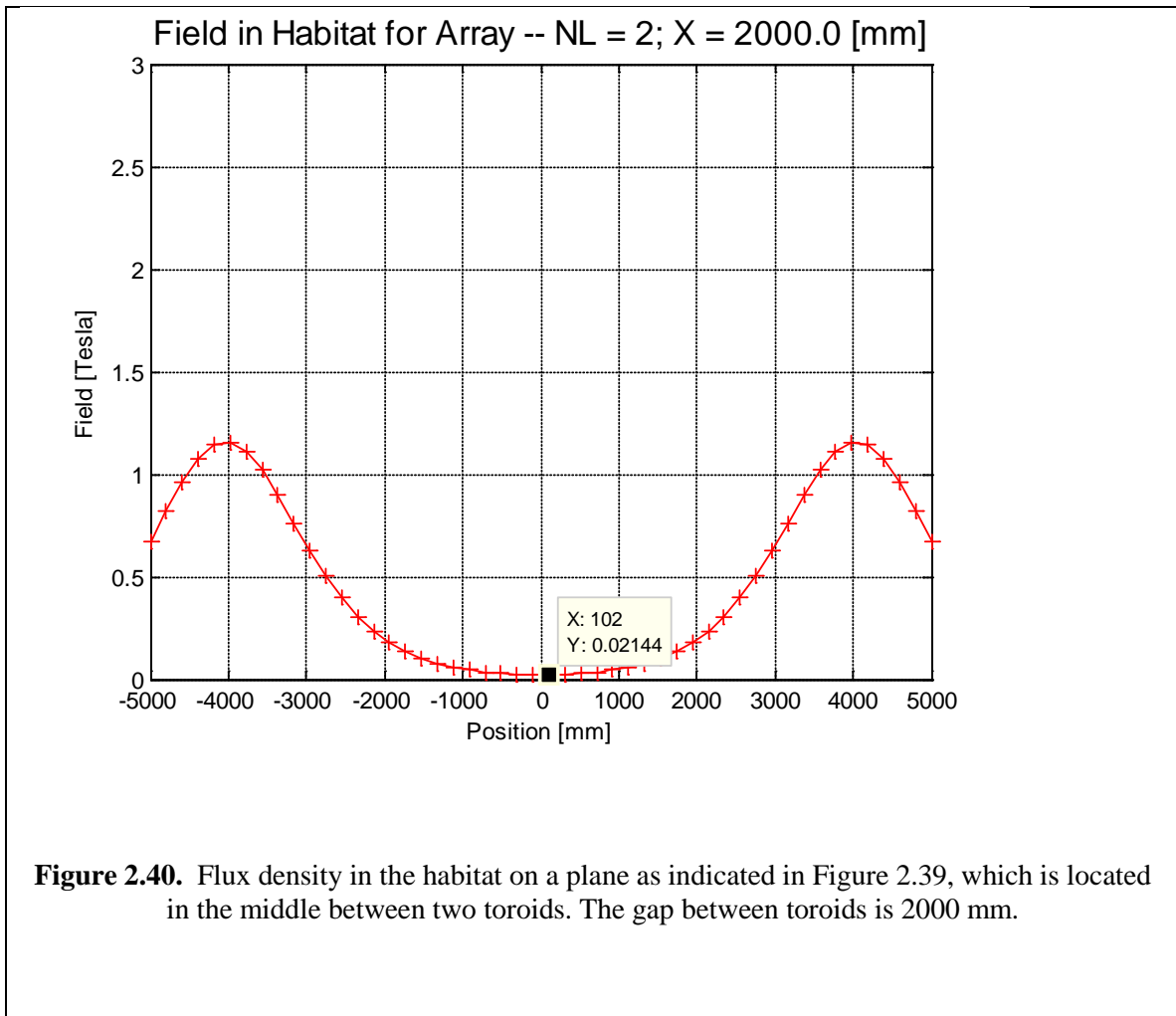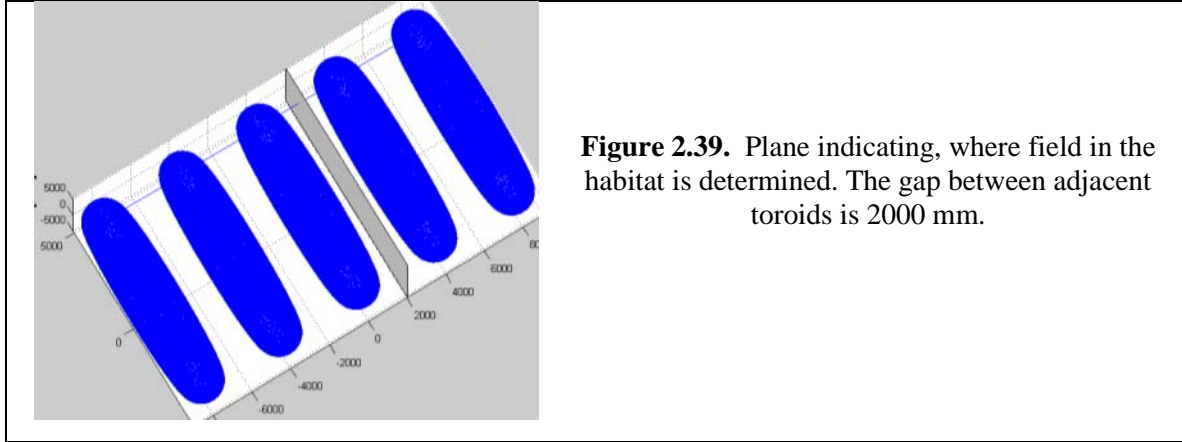
As mentioned before, due to the fact that strong fields are present in the gaps between adjacent toroids, large repulsive forces are present. These forces for the 3 analyzed spacings are presented in Figure 2.41.

Coil Spacing [mm]	Axial Force [MN]	Axial Load [ton]
500	67.8	6780.
1000	40.3	4025.
2000	17.8	1776.

Figure 2.41. Top: Sketch indicating the field direction in the gap between two adjacent toroids. Bottom: Axial forces acting between two adjacent toroids for given toroid spacing.
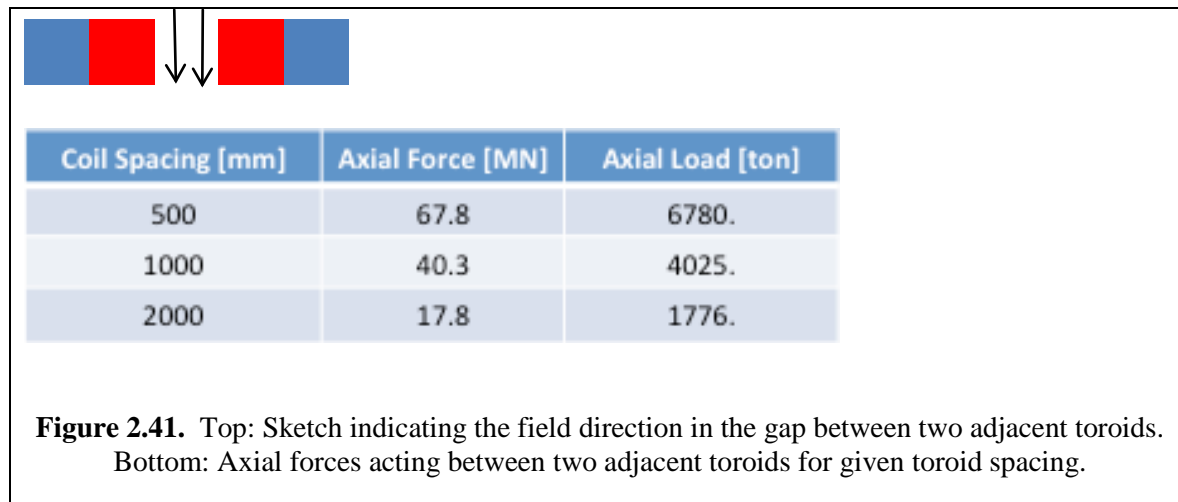
The resulting forces for a case, where one toroid in the middle between its two neighbors is not active, are presented in Figure 2.42.

Coil Spacing [mm]	Axial Force [MN]	Axial Load [ton]
500	9.3	930.
1000	5.4	535.
2000	2.04	204.

Figure 2.42. Top: sketch indicating the field direction in the gap between toroids with the toroid in between missing. Bottom: Axial forces acting between the two outer toroids for given toroid spacing.
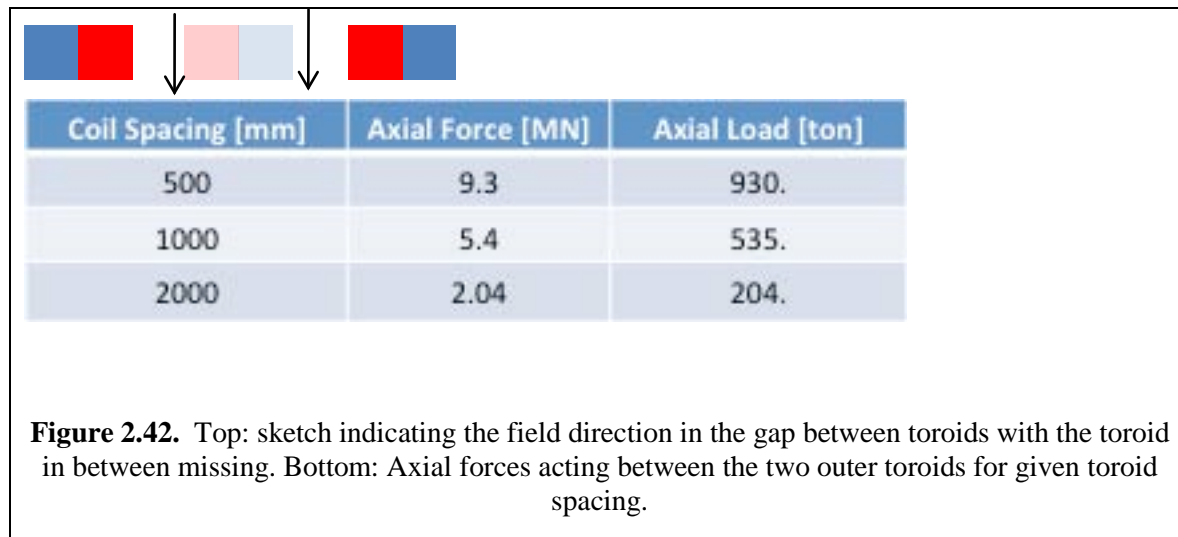
The presented analysis of toroidal coils, which are based on DH coils bent to a full circles with resulting radial fields, can be summarized as follows. On the positive side this configuration system puts no radial pressure on the habitat and the flux density in the habitat away from its cylinder wall are small. However, large repulsive forces act between the toroids in the axial direction and the field in the toroid aperture is significantly smaller than originally in the unbent DH coil. With a transport current of about 54 kA the field in the two-layer straight DH is about 2 Tesla. Due to flux sharing between adjacent toroids however, the field in the apertures is significantly reduced. It would be necessary to increase the

transport current to reach 2 Tesla. The field enhancement of this configuration has not been analyzed. However, it is known that two-layer DH coils in general show significant field enhancement. By bending the DH to a toroid this field enhancement would get even more pronounced. Finally, the radial field direction would not bent incoming charged particles that point toward the habitat center, and the resulting shielding efficiency of this configuration is expected to be poor.

2.2.2. Toroids with Axial Field Direction

In a similar approach as shown in the previous section, a DH base coil with 2-m diameter can be generated with a magnetic field pointing in the Z-direction as shown in Figure 2.43. Based on the fact that a two-layer DH coil is being used, only a transverse magnetic field is presented and the axial field, which still exists in each single layer, is practically completely canceled. The DH coil is then bent in the X-Y plane, as shown in Figure 2.44 to form a complete toroid. In order to fit around the spaceship cylinder, the toroid is rotated around the Y-axis (the spaceship cylinder axis coincides with the X-axis). The length of the generated DH has been chosen to form a toroid that fits around the spaceship diameter of 6 m. As in the previous case, by bending each of the two layers individually, the tilted coil ends of the DH fit exactly together when bent to a circle, without leaving any gap between the two ends.
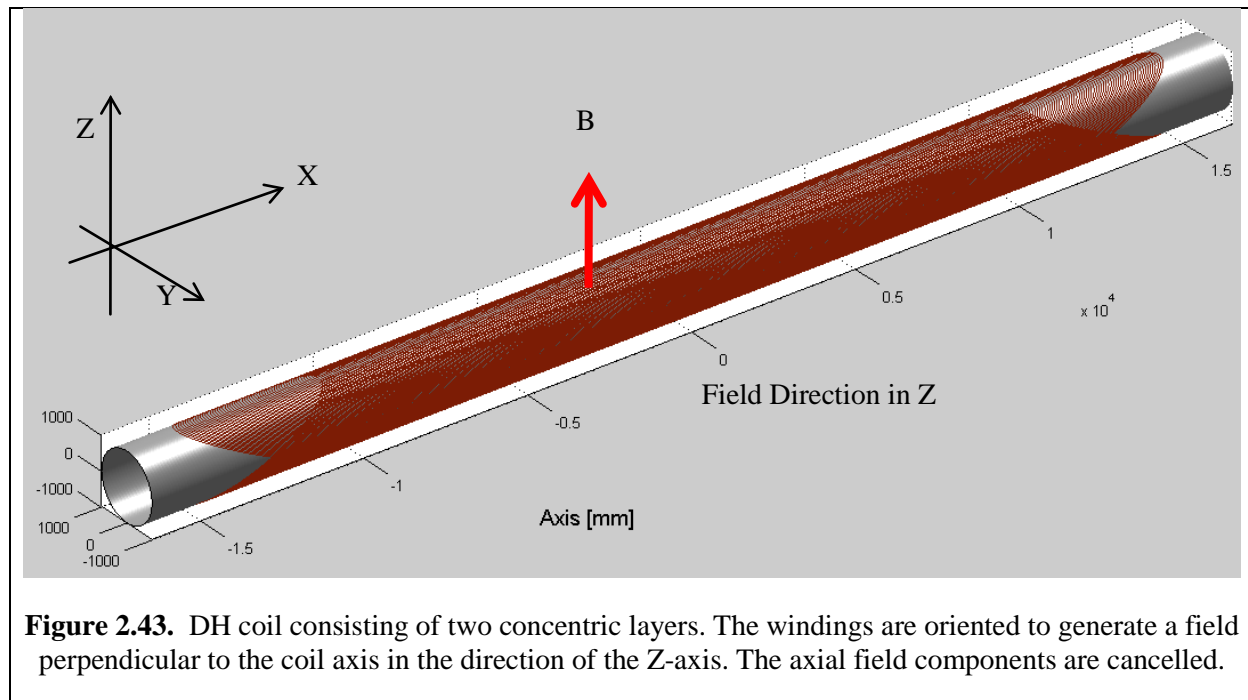
Figure 2.43. DH coil consisting of two concentric layers. The windings are oriented to generate a field perpendicular to the coil axis in the direction of the Z-axis. The axial field components are cancelled.
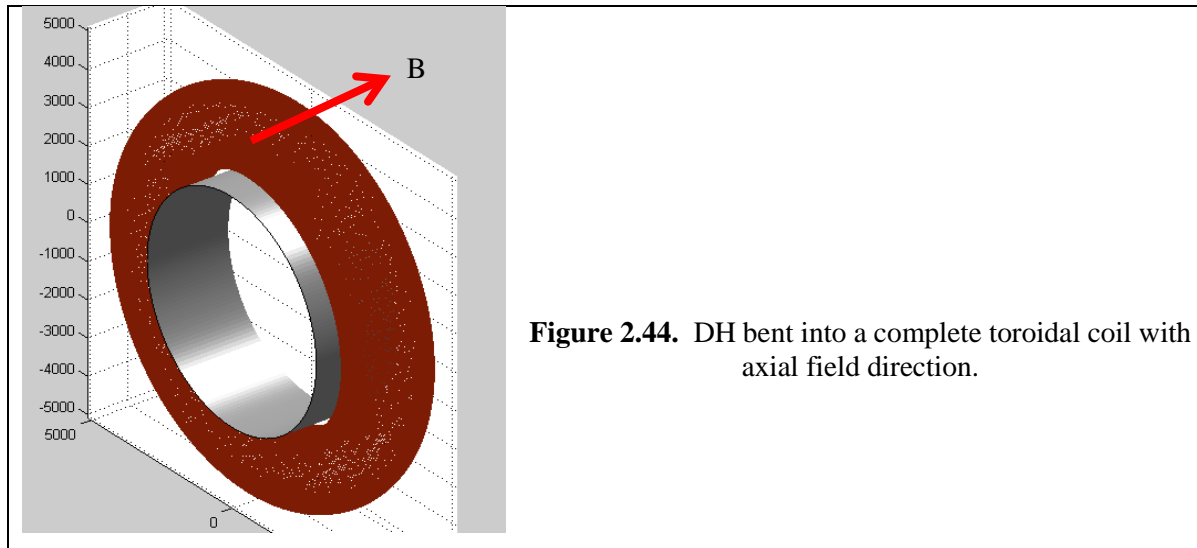
Figure 2.44. DH bent into a complete toroidal coil with axial field direction.

Based on the field direction in the straight DH coil, the field direction of the final toroid is in the axial direction. The resulting field direction can be seen in Figure 2.45, which shows a cross section through the toroidal coil. The plane of the cross section is shown on the left hand side of the figure; the flux density and the field direction are shown on the right of Figure 2.45. As can be seen from the color-coding in the cross section and the color bar, the flux density is about 2 Tesla. However, it is important to point out that the external field of the toroid, as generated here, is not zero on the outside. Due to the fact that the flux inside of the straight DH coil is perpendicular to the coil axis, the flux clearly extends to the outside of the aperture.

Figure 2.45. Left: The gray plane shows the cross section used for field calculation. Middle: Color-coded flux density distribution inside of toroid aperture and in surrounding space. Right: Color bar showing the flux density in Gauss (note factor 10^4).
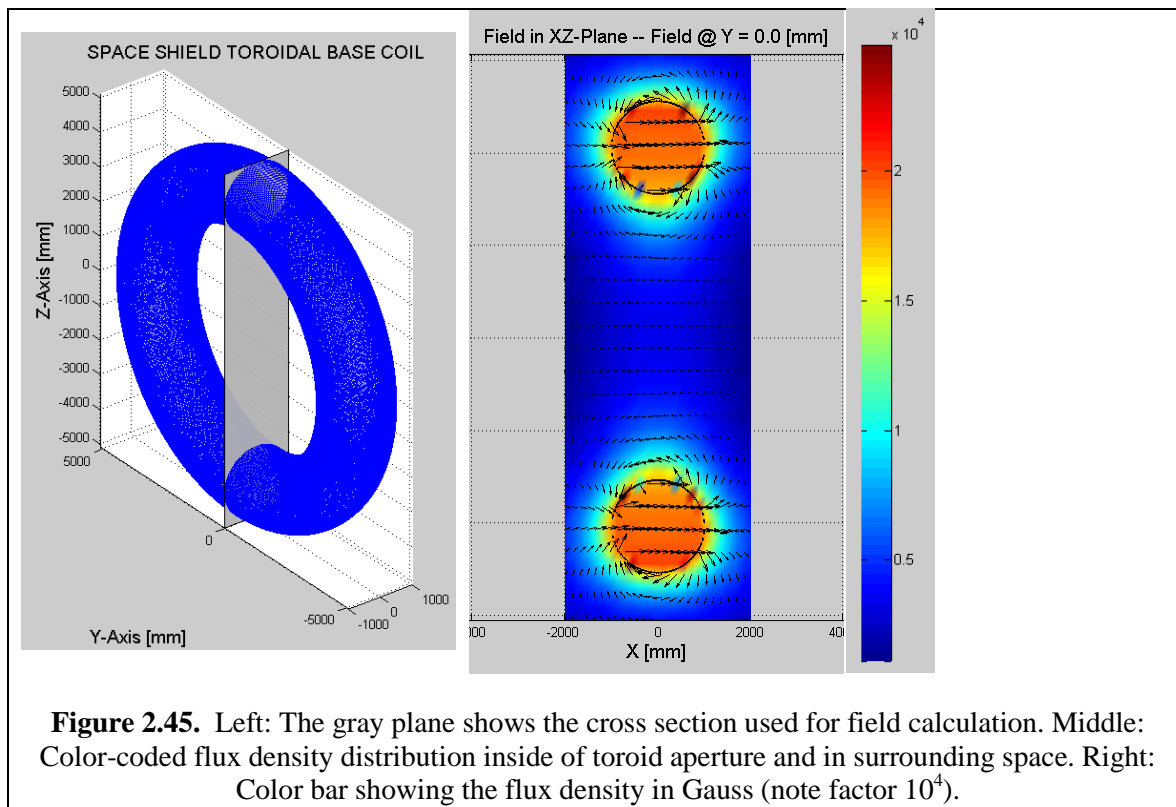
Several of such toroidal coils can be stacked up along the length of the spaceship habitat to supply shielding over the full length. A cross section through the resulting array consisting of 5 individual toroids is shown in Figure 2.46. The distance in axial direction between two of the toroids is 500 mm.

With the current direction in all coils is in the same direction, the flux leaving one coil enters the neighboring coil, where it enhances the field. Since the toroid at the end of the system only has a neighboring coil on one side, the field enhancement is weaker in the end coils. The flux density in the gap between two adjacent toroids leads to attractive forces between the coils.

As in the previous section for toroids with radial field direction, configurations with different spacings have been analyzed, and for all cases the flux density in the habitat has been determined. The following figures show different cases that have been analyzed. The figure captions describe the toroid spacing and the location of the intersecting planes used for flux density calculations in the spaceship habitat. Finally, forces acting between the toroids for spacings of 500, 1000 and 2000 mm are summarized in Figure 2.52 and Figure 2.53.

Figure 2.46. Flux density distribution of 5-toroid array with 500-mm gap between adjacent coils.
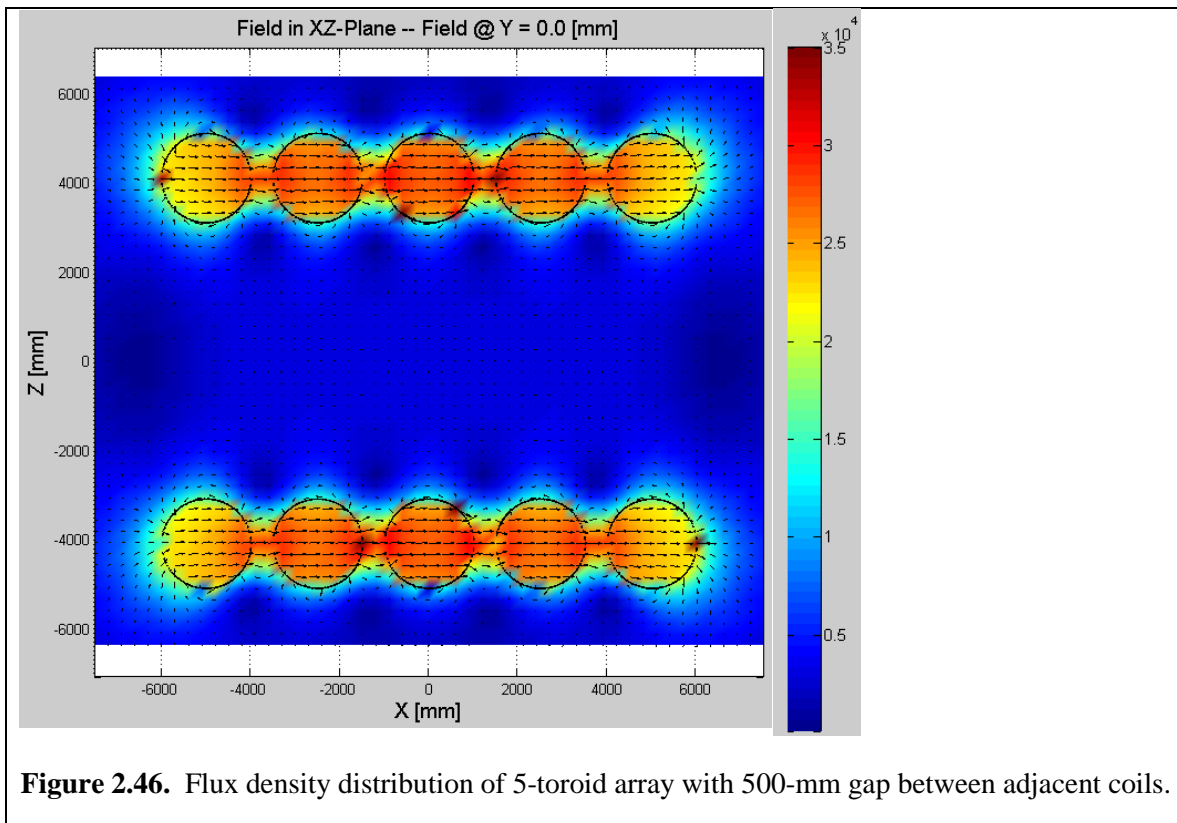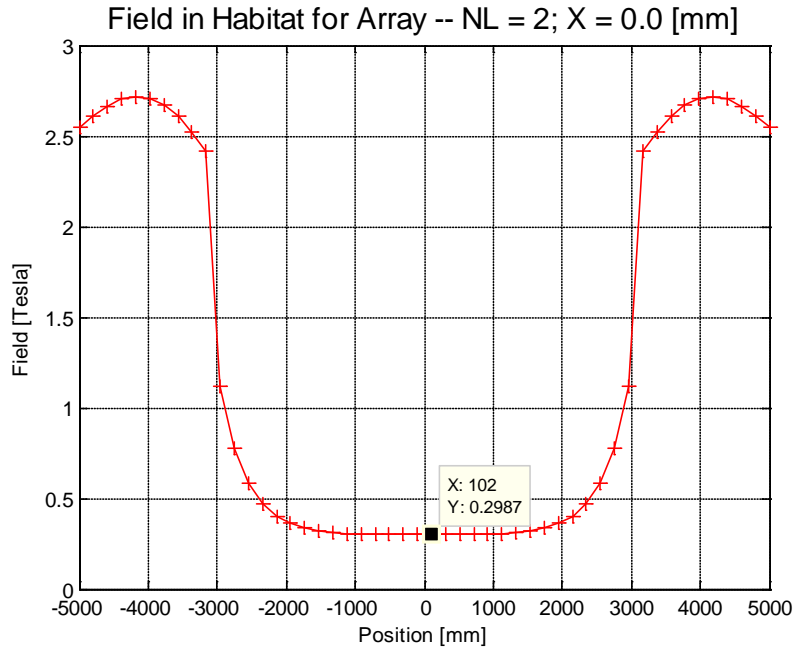
Figure 2.47. Intersection through middle of toroid coil. Gap 500 mm
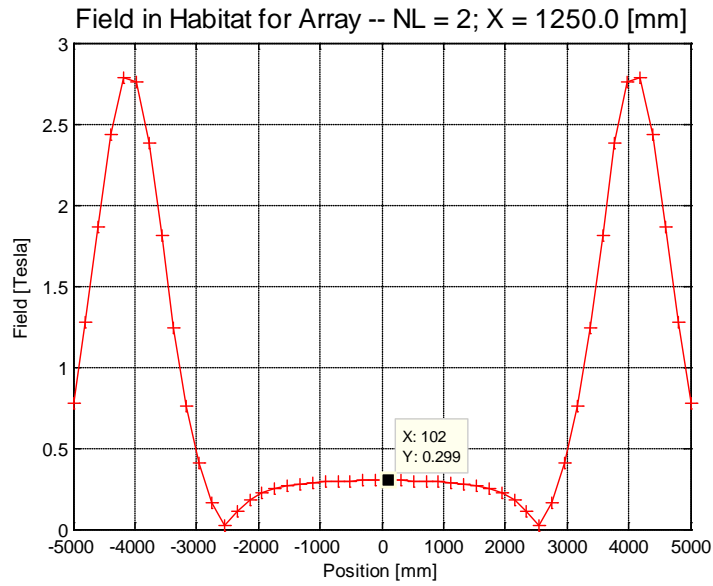
Figure 2.48. Intersection in the middle between two adjacent toroids. Gap 500 mm

MAARSS
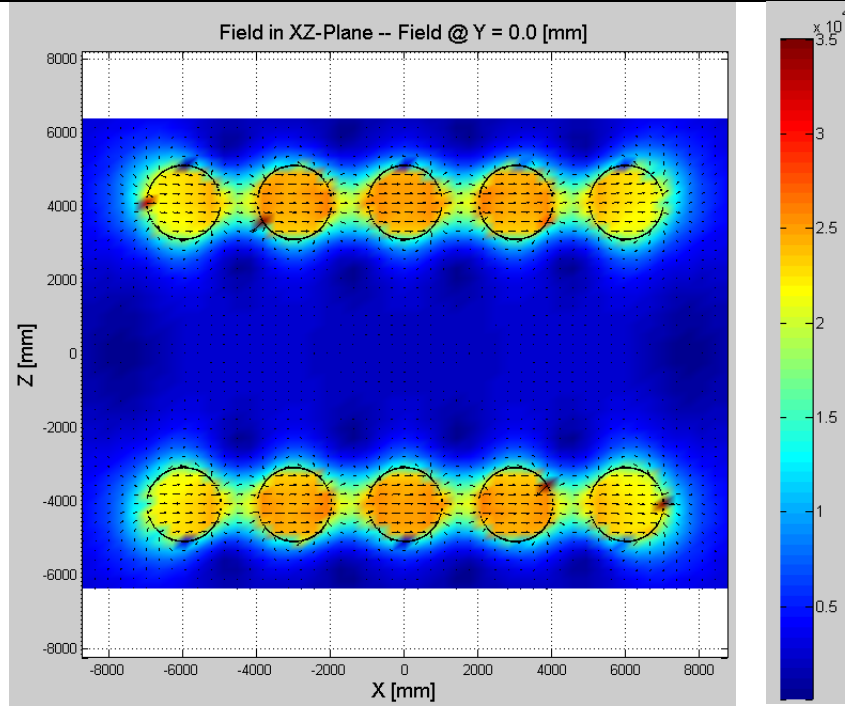
Figure 2.49. Flux density distribution of 5-toroid array with 1000-mm gap between adjacent coils.
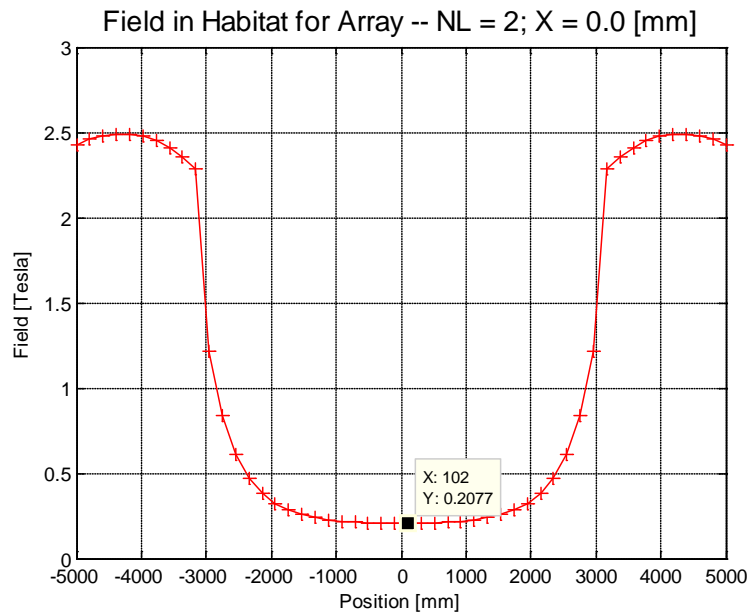
Figure 2.50. Flux density along a line perpendicular to spaceship axis on a plane through a toroid. Gap between toroids 1000 mm.

Figure 2.51. Flux density along a line perpendicular to spaceship axis on a plane in the middle between two toroids. Gap between toroids 1000 mm.

Coil Spacing [mm]	Axial Force [MN]	Axial Load [ton]
500	60.58	6058
1000	34.77	3477
2000	14.59	1459

Figure 2.52. Top: Sketch indicating the field direction in the gap between two adjacent toroids. Bottom: Attractive force acting on the end coil.

Coil Spacing [mm]	Axial Force [MN]	Axial Load [ton]
500	7.60	760.
1000	4.58	458.
2000	2.17	217.

Figure 2.53. Top: sketch indicating the field direction in the gap between toroids with the one in between missing. Bottom: Corresponding attractive force acting on the end coil.

The presented analysis of toroidal coils, which are based on DH coils bent to full circles with resulting axial fields, can be summarized as follows. On the positive side this configuration system puts no radial pressure on the habitat. However, the flux density in the habitat is very large, i.e., in the range between 0.2 Tesla and 0.3 Tesla depending on the toroid spacing. Instead of large repulsive forces, with the axial field directions strong attractive forces act between toroids. The whole configuration tries to bunch together in the mid plane that is perpendicular to the spaceship axis. Due to flux sharing between neighboring coils, the field in the toroid aperture is significantly larger than originally in the unbent DH coil.

The field enhancement of this configuration has not been analyzed. However, it is known that two-layer DH coils in general show significant field enhancement. By bending the DH to a toroid this field enhancement would get even more pronounced. The field enhancement due to flux sharing can most likely be neglected in this respect, since the operational current could be reduced accordingly to produce a flux density of 2 Tesla in the toroid apertures.

2.2.3. A 6+1 Configuration

All field configurations that have been analyzed so far assumed integrated fields in the individual coil apertures of about 4 Tesla*meter. However, while the performed Monte-Carlo shielding efficiency calculations show that higher integrated fields are required for many missions, the considered coil configurations show already shortcomings and technical difficulties for the assumed field integral of 4 Tesla*meter. Key issues that have been identified are unacceptable high fields in the spaceship habitat, large compressive forces acting on the habitat, and the issue of building coils that are flexible enough, so that they can be folded for the launch and expand under acting magnetic pressure when excited. All of these issues become even more pronounced for higher field integrals.

To achieve expandability of coils, single layers are the most realistic approach, and the DH coil configuration is therefore excluded. Single layers of DH coils, i.e., solenoidal windings with tilted turns, which simultaneously provide axial and transverse magnetic fields, have been considered under this project. Such configurations could have sufficient flexibility, but would still have the other disadvantages of the DH configuration.

Figure 2.54. Coil configuration consisting of 6 solenoid coils surrounding a cylindrical spaceship habitat.
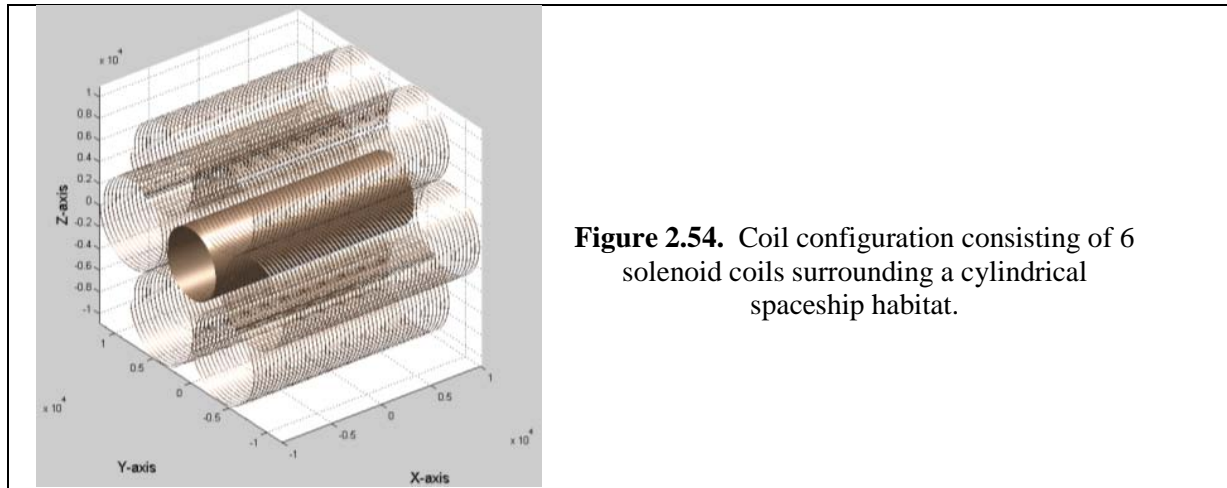
Concerning scalability to higher integrated fields it seems clearly advantageous to consider larger diameter coils instead of increasing the field strength (flux density). This is due to the fact that the forces acting on coil windings and the resulting magnetic pressure increase with the square of the field strength, and a significant increase in coil support structure is needed for increased field strength. Furthermore, the current carrying capacity of superconductors decreases with field strength, and for this reason lower field strength is preferred.

It was therefore decided to investigate a configuration, which consists of single-layer solenoidal coils that surround the spaceship habitat. Such a system is shown in Figure 2.54. While the solenoidal coils are the easiest solution in respect to coil manufacturing and put no pressure on the habitat, since they repel each other, they still have the problem that flux from the solenoids ends traverses the habit. A potential solution to this flux return problem would be to channel the flux with additional coils from one solenoid to another. Such a solution is in principle possible and is shown in Figure 2.55 and Figure 2.56. Such coil configurations would solve the problem of flux density in the habitat, but would require very complex coils, and the coil bends would be subject to very large forces to keep them in the required shape. These solutions have therefore been discarded from further analysis.

Figure 2.55. Left: Two flux channel coils, i.e., solenoids in which the flux passes from one end to the other. Right: Two solenoids with bent coil ends to facilitate flux return from one coil end to the other.
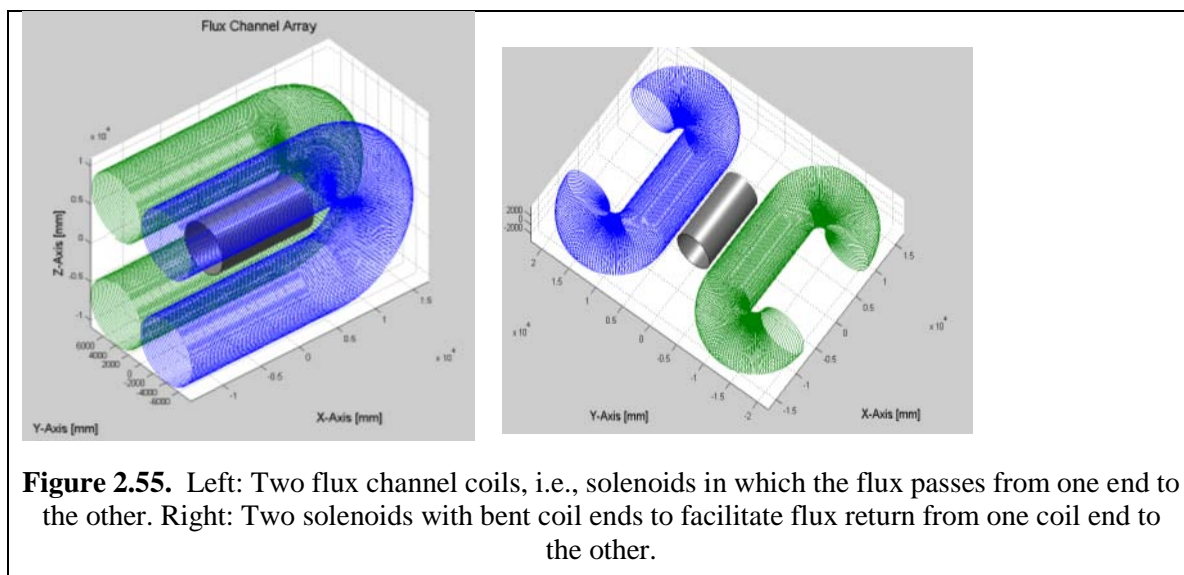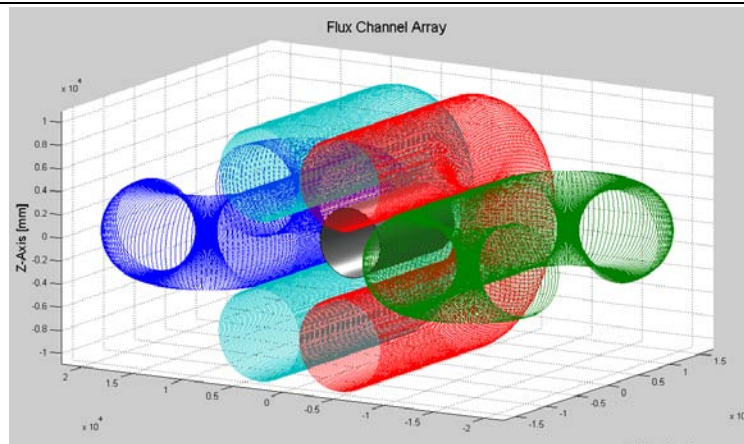
Figure 2.56. Complete shielding array consisting of 2 flux channel coils and 2 solenoids with coil ends that bend the return flux away from the habitat.

After analyzing these different coil configurations a novel concept was considered, namely compensating the flux, which returns through the habitat with an additional coil that surrounds the habitat. This concept has many advantages and emerged as the most promising solution for an active magnetic shielding system. It consists of 6 solenoidal coils with 8-m diameter and lengths of 15 m to 20 m which surround the spaceship habitat.

A solenoidal geometry is well suited to the application of a wide (50 mm to 100 mm) 2nd generation tape conductor. The single-layer coils, the preferred solution for expandable coils, operate at a current of about 40 kA. The field in the individual solenoids is 1 Tesla. Given the 8-m diameter of the solenoids the integral BdL of an individual coil is 8 Tesla*m, which is a substantial improvement in shielding efficiency over the original assumed 4 Tesla*m.

The solenoids are arranged at a radial distance of 1 m around the central spaceship habitat, which is assumed to have a diameter of 6 m. The extra space between the habitat and the shielding coils is needed for mechanical reasons.

Solenoidal coils have far reaching external fringe magnetic fields, which can affect the shielding efficiency. However, due to this fringe magnetic field, a substantial flux leaks into the habitat region. This field can be completely canceled with an additional compensation coil that surrounds the habitat cylinder in close proximity (see Figure 2.57). This compensation coil also functions as a thermal shield against thermal radiation from the habitat. Since the habitat itself constitutes a large heat source in deep space, the shielding of its thermal radiation is of significant value.

The complete system of 6 solenoid coils with the compensation coil surrounding the spaceship habitat is shown in Figure 2.58. The individual solenoids are 20 m long and have a diameter of 8 m. The length of the compensation coil is to be determined; its length has to be optimized. The flux density in an individual, isolated solenoid coil is shown in Figure 2.59. With an operational current of about 43 kA the flux density is about 1 Tesla over a central length of about 10 m. The coil, as shown, consists of 400 turns of a 50-mm wide 2nd generation YBCO tape.

Figure 2.57. Shielding solenoid coil surrounding the cylindrical habitat volume of the spaceship. The length is TBD and needs to be optimized.

Figure 2.58. System of 6 solenoid coils surrounding the habitat (shown in gray) with a compensation coil around the habitat (shown in red), and the spaceship habitat (shown in darker gray on the inside) with a length of 10 m and a diameter of 6 m.
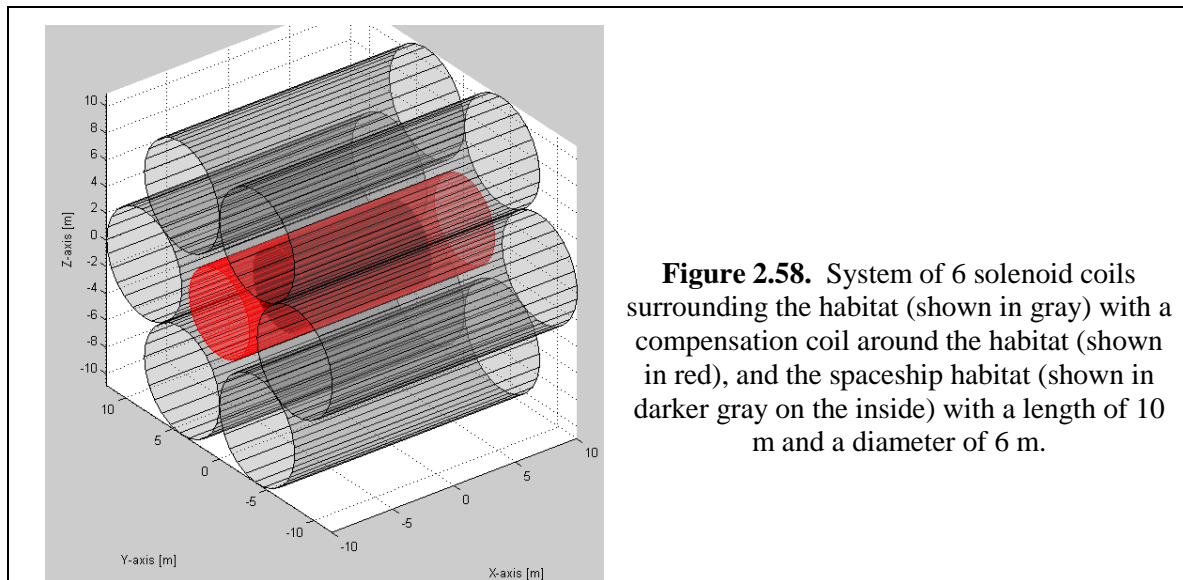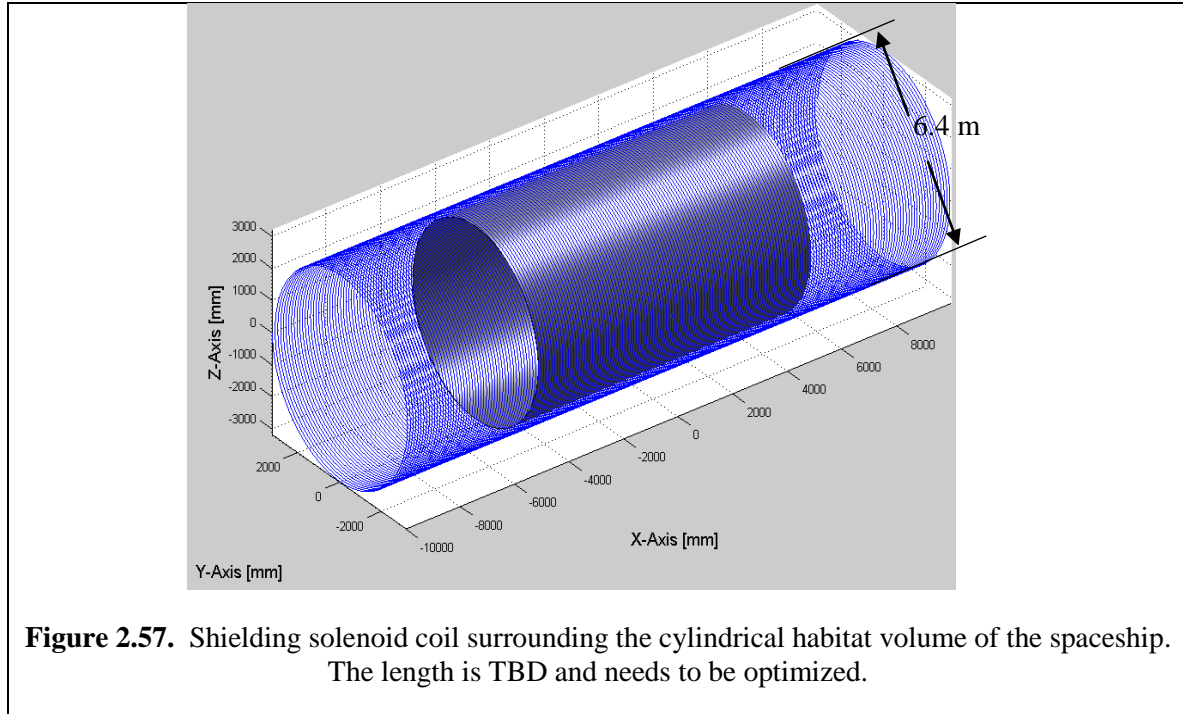
The flux density of the complete system in the cross section shown in Figure 2.60 has been determined and is presented in Figure 2.61. As can be seen the flux density in the central part in axial direction of the solenoids is about 1 Tesla. The flux density in the habitat region with a length of 10 m is to a good approximation constant and therefore facilitates the realization of a compensation solenoid, which cancels the flux density in the habitat. To cancel the field in the habitat the current direction of the compensation coil is opposite to the current direction in the outer shielding solenoids.

Figure 2.59. Axial field of solenoid base coil with the following parameters: Coil Radius = 4000 mm, Number of turns = 400, tape spacing = 50 mm, coil length = 20,000 mm, and operational current = 43,500 A.

Figure 2.60. Shielding solenoid coils showing equatorial plane used for field analysis.

Figure 2.61. Flux density distribution in the equatorial plane shown in Figure 2.60.
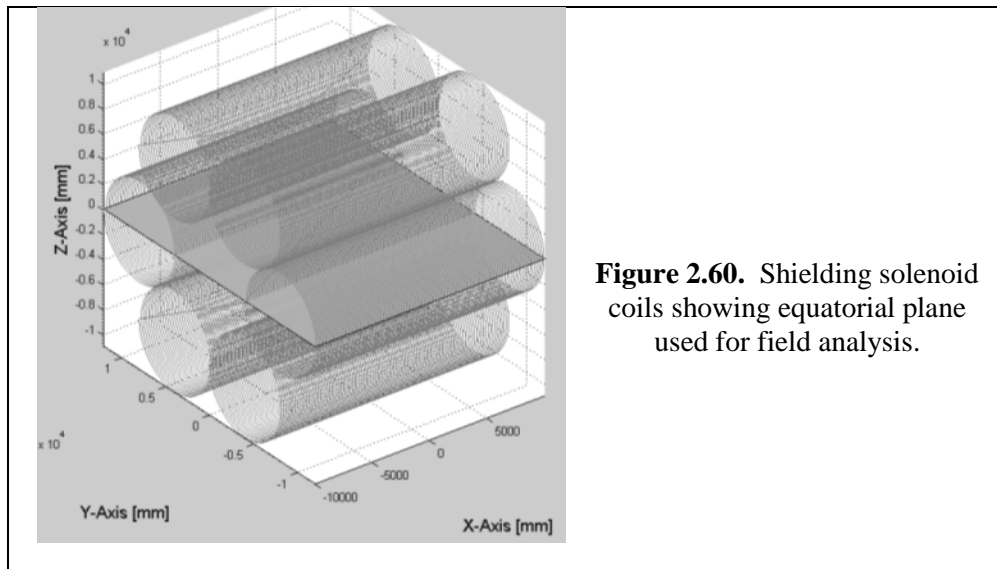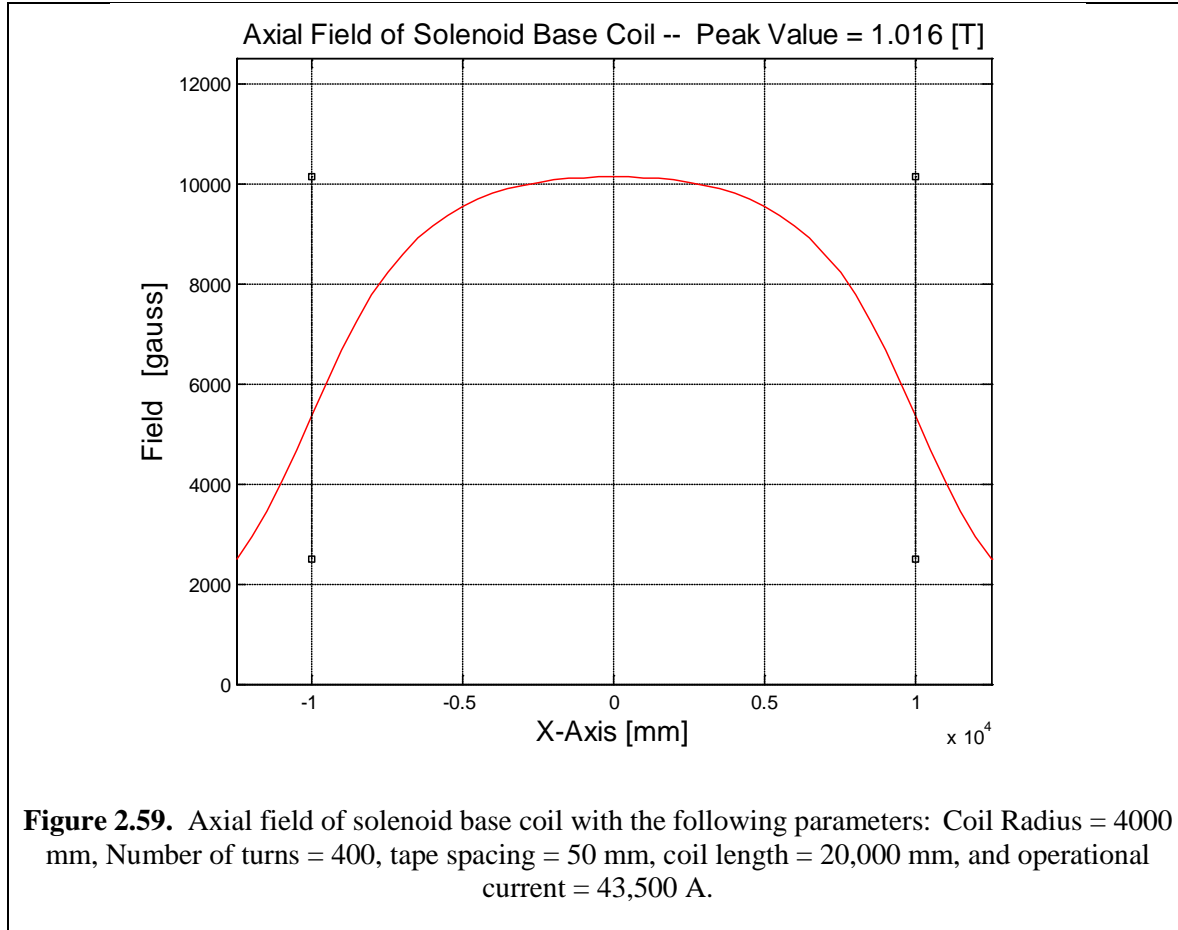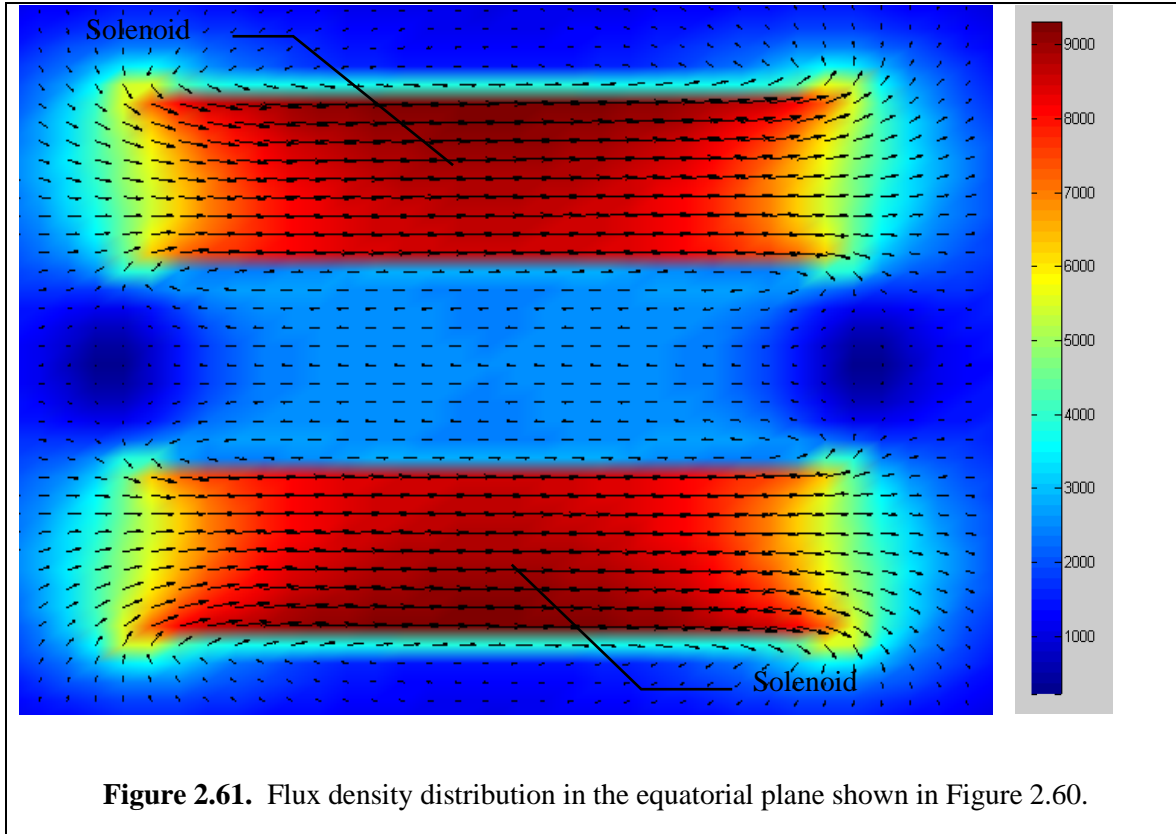
The integrated field (BdL) along a straight line passing through the center of a shielding coil has been determined. Due to the return flux from all shielding solenoids, which is opposite to the internal flux, the flux density in the array configuration is affected and slightly reduced. Figure 2.62 shows an isolated solenoid next to the habitat. The corresponding integrated field is presented in Figure 2.63.

Figure 2.62. Individual solenoid coil next to habitat cylinder.

45
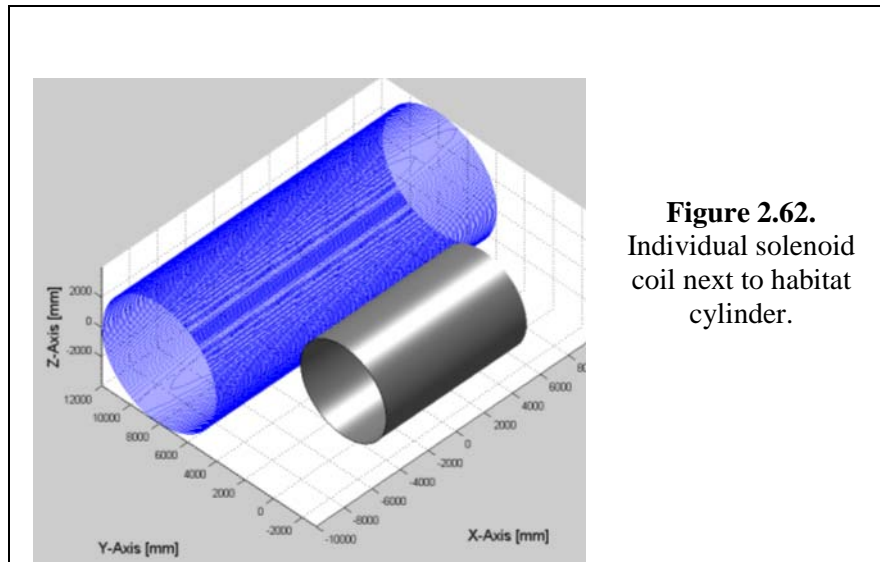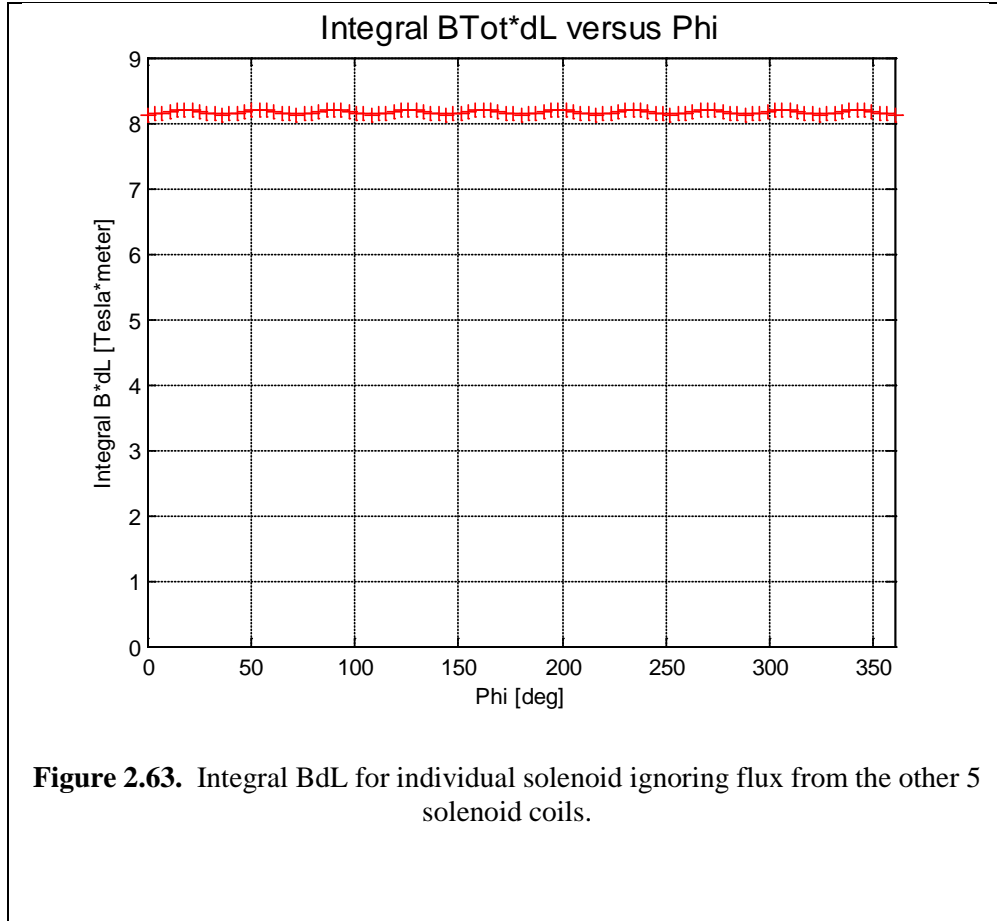
Figure 2.63. Integral BdL for individual solenoid ignoring flux from the other 5 solenoid coils.

As can be seen in Figure 40, the integrated field in this case is about 8 Tesla*meter. However, the integrated field when determined in the array configuration is slightly reduced. The analyzed configuration is shown in Figure 2.64. The corresponding integrated field presented in Figure 2.65 is reduced and shows a value of about 7 Tesla*meter. An increase in operational current would bring the value back to 8 Tesla*meter.
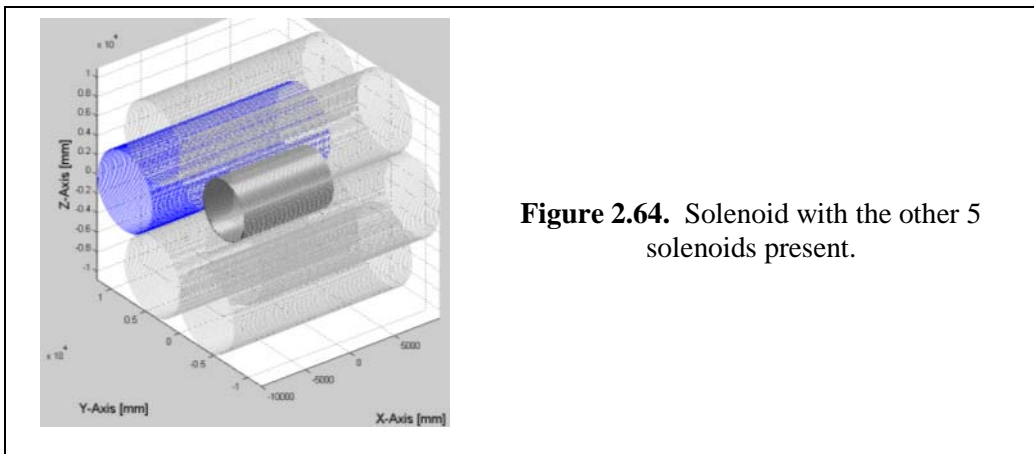
Figure 2.64. Solenoid with the other 5 solenoids present.

Figure 2.65. Integral BdL in individual solenoid coil with the other 5 solenoids present and contributing to the flux density.
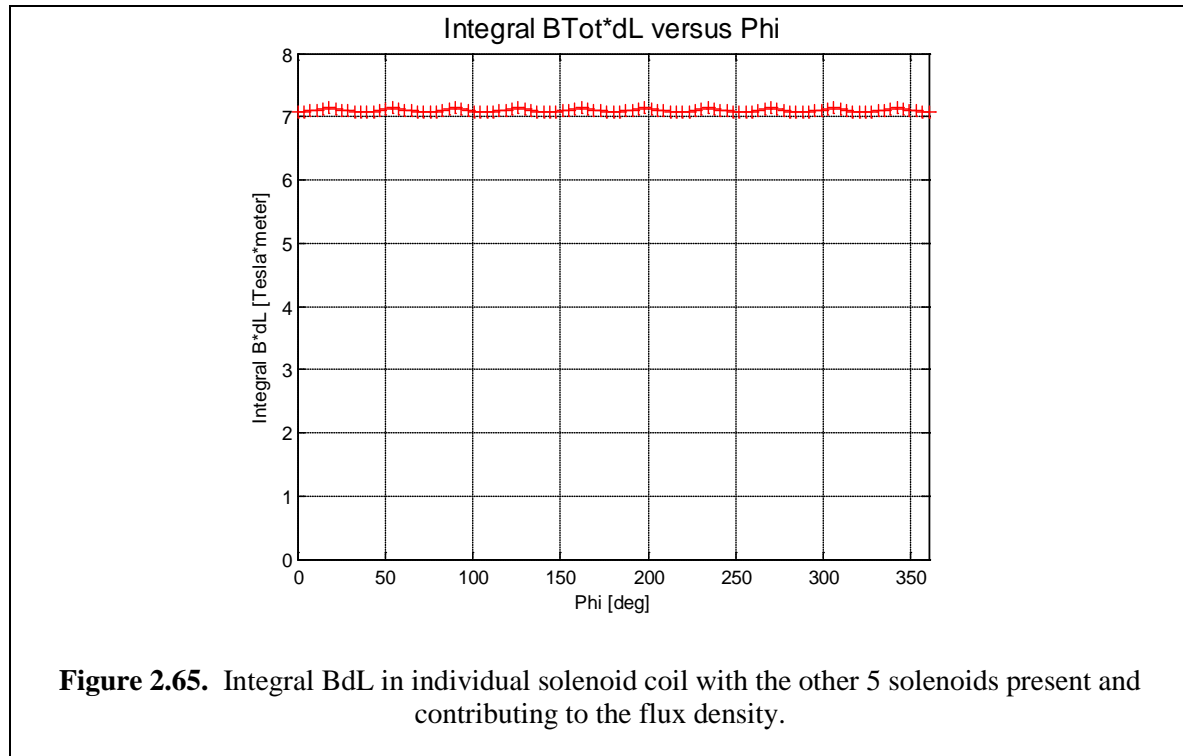
The flux density inside of the habitat without compensation coil is presented in Figure 2.66 showing an almost constant value of about 2500 Gauss over the habitat length of about 10 m. With a simple straight solenoid as described above this flux density can be reduced to a value of less than 100 Gauss. Optimizing the conductor density along the coil length would fully reduce the flux density to values of a few Gauss over the full length of the compensation coil.

In summary it can be said that the shielding array consisting of simple straight solenoids with a compensation coil surrounding the habitat constitutes by far the best solution that could be identified during this study. The compensation coil does not only eliminate the problem of flux density in the habitat, it also functions as a thermal shield against the main heat source in deep space. The cryogenic system for the compensation coil can be located in the spaceship itself and does not constitute an additional heat source seen by the outside shielding coils.

Figure 2.66. Field in Habitat without Compensation Coil.

Figure 2.67. Field in Habitat with Compensation Coil.
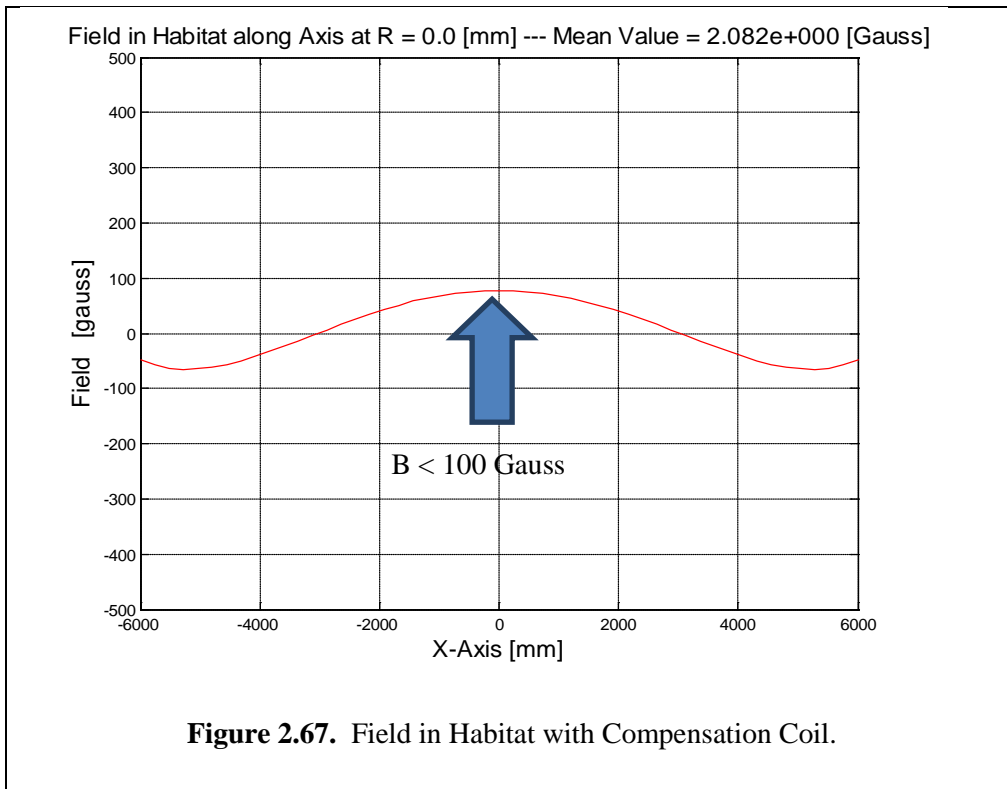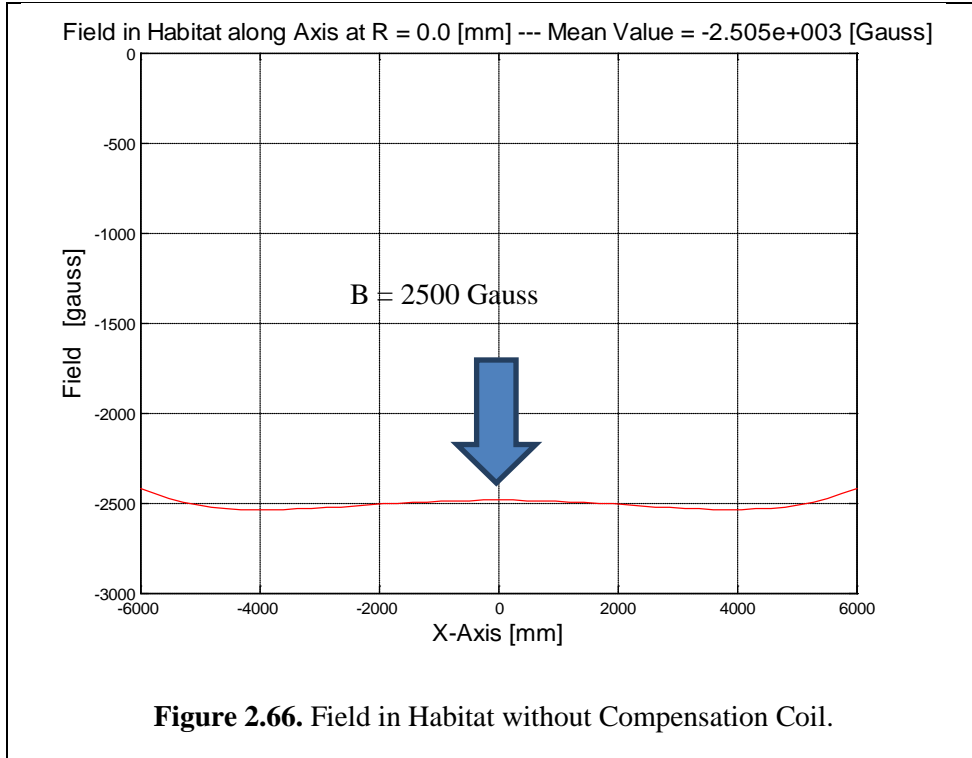
2.3. Feasibility of Implementing Potential Shielding Configurations

A list of required key parameters and features are presented in Table 2.4, which can be used to compare advantages and disadvantages of various shield configurations. It is difficult to assign objective ratings to all parameters without a more detailed engineering study of the various configurations. The "grades" assigned have therefore been limited to two categories, which are color-coded in the table below. All feature assessments, which do not seem to cause problems or might be promising are simply labeled "okay" and assigned a green color. All features that are difficult to achieve, will cause problems, or are simply bad in expected performance are assigned a reddish color and are labeled "high", "bad" or "difficult".

Table 2.4: Table rating the feasibility of required technical categories for all considered shielding configurations.

Winding Configuration	Shielding Efficiency	Field in Habitat	Mechanical Stability	Expandability	Coil to Coil Forces	Forces on Habitat	Cooling	Peak Field Enhancement	Quench Safety	Ease of Construction	Scalability to Higher Fields
Multi Layer DH Wedge	okay	high	bad	difficult	large	large	difficult	bad	bad	difficult	difficult
Multi Layer DH Circular	okay	high	okay	difficult	large	large	difficult	okay	okay	difficult	okay
Single Layer DH Circular	okay	high	okay	okay	large	large	okay	bad	okay	okay	okay
Solenoid Multi Layer	okay	high	okay	difficult	okay	large	difficult	okay	okay	okay	okay
Solenoid Single Layer	okay	high	okay	okay	okay	large	okay	okay	okay	okay	okay
Solenoid with Compensation coil	okay	zero	good	okay	okay	okay	okay	okay	okay	okay	okay
Multi Layer DH Toroid	okay	high	okay	difficult	large	large	difficult	bad	okay	difficult	okay
Single Layer DH Toroid	okay	high	okay	difficult	large	large	okay	bad	okay	okay	okay
Single Layer DH with Solenoid Ends	okay	high	okay	difficult	large	large	okay	bad	okay	dificult	okay

Based on the current state of the analysis a single layer solenoid coil, augmented with a compensation coil that surrounds the spaceship habitat, is the only shield configuration that looks promising in all features and aspects.

In general it seems the best approach to have coils, which only consist of a single conductor layer. Such coils will be the most flexible and therefore will make it much easier to construct coils that are expandable. Concerning cooling single layer coils will also offer significant advantages. A cooling system that guarantees a sufficient uniform temperature throughout the whole coil winding for very large superconducting coils will be technically challenging. If, radiation cooling in deep space is sufficient to maintain the required operational temperature, the cooling issue is probably solved. However, effective radiation cooling for a multi-layer coil is most likely much more difficult to achieve. Single-layer coils offer the additional advantage that the operational current will be very high. Although, this might seem counterintuitive, given the persistent mode operation of the coils and the flux pump excitation, high operational currents should not constitute a major technical difficulty. From a quench protection point of view high current and correspondingly low inductance is actually the preferred operational mode. From a conductor point of view, the estimated operational current of about 40 kA should not constitute a major technical problem. Existing YBCO tape conductors are not too far away from the required current carrying capacity. Furthermore, so-called Roebel cables for YBCO conductor are under development, which could already handle the required current levels.

The compensation coil approach, which offers many advantages, as described above, could also be applied to some of the other field configurations, which were rated as less promising in Table 2.4, and

could solve the issue of large fields in the spaceship habitat. However, for most of the non-solenoid configurations the flux density in the habitat is not constant, and a shielding coil that eliminates the flux everywhere in the habitat would be rather complex.

However, it is important to emphasize again that the concept of a compensation coil surrounding the habitat, is of great value, and the development of this concept can be regarded as an important outcome of this project. The very important advantage of the compensation coil, independent of eliminating any fringe magnetic field in the spaceship habitat, is the thermal shielding between habitat and the surrounding shielding coils. Without this thermal shielding, the spaceship would constitute a major heat load for the shielding coils. Without this heat load, radiation cooling alone could become feasible with sufficient performance improvements of the superconductor. The cooling of the compensation coil itself is a lesser problem, since the cooling system can be inside or attached to the habitat.

2.4. Implementation of Expandable Coils

The support structure for expandable superconducting coils requires some unique mechanical features, which are normally not needed or implemented in the design of large magnets. First and foremost the materials used for the conductor support has to accommodate the required shape change of the coil. Simultaneously, the material needs to be flexible enough, so that the expandable coil will approach its final shape already at a rather low excitation current, where the Lorentz forces are only a fraction of their final value. Under these conditions the HTS conductor is still far away from its critical surface during most of the expansion cycle and therefore has large operational margin. In particular, the support structure should guarantee a smooth approach to the final shape without sudden abrupt movements. Such jerks of the conductor under the effect of acting Lorentz forces are a main reason for premature quenching in LTS coils. As pointed out in the section on quench protection, HTS conductors are rather forgiving in this respect and should allow this unprecedented operational mode of a superconducting coil.

In order to understand in a semi analytical way, how the expansion process of the coil has to proceed with minimum energy release into the winding, we can define an energy density e_f for the acting frictional forces as follows:

$$e_f = \mu_f \cdot f_{Lorentz} \cdot \Delta r$$

In this equation μ_f is the frictional coefficient, $f_{Lorentz}$ is the Lorentz force density and Δr is a given conductor movement. Based on this relationship one can define a frictional power density as:

$$p_f = \mu_f \cdot f_{Lorentz} \cdot \Delta r / \Delta t$$

From this equation it is obvious that a required condition for the expansion process is a steady, slow expansion rate $\Delta r / \Delta t$. In this case the energy release due to frictional forces is small. Additionally, it is required that the frictional coefficient μ_f is as small as possible.

The concept considered for the coil support with the required features is as follows. The YBCO tape conductor of a cylindrical coil is sandwiched between 2 layers of woven fabric mats made from Kevlar or Zylon. Zylon, with the extremely high tensile strength of about 5.4 GPa, is cryogenically qualified, and

the fiber material is available with metal coating (e.g. gold), which would enhance radiation cooling of the coils in deep space. The 2 mats will be stitched together following the edges of the superconducting tape, thereby preventing the helical winding to slip under the effect of Lorentz forces in a solenoidal winding.

The fabric cylinder containing the superconducting coil needs an additional support structure to make sure that the coil axis remains straight and in case of a solenoidal winding to counteract the axial forces of such a winding, which try to bunch the conductors together in axial direction. The main feature of this support is a lightweight composite "Strongback" as shown in Figure 2.68. The design is scalable, but as shown, is meant for coils with 8-m diameter and a length of about 20 m.

The inner strongback has a diameter of about 1-m and has many cutouts (not shown) to minimize its weight. "Spokes" with a length of about 1 m and rounded ends extend to the outside. The contour length of the strongback structure has been designed to match the circumference of a fully inflated coil of the nominal diameter.

To "deflate" the coil so that it follows the contour of the inner structure, a light vacuum could be pulled. Under the effect of the acting magnetic pressure the coil will inflate when excited.

The fabric cylinder containing the coil is attached to the spokes of the strongback via flexible struts as shown in Figure 2.69 and Figure 2.70. The star-shaped strongback structure enables a dense packing of several coils for the launch into space. This is shown in Figure 2.71.

Diameter of inner Hub: ~ 1000 mm
Spoke Length: ~ 1000 mm

Strongback Spoke

Superconductor draped on to coil Strongback

"Coil Strongback"
A lightweight composite structure

Figure 2.68. Conceptual design of coil support structure

Figure 2.69. Concept of coil flexible coil attachment to the inner strongback support structure.

Figure 2.70. Concept view of fully expanded solenoid coil.

Figure 2.71. Concept of coil stacking for launch into space.

2.5. Expandable 6+1 Coil System Mass

In support of a mass comparable for the 6+1 coil system expandable to 8 meter diameter and 20 m length, the coils were simply mass estimated by multiplying the circumference by the mass per unit length of HTS YBCO conductors fabricated today. The sandwich blanket was estimated based on Zylon fabric mass over the surface area needed to hold the superconductor in place and to provide the necessary structural support. The mass of the 6 coils is estimated at 36 metric tons and the compensator coil at ~ 2 metric tons (see Table 2.5). The mass of the thermal system is offered in section 3.4 and the total mass and power requirements of the full system with contingency is provided in section 9 with the mission concept in mind.

Table 2.5 Mass of Expandable Coils

Coil System	Mass (kg)
Strong-back, 20 m carbon	2714
Conductor, 20 m coil	503
Blanket - for coil & structural support	2895
Coil, strongback & blanket	6112
6 coils total	**36672**
Compensator coil	**2126**

3. Thermal Design Concept

S.W. Van Sciver - Florida State University

3.1. Introduction

Herein we describe the requirements and options for the cryogenic cooling system that is needed to support the superconducting magnets for the NIAC study of a spacecraft active magnetic shielding system. Some of these requirements are general while others are design specific. In the case of design specific requirements, this document focuses on the coil design configuration consisting of six by 1 Tesla solenoids surrounding a field compensation coil that in turn surrounds the habitat. Two options are suggested to meet the cool-down and steady refrigeration load for the coil system.

The conceptual design of the magnetic shielding system has several pre-determined assumptions.

- The superconducting magnets are to be made with HTS material and operate in the range of 40 K. Actually, the operating temperature of the coils should be a variable that is optimized as part of the design process. This is an issue that should be considered in a Phase II effort as the cost of the additional superconductor may be compensated for by the savings in the power requirements for the cooling system.
- The coils will not be contained within their own vacuum chamber but will rely on ambient space vacuum and radiation shielding for thermal insulation. Any coil vacuum chamber suitable for atmospheric pressure on earth is deemed to be too heavy to be launched.
- Since the coils will not be thermally insulated until in space and in their final configuration, they will need to be launched warm (T ~ 300 K). This establishes magnet cool-down requirement on the cryogenic system, which could easily determine its size. This cool-down requirement also precludes the use of storable cryogens as primary cooling source.
- Coil cooling will be provided by a number of cryocoolers[1] operating between the coil temperature and ambient heat rejection temperature. Most often ambient heat rejection is assumed to be at or near 300 K, but this is another variable that may need to be optimized.
- The coils will need to be actively powered to maintain constant magnetic field. Any coil powering system will have an associated thermal load. This load will include the

---

[1] Cryocooler is a generic term that refers to closed cycle cryogenic refrigeration systems. Common thermodynamic cycles used in cryocoolers are: Stirling, Gifford McMahon, Brayton and Collins.

transient cool-down load as well as the steady heat load due to things like support structure and current leads.

- The cryogenic system must be capable of cooling down the coil assembly and removing the steady state heat loads. These loads include:
- Thermal radiation from other sources (sun, earth and crew module).
- Resistive loads in the coils due to joints or index losses in the superconductor.
- Conductive loads due to supports and current leads that have one end at high temperature (~300 K).
- AC losses due to charging the magnets.

The superconducting magnets represent a thermal mass that must be cooled to low temperature and maintained at that operating temperature for the duration of the mission. In the present design, Figure 3.1, the coil system consists of six 8 m diameter superconducting solenoids arranged outside the 6 m outer diameter habitat with an additional field compensation surrounding the module. The six solenoids have a diameter of 8 m and length of 20 m and a flux density of 1 T. The compensation coil has a diameter of approximately 8 m a length of 20 m and a flux density of about 0.01 T.
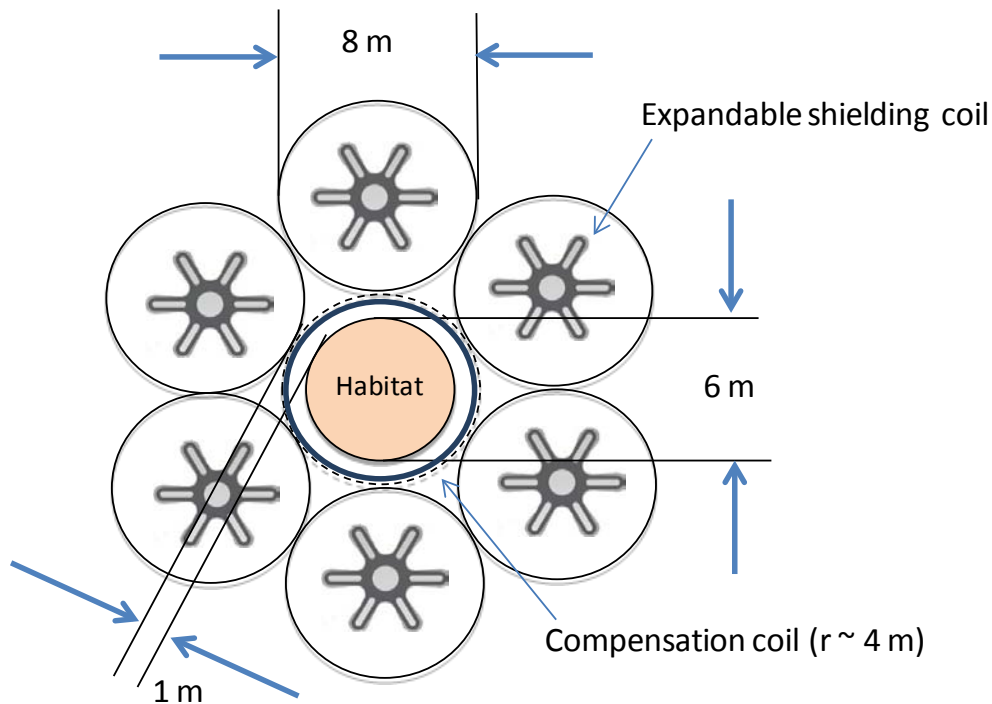
Figure 3.1 Shielding coil configuration

3.2.   Cool-down Requirements

The cool-down requirement is driven by the cold mass of the superconducting coil system, which is estimated to be 7.5 tons per coil of the six shielding coils. This number is based on the total of the mass of the superconductor, backbone that supports the flexible coils and the structural mat that is envisioned to support the electromagnetic loads. It is assumed that the compensation coil is small and does not contribute significantly to the total mass. This mass estimate does not include that of the cooling system, described below.

The total cool-down enthalpy of each 7500 kg coil from 300 K to 40 K is estimated to be 1275 MJ (assuming that the thermal properties of the coils are similar to that of aluminum). This thermal energy must be extracted before the magnet can be energized and expanded. The cool-down of the coils can be achieved by a combination of radiation heat exchange to deep space and active cooling cryocoolers.

The radiation cooling to deep space may be effective to bring the coils to near operating temperature. However, the effectiveness of this process is depends on how well the coil system is thermally shielded from other sources (sun, earth). If the coils were only radiating to deep space, the cooling from 300 K to 40 K should take about one month assuming an emissivity of 0.5. Alternatively, if we assume that the coils are located behind a sun shield at a nominal 170 K with a low emissivity back surface the coils could achieve a minimum temperature of 70 K to 100 K. Thus, radiation cooling can assist with bringing the coils to low temperature, but is not expected to supply enough cooling to achieve the desired operating temperature or to remove the steady heat load during operation. Further the habitat radiation cannot be easily radiated to deep space as it is surrounded by the field compensation coil.

Therefore, to bring the coil system to 40 K will almost certainly require a set of cryocoolers with flexible thermal links to the expandable coil system. In general, cryocoolers have a cooling power that is a function of the cold temperature, $Q_c(T)$, decreasing as the temperature decreases. If $Q_c(T)$ is known for the cryocooler system, one can calculate the time to for the coils to reach the operating temperature. For example, assuming each coil has a steady heat removal $Q_c(40 K) = 100$ W, a reasonable value as is discussed below. Such a cryocooler typically would have a cooling power $Q_c(80 K) = 250$ W, while above 80 K, the cooling power may increase or level off.   To make a conservative estimate of the cool-down time, the cooling power is assumed to be constant 250 W between 300 K and 80 K and then decrease linearly to 100 W at 40 K. Based on these assumptions, the time to cool each magnet from 300 K to 40 K is about 75 days. This time is dominated by the high temperature region. For example, assuming an initial coil temperature of 80 K, it then only takes about 4 days to cool from 80 K to 40 K. Note that these calculated cool-down times neglect any added heat removal by radiation.

3.3.   Operational Cooling Requirements

Once the magnet system is cooled to its operating temperature, it can then be energized. During operation there will be thermal loads on the cryogenic system that will need to be removed by the cryogenic refrigeration system. There are essentially two classes of such heat loads: 1) internal loads coming from the coils themselves and 2) external loads coming from other sources that are mainly the result of the large temperature difference between the coil and the ambient. The internal loads include transient losses associated with ramping the coil to field as well as DC losses when the magnet is at field

(superconductor index losses and losses in resistive joints). The ramping hysteresis losses for YBCO tape (multiple 50 mm wide and ~0.2 mm thick tapes in parallel) were estimated based on the operating current of 40 kA to be approximately 60 kJ. If the coils are ramped to field in 24 hours, this corresponds to an added heat load of 0.7 W/coil. Such a load is probably small compared to the radiation load and thus not a large issue for the cooling system.

The other major heat load on the coil system is due to the radiant flux from the crew module, the earth and sun. The radiant load from the habitat is a significant contribution. The space between the habitat and the compensation coil (at 40 K) is something less than 1 m. This area should be shielded with multilayer insulation with an assumed average heat flux of 1 W/m^2 between these two surfaces. For the entire installation, this results in a total thermal load of 380 W on the compensation coil, which must be picked up by cryocoolers.
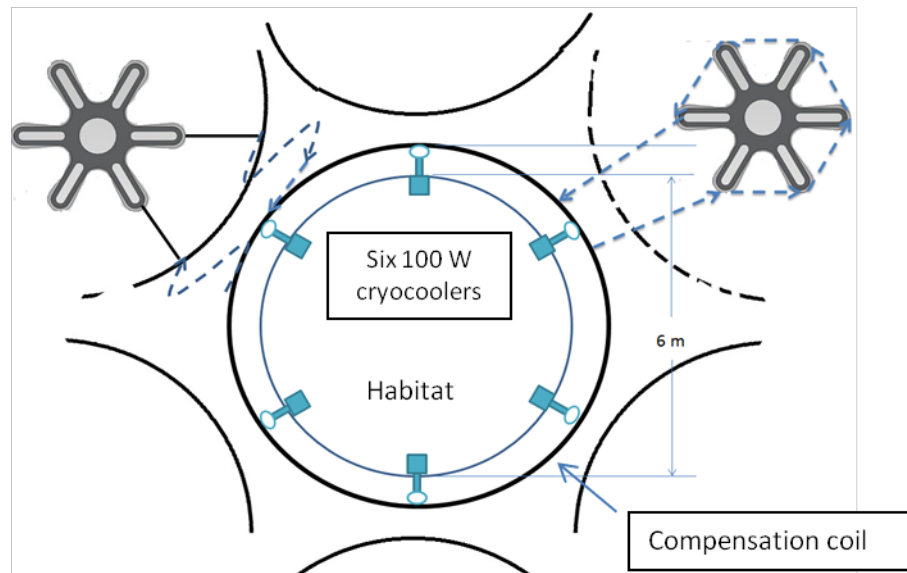
Figure 3.2 Habitat with Stirling cryocoolers attached to the compensation coil.

Two options have been considered to supply cryogenic refrigeration to the superconducting magnet system. The first option would utilize six Stirling cycle cryocoolers, schematically shown attached to the inner bore of the compensation coil, Figure 3.2. These cryocoolers are thermally anchored to a high thermal conductivity bore tube onto which the coil is wound. The radiant load from the habitat is then picked up by the bore tube and conducted directly to the cryocoolers. In this way, the compensation coil forms an isothermal (40 K) surface surrounding the habitat that picks up the habitat thermal radiation as well as that from the inner facing turns of the six shielding coils. Note that the warm end of these cryocoolers would be located within the habitat, so that maintenance could be performed from

there. At least two additional cryocoolers would be necessary to ensure redundancy and allow change out for repairs.

A thermal link must be established between the 40 K shield attached to the compensation coil and the outer six 1 T coils. Since the outer coils are to be flexible and expand in space, at least part of the thermal link must also be flexible. A solid conductive link reaching to the outer edge of these six coils is not feasible due to the large mass required and anticipated stiffness. A thermally conductive material could be incorporated in the outer coil structure, but this will significantly increase the mass of the coils.

For this first option, cooling to the outer coils could be provided by flexible, low pressure helium gas circulation loops driven by low pressure head helium fans. These gas cooling loops could be made of a light weight tubular material (approximately 1" inner diameter) wrapped around the outside of the coils, see Figure 3.3. Several cooling circuits could be in parallel and supplied by one helium gas fan that was attached to cryocooler or the cold shield on the compensation coil. The pressure drop through each circuit would be quite small, of order 200 Pa, and each circuit would be able to pick up 10 W at 40 K with only a 2 K temperature rise in the flow circuit.

Since the Stirling cryocoolers are closed cycle, this option would require a high performance heat exchanger be attached to each cryocooler cold head to remove the heat load from the flowing helium gas.
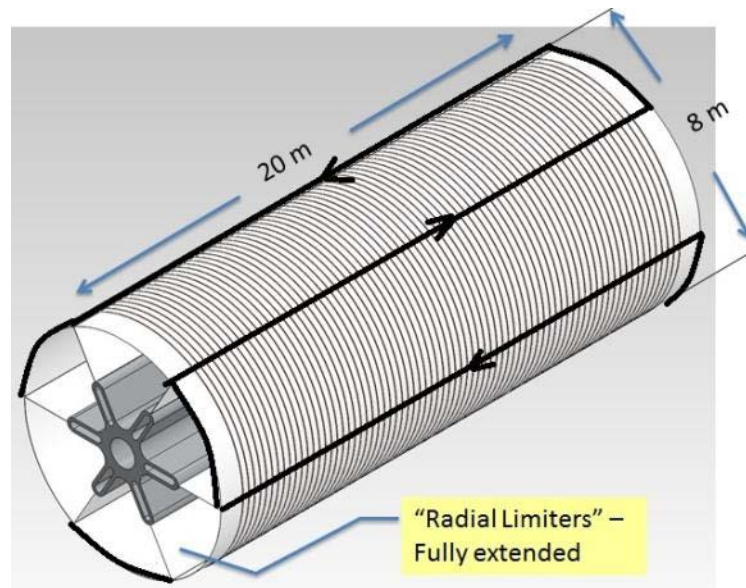
Figure 3.3 Shielding coil with helium gas cooling tubes attached on the outer surface.

The second option for cooling the superconducting magnets would utilize a single Brayton cycle cryocooler to supply cold helium gas to the entire superconducting magnet system, Figure 3.4. One potential advantage of the Brayton cycle in this application is its ability to supply cold helium gas directly to the magnet system through flexible tubing similar to that described above. However, unlike the Stirling cryocooler based system, the Brayton cycle cryocooler may be configured to supply cold gas directly from its cycle to the load depending on flow rate requirements thus eliminating the need for the extra heat exchangers and helium gas fans. This option could have a significant advantage by minimizing

the additional hardware required for the system. However as above, option 2 would require a redundant cryocooler be installed to pick up the thermal load should the cooling system need maintenance or repair, see Figure 3.4.
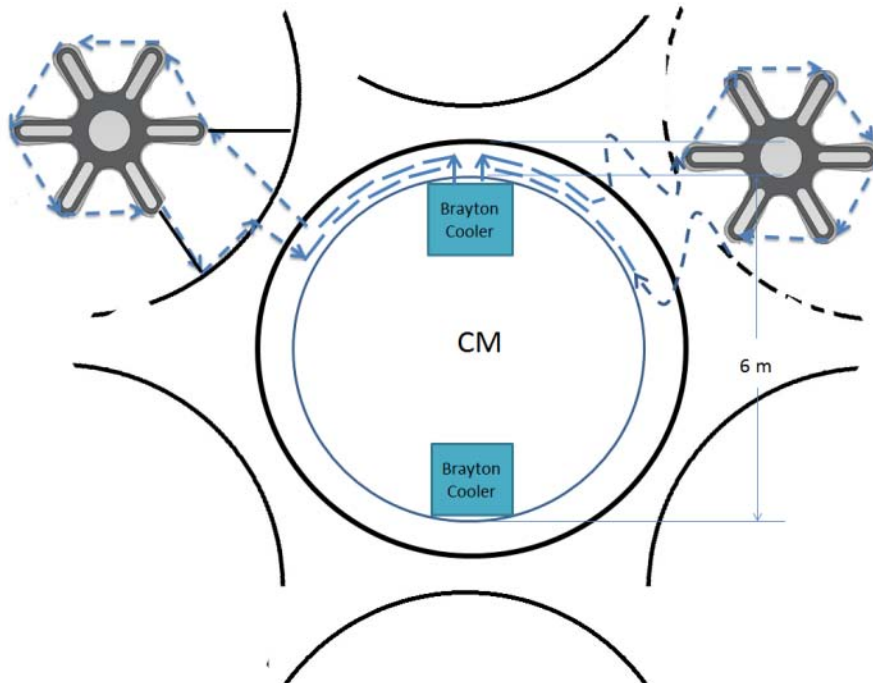
Figure 3.4 Habitat with Turbo-Brayton cryocoolers supplying cold gas to coil system.

3.4. Cryogenic system power and mass requirements

Mass rollup

- Cryocoolers (8 x 100 W at 40 - 60 K) = 800 kg (220 kg for option 2)
- Circulators (6 x 6 kg) = 36 kg (not needed in option 2)
- Connecting tubing = 200 kg
- Heat exchangers (6 x 30 kg) = 180 kg (not needed in option 2)
- **Total without contingency = 1216 kg (440 kg for option 2)**
- does not include radiators

Power rollup

- 600 W with COP 32 W/W = 19200 W x 1.25 contingency = **24 kW**. This is based on assuming that 380 W is needed to cool the compensation coil and the remainder available to cool the outer coils.

4. Superconductors

R. Meinke - Advanced Magnet Lab

While it is conceivable that the ideal superconductor that can carry large operational currents at fields in the Tesla-range at almost room temperature might be discovered in the future, the design approach of this project is predicated on conductors that are already available and have been qualified for high field applications, although with lesser performance. Based on this approach only six materials can be considered for large-scale, high-field application, as required for the radiation space shield. These conductors with their key performance parameters are listed below. These conductors can be grouped into two categories, i.e., low-temperature and high-temperature superconductors.

4.1. Low Temperature Superconductors (LTS):

NbTi Conductor:

The most used superconductor for existing magnets for research and medical applications is niobium-titanium (NbTi). The conductor typically operates near liquid helium temperature, i.e., 4.2 K with a critical current density of about 3000 A/mm^2 at 4.2 K and a field of 5 Tesla. NbTi wires are rather flexible and therefore well suited for coil manufacturing. Magnets based on NbTi can reach fields of up to about 10 Tesla.

Nb$_3$Sn Conductor:

For fields above 10 Tesla and temperatures near liquid helium niobium-tin (Nb$_3$Sn) has successfully been used. Although, the conductor can still carry significant currents at 20 Tesla, its critical current density is typically given at 12 Tesla and 4.2 K, and current densities of up to 3000 A/mm^2 have been achieved. The conductor, however, is brittle and is therefore more difficult in coil manufacturing, requiring in most applications the so-called wind-and-react approach. In this manufacturing technique the coils are wound with a "green" conductor, and the superconductor is formed by a high-temperature reaction process of the whole coil.

4.2. High Temperature Superconductors (HTS):

BSCCO-2223 Conductor:

Bismuth-strontium-calcium-copper-oxide conductors are in the form of tapes, which are typically 4 mm wide with a thickness of 0.2 mm. These tapes can typically carry current of 200 A at 77 K and self-field (~0 Tesla). The current carrying capacity rises significantly at lower temperatures with typical values of more than 1.5 - 2.5*160 A at 20 K and 5 Tesla. Like most HTS conductors the tapes are anisotropic, i.e. the current carrying capacity depends strongly on the direction of the external field.

BSCCO-2212 Conductor:

This bismuth-strontium-calcium-copper-oxide material is also available in form of round wire with 0.8-mm diameter. Due to the brittleness of this conductor a wind-and-react coil manufacturing process is required, which is difficult to use for large coils. Typical current carrying capacity of BSCCO-2212 at 20 K

and 4 Tesla is about 200 A. However, very large fields can be maintained at 4.2 K, these are in excess of 45 Tesla.

YBCO Conductor:

Yttrium-barium-copper-oxide conductor is available in tape form with 4-mm width and a thickness of less than 0.2 mm. Tapes with larger widths are under development. Tapes can carry close to 1000 A at 77K and self-field (~0 Tesla). As explained below, this is the most promising conductor for the large magnets of the radiation space shield, and detailed performance parameters are given below.

MgB_2 Conductor:

Magnesium-boride conductors are available in tape and wire form. The critical temperature of MgB_2 is about 39 K, however the current densities and fields of practical applications require operation in the range of 20 K or below. The conductors are available in reacted or unreacted form. However, the reacted conductor is again very brittle, and wind-and-react coil manufacturing is required for many applications. Round wires which are isotropic can carry currents of about 30 A at 21.5 K and 4 Tesla.

4.3. Choice of Superconductor for Radiation Shield Coils

A useful diagram that helps to decide in the choice of superconductor for the space shield application is shown in Figure 4.1, which shows the technical complexity of superconducting applications as a function of operational temperature. As indicated by the blue curve in this figure, the cryogenic stability increases significantly with increasing temperature. This is due to the fact that the specific heat of (almost) all materials increases with temperature, shown for YBCO in Figure 4.2. As can be seen in Figure 4.2, the specific heat rises rapidly with temperature in particular for temperatures above a few degrees Kelvin.

However, for the same reason the quench propagation velocity (about 2 cm/sec for HTS and typically several m/sec in LTS conductors) in the conductor decreases with temperature and quench protection becomes more and more difficult with increasing temperature. This is indicated by the red curve in the figure, which shows magnet protection. Sufficiently rapid quench detection based on voltage detection across the normal conducting zone in HTS conductors is therefore impractical. By the time a detectable voltage has been developed the temperature near the quench origin has risen to values that can destroy the conductor. Quench protection of HTS coils is therefore more and more difficult with increasing temperature, and coils operating at higher temperature have to be designed with sufficient margin, so that the probability of a quench is extremely small.
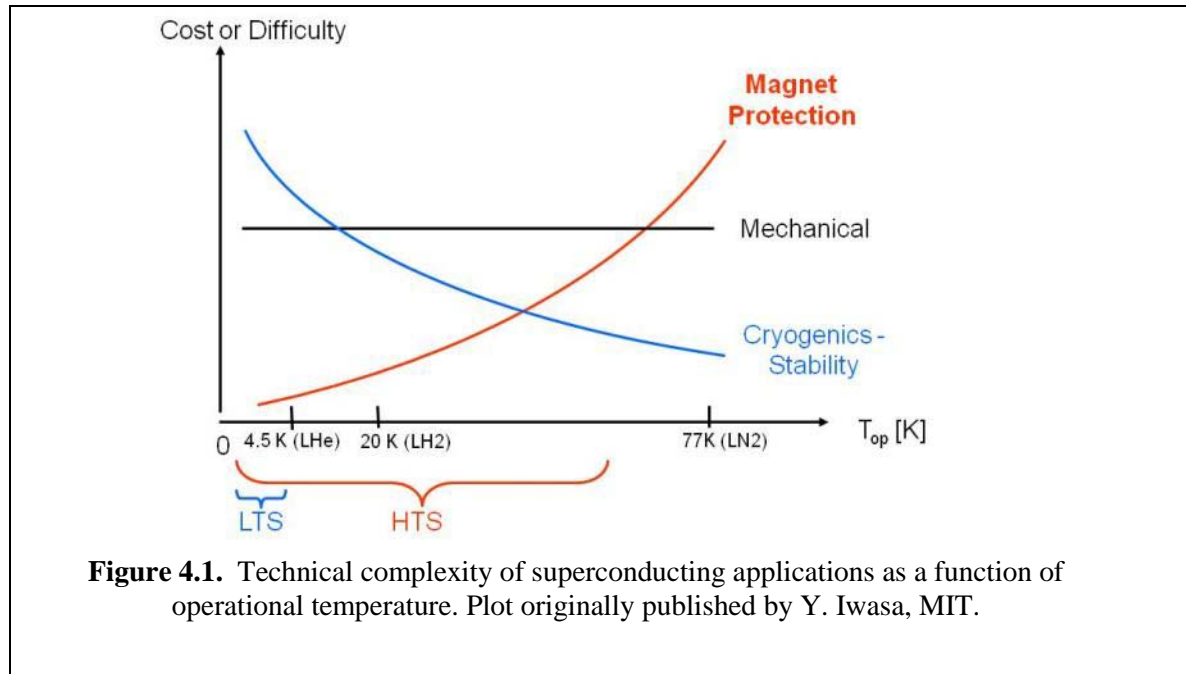
Figure 4.1. Technical complexity of superconducting applications as a function of operational temperature. Plot originally published by Y. Iwasa, MIT.

YBCO Specific Heat versus Temperature
NIST WEB-HTS Database

$y = 8E\text{-}12x^6 - 9E\text{-}09x^5 + 4E\text{-}06x^4 - 0.0008x^3 + 0.0824x^2 - 0.9193x + 1.9692$
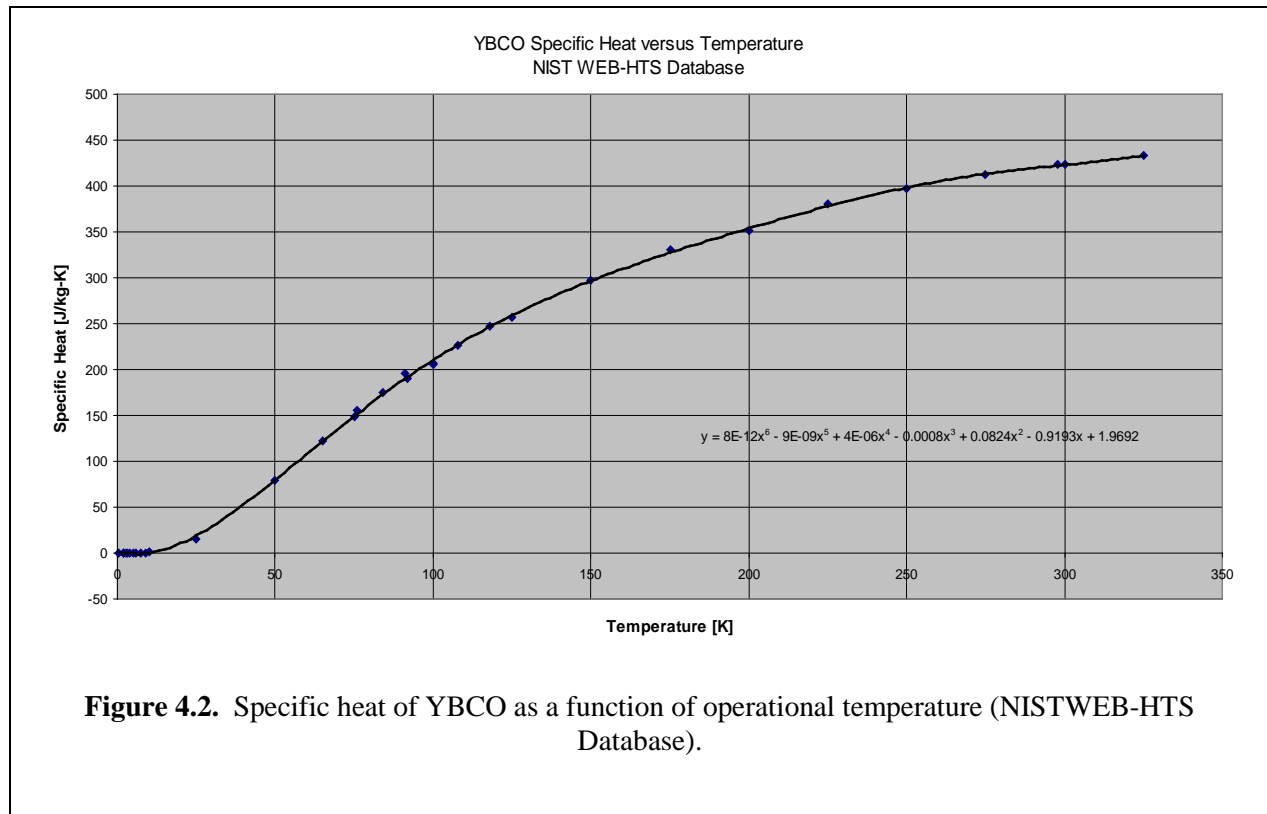
Figure 4.2. Specific heat of YBCO as a function of operational temperature (NISTWEB-HTS Database).

To initiate a quench in a superconductor, a certain amount of energy has to be introduced into the conductor. For LTS conductors wire movements under the effect of Lorentz forces are a main reason for premature quenches, i.e. quenches below critical current, field and temperature of the conductor. To avoid wire movements, heavy coil support structures are needed, and coils based on LTS conductor are therefore extremely heavy and completely impractical for radiation shields, which have to operate in space and need to be launched.

For completeness other sources of energy deposition into superconducting coils that can initiate a quench are shown in Figure 4.3. Due to the large temperature margin and specific heat of HTS conductors, wire motions in such coils do not initiate quenches, and also the other sources shown in the graph are of minor relevance. Even heat leaks, which would lead to an increase in temperature, are of minor importance, since the surrounding temperature in space is already very low, as long as direct sunlight can be shielded.

Figure 4.3: Disturbance energy spectrum acting in superconducting devices presented as energy density in mJ/cm3 versus time duration of the acting disturbance.[2]
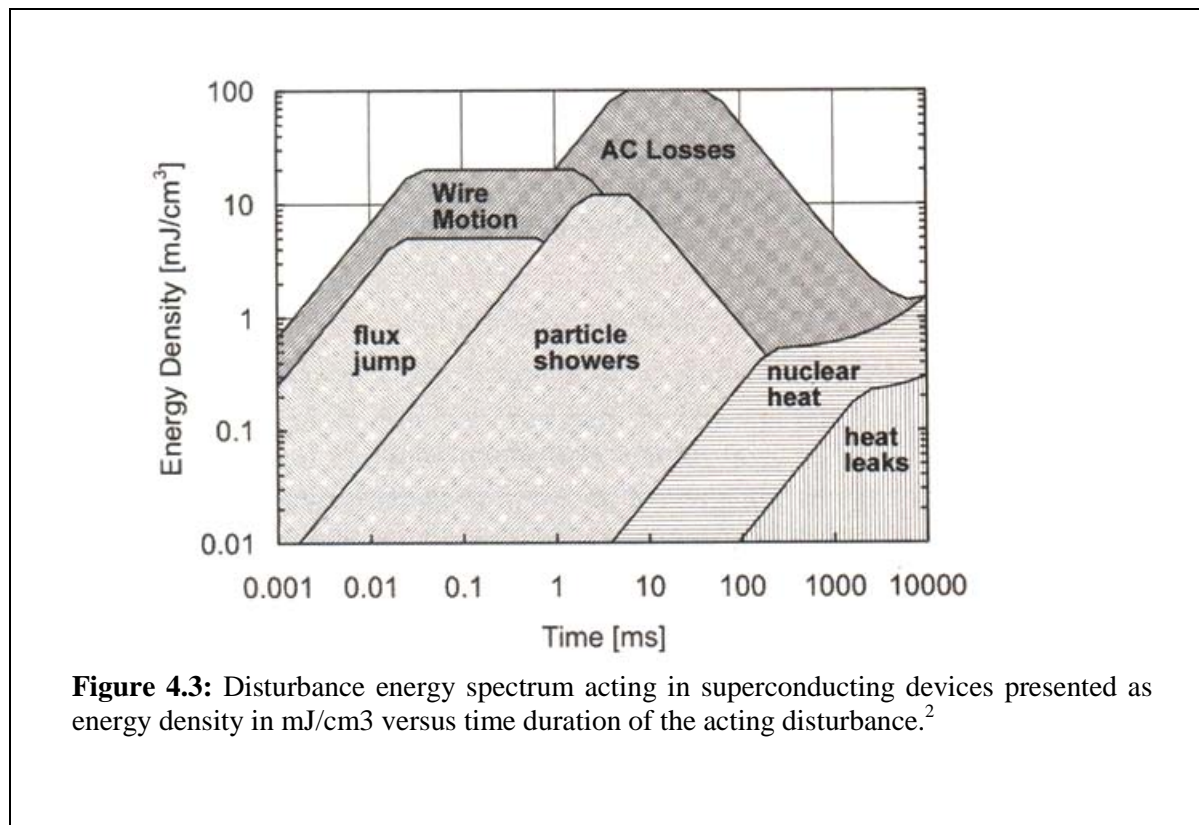
 A comparison of energies needed to initiate a quench for LTS and HTS conductors[2] together with the allowed temperature range for operation is summarized in Table 4.1. As can be seen from the table, the

2 Stability and Protection of SC Magnets – A Discussion", Y. Iwasa, IEEE Transactions on Applied Superconductivity, p. 1615, June 2005.

energy to initiate a quench in an HTS superconducting coil operating above 30 K is about 4 orders of magnitude larger than for an LTS coil operating at 4.2 K. Conductor movements under the influence of Lorentz forces acting on the conductors inside of the coil are therefore highly unlikely to initiate a quench. This is of particular importance for the realization of the radiation shielding coils that should be expandable under the effect of Lorentz forces. As pointed out in other parts of this document the shielding coils are very large and require some folding to fit into any practical space launch systems.

Conductor	T_{op} [K]	ΔT_{op} [K]	Emax [mJ/cm^3]
LTS	2.3	0.5	0.2
LTS	4.2	0.5	0.5
LTS	4.2	1	1.2
HTS	4.2	20	300
HTS	10	15	700
HTS	30	10	3700
HTS	70	5	8400

Table 4.1. Allowed temperature and energy margins of LTS and HTS superconductors. Stability and Protection of SC Magnets – A Discussion", Y. Iwasa, IEEE Transactions on Applied Superconductivity, p. 1615, June 2005.

4.4. Key Performance Parameters of YBCO Conductor

As mentioned above, YBCO is an HTS conductor in tape form. A thin layer of about 0.8 μm thickness is applied to an appropriate substrate. A typical tape conductor is shown in Figure 4.4. The critical current of an advanced 2nd Generation (2G) conductor from American Superconductor (ASC) is shown in Figure 4.5. The performance data shown here are from Data from "2nd Generation HTS Wire – An Assessment", A. Malozemoff, ASC. The 2G-conductors produced by ASC and Super Power contain nano-dots for flux pinning, which increase the critical current density under external fields. Tapes with a width of 40 mm are available. The goal is to produce tapes with 100 mm width.

The critical current of YBCO conductor depends on the field direction relative to the tape surface. In general the critical current for a given temperature and field is significantly larger for a field parallel to the tape surface than perpendicular. The performance achieved by ASC is shown in Figure 4.6.

Figure 4.4. Actual 2nd Generation YBCO tape from American Superconductor with a tape width of 4 cm and a thickness of 0.21-0.23 mm.
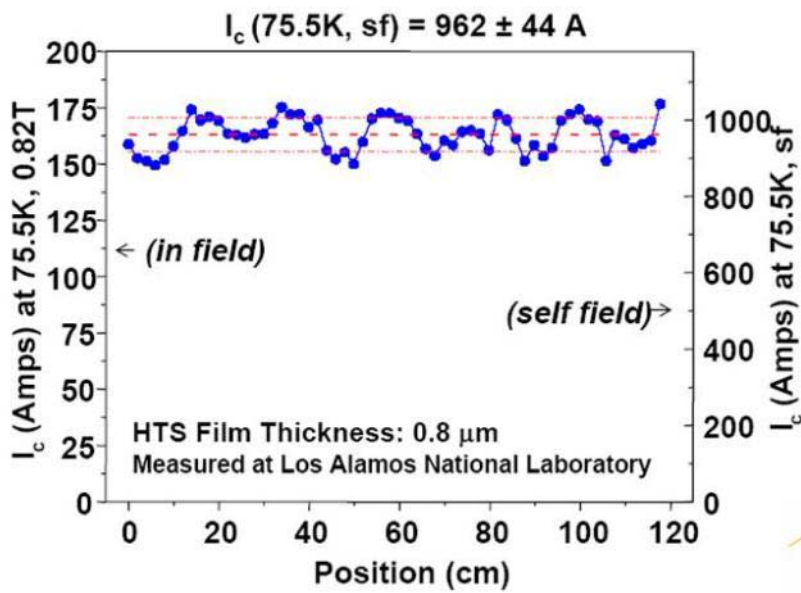
Figure 4.5. Current carrying capacity of 4-cm wide and 120 cm long YBCO tape. The left vertical axis is for an external field of 0.82 T; the right vertical axis is for the self-field (~0 Tesla) condition, i.e., no additional external field.
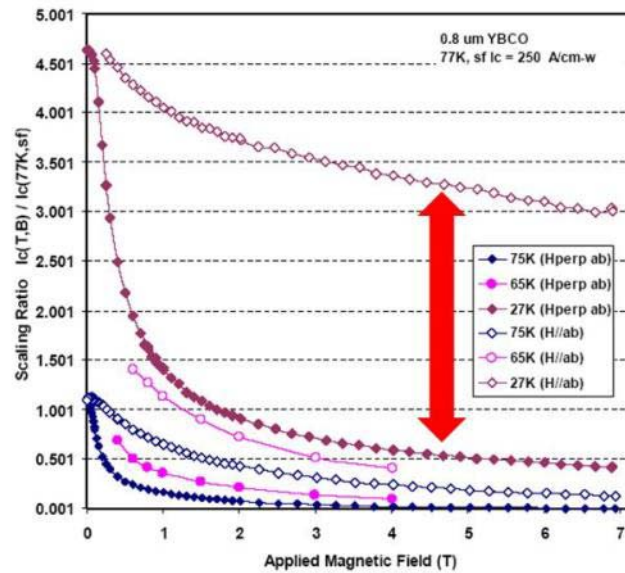
Figure 4.6. Performance of 2G YBCO tape. The plot shows a scaling factor for the critical current as a function of applied magnetic field for various operational temperatures and for field directions perpendicular to the tape (H perp ab) and the field direction parallel to the tape (H // ab). The red arrow indicates a 5 times higher critical current for the parallel field direction.

4.5. Performance Requirements for Radiation Shield

As shown in this document the design goal for a conductor should enable operation at 40 kA in a tape conductor with a width of 50 mm at a field of about 1 Tesla and a temperature of about 40 to 50 K.

Existing YBCO conductor does not achieve such a performance. However, the current carrying capacity of YBCO conductor has rapidly improved with time, and the performance required for the radiation space shield application should be achievable within a realistic time span. We are in particular optimistic in this respect, since most other potential applications of YBCO conductor also require significant improvement in current carrying capacity. The manufacturing process of YBCO conductor is very complex, as can by appreciated, when considering the complex build-up of the conductor that is shown in Figure 4.8, and conductor cost is therefore currently too high for most industrial applications. Given the complex manufacturing process of the conductor, the most realistic way of reducing the conductor cost as measured in dollar per kA*meter, is by increasing the current carrying capacity, and it is therefore mandatory for companies developing YBCO conductor to increase current carrying capacity of the conductor.

 Given the current state of YBCO conductor development the following conclusions can be drawn. A conductor with a YBCO layer of 2 μm instead of the current 0.8 μm thickness is close to realization. It should furthermore be feasible with existing technology to apply the YBCO layers to both sides of the substrate. Assuming the currently achieved current density for the two layers with the assumed

thickness of 2 μm would result in a five-fold increase in current carrying capacity. As shown in Figure 4.6, the existing conductor can carry 250 A per cm of tape width, and this capacity increases by about a factor of 3.5 at 27 K. It can therefore be estimated that a 50 mm wide tape with two conductor layers of 2 μm each at 27 K could carry the following current:

$$I_c = 250*5*5*3.5 \sim 21,875 \text{ A}$$

It is encouraging to see that this value is not too far off from the required conductor performance for the radiation space shield designed under this project. However, it is also clear from Figure 4.6 that the field direction in respect to the tape is of utmost importance, since the current carrying capacity can differ by as much as a factor of 5 depending on field direction. However, a recent improvement to 2G-conductor with zirconium doping, implemented by Super Power shows that the very strong angular dependence of the critical current could be significantly reduced. As shown in Figure 4.7 the difference between parallel and perpendicular field direction can be reduced to a factor of 2. In general the performance of 2G-conductor is rapidly improving[3] (HTS4 Fusion Workshop, 2011) and even better performance than assumed here can be expected.

Figure 4.7. critical current versus field direction for zirconium-doped 2G-conductor from Super Power.

---
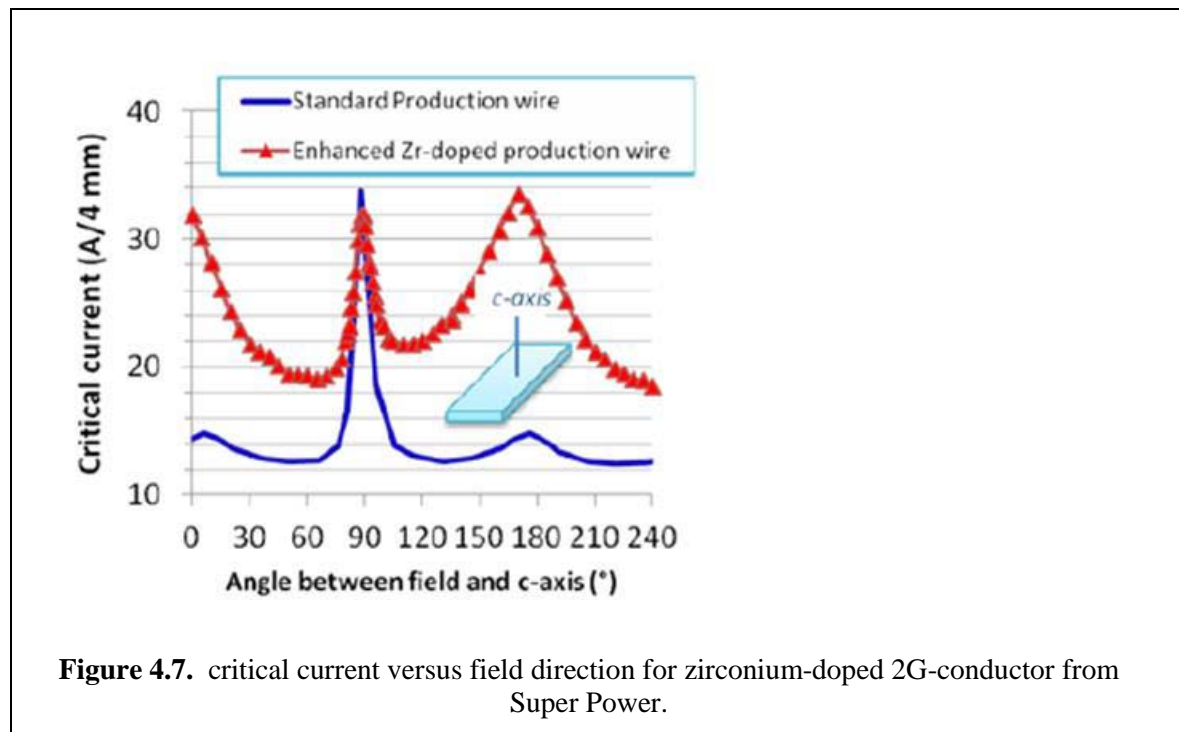
[3] HTS4 Fusion Workshop, May 26-27, 2011, Karlsruhe, Germany

For an estimate of the weight of a given shield coil the weight of the tape conductor is needed. This can be estimated from the build-up of the conductor shown in Figure 4.8. The weight of a 50-mm wide tape has been estimated to be about 0.040 kg, based on the copper density of ρ_{Cu} = 8920 kg/m^3 and a hastelloy density of $\rho_{Hastelloy}$ = 8220 kg/m^3 .

Figure 4.8. Build-up of 2G YBCO tape conductor from Super Power
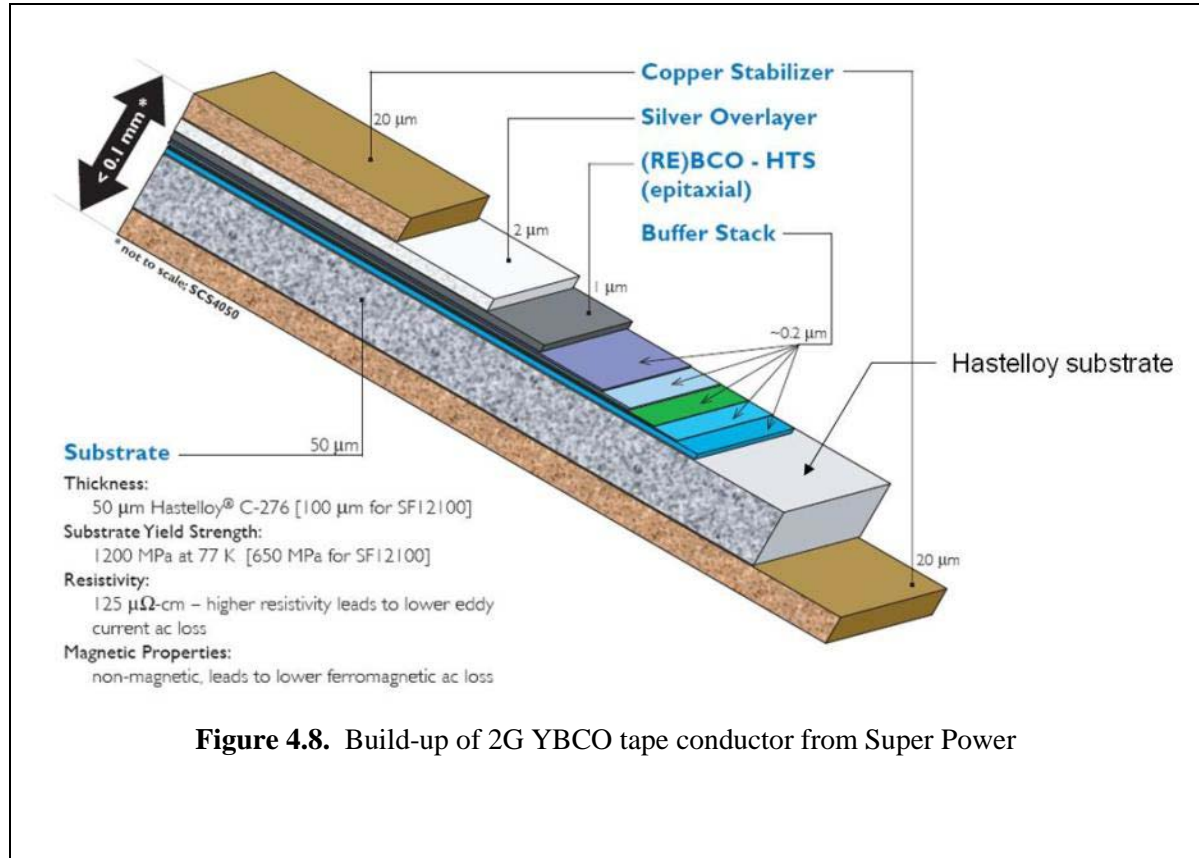
4.6. Stored Magnetic Energy and Operational Risk

Any volume V [m^3] filled with a magnetic field of flux density B [T] contains potential energy E [Joule], which is given by the following equation:

$$E = \int \frac{B^2}{2 * \mu_o} \, dV \,,$$

where $\mu_o = 4\pi \, 10^{-7}$ [$V \, s \, A^{-1} \, m^{-1}$] is the permeability of vacuum.

Large magnets operating at high fields, like for example particle accelerator dipoles or fusion magnets typically store energies in the range of several MJ. The potential of storing large amounts of energy in magnetic fields is used in SMES devices, where SMES stands for superconducting magnetic energy storage, and very large SMES systems for even diurnal load leveling of the power grid with storage capacities of hundreds of GJ have been under consideration[4].

As mentioned above each base solenoid of the radiation shield with a volume of about 1000 m^3 and a flux density of 1 Tesla stores about 400 MJ. Since it takes only about 0.7 MJ to melt 1 kg of copper, starting at a temperature of 50 K, the energy stored in a single base coil of the radiation shield is sufficient to melt about 570 kg of copper. This large amount of stored energy could be used for mission tasks that require significant amounts of energy with high power, but the energy has to be handled with great care to avoid damage to the mission-critical radiation shield. An uncontrolled release of this energy into the coil itself would cause significant damage to the magnet with high probability.

4.7. Quench Avoidance and Protection

If the critical temperature, field or current density of a superconductor are exceeded by a sufficient amount, a rapid transition from the superconducting to the normal conducting state, called quench, is initiated. Since the specific heat of materials vanishes near absolute zero of temperature, very small amounts of energy are sufficient to initiate a quench in low temperature superconducting (LTS) magnets, which typically operate near 4.2 K or even below. At these operational temperatures even microscopic conductor movements of a few microns can release sufficient amounts of energy to initiate a quench, and for many LTS magnets quenching of the coil cannot be totally excluded. Quench detection and quench protection are therefore important considerations for the safe operation of LTS magnets.

However, even certain LTS magnets are not allowed to quench, except in the case of complete system failures like extended power outages, fires or other catastrophic events. MRI magnets for medical applications are an example of such quench-safe superconducting magnets. These magnets have to be designed and operated with large operational margin for temperature, field and current density.

---

[4] In the beginning of the 90th an EBASCO team developed a conceptual design, the Engineering Test Module (ETM), of a very large SMES unit, with a storage capacity of 5000 MWh (unpublished, private communication).

Depending on coil construction and resulting conductor stability superconducting wires in coils can move under the effect of strong Lorentz forces and release energy into their surrounding due to frictional forces. The largest amount of potential conductor movement inside a coil of given design can be estimated, as well as the energy that is released in the event of such a conductor movement. If the energy needed for a coil to quench, i.e., the minimum quench energy, substantially exceeds the energy released by possible conductor movements, no quench can be initiated due to this effect. Such magnets will not show any premature quenching below the critical parameters of temperature, field and current density, and therefore will only quench in the case of uncontrollable, catastrophic events like a failure of cooling.

High temperature superconducting (HTS) magnets in contrast to LTS ones are much less likely to quench caused by energy release from conductor movements. This is mainly due to the fact that the specific heat increases rapidly with temperature, and a much higher amount of energy is needed to raise the temperature in a given conductor volume above the critical temperature of the superconductor. This can be seen from Figure 4.9, which again shows the specific heat of YBCO as a function of temperature.

YBCO Specific Heat versus Temperature
NIST WEB-HTS Database

$y = 8E\text{-}12x^6 - 9E\text{-}09x^5 + 4E\text{-}06x^4 - 0.0008x^3 + 0.0824x^2 - 0.9193x + 1.9692$

Figure 4.9. Specific heat of YBCO as a function of temperature showing the significant increase of specific heat between 4.2 K (LTS operation) and about 50 K (HTS operation).
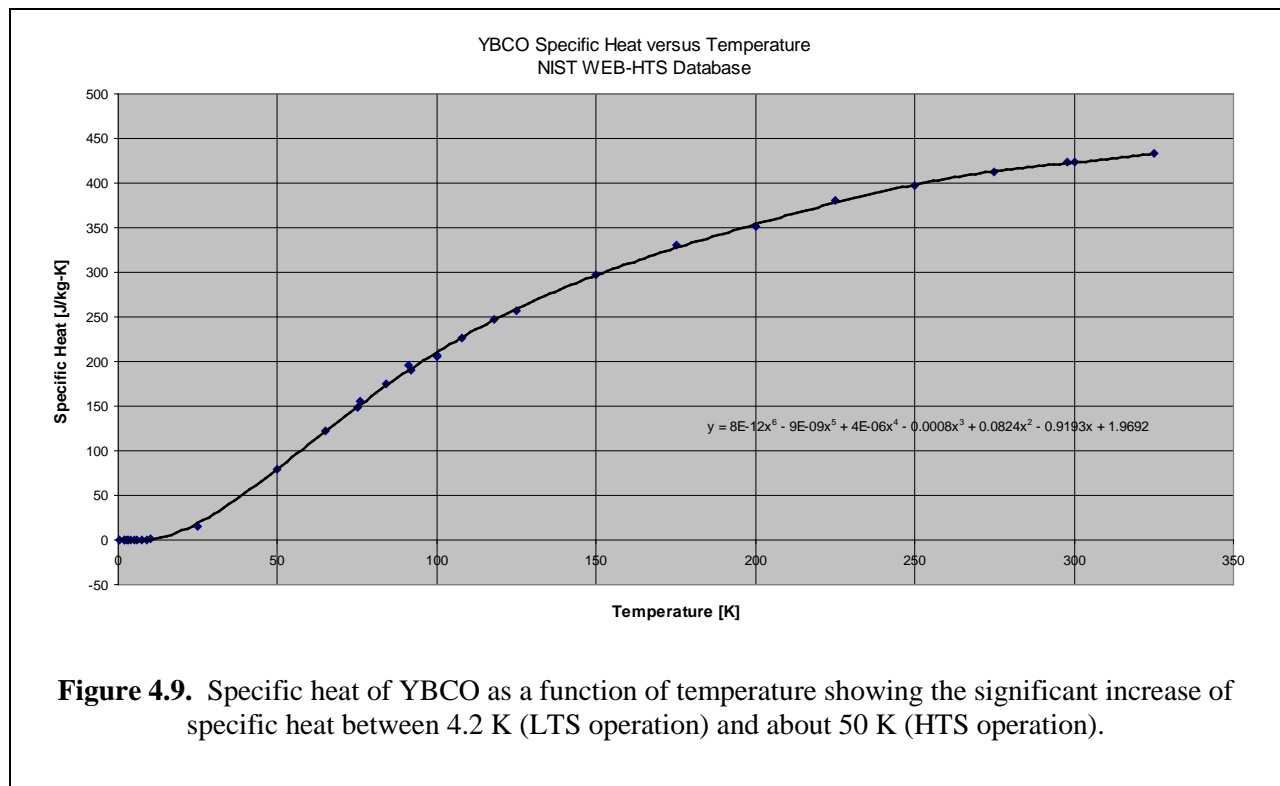
It is important to point out that the relative high minimum quench energy of HTS superconductors is the enabling feature for the realization of expandable coils. However, it will be of utmost importance for a successful realization of expandable coils to develop appropriate coil support structures. The materials used for the conductor support should allow shape changes at Lorentz forces that are significantly smaller than the forces acting at full coil excitation. In this case, the expandable coil will approach its final shape already at a rather low excitation current, where the superconductor is still far away from its critical surface and therefore has large operational margin. The support structure also should guarantee

a smooth approach to the final shape without sudden abrupt movements. Such jerks of the conductor under acting Lorentz forces, often described as stick-slip, are one of the reasons for premature quenching in LTS coils. However, even high-field LTS magnets can show quench-free operation with modest shape changes and conductor movements, if these changes proceed in a smooth way. Large dipole magnets operating at 5 Tesla that were built for the HERA accelerator at DESY in Germany, changed their whole coil cross section by about 2% or about 0.6 mm without any quenching[5]. It is a safe assumption that stick-slip conductor movements of much smaller distance would initiate quenches in these magnets.

Some passive quench protection system for worst-case scenarios will still be needed for the large coil system of the radiation space shield array. The standard technique for extracting the stored energy from a large superconducting coil is based on dump resistors, which are switched in parallel to the coil in case of a quench. The concept is shown in Figure 4.10.

Figure 4.10. Schematic layout for passive quench protection of large coil system.
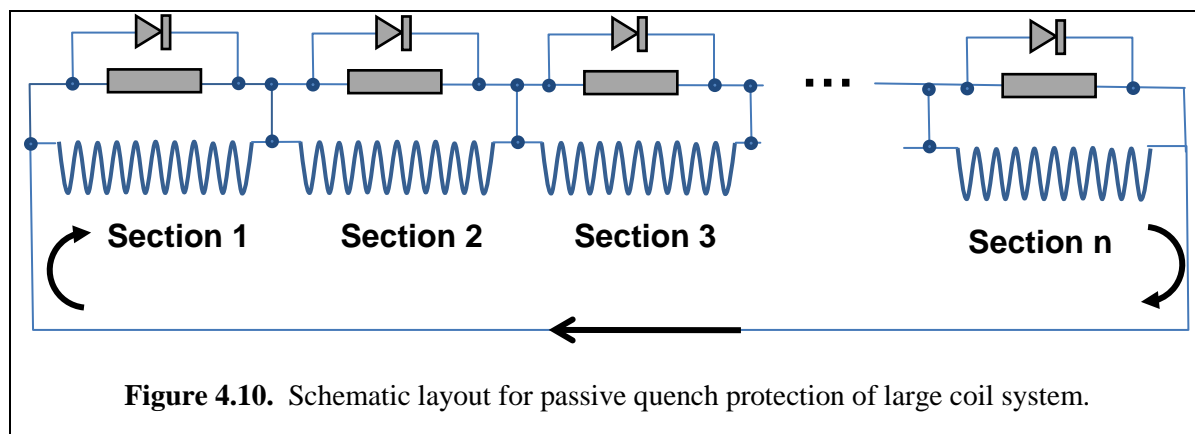
In the conceptual system shown Figure 4.10 a single shielding coil is subdivided into separate sections, which are individually shunted with dump resistors. Such a subdivision might be required to keep the voltage across a dump resistor in case of energy extraction within a safe limit. Since the product of operational current and dump resistor value determines the voltage at the coil terminals in case of energy extraction, only a very small resistivity of the dump resistors is allowed. However, for an efficient energy extraction a large resistance is preferred. It is currently TBD, if such a subdivision is actually required, or if a single dump resistor for a whole shield coil would be sufficient. In order to avoid that the energy stored in the non-quenching sections is dumped into a quenching section, diodes are placed in parallel to the dump resistors.

---

[5] R. Meinke, private communication.

4.8.   Operational Current Considerations

Large superconducting magnets preferentially operate at high currents, in order to facilitate quench protection of the coils, i.e., to reduce the peak temperature and peak voltage that are reached in case of a quench. While the energy stored in a magnetic field of a given volume and flux density is independent of operational current, I, the inductance, L, of the coil will decrease with increasing operational current, given by the following relation:

$$E = \frac{1}{2} * L * I^2.$$

Since the peak voltage and the peak temperature reached during a quench increase with inductance, which itself decreases with the square of the operational current, the highest possible operational current, I, is the preferred operational condition to facilitate quench safety of the coil.

Large magnets often require active quench protection systems consisting of heaters that spread the stored energy over a large area of the coil, thereby reducing and avoiding the risk of local overheating. However, an active quench protection system would significantly increase the technical complexity of magnetic radiation shielding, and a passive quench protection, as shown above, is therefore strongly preferred. To avoid active quench protection, it is mandatory to operate the coils at very high currents, and an operational current of about 40 kA was chosen. This current level seems achievable with modest improvements of high temperature YBCO superconductor, as described in section 4.2.

A high current level of about 40 kA also allows reaching the nominal field of 1 Tesla with a single conductor layer, which significantly facilitates the realization of an expandable coil. A multi-layer coil that is flexible enough to allow shape changes during the coil expansion would be difficult to realize. Furthermore, the cooling of a multi-layer coil would represent a much more difficult technical problem. In contrast, operating around 50 K might be possible with only radiation cooling to the deep space surrounding (2.7 K), if direct sunlight can be avoided.

4.9.   Superconducting Coil Reliability
S. Winter - Johnson Space Center, NASA

Plans to evaluate the phase I system concept for ruggedness and survivability were in place. Risk analyses were considered to find failure modes and associated causes and research was conducted on available technical literature for existing systems for relevant failure data. However, such data is limited with the newly manufactured technology. In this case, a physics of failure model is considered to investigate failure causes of interest.

5. Flux Pump Excitation

R. Meinke - Advanced Magnet Lab

The required operational current of about 40 kA for each coil will be supplied by a flux pump, a relatively small superconducting device that allows charging of superconducting coils operating in persistent mode.

The basic principle of a flux pump is show in Figure 5.1. The persistent mode operation of the superconducting coil is achieved by shunting the coil with a flux gate, i.e., another piece of superconductor, which is able to carry the transport current of the coil with sufficient margin in part of its total width. A permanent magnet mounted to a rotating arm traverses the flux gate and the coil leads attached to the flux gate during its rotation. The flux density of the permanent magnet, where it crosses the flux gate, is sufficiently strong to initiate a transition of this spot to the normal conducting state, introducing an amount of flux $\Delta\Phi$ into the flux gate and the transport current loop of the coil. The flux gate has to be sufficiently wide that the transport current of the coil can still be shunted without interruption. The coil leads connected to the flux gate have a critical field larger that the field of the permanent magnet and are therefore not affected, when the magnet crosses during its rotation. In this case, for each rotation of the permanent magnet around its axis, a certain amount of flux $\Delta\Phi$ is introduced into the superconducting loop consisting of the coil and the flux gate.

Figure 5.1. Schematic implementation of a superconducting flux pump for the charging of a coil, which operates in persistent mode.
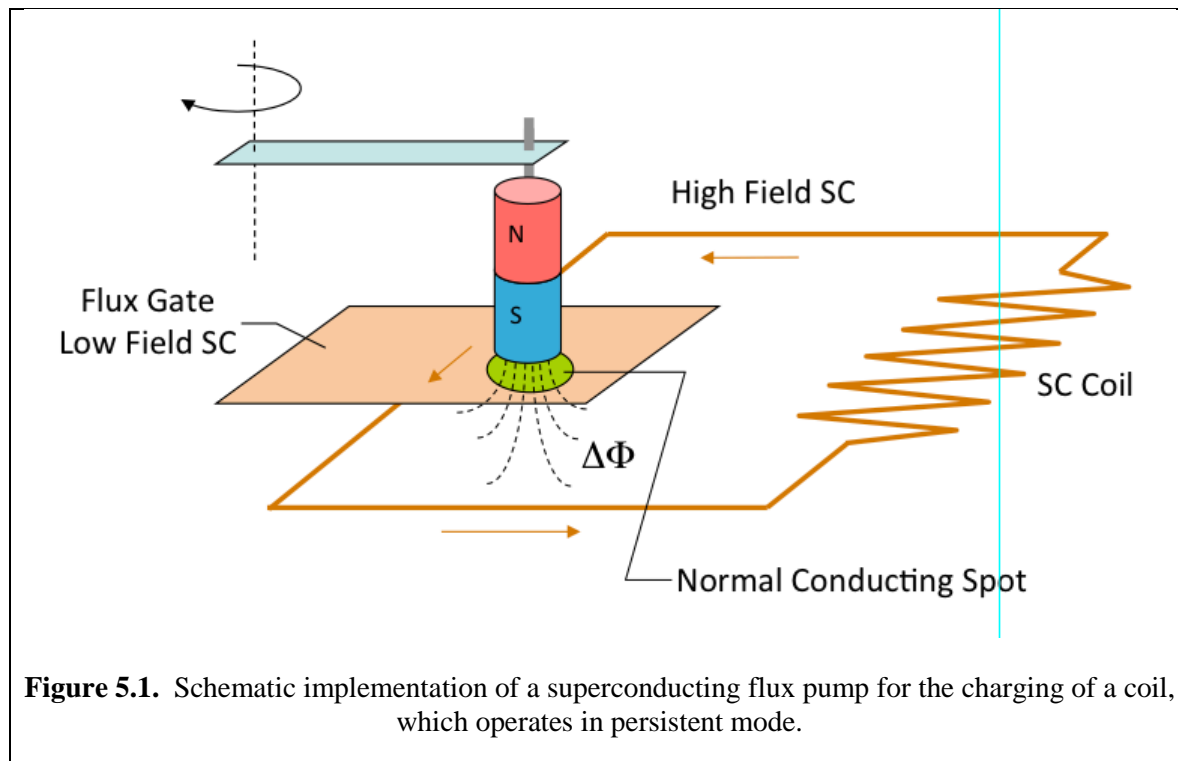
While the system shown in Figure 5.1 is fully functional, a slightly different implementation of a flux pump has been successfully used for applications with high currents as needed for the space shield[6], and such a system is currently envisioned for the radiation shield coils. The system is shown in Figure 5.2.

The system is driven by a transformer, which is normal conducting on its primary side (left) and superconducting on the secondary side (right). Thermally or magnetically activated superconducting switches, S1 and S2 are opened and closed with appropriate timing so that flux is introduced into the persistent mode coil (far right) with each half-wave of the driving alternating current (AC). The frequency of the AC is matched to the switching speed of the superconducting switches, which in principle can be simple pieces of superconductor. They can be surrounded by small, pulsed heaters or pulsed magnets. By activating one of the heaters or a pulsed magnet, superconductivity in the attached superconductor is broken, and the switch transitions to a state of high resistivity. Since the other switch is still superconducting, the difference between resistivity of switch open and closed is many orders of magnitude as needed.

The system shown in Figure 5.2 has been successfully used to achieve 26.4 kA in the secondary. The charging rate of the system was 5.4 MJ/hour with a primary current of 35 A and a frequency of 0.1 Hz. Based on a comparable performance it would take in the order of 100 hours to charge a shielding coil with a stored energy of 400 MJ.
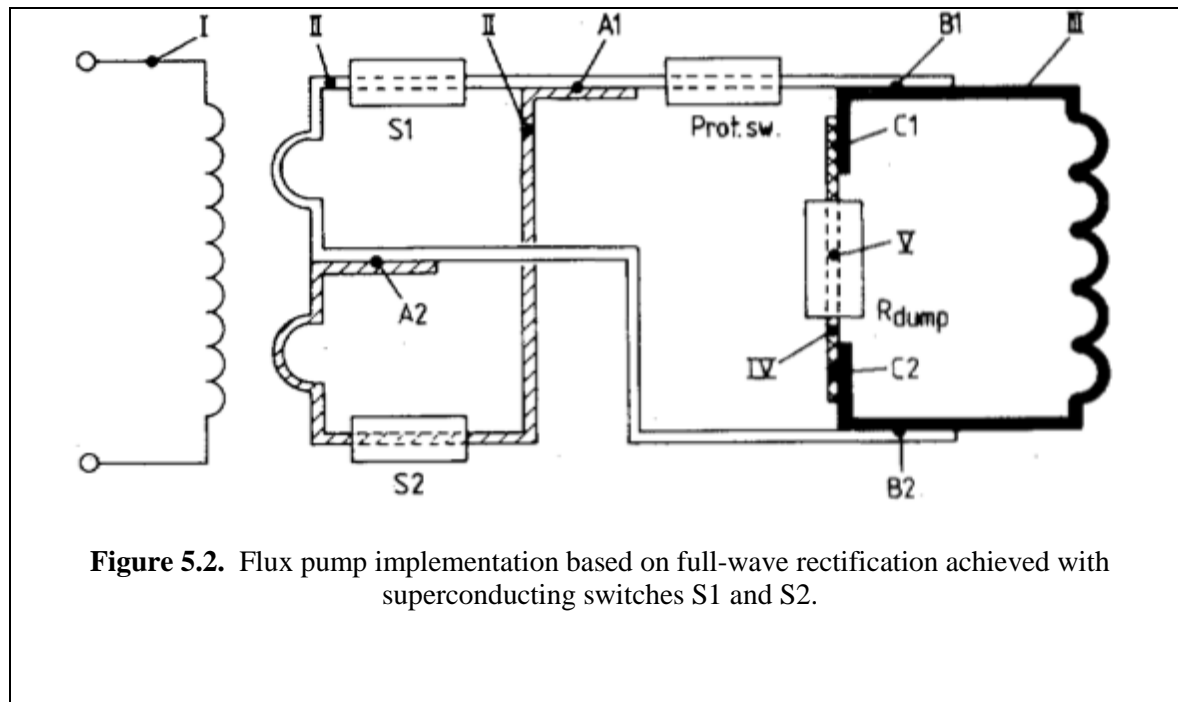
Figure 5.2. Flux pump implementation based on full-wave rectification achieved with superconducting switches S1 and S2.

[6] H.J. ten Kate et al., A Thermally Switched 9 kA Superconducting Rectifier Flux Pump, IEEE Transactions on Magnetics, Vol. Mag-17, No.5, Sept. 198

As can be seen from Figure 5.2, several superconducting splices are needed for the implementation of the system, i.e., enable persistent mode operation. In Figure 5.2 these connections are labeled A1, A2, B1, B2, C1 and C2. The last two are needed for the connection of a dump resistor or load for energy extraction from the coil. The system shown was based on LTS conductor, for which superconducting splices are a well-established technology. For example, MRI systems operate in persistent mode and therefore require superconducting splices. However, for YBCO conductors superconducting splices or those with sufficiently low resistivity do not yet exist and related R&D is required. Currently YBCO splices with a resistivity of 10^{-8} ohm have been achieved, which would constitute losses of about 16 W ($P=R*I^2$) per splice; a totally unacceptable loss. We think it will be possible with some R&D to achieve a splice resistivity of less than 10^{-12} ohm, which would reduce the splice joint loss to about 1 mW, which is most likely acceptable. With a constant operation of the flux pump such losses even for a large number of splices could be accommodated. It also would be required to make sure that heat in the vicinity of the splice joints does not accumulate and affect the operational temperature of the superconductor

For the overall operation of the radiation shield it is anticipated that each shielding coil is independent, having its dedicated flux pump. A control system is needed to guaranty that all coils are excited at the same rate to avoid force imbalances between the coils and flux leakage into the habitat. The flux pumps can be powered by a solar power array. The schematic layout of the system is shown in Figure 5.3.
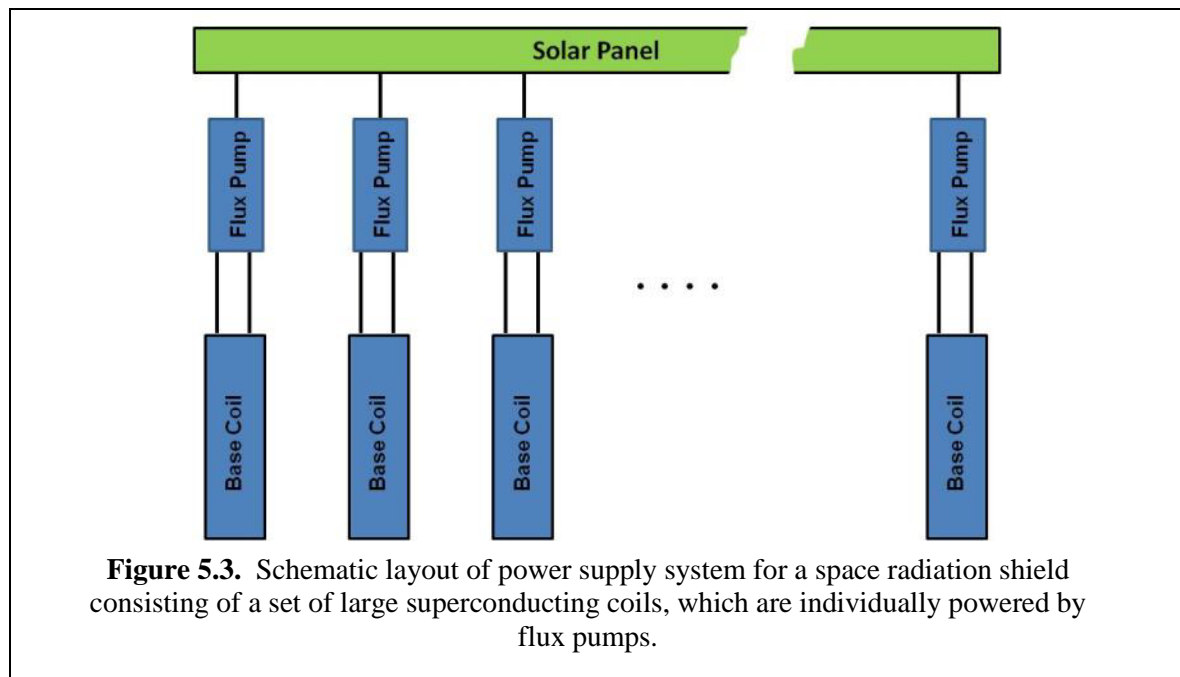
Figure 5.3. Schematic layout of power supply system for a space radiation shield consisting of a set of large superconducting coils, which are individually powered by flux pumps.

6. Performance Evaluation of the Extendable Solenoid Shield

W. J. Burger, Università Degli Studi di Perugia, I-06231 Perugia (PG), Italy

The performance of the active shield configuration is evaluated in terms of the organ dose equivalent obtained from a Monte Carlo simulation. The method used for the dose determination and the description of the solenoid shield in the simulation are presented. The performance of the 8 Tm solenoids have been evaluated for galactic cosmic-rays (GCR) at solar minimum, and for a worst week solar energetic particle (SEP) event. The GCR dose levels for a 20 Tm configuration are also presented.

6.1. Physics Simulation

The performance of the 6+1 expandable solenoid coil configuration has been evaluated with a physics simulation based on GEANT3[7]. The program performs particle propagation in magnet fields and materials with a detailed treatment of electromagnetic interactions. Hadron interactions of protons, helium nuclei, the generated secondary singly-charged meson and baryons, and secondary deuterons and tritons are simulated with GEANT-FLUKA[8]. The Relativistic Quantum Molecular Dynamics model (RQMD) [9] is used for the hadron interactions of higher charge nuclei.

GEANT3, a FORTRAN code which is no longer supported, and has been replaced by the C++ program GEANT4[10]. The present simulation is a modified version of the simulation program of the AMS experiment[11] which incorporates both C++ and FORTRAN code, and may be compiled with either GEANT3 or GEANT4. The magnetic shield study was implemented in the GEANT3 version [12]. The simulation program has been used in a study to evaluate the performance of active radiation screen designs based on HTSC double-helix solenoid and toroid configurations[13].

---

[7] R. Brun et al., GEANT -Detector description and simulator tool, CERN Program Library Long Write-up W5013, CERN, Geneva (1993).

[8] A. Fass`o, A. Ferrari, J. Ranft and P.R. Sala, FLUKA: present status and future developments, proceedings of 4th International Conference on Calorimetry in High Energy Physics, La Bidola (Italy) 21-26 September 1993, World Scien H. Sorge, Physical Review C, volume 52, number 6 (1995) 3291. tific, pp. 493-502.

[9] H. Sorge, Physical Review C, volume 52, number 6 (1995) 3291.

[10] S. Agostinelli et al., Nucl. Instr. and Methods A, 506 (2003) 250.

[11] M. Aguilar et al., Phys. Reports, 366 (2002) 331.

[12] V. Choutko, H. Hofer and S.C.C. Ting, The AMS Experiment and Magnet Faraday Cage for Human Space Exploration, presented at the NASA Active Radiation Shielding Workshop, Ann Arbor, MI, August 17-18, 2004.

[13] R. Battiston, W.J. Burger et al., An Active Radiation Screen Design Based on Superconduction Double-Helix Solendoids, Proceedings of the 5th IAASS Conference "A Safer Space for a Safer World", Versailles, France 17-19 October 2011 (ESA SP-699, January 2012); R. Battiston, W.J. Burger et al., ESA ARSSEM report, http://arxiv.org/abs/1209.1907

In terms of the physics processes relevant to the present application, GEANT3 remains a reference. The modeling of the electromagnetic interactions was well-established by the time of the last release of the GEANT3 code, and many of the current nuclear interaction models are anterior to this date.

The reliability of any model depends on the availability of experimental data. An important source of uncertainty is the lack of nuclear fragmentation measurements for high charge nuclei, which are responsible for a significant fraction of the GCR dose. The largest uncertainty is attached to the biological effects induced by the recorded energy losses, in particular those due to the higher charge nuclei[14].

6.2.   Dose Equivalent Calculation

The ionization energy losses recorded during the track propagation dE_i are converted to an dose equivalent ϵ_i (Sv) by multiplying the absorbed dose $\frac{dE_i}{m}$ (Gy), where m is the mass of the volume considered, by the quality factor $Q(L)$ defined by the unrestricted linear energy transfer in water L (keV/µm):

$$\epsilon_i = Q(L) \cdot \frac{dE_i}{m}$$

$$\text{with } L = \frac{dE_i}{dx} \text{ and } Q(L) = \begin{cases} 1 & \text{for} & L \leq 10 \\ 0.32 \cdot L - 22 & \text{for} & 10 < L < 100 \\ 300/\sqrt{L} & \text{for} & L \geq 100 \end{cases}$$

The total dose equivalent d_z (E_j) for an exposure time t, due to GCRs of charge Z and kinetic energy E_j is the sum of the dose equivalents recorded for N_j incident particles generated with the flux f_z (E_j) (cm^{-2}sr^{-1}s^{-1}MeV^{-1}), in the energy interval ΔE_j, over the acceptance A (cm^{2}sr):

$$d_z(E_j) = \sum_i \epsilon_i \cdot \frac{A}{N_j} \cdot f_z(E_j) \cdot \Delta E_j \cdot t$$

The total GCR dose D is obtained by extending the generation over suitable ranges in charge and kinetic energy. The contribution from charge Z is

$$d_z = t \cdot \sum_j \left[\sum_i \epsilon_i \right]_j \cdot A \cdot \sum_j \frac{f_z(E_j) \cdot \Delta E_j}{N_j}$$

and the total dose equivalent including all charges up to Ni, $D = \sum_{z=1}^{z=28} d_z$.

---

[14] M. Durante and F. Cucinotta, Rev. Mod. Phys., volume 83 (2011) 1245.

The kinetic energy spectra $f_z (E_j)$ are taken from the CREME 2009 GCR model [15] which extends over the energy range 1 to 10^5 MeV/n. The GCR fluxes for solar minimum and maximum conditions are shown in Figure 6.1. The integrated fluxes for the two periods are presented in Figure 6.2. A reduction of 45-60 % is observed in the GCR fluxes between the solar maximum and minimum.

The human body is represented in the simulation as a 24 cm diameter, 180 cm long water-filled cylinder. The cylinder is subdivided to define the regions used to compute the dose associated with the skin and blood-forming organs (BFO), respectively the first 2 mm at the surface of the cylinder and a 2 mm thick layer located a depth of 5 cm from the cylinder surface (Figure 6.3). The body dose refers to the ionization losses recorded in the full volume of the cylinder.

The annual dose equivalents in free space obtained with the simulation at solar minimum (maximum) are 117.7 (71.0), 62.4 (39.5) and 51.5 (30.1) cSv for the skin, BFO and body respectively[13].

---

[15] Cosmic Rays Effects on Micro Electronics (CREME), https://creme.isde.vanderbilt.edu/CREME-MC
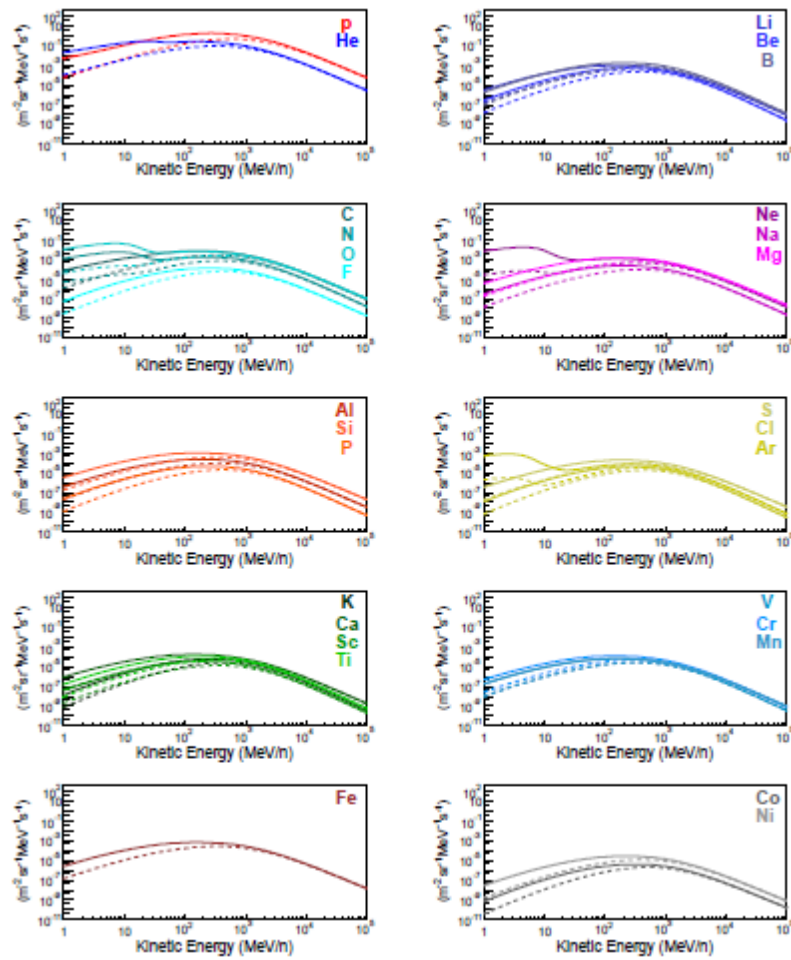
Figure 6.1 The GCR spectra for a solar maximum in 1990 (dashed lines) and a solar minimum in 1977 (solid lines) from the CREME 2009 GCR model[15].
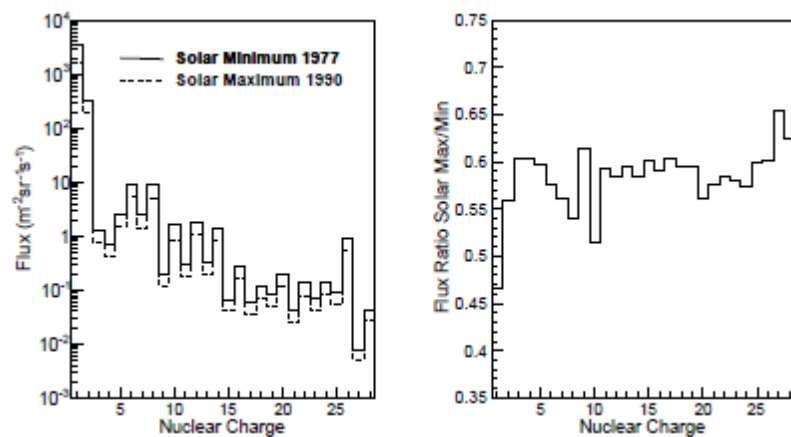
Figure 6.2. The energy-integrated GCR nuclei fluxes for the solar minimum and maximum periods (left) and the flux ratio (right). The smaller reduction of the fluorine flux is explained by the absence of an anomalous component.

H₂O cylinder: Ø 24 cm, length 180 cm
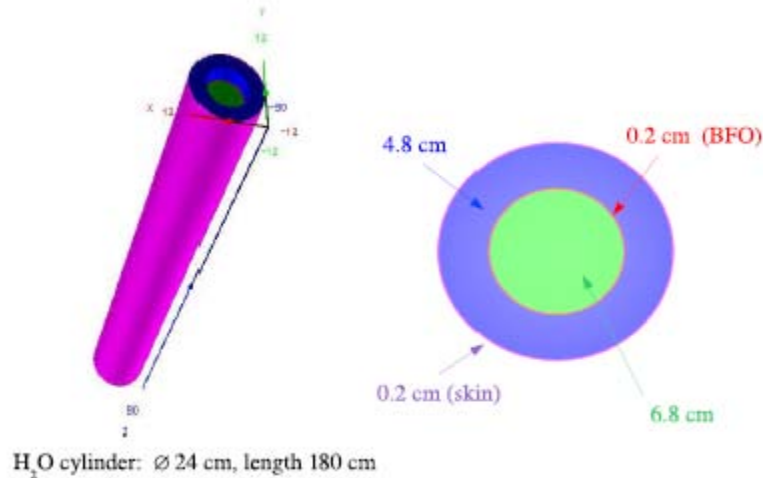
Figure 6.3 The cylindrical water volume used to compute the dose of the skin and blood-forming organs (BFO). The total body dose refers to the full volume of the 24 cm diameter, 180 cm long cylinder (81.4 kg).

6.3.   Simulated Magnetic Shield Configuration

The simulated magnetic shield configuration consists of six, 8 m diameter, 20 m long HTSC solenoids, which surround a 6 m diameter, 10 m long cylindrical habitat (Figure 6.4). The radial distance between the center of the habitat and the centers of the solenoids is 8 m. A uniform 1 T field in the +z direction is present in the cylindrical volumes delimited by the coil dimensions.

A 6.4 m diameter, 20 m long HTSC compensation solenoid surrounds the habitat. The field of the compensation solenoid would be oriented in the −z direction in order to minimize the field inside the habitat. The structural elements of the compensation solenoid are included in the simulation. However, the magnetic field regions are limited to the cylindrical volumes of the shield solenoids. The habitat is field free. The details of the resultant field outside the solenoids are not taken into account in the present study.

The YBCO conducting tape of the HTSC solenoid coils consists of a 50 μm thick substrate layer, two 30 μm thick layers of copper, a 2 μm thick layer of silver and a 1 μm thick (RE) BaCu-O HTSC layer. The chemical composition of the Hastelloy C-276 substrate is presented in Table 6.1. The average density and radiation length of the substrate are similar to copper. Consequently, the HTSC coils are represented in the simulation by 110 μm thick copper cylinders. The 30 μm thickness of the copper layers of the tape was chosen to yield a mass corresponding to the AML estimate for the 20 m long, 8 Tm coil (500 kg) (see Table 2.5)
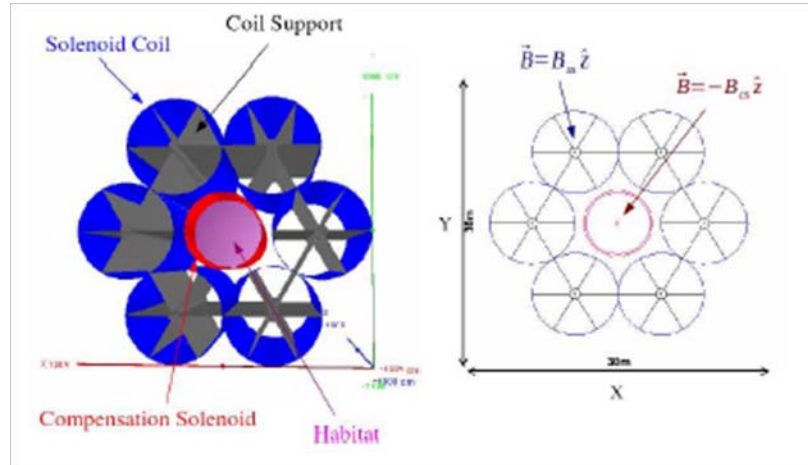
Figure 6.4. The structural elements in the simulation of the magnetic shield configuration (left). View of the configuration in the plane perpendicular to the solenoid axis (right). The shield solenoids flux density B_{ss} is 1 T. The flux density of the compensation coil B_{cs} is chosen to cancel the cumulative return flux of the shield solenoids in the habitat. The magnetic field regions in the simulation are confined to the cylindrical volumes delimited by the six shield coils.

The support structures of the extendable solenoid coils are represented in the simulation by a 1 m diameter, 1 cm thick, 20 m long graphite cylinder located in the center of each coil. The six radial spokes are represented by six 2.5 mm thick, 3.5 m wide, 20 m long graphite plates.

The compensation solenoid consists of a 111 μm thick copper cylinder and a 2.4 mm thick graphite support cylinder. The 6 m diameter cylindrical habitat is filled with air and includes a 1.8 cm thick aluminum outer shell. The list of the structural elements in the simulation are given in Table 6.2. The quoted thicknesses represent the minimal material thickness traversed by the particles.

Table 6.1 Composition of Hastelloy C-278 substrate of typical YBCO tape conductor: Z nuclear charge, ρ density, χ_o radiation length, M_A molecular mass.

	Z	% mass	$\rho\,(\mathrm{g/cm^3})$	$\chi_o\,(\mathrm{cm})$	$M_A\,(\mathrm{g/mole})$	% atoms
Ni	28	55.4	8.90	1.42	58.69	59.2
Co	27	3.5	8.70	1.57	58.93	2.7
Cr	24	16	7.18	2.08	52.00	19.3
Mo	42	16	10.2	0.96	95.96	10.5
W	74	4	19.3	0.35	183.84	1.4
Fe	26	5	7.87	1.76	55.84	5.6
Si	14	0.08	2.33	9.37	28.09	0.2
Mn	25	1	7.44	1.97	54.94	1.0
C	6	0.02	2.21	19.3	12.01	0.1
Avg.	29.1		8.83	1.54		100.0
Cu	29		8.96	1.43		

Table 6.2 List of the structural elements in the 8 Tm shield simulation. The quoted total mass in the simulation includes the six shield solenoids (33 456 kg), the compensation solenoid and the aluminum shell of the habitat.

element	no.	material	thickness (mm)	mass (kg)
shield solenoid				
coil	1	Cu	0.111	500
support cylinder	1	graphite	10	2 763
radial plate	6	graphite	2.5	388
total mass 5 591 kg				
compensation solenoid				
coil	1	Cu	0.111	400
support cylinder	1	graphite	24	2 132
total mass 2 532 kg				
habitat	1	Al	18	10 136
total mass in 8 Tm simulation 46 214 kg				

The performance evaluation of the active shield design requires an accurate description of the materials of the shield and the spacecraft. For example, the 1.8 cm aluminum shell of the habitat reduces by 35% the free space skin dose, and by 30% the free space BFO and body doses at solar minimum conditions[13]. The final optimization of the design in terms of performance and mass must take into account the elements of the spacecraft, such as the propulsion system, payload modules and the material present in the habitat.

In the present study, a single habitat module is considered. The details of the coupling of the habitat to the rest of the spacecraft are ignored. The immediate aim is to evaluate the performance of the expandable shield configuration with respect to the required active shield mass.

6.4.   Barrel and Endcap Regions

Figure 6.5 shows the generation surface in the GEANT3 simulation. Events are generated uniformly over the 30 × 30 × 30 m^3 cube. At each generation point, the particle direction is chosen randomly over the polar and azimuthal angles at the surface of the cube.

The particles generated in the barrel region, the four lateral cube sides located in the *xz* and *yz* planes, traverse the magnetic shield surrounding the habitat. The effect of the 8 Tm field of the shield solenoids on 3 GV protons is illustrated in Figure 6.6. In this specific example, the initial proton direction was chosen along the line passing through the center of the habitat in order to highlight the effect of the field.
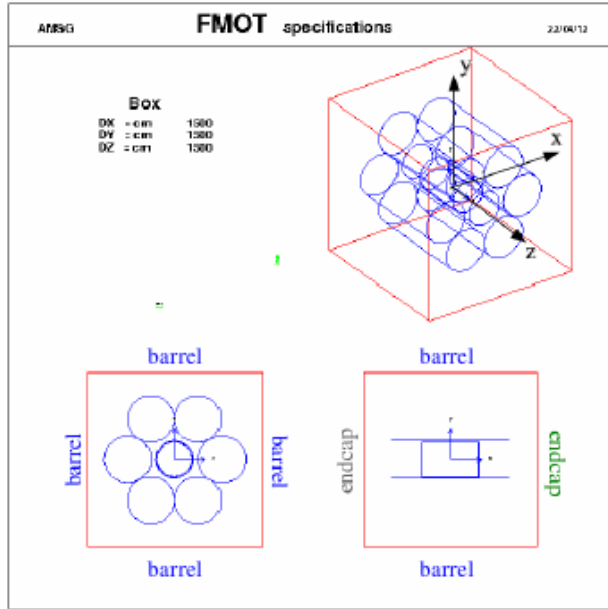
Figure 6.5 The generation surface in the simulation, a 30 x 30 x 30 m^3 cube (red). The four lateral sides in the *xz* and *yz* planes correspond to the barrel region. The *xy* planes at $z = \pm15$m are referred to as the endcap regions.
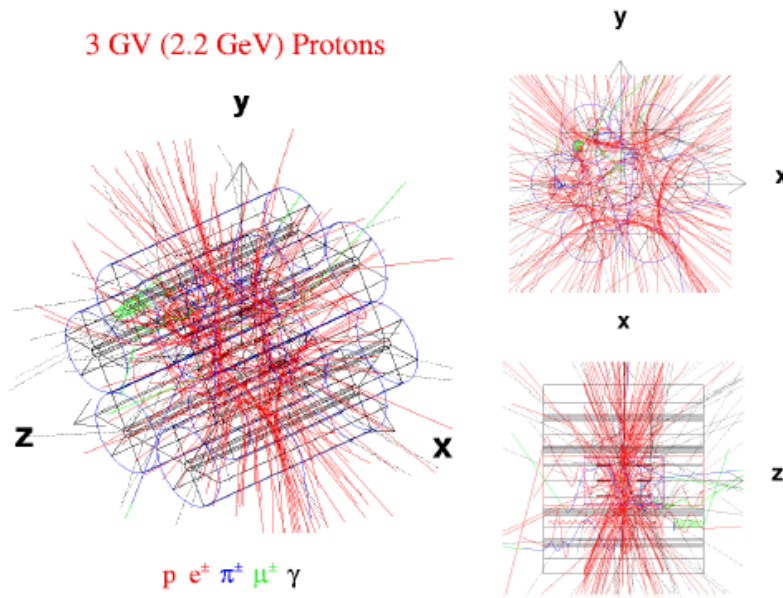
Figure 6.6 The trajectories of incident 3 GV protons and the secondary particles created in the materials present in the simulation. The protons were generated over the barrel region directed towards the center of the habitat. The more restrictive generation results in an event sample where the effect of the 8 Tm field is clearly visible in the *xy* projection (upper right). Particle types by color: protons, electrons and positrons (red); charged pions (blue); muons (green) and photons (black).

$$2\sin\frac{\theta}{2} \;=\; \frac{L}{r} \;=\; \frac{BL}{R}$$
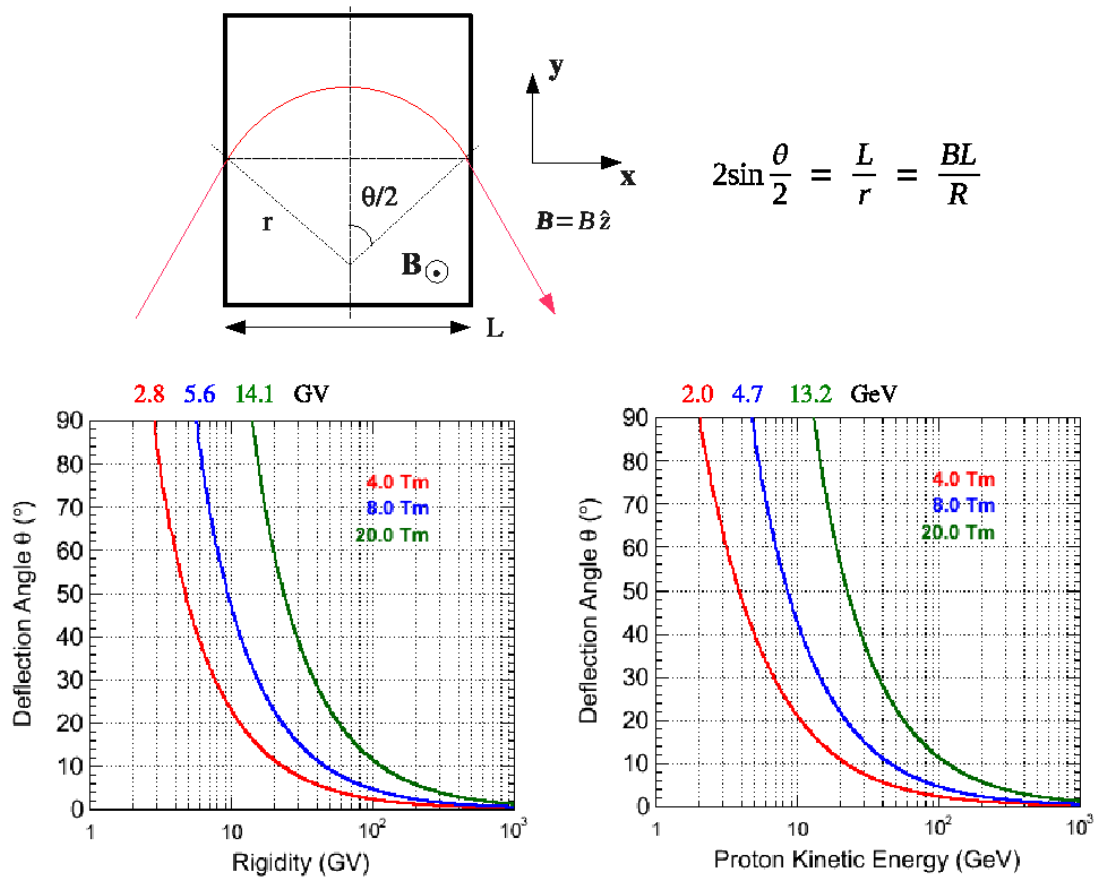
Figure 6.7 The deflection of the particle trajectory in the plane perpendicular to the field as a function of rigidity for three values of *BL* (lower left) and for protons, as a function of kinetic energy (lower right). The values of rigidity and kinetic energy corresponding to a 90° deviation from the incident direction are indicated.

The deflection angle θ in the plane perpendicular to the direction of the field with a flux density B is given by the expression

$$2sin\frac{\theta}{2} = \frac{BL}{R},$$

where L is the length of the field region in the plane, and R the particle rigidity, i.e. the ratio momentum-to-charge of the particle. The relations between the deflection angle and rigidity, and the proton kinetic energy, are shown in Figure 6.7 for three values of BL. With a conservative lower limit of 90° for the deflection necessary to avoid the habitat, the corresponding rigidity cutoff for the 8 Tm field is 5.6 GV.

The trajectories of 3, 5 and 7 GV protons, and the secondaries produced in the simulation, are shown in the *xy* projection in Figure 6.8. The protons were generated in the barrel region in the direction of the habitat center. The tracks of the primary 3 GV protons are deflected before reaching the habitat. The deflection in the solenoid field results in trajectories which are nearly tangent to the cylindrical surface of the habitat for the 5 GV protons. There is no indication of a significant deflection of the 7 GV protons.
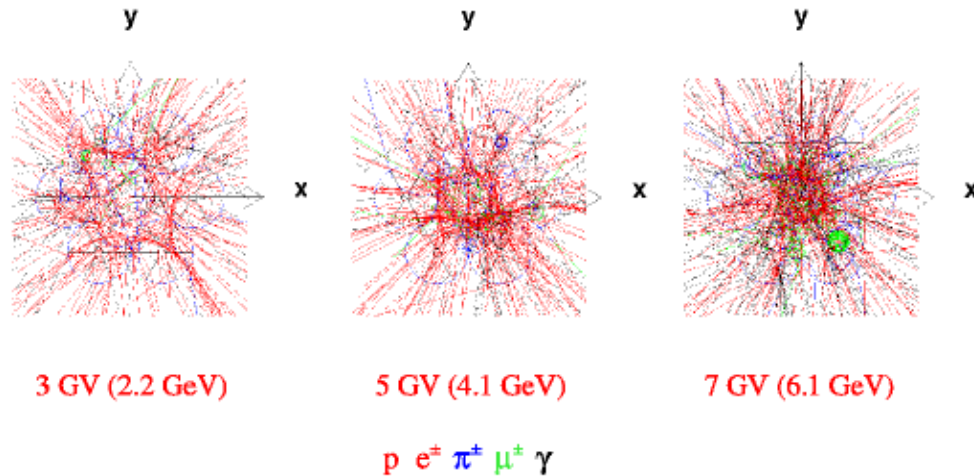
Figure 6.8 The trajectories in the *xy* projection of 3, 5 and 7 GV incident protons and the secondary particles created in the materials in the simulation. The initial direction of the protons was chosen along the line passing through the center of the habitat. Particle types by color: protons, electrons and positrons (red); charged pions (blue); muons (green) and photons (black).

The observed behavior is consistent with the calculated rigidity cutoff of 5.6 GV, considering the average L of the particles traversing the cylindrical solenoids is smaller than the 8 m diameter. The corresponding kinetic energy cutoff (4.7 GeV) implies that the 8 Tm shield solenoid configuration would deflect protons up to energies above the GCR proton peak energy (Figure 6.1).

A particle traversing the solenoid configuration in the direction of smaller (larger) r = $(x^2 + y^2)^{1/2}$, will be deflected in the direction of larger (smaller) r. The first case applies to the particles generated in the barrel region for rigidities up to the cutoff, above which the particles traverse completely the field region.

The performance of the solenoid shield configuration is symmetric with respect to the motion in z, i.e. particles traveling in the $\pm z$ directions experience the same deflection to larger r away from the habitat. The symmetry does not exist for a toroid configuration with an azimuthal field about the z axis. In this case, the particles will be directed away from the habitat only in one z direction, in the other they will be deflected towards the habitat. Consequently, a passive absorber is required to close one end of spacecraft, with lateral dimensions sufficiently large to cover both the habitat and the magnet field volume[12, 13].

However, the solenoid field configuration does not provide protection for the particles of the endcap regions, the two xy planes at z = ±15m in Figure 6.5. The relative contribution of these acceptance regions to the total dose is minimized by increasing the distance between the endcap planes and the habitat, i.e. extending the length of the shield solenoids.
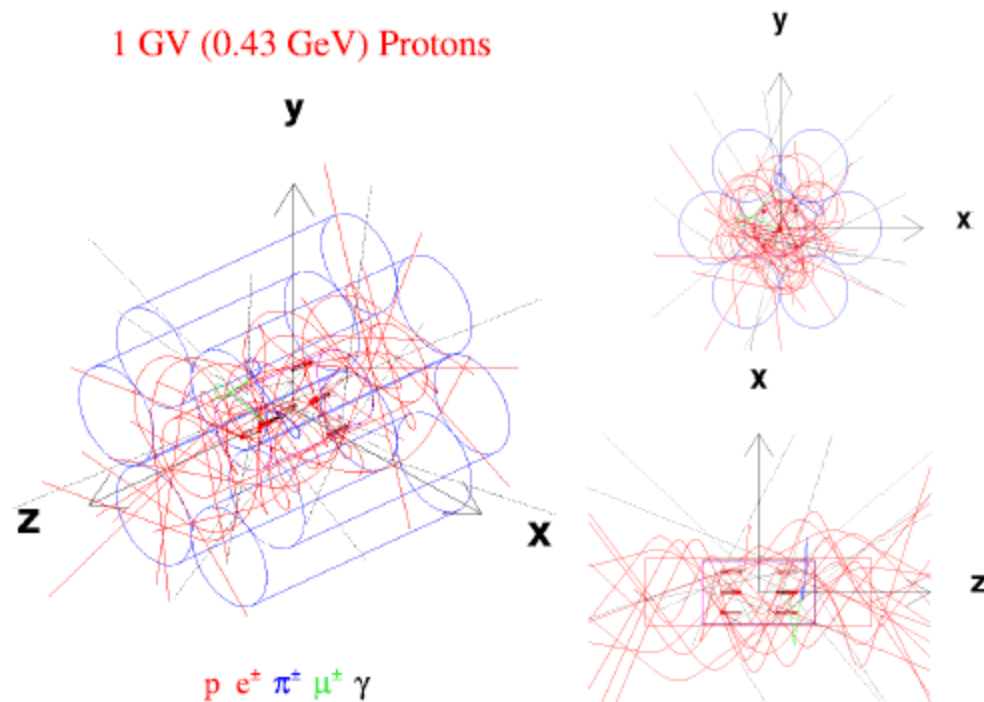
Figure 6.9 The trajectories of incident 1 GV protons and the secondary particles created in the materials present in the simulation. The protons were generated in the endcap regions over the full angular acceptance. The events were selected by requiring at least one ionization loss in the water cylinders (red crosses). The support structures of the shield solenoids are present in the simulation but suppressed in the event display. The coils of the shield solenoids do not appear in the *xz* projection since the configuration geometry is drawn in the plane $y = 0$; Particle types by color: protons, electrons and positrons (red); charged pions (blue); muons (green) and photons (black).

In the endcap regions, particles may traverse the solenoid configuration in the direction of increasing r, as illustrated with 1 GV protons in Figure 6.9. The protons were generated over the full acceptance of the endcap planes. The displayed events were selected by requiring at least one ionization loss in the water cylinders of the habitat. The protons which enter the solenoid field in the direction of increasing r execute an oscillatory motion, reflected back-and-forth between the shield solenoids surrounding the habitat. In this case, the protons below the rigidity cutoff contribute to the dose.

The materials of the solenoid coils and support structures, and the 1.8 cm aluminum shell of the habitat, provide passive shielding in the endcap regions. Additional material will be present once the habitat is coupled to the other payload modules of the spacecraft.

The dose reduction in the barrel region is used to evaluate the performance of the extendable field shield. The total doses quoted for the full acceptance serve to indicate the relative importance of the barrel and endcap regions for the chosen solenoid dimensions, and consequently, the potential gain of an optimization of the shielding in the two regions.

6.5.   Annual GCR Dose Equivalents

The annual BFO dose equivalent for GCR protons, helium nuclei, and the nuclear charge groups 3 ≤ Z ≤ 10, 11 ≤ Z ≤ 20 and 21 ≤ Z ≤ 28, are presented in Figure 6.10. In each case, the total dose recorded in the water cylinders, and the contributions of the barrel and endcap regions are indicated.
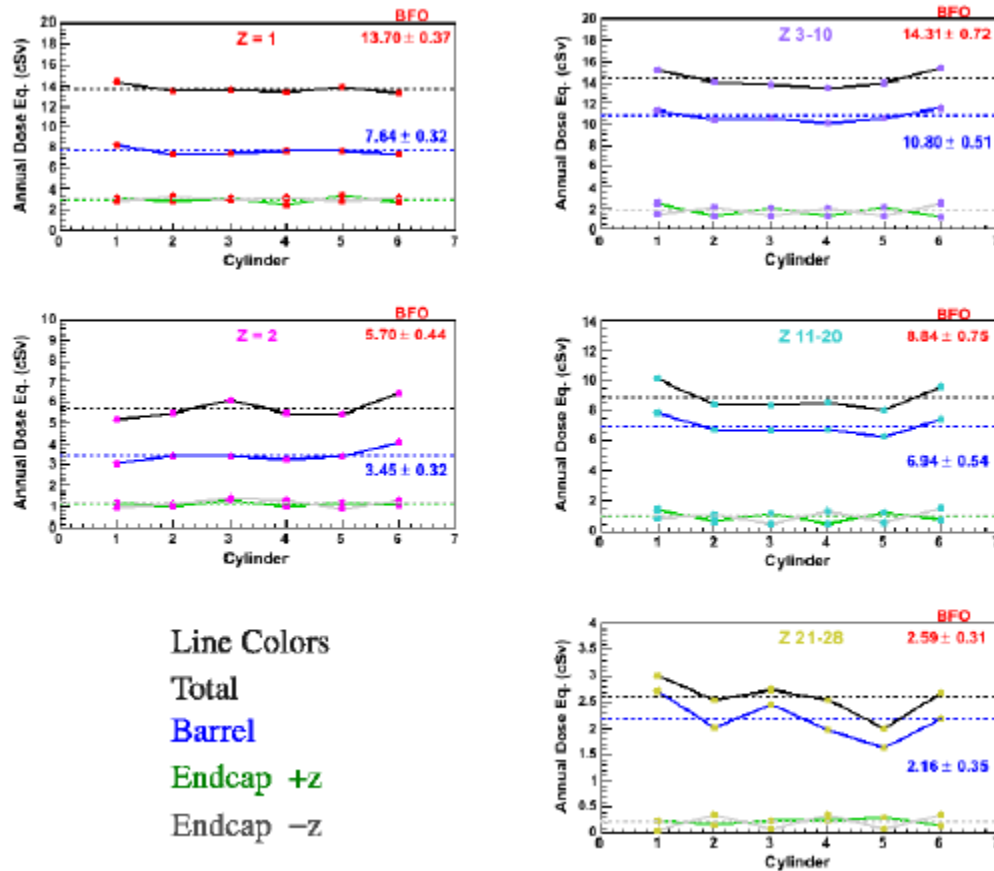
Figure 6.10 The BFO dose equivalents recorded in the six water cylinders for the 8 Tm extendable solenoid shield for GCR protons, helium nuclei, and the nuclear charge groups: $3 \leq Z \leq 10$, $11 \leq Z \leq 20$ and $21 \leq Z \leq 28$. The average values of the six cylinders and the root-mean-square variations are quoted for the total (red) and barrel region (blue) doses.

The positions of the six cylinders, which are used to sample the dose levels on and off the axis in each half-volume of the cylindrical habitat, are shown in Figure 6.11. A clear correlation is observed in the endcap regions where the +z events produce systematically higher dose levels in the upstream cylinders 1, 3 and 5, and vice versa for the −z events and the downstream cylinders 2, 4 and 6.

The average values and root-mean-square variations of the total dose, and the dose corresponding to the barrel region, are indicated in Figure 6.10. The contribution of the barrel region, which represents 56% of the total dose for protons, increases with charge attaining 83% of the total dose for the highest charge nuclei. The trend is explained by the charge dependence of the ionization energy loss Z^2 , which

increases the efficiency for the higher charge nuclei, of the passive shielding present in the endcap regions.
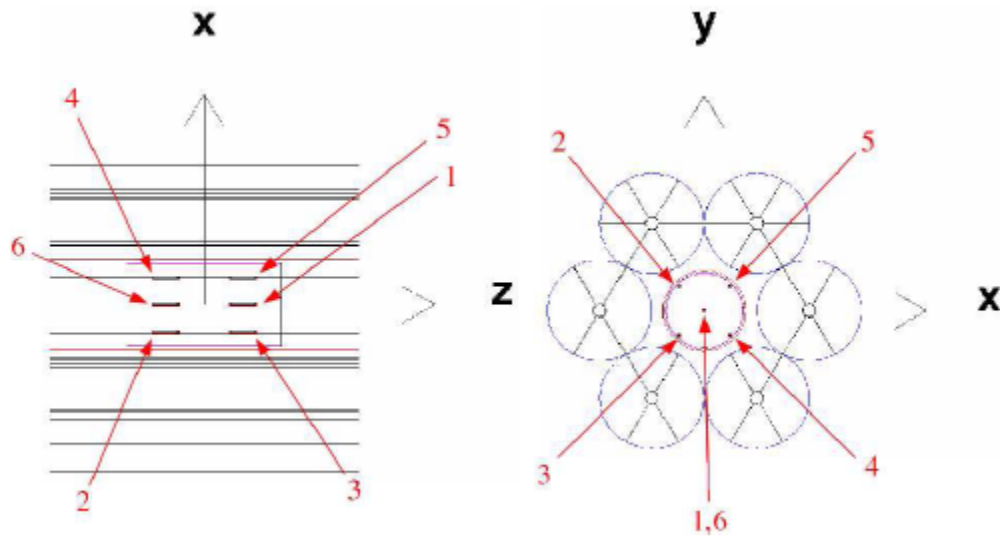
Figure 6.11 The location of the six water cylinders in the habitat.

Table 6.3 Annual GCR dose equivalents (cSv/rem) for the 8 Tm extendable solenoid shield.

Z	Total			Barrel		
	skin	BFO	body	skin	BFO	body
1	14.4 ± 0.3	13.7 ± 0.4	13.4 ± 0.2	7.9 ± 0.3	7.6 ± 0.3	7.4 ± 0.2
2	6.6 ± 0.2	5.7 ± 0.4	5.6 ± 0.1	3.8 ± 0.2	3.4 ± 0.3	3.4 ± 0.1
3-10	22.5 ± 1.4	14.3 ± 0.7	7.5 ± 0.4	15.4 ± 0.7	10.8 ± 0.5	5.2 ± 0.3
11-20	18.4 ± 1.3	8.8 ± 0.7	7.1 ± 0.6	12.7 ± 0.8	6.9 ± 0.5	5.2 ± 0.4
21-28	8.1 ± 1.3	2.6 ± 0.3	2.7 ± 0.3	5.7 ± 0.8	2.2 ± 0.3	2.0 ± 0.3
total	70.0 ± 2.3	45.1 ± 1.2	36.3 ± 0.8	45.5 ± 1.4	30.9 ± 0.9	23.2 ± 0.6
fraction of total dose				0.65	0.69	0.64

The results for the 8 Tm shield configuration are summarized in Table 6.3. The quoted errors are the root-mean-square variations of the average doses recorded in the six cylinders. The latter reflect the inhomogeneity of the dose levels in the habitat, and eventual fluctuations in the recorded energy losses due to the available statistics. The total and barrel BFO equivalent doses, 45.1 and 30.8 cSv, may be compared to the 50 cSv annual limit used for low earth orbit (LEO) [16]. The contribution of the endcap regions to the total skin, BFO and body dose equivalents is ~35%.

---

[16] Radiation Effects and Shielding Requirements in Human Missions to the Moon and Mars, D. Rapp, Mars Volume 2, 46-71 (2006); doi:10.1555/mars.2006.0004

6.6.　　　Dose Equivalents for SEP Events

The proton flux of the CREME 1996 worst week model is shown in Figure 6.12. The kinetic energy spectra is characterized by a significantly higher flux than for the GCR protons below ~ 1 GeV. Above 2-3 GeV, the SEP proton flux decreases rapidly below the GCR level. The 8 Tm solenoid shield configuration, with a proton kinetic energy cutoff of ~ 4.5 GeV (Figure 6.7), would in principle, deflect effectively the relatively low energy SEP protons.
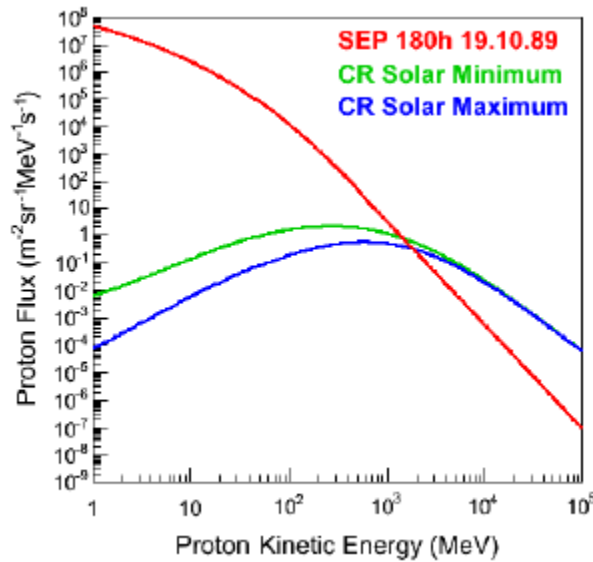
Figure 6.12 The proton fluxes for the SEP event of October 1989 from the CREME 1996 worst week model[15], compared with the solar maximum and minimum GCR proton fluxes of 1990 and 1977 from the CREME 2009 GCR model[15].
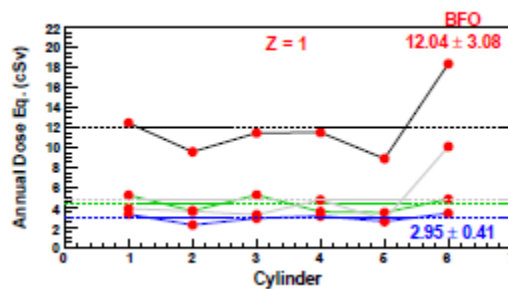
Figure 6.13 The BFO dose equivalents recorded in the six water cylinders for the 8 Tm extendable solenoid shield for the proton fluxes of the October 1989 SEP event. The average values and root-mean-square variations are quoted for the total (red) and barrel region (blue) doses. Line colors correspond to the total (black), barrel region (blue), and the +z (green) and −z (gray) endcap regions.

The simulation was used to calculate the dose equivalents for the 180 h SEP event. The protons were generated uniformly over the 30 × 30 × 30 m³ cube (Figure 6.5). The BFO dose equivalents of the six cylinders are shown in Fig.13. The average recorded skin, BFO and body dose equivalents in the barrel region are 5.2 ± 1.6, 3.0 ± 0.4 and 3.3 ± 0.3 cSv. The corresponding total dose equivalents, respectively 36.6 ± 6.2, 12.0 ± 3.1 and 16.8 ± 2.1 cSv, are dominated by the contribution of the low energy protons trapped by the solenoid shield in the endcap regions (Figure 6.9).
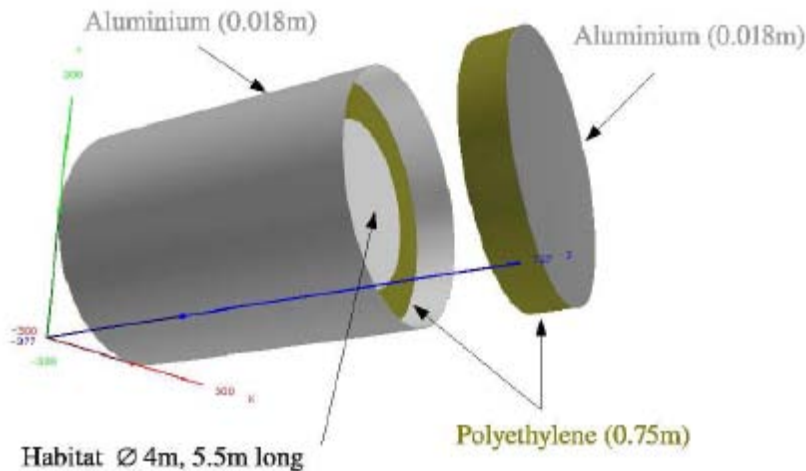
Figure 6.14 The 75 cm thick polyethylene shield configuration.

The simulation was used to determine the thickness of a polyethylene shield with comparable performance. The passive shielding configuration used for the study is shown in Figure 6.14. The relative positions of the six water cylinders in the 4 m diameter, 5.5 m long cylindrical habitat are the same as those shown in Figure 6.11. A 10 × 10 × 10 m³ generation cube was used to cover the full acceptance.

The BFO dose equivalents at the six cylinder positions for the polyethylene thicknesses of 50 and 75 cm are shown on the left in Figure 6.15. The contribution of the barrel region to the total dose is 75% for the 50 cm thick passive shield. With the 75 cm thick configuration, a significantly higher dose was recorded in the one of the upstream, off-center cylinders for the events generated in the +z endcap region. In this case, the barrel contribution represents 55% of the total BFO dose equivalent.

The average total and barrel region BFO dose equivalents for shield thicknesses of 25, 50, 75 and 100 cm are presented on the right in Figure 6.15. The error bars represent the root-mean square variations of the average values of the six cylinders. A shield thickness of ~ 75 cm provides a performance comparable to the 8 Tm solenoid shield in the barrel region. The corresponding polyethylene mass would be 141 t for a 6 m diameter, 10 m long cylindrical habitat. In comparison, the mass of the solenoid shield in the simulation, including the compensation solenoid, is 36 t.

Due to the thickness (mass) required, a passive shield solution implies a reduced volume, a shelter which would be occupied for a relatively short time periods, up to a week for the longest SEP events. The active solenoid shield, with sufficient passive shielding in the endcap regions, could provide comparable protection for the entire habitat.

The BFO dose equivalents in the endcap regions are 7.6 ± 5.9, 1.6 ± 2.0, 2.0 ± 2.4 and 0.2 ± 0.4 cSv respectively, for the 25, 50, 75 and 100 cm thick polyethylene passive shields. The dose levels of the 50 and 75 cm thick passive shields are comparable to the barrel dose of the solenoid shield configuration. Based on the results of the two simulations, the addition of two 6 m diameter, 50 cm thick polyethylene plugs (24.8 t) in the endcap regions of the active screen results in a BFO dose equivalent for the SEP event of ~ 5 cSv, for a total shield mass of 60.8 t.
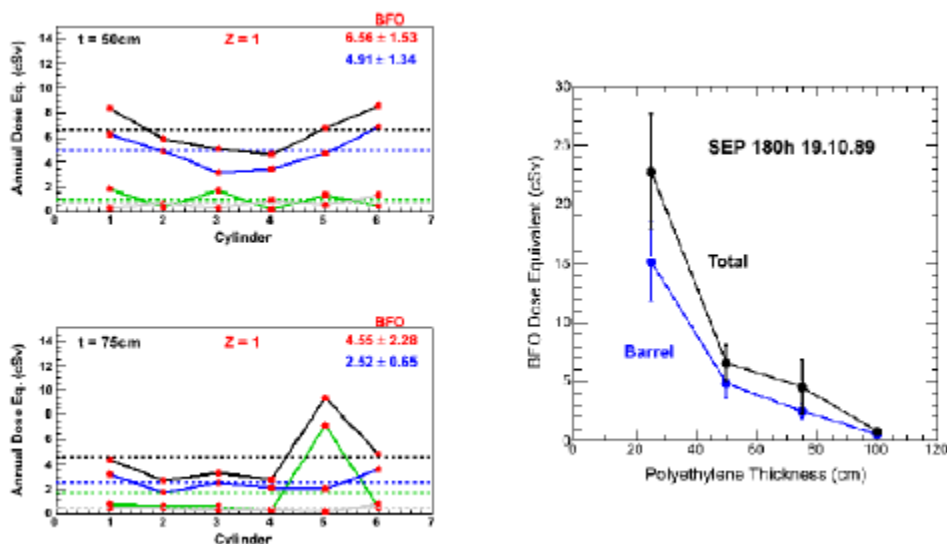
Figure 6.15 At left, the BFO dose equivalents for the proton fluxes of the October, 1989 SEP event at the six cylinder positions, for polyethylene shield thicknesses of 50 and 75 cm. The average values and root-mean-square variations are quoted for the total (red) and barrel region (blue) doses. Line colors correspond to the total (black), barrel region (blue), and the +z (green) and −z (gray) endcap regions. At right, the total and barrel region BFO dose equivalent for 25, 50, 75 and 100 cm thick polyethylene shields.

6.7.   20 Tm Solenoid Shield

The annual BFO dose equivalents recorded in the six water cylinders for a 20 Tm solenoid shield configuration are shown in Figure 6.16. In the simulation, the thicknesses of the solenoid coils and support structures were doubled in order to take into account the expected mass required for the higher field density. The total and barrel region annual dose equivalents are listed in Table 6.4. The barrel region doses of the 8 and 20 Tm field configurations are compared in Table 6.5.

The increase of the field density results in an further 25% reduction in the dose levels of the barrel region. The reduction in the total doses is relatively small (~ 5%), since the lower doses in the barrel region are compensated by an increase of the dose levels in the endcap regions for the higher field configuration.
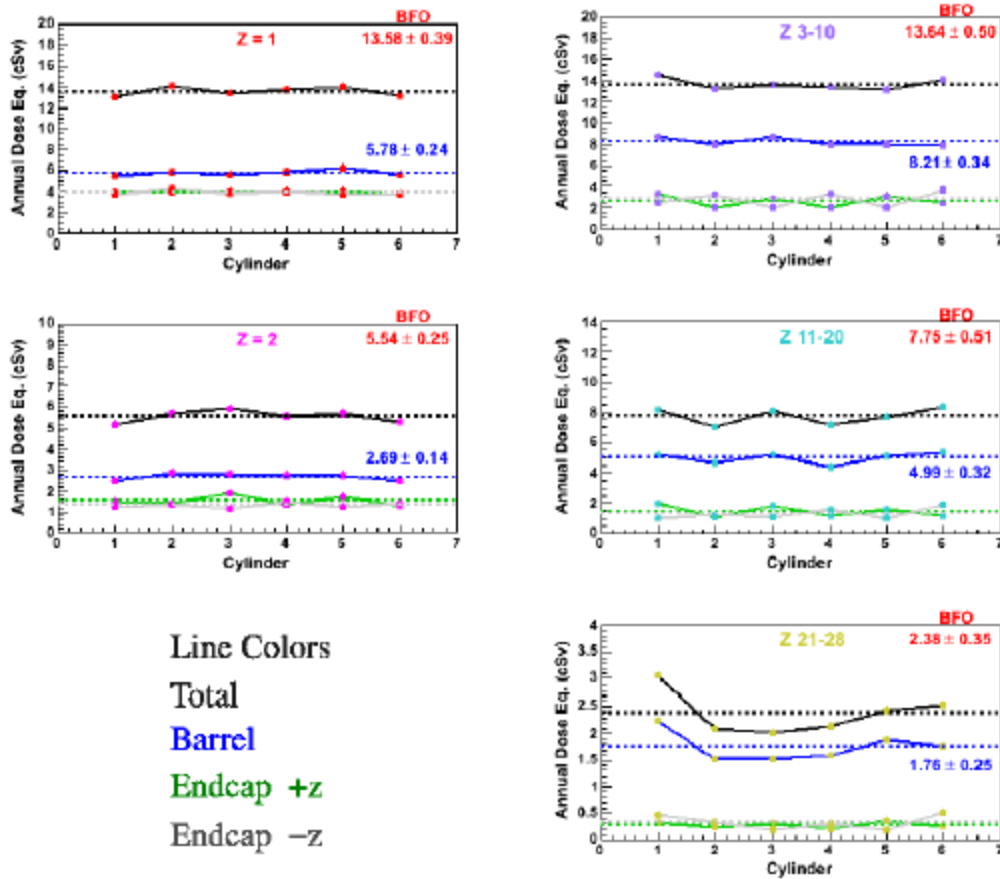
Figure 6.16 The BFO dose equivalents recorded in the six water cylinders for the 20 Tm extendable solenoid shield for GCR protons, helium nuclei, and the nuclear charge groups: $3 \le Z \le 10$, $11 \le Z \le 20$ and $21 \le Z \le 28$. The average values of the six cylinders and the root-mean-square variations are quoted for the total (red) and barrel region (blue) doses.

Table 6.4 Annual GCR dose equivalents (cSv/rem) for the 20 Tm extendable solenoid shield.

Z	Total			Barrel		
	skin	BFO	body	skin	BFO	body
1	14.6 ± 0.5	13.6 ± 0.4	13.5 ± 0.3	6.4 ± 0.3	5.8 ± 0.2	5.9 ± 0.2
2	6.5 ± 0.4	5.5 ± 0.2	5.6 ± 0.1	2.9 ± 0.3	2.7 ± 0.1	2.6 ± 0.1
3-10	21.0 ± 1.2	13.6 ± 0.5	6.7 ± 0.3	11.3 ± 0.3	8.2 ± 0.3	3.3 ± 0.1
11-20	15.6 ± 1.3	7.7 ± 0.5	6.1 ± 0.5	8.1 ± 0.4	5.0 ± 0.3	3.5 ± 0.2
21-28	6.9 ± 1.3	2.4 ± 0.4	2.4 ± 0.4	4.2 ± 0.7	1.8 ± 0.2	1.6 ± 0.2
total	64.6 ± 2.3	42.8 ± 0.9	34.3 ± 0.8	32.9 ± 1.0	23.5 ± 0.5	16.9 ± 0.4
fraction of total dose				0.51	0.55	0.49

Table 6.5 Annual GCR dose equivalents (cSv/rem) for the 8 Tm and 20 Tm extendable solenoid shields in the barrel region. The shield masses in the simulation are indicated.

Z	8 Tm / 36 t			20 Tm / 72 t		
	skin	BFO	body	skin	BFO	body
1	7.9 ± 0.3	7.6 ± 0.3	7.4 ± 0.2	6.4 ± 0.3	5.8 ± 0.2	5.9 ± 0.2
2	3.8 ± 0.2	3.4 ± 0.3	3.4 ± 0.1	2.9 ± 0.3	2.7 ± 0.1	2.6 ± 0.1
3-10	15.4 ± 0.7	10.8 ± 0.5	5.2 ± 0.3	11.3 ± 0.3	8.2 ± 0.3	3.3 ± 0.1
11-20	12.7 ± 0.8	6.9 ± 0.5	5.2 ± 0.4	8.1 ± 0.4	5.0 ± 0.3	3.5 ± 0.2
21-28	5.7 ± 0.8	2.2 ± 0.3	2.0 ± 0.3	4.2 ± 0.7	1.8 ± 0.2	1.6 ± 0.2
total	45.5 ± 1.4	30.9 ± 0.9	23.2 ± 0.6	32.9 ± 1.0	23.5 ± 0.5	16.9 ± 0.4
fraction of 8 Tm dose				0.72	0.76	0.73

6.8. Summary

The 8 Tm solenoid shield yields annual dose equivalents compatible with the limits established for low earth orbit (LEO) for a 6 m diameter, 10 m long cylindrical habitat, with a estimated shield mass of ~ 40 t (see Table 2.5 regarding estimated mass). The endcap regions of the habitat must be protected by passive shielding. The coupling of the habitat to the spacecraft and the presence of other payload modules will contribute. With material comparable to 50 cm thick polyethylene in the endcap regions, the active shield would protect the habitat from the protons of SEP events.

The increase in the field density from 1 to 2.5 T results in a modest reduction of the dose levels (25%) with respect to the estimated factor 2 increase required for the shield mass. In view of the more restrictive exposure limits for long-duration missions, the differences between the dose levels in Table 6.5 are not negligible.

The Monte Carlo statistics are summarized in Table 6.6. The GCR nuclei were generated according to their relative abundance, e.g. the ratio proton-to-helium is 10:1 in the quoted event statistics.

Table 6.6 Monte Carlo statistics

configuration	type	particle	events (M)
8 Tm shield	GCR	p, He	500
8 Tm shield	GCR	$3 \leq Z \leq 28$	350
8 Tm shield	SEP	p	300
100 cm polyethylene	SEP	p	50
75 cm polyethylene	SEP	p	300
50 cm polyethylene	SEP	p	250
25 cm polyethylene	SEP	p	200
20 Tm shield	GCR	p, He	500
20 Tm shield	GCR	$3 \leq Z \leq 28$	300

7. Passive Shielding Comparison

R. Singleterry - Langley Research Center, NASA

The OLTARIS (On-Line Tool for the Assessment of Radiation In Space) (Singleterry, R.C., 2011; Singleterry, R.C., NTR 2010; https://oltaris.nasa.gov, 2012) code system is used to generate whole body Effective Dose equivalents (ED) (NCRP Report 132, 2000) in mSv/day for various materials with various thicknesses in gm/cm^2. For each material, the ED versus shielding thickness (g/cm^2) is converted to ED versus total mass in metric tonnes. These data are then converted to ED versus the number of heavy vehicle lift launches at 89,375 lbm per launch to trans-Mars injection (TMI). With these data, the number of days before a recommended radiation exposure is reached is then determined.

The Constellation Program used a recommended cumulative exposure of 150 mSv (NASA CxP, 2009) to ensure that the career permissible risk of 3% radiation exposure induced death at a 95% confidence level (NASA STD 3001, 2007) was not reached. While that exposure was intended for a particular solar proton event, it is used here as a reasonable approximation for what a design criterion might be for Galactic Cosmic Rays (GCR)(O'Neill, P.M., Advances in Space Research 37, 2006).

This engineering analysis starts with determining the ED with the OLTARIS tool at numerous sphere thicknesses from 0.0001 to 1000 gm/cm2 in four materials: aluminum (ρ = 2.7 gm/cm3), liquid hydrogen (ρ = 0.07099 gm/cm3), high density polyethylene (ρ = 0.941 gm/cm3), and water (ρ = 1 gm/cm3). The 1977 solar minimum GCR spectrum was used as the boundary condition.

The mass of the material in the vehicle shell can be determined and compared to the calculated ED inside the vehicle. Figure 7.1 shows the results. At a total shielding mass of about 500 metric tonnes, liquid hydrogen (orange line) has the same ED as water or polyethylene (dark and light green line, respectively). The cross-over is because of the density of liquid hydrogen and how it affects the volume and mass. To show that this is an effect of the material density and not of the physics behind the calculation of ED, consider the following example. If the density of liquid hydrogen is increased to the same order of magnitude as water or polyethylene, 1 gm/cm3, then this cross-over does not occur until 5000 metric tonnes. Also in Figure 7.1 the black lines denote the mass of a number of heavy lift launches at 89,375 lbm per launch. The 89,375 lbm launch mass is derived from the initial mass to low Earth orbit value for the Space Launch System of 286,000 lbm (NASA Auth. Act, 2010) with a gear ratio of 3.20 (Rapp, D., 2008) for TMI.
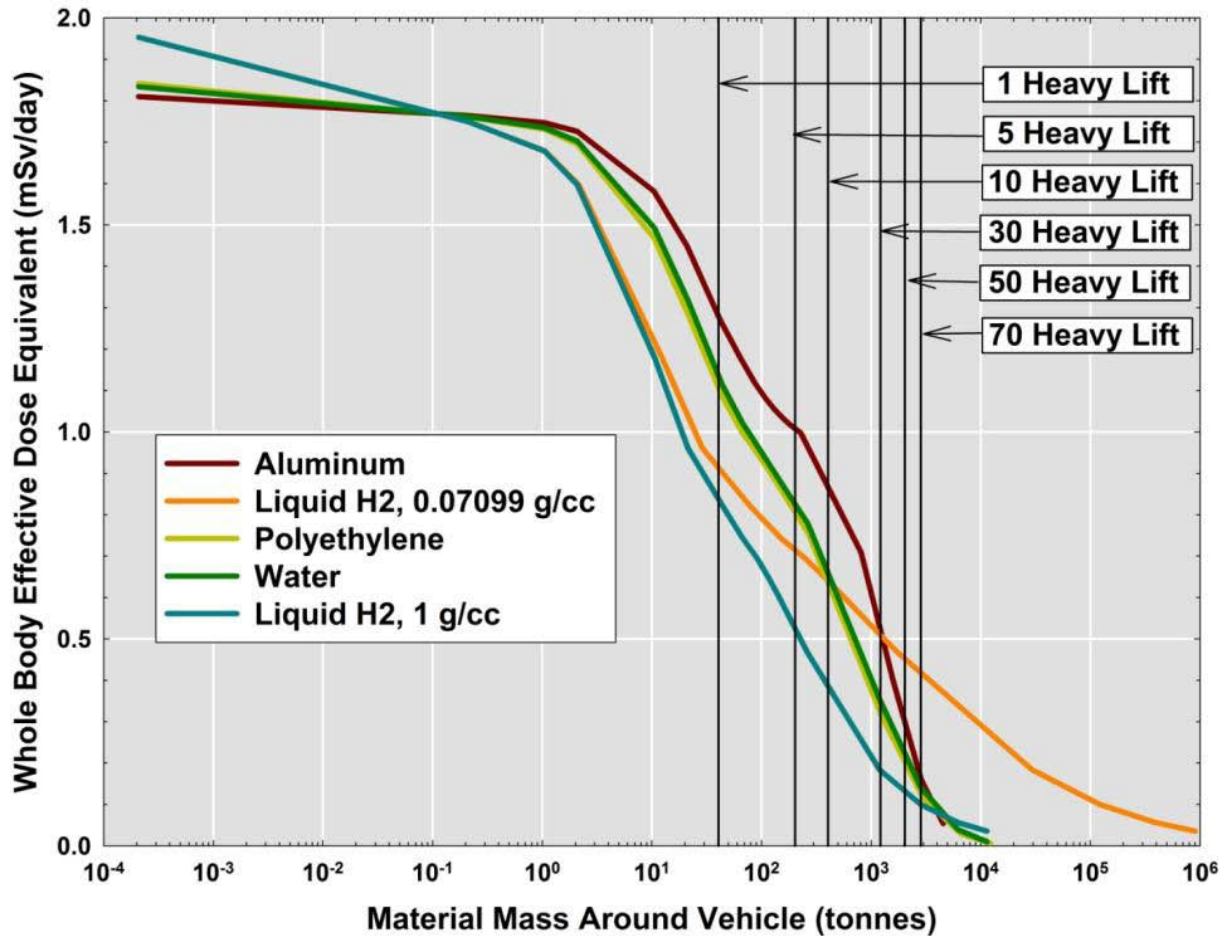
Figure 7.1. Whole body effective dose equivalent versus mass with the number of heavy lift launches enumerated

The exposure rates in Figure 7.1 can be used to calculate the number of days before the exposure of 150 mSv is reached. The assumption used here is that the exposure rate is constant over the number of days. The variation of the dose over the solar cycle, an 11 year cycle, is on the order of a factor of 2 (O'Neill, P.M., 2006). Therefore, this can be viewed as a conservative estimate of the number of days an astronaut can stay in deep space and not exceed the recommended exposure.

A mission designer usually has knowledge of the mission duration due to constraints that cannot be overcome with current technologies (e.g. orbital dynamics and propulsions systems). The designer must then determine the mass required to meet crew exposure limits over the specified mission duration. Therefore, Figure 7.2 plots days to the exposure of 150 mSv as the independent variable to the number of heavy lift launches needed to get the required shielding mass to TMI. Again, liquid hydrogen at 1 gm/cm3 (blue line) is included in the figure. It is evident that liquid hydrogen at nominal density (orange line) isn't the best shielding material if the mission is longer than 225 days, but water and polyethylene are better shielding materials for longer missions. However, if the density of liquid hydrogen is increased (blue line), it becomes a better shield material than water or polyethylene to greater than 1600 days.
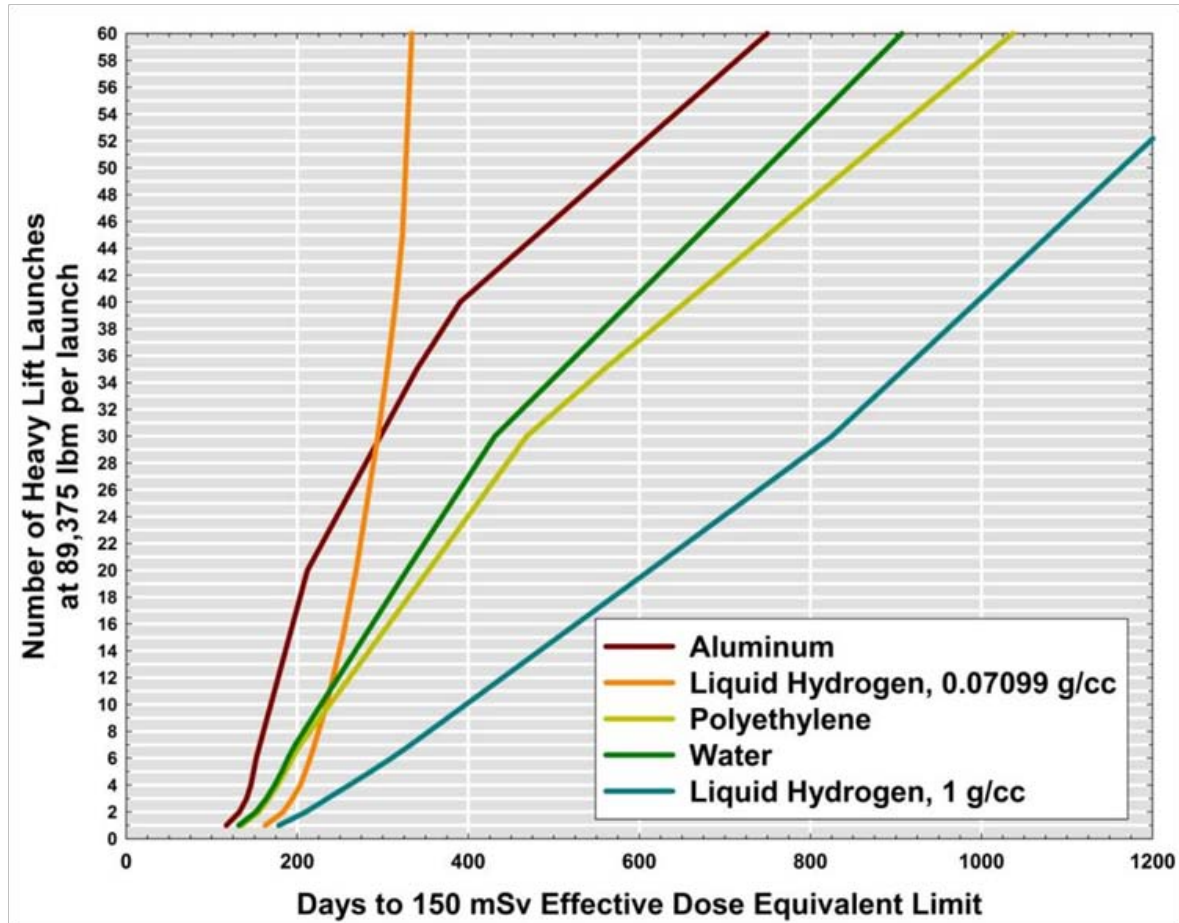
Figure 7.2. Number of heavy lift launches to place enough mass into TMI or TLI to protect an astronaut for a given number of days

One of the major findings of this study is that for a single launch of just shielding materials, if water or polyethylene is used, the mission length is recommended not to exceed 130 days. Aluminum reduces the recommended mission duration. Nominal density liquid hydrogen only increases the mission duration to approximately 160 days. Even the unobtainable density liquid hydrogen only increases the mission duration to about 175 days. The latest proposed Mars mission (NASA DRA 5.0, 2009) has a 200 day transit to Mars and a 200 day transit from Mars. It also has a 500 day stay on the surface. The surface stay is not addressed by this analysis; however, for the 400 days in deep space, Figure 7.2 indicates that 24 heavy lift launches are needed of pure polyethylene to enable this transit. The figure also shows that nominal density liquid hydrogen would not provide sufficient shielding to satisfy the recommended exposure.

The primary finding of this analysis is that for shielding to be provided solely by mass around a deep space vehicle, a large number of heavy lift launches are needed to meet the recommended exposure, an ED of 150 mSv. For the Mars Design Reference Architecture 5.0, it will take 24 heavy lift launches of pure polyethylene to meet the recommended exposure not including the surface stay. The long held belief that liquid hydrogen is the best shielding material needs to be qualified. For missions that last longer than 225 days, the same mass of polyethylene or water allow more days for a mission than liquid

hydrogen. A single launch of pure shielding material can only protect the astronauts for 130 days for water or polyethylene and 160 days for nominal density liquid hydrogen. An engineering analysis that includes the density of the materials being used with a vehicle geometry is needed to fully understand the characteristics that a long duration, deep space mission can have.

The analysis described in this paper shows that vehicle mass cannot be the sole shielding mechanism for long duration, deep space missions. There are numerous ways to increase the number of days an astronaut can stay in deep space and not exceed the recommended exposure. The NASA Office of the Chief Technologist has a roadmap, Technology Area 06 (Hurlbert, K., 2010), that suggests and is actively researching improvements.

8. Analytical Model Coupled with HZETRN for Estimation of Dose Equivalent

S. Washburn - University of Colorado, Boulder

Determination of dose equivalent values inside the radiation shield environment often involves lengthy and computationally intensive Monte-Carlo analysis. In order to evaluate the large trade space of design parameters associated with a solenoid magnetic radiation shield design we have developed an analytical model for the determination of flux, and the resulting dose equivalent, inside the magnetic shield due to the GCR radiation environment. This analytical model was then coupled with NASA's radiation transport code HZETRN to account for the effects of structural mass and passive shielding associated with an actual vehicle design.

The initial analysis was conducted utilizing a representative "quasi-spherical" model to simplify the calculations. Although the assumptions made for this spherical representation are not entirely realistic, a discussion of its development is presented since it lends itself to the analysis of more complex geometries. Additionally, results for the quasi-spherical model are presented since they may provide a unique reference for alternate geometric configurations not discussed here.

Following the layout for the quasi-spherical case, a model is developed for a cylindrically shaped magnetic shield with an axially directed magnetic field (solenoid design). Results are discussed for a theoretical infinitely long cylinder, where the resulting flux entering from the ends of the cylinder is reduced to zero, as a limiting case for this design. Finally the more realistic open-ended cylinder configuration is presented as an actual design case and for comparison of the model with the Monte-Carlo results presented in section 6.5.

8.1.   GCR Flux

The flux model utilized in this analysis is the Badhwar-O'Neill 2010 (BO'10) model (O'Neill, 2010). This is important to note since there are significant differences between the BO'10 model and those used in previous literature and analysis such as the BO'04 model, CREME96, and CREME09 models. Of greatest significance, the BO'10 model has substantially lower flux profiles for both proton and alpha particles in the energy ranges below 10^4 MeV/n.

The BO'10 model itself provides the GCR energy spectrum for 1.0 to $1.0e^6$ MeV/n for elements with Z equal to 1 through 94. This study only takes into account elements with Z of 1 through 28 since the resulting dose equivalent for elements with Z greater than 28 provides a negligible contribution to the total dose equivalent. The model output is the omnidirectional, differential flux given in # of nucleons per m^2 per second per steradian per MeV/n (kinetic energy per nucleon) and is assumed to be isotropic.

The selected model GCR output used in this analysis is based on a selected input phi value of 481. Phi is the solar modulation parameter, where a lower phi value corresponds to a higher flux. The selected value corresponds to the lowest recorded phi value for the 1977 solar minimum and is used for this analysis.

8.2.   Charged Particle Motion in a Magnetic Field

We now want to examine how the GCR flux which passes through a point inside the magnetic field is affected by the magnetic field itself (B-Field). The motion of charged particles as they pass through a magnetic field are governed by the Lorenz Force which is given by:

$$\vec{F} = q\vec{v} \times \vec{B} \qquad F = qv_\perp B$$

(8.1a,b)

One can see that this force affects particle motion perpendicular to the magnetic field lines while the velocity component parallel to the magnetic field remains unaffected. Since the high energy particles which comprise the GCR flux can have kinetic energies in the GeV/nucleon range, relativistic equations must be utilized. We can show that this force results in the particle's motion in the plane perpendicular to the magnetic field being circular, resulting in the equation for the radius of curvature of a charged particle in a magnetic field, also known as the Larmor radius or gyroradius.

$$r_L = \frac{\gamma m_0 v_\perp}{qB}$$

(8.2)

We can see that as the energy, and therefore velocity, of a given particle increases, its Larmor radius will also increase making the particle more difficult to deflect. Additionally as the strength of the magnetic field B is increased the Larmor radius will decrease, resulting in greater deflection of the particles as they pass through a stronger magnetic field.

8.3.   Quasi-Spherical Model

8.3.1. Flux Inside the Magnetic Shield

In order to simplify the complex calculations for determining the GCR flux inside a magnetic field we begin by looking at a simplified spherical approximation, which we will term the "quasi-spherical" model. This model makes the following assumption about the magnetic field:

a) the field is uniform in magnitude,

b) the field is confined to a spherical geometry of specified diameter, and

c) the field is always perpendicular to an incident particle.

The later of these assumptions is the reason for the term "quasi-spherical," because while the geometry is spherical, the assumption that the magnetic field is always perpendicular to an incident particle for a spherical configuration is not an achievable property. However this assumption, in conjunction with the symmetry of the spherical configuration, allows the problem to be reduced from 3 dimensions to 2 dimensions as shown below.
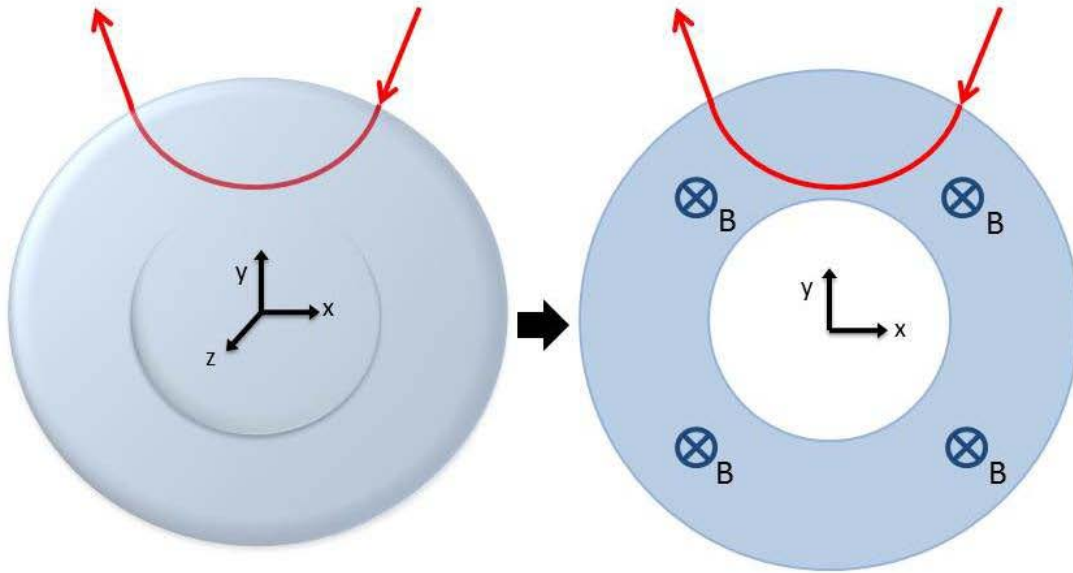
Figure 8.1. Quasi-Spherical Model, 3D to 2D
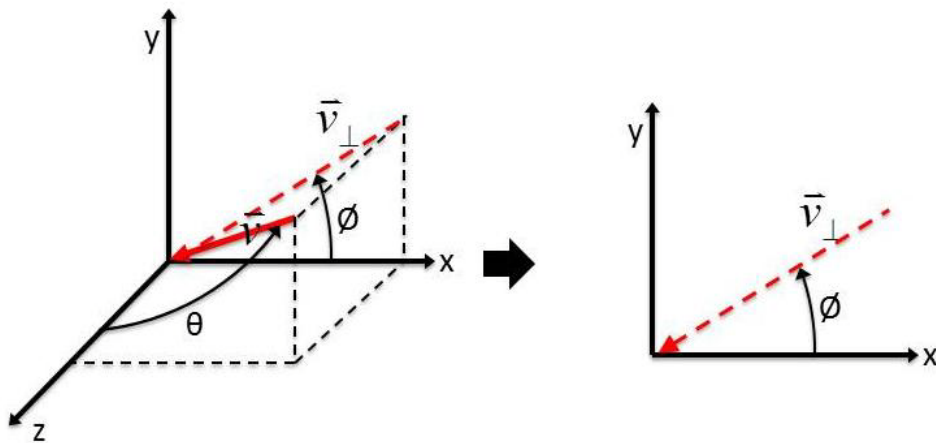
Figure 8.2. Quasi-Spherical Model, 3D to 2D Coordinates

We begin with a point P inside the volume of the magnetic shield. The GCR flux passing through this point can be written as:

$$\Psi_i(T) = \int_{\theta=0}^{\theta=\pi} \int_{\phi=0}^{\phi=2\pi} \Phi_i(T,\theta,\phi) \cdot \sin\theta \cdot d\theta \cdot d\phi$$

(8.3)

Where Φ_i is the GCR omnidirectional, differential flux of particle z_i as a function of the particle's kinetic energy, T.

We now want to look at how the flux passing through that point is affected by the magnetic shield as a function of the approach angles θ and ϕ. Because we have made the assumption that the magnetic field is always perpendicular to an incident particle, we can integrate the flux over the angle θ, reducing the problem from 3 dimensions to 2 dimensions, and look only at the x-y plane and how flux penetrates the point as a function of the angle ϕ.

$$\Psi_i(T) = 2 \cdot \int_{\phi=0}^{\phi=2\pi} \Phi_i(T,\phi) \cdot d\phi$$

(8.4)
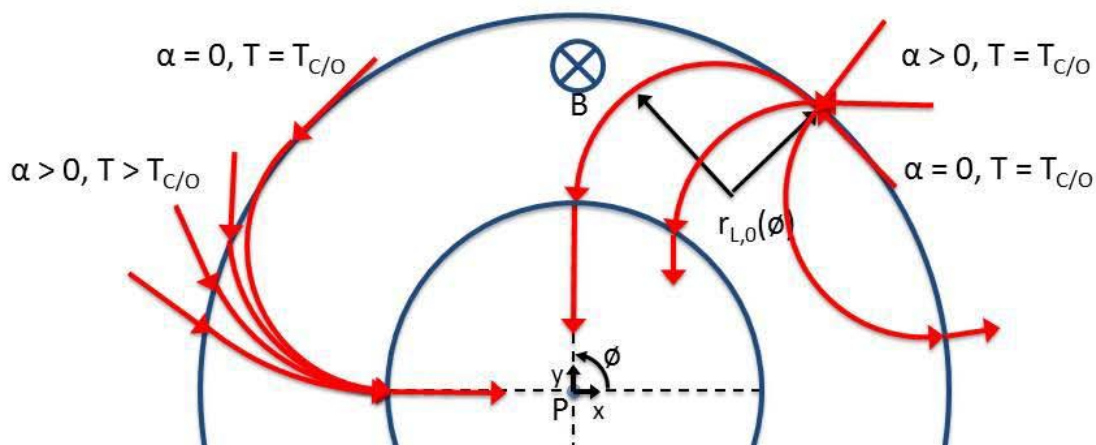
Figure 8.3. Flux Through Point P Inside Quasi-Spherical Model

We begin by defining the angle of incidence, α, as the angle formed between the velocity vector of the particle and the surface of the magnetic field where the particle intersects it. Looking at Figure 8.3 we can see that for given angle ϕ, the limiting trajectory for a particle passing through our point of interest is associated with α equal to 0. A particle on this limiting trajectory will enter the magnetic field at a glancing angle ($\alpha = 0$), curve through the magnetic field along a circular path whose radius is equal to the particle's Larmor radius, and exit the magnetic field into the interior of the shield where the particle will pass through point P along the given approach angle ϕ. Particles with a larger Larmor radius, and thus higher energy, will pass though point P along the same angle ϕ but will enter the shield at higher angles of incidence ($\alpha > 0$) and enter at a different point along the boundary of the magnetic field (shown on the left side of Figure 8.3). Particles with a smaller Larmor radius, and thus lower energy, will be unable to pass through point P along approach angle ϕ, regardless of angle of incidence or where the particle intersects the magnetic shield (illustrated on the right side of Figure 8.3). Therefore the Larmor radius associated with the limiting trajectory described above defines the lower limit or cutoff energy of a particle passing through point P from a given approach angle ϕ and varies as a function of this angle. We will define this as the critical Larmor radius, $r_{L,0}$.

8.3.2. Critical Larmor Radius and Cutoff Energy

We now wish to look at the geometry of our limiting case and determine a relationship between the critical Larmor radius $r_{L,0}$ and the geometry of our shield: r_p, the radial distance of point P from the center; r_i, the inner radius of the magnetic field; and r_o, the outer radius of the magnetic shield.
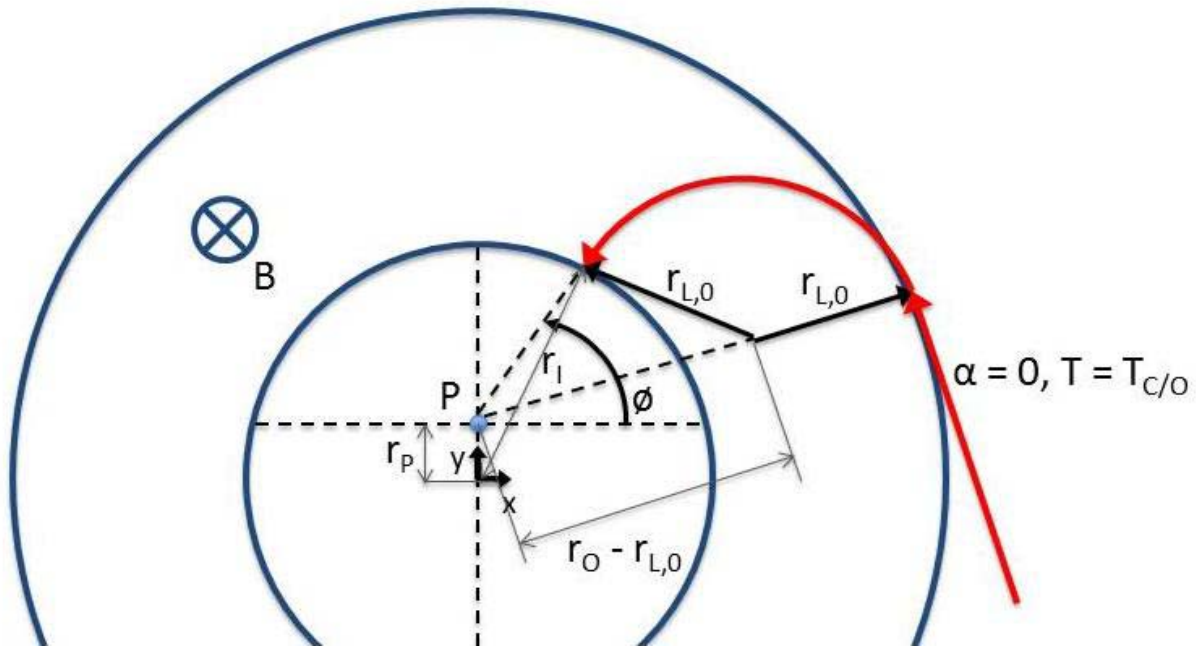
Figure 8.4. Geometry of Critical Larmor Radius

Using only the geometric relationships of the configuration shown in Figure 8.4 above, we can show that the following is true:

$$r_{L,0}(\phi) = \frac{r_O^2 - r_I^2}{2(r_O - r_P \cos\phi)}$$

(8.5)

We have assumed that the velocity is always perpendicular to the magnetic field, $v = v_\perp$. Using Equation 8.2 above and given that:

$$\gamma = \frac{1}{\sqrt{1 - \frac{v^2}{c^2}}}$$

(8.6)

And,

$$T = m_0 c^2 (\gamma - 1)$$

(8.7)

We can derive an expression relating the particle's kinetic energy and the Larmor radius.

$$T = \sqrt{(r_L qBc)^2 + (m_0 c^2)^2} - m_0 c^2$$

(8.8)

Since Equation 8.5 defines the critical Larmor radius as a function of ϕ and Equation 8.8 defines kinetic energy as a function of Larmor radius, we may use Equation 8.8 to determine the minimum kinetic energy, or cutoff energy ($T_{C/O}$), which will penetrate point P as a function of angle ϕ, by substituting Equation 8.5 for r_L in Equation 8.8.

$$T_{C/O}(\phi) = \sqrt{\left(\left(\frac{r_O^2 - r_I^2}{2(r_0 - r_P \cos\phi)} \right) qBc \right)^2 + (m_0 c^2)^2} - m_0 c^2$$

(8.9)

Tables of the cutoff energy values at the center of the quasi-spherical model for various field strengths and thicknesses can be found in Appendix A: Additional Analytical-HZETRN Model Data.

8.3.3. Cutoff Energy Bounds

It is important to note that the cutoff energy refers to the minimum energy a particle can have and still pass through point P along approach angles θ and ϕ. We may observe that the cutoff energy is a function of the angles θ and ϕ for a given point inside the magnetic field and can be shown to have an upper and lower bound for a given magnetic field geometry. As illustrated in the upper section of Figure 8.5, the lower bound on the cutoff energy for the interior of the magnetic field is defined by a particle of grazing incidence ($\alpha = 0$) whose energy results in a Larmor diameter equal to the thickness of the magnetic field ($2r_L = r_O - r_I$). This Larmor radius is small enough so that the particle is bent completely away from the interior of the magnetic shield regardless of the particle's angle of incidence, α. The upper bound on the cutoff energy for the interior of the magnetic field is defined by a particle of grazing incidence ($\alpha = 0$) whose energy results in a Larmor diameter equal to the sum of the magnetic field's inner and outer radius ($2r_L = r_O + r_I$). This is illustrated in the lower section of Figure 8.5. This Larmor radius is large enough so that the particle can penetrate any point inside the magnetic field for different values of α. Therefore the cutoff energy at a specific point P inside the magnetic field will vary between these upper and lower bounds as a function of approach angles θ and ϕ.
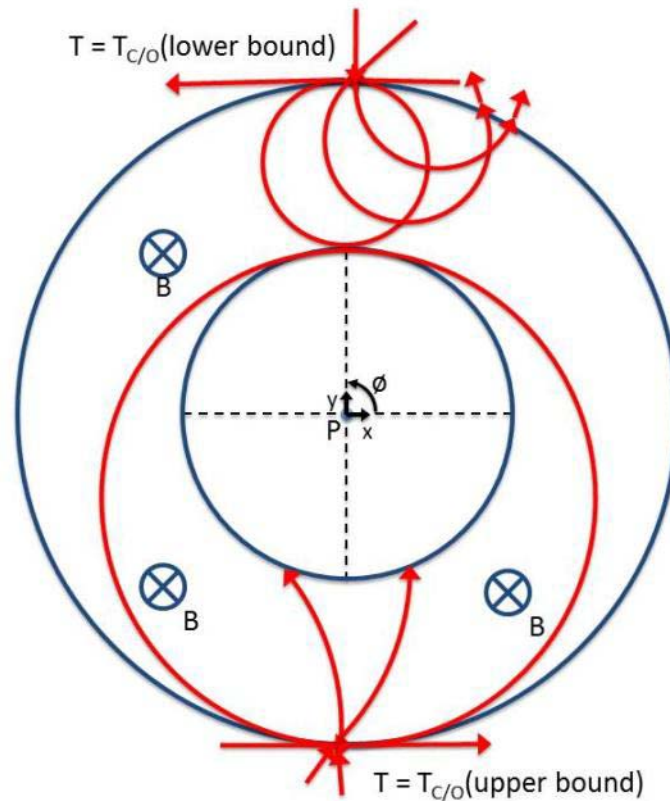
Figure 8.5. Upper and Lower Cutoff Energy Bounds Inside Quasi-Spherical Model

The concept of how an isotropic flux is affected by the magnetic field is difficult to visualize so we offer some explanation here. A point sitting in deep space will have the full GCR differential flux spectrum pass through it evenly from all directions in space (or all approach angles θ and φ). If a magnetic field is suddenly created around this point, a distortion or "warping" of the flux passing through that point will occur. Particles which previously passed through this point will now be bent away, particles which originally would not have passed through the point are diverted into it. However, not all particles are energetic enough to penetrate the interior of the magnetic field and particles with energies below the minimum cutoff energy are bent completely away from the interior of the magnetic field. Conversely, particles with energy greater than the maximum cutoff energy are so energetic that they will penetrate and can reach any point in the interior of the magnetic field. Therefore this distorted or "warped" flux inside the magnetic shield only occurs for particles energetic enough to penetrate to the field's interior.

8.3.4. Dose Equivalent Variation with Radial Distance

We now examine how the dose equivalent at point P varies as a function of the radial distance from the center of the sphere (r_P). By plotting dose equivalent as a function of r_P for various B-field strengths, we can see that the values of dose equivalent vary little as we move further away from the center of the sphere as shown in Figure 8.6.
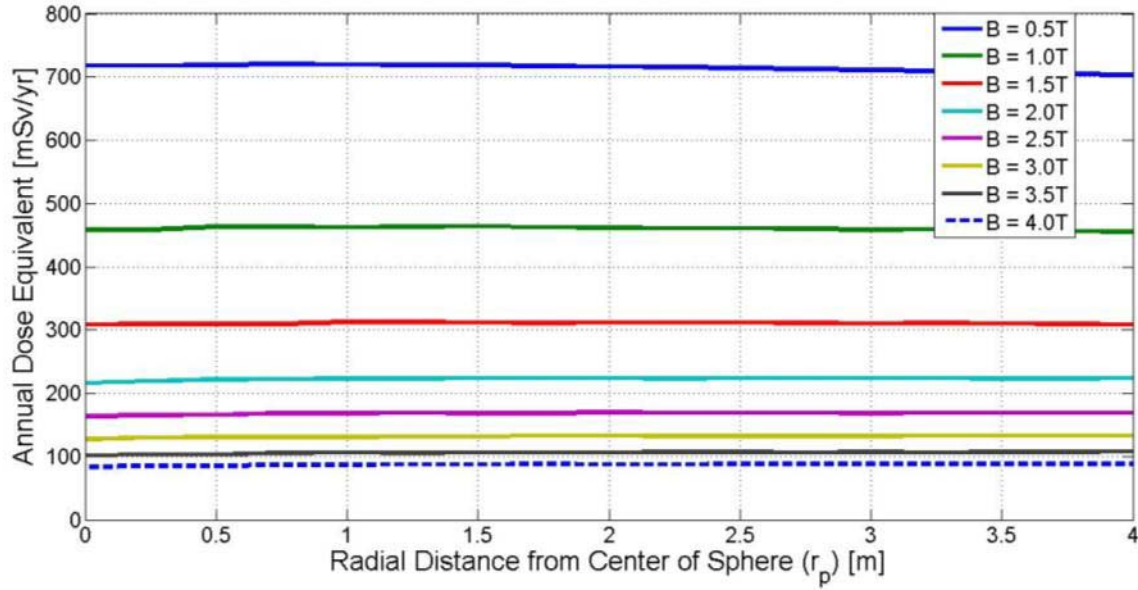
Figure 8.6. Dose Equivalent vs Radial Distance from Center of Quasi-Spherical Model (r_i = 4m, r_o = 12m)

Visually, we can see the reason for this by looking at Figure 8.8 below and observing how the critical Larmor radius $r_{L,0}$, and thus $T_{C/O}$, vary with ϕ. For a point P, which is offset from the center of the sphere ($r_P \neq 0$), the critical Larmor radius $r_{L,0}$ is at its maximum at ϕ = 0 for the given value of r_P. As ϕ increases from 0 to 2π, the critical Larmor radius $r_{L,0}$ decreases, with the minimum occurring at $\phi = \pi$, and then increases again with the average values occurring at $\phi = \pi/2$ and $3\pi/2$. Looking at Equation 8.9 we can see that, because the cutoff energy is a function of $\cos(\phi)$, at these average values of ϕ the cutoff energy is identical to the cutoff energy at the center (r_P = 0).

$$T_{C/O,Center} = \sqrt{\left(\left(\frac{r_o^2 - r_I^2}{2r_0}\right)qBc\right)^2 + \left(m_0 c^2\right)^2} - m_0 c^2$$

(8.10)

105
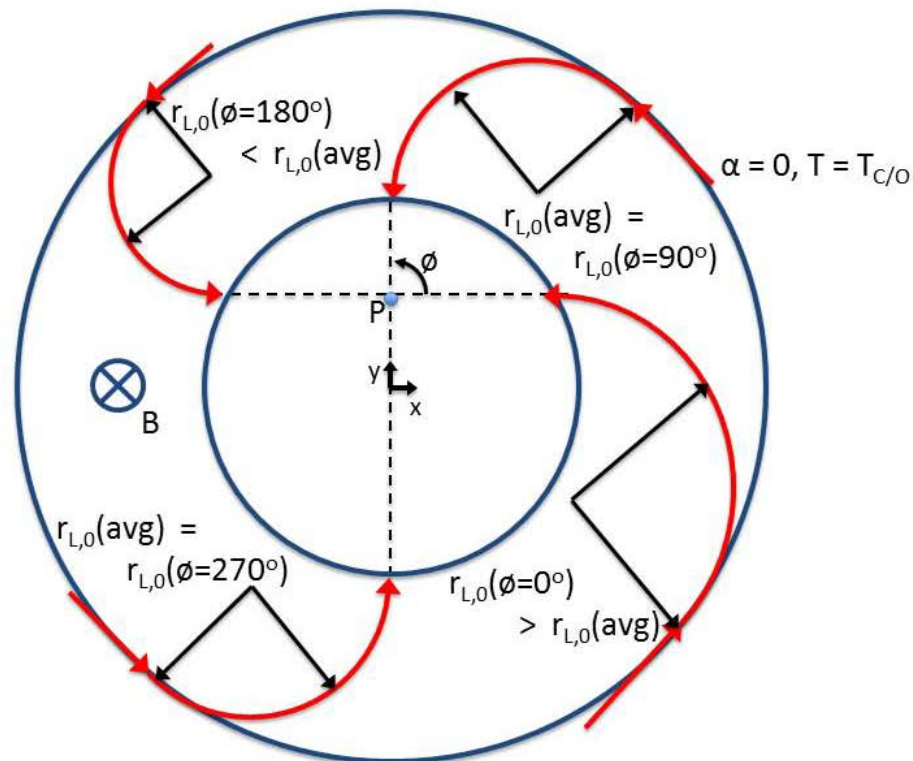
Figure 8.7. Critical Larmor radius as a Function of θ

Although the average cutoff energy for r_P greater than zero is equal to the cutoff energy at the center of the sphere ($r_P = 0$) there is still a slight variation in the resulting dose equivalent as point P is moved away from the center .This is due to the fact that the mass stopping power and quality factor terms which comprise the dose equivalent equation are not linear functions of energy (ICRP 60, 1990). However, this variation is minor and we can reasonably assume that the dose equivalent at the center of the sphere is representative of the dose equivalent at any point inside the sphere.

We can also observe above, in Figure 8.7, that as r_P increases, we approach the upper and lower bounds for the cutoff energy at $\phi = 0$ and π. When r_P is equal to r_i (i.e. P is at the inner surface of the magnetic field) we can see that the cutoff energy at $\phi = 0$ is equal to the cutoff energy upper bound and at $\phi = \pi$ it is equal to the cutoff energy lower bound for the given shield geometry.

8.4.   Solenoid Magnetic Field Model: Infinite Cylinder

8.4.1.   Flux Inside the Magnetic Shield

The equations governing the flux and dose equivalent inside a solenoid magnetic field design develop in a simple and straightforward way from those derived in the quasi-spherical model. Since magnitude of the particle's velocity components, both parallel and perpendicular to the magnetic field, remain unchanged as the particle passes through the magnetic field we may project the particle's motion for a given value of θ into the x-y plane. Therefore the determination of critical Larmor radius $r_{L,0}$, and energy cutoff $T_{C/O}$ as a function of ϕ are identical to those shown for the quasi-spherical case.
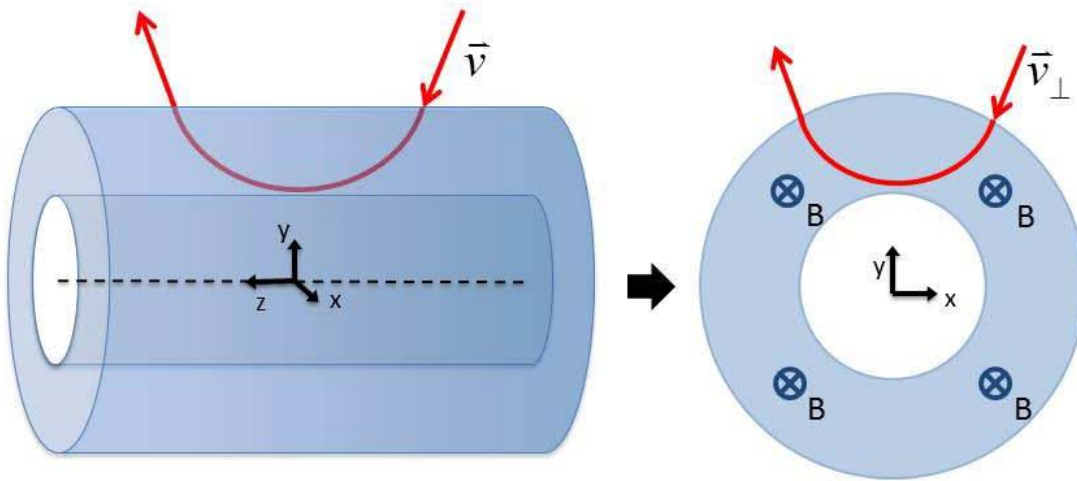
Figure 8.8. Cylinder Model, 3D to 2D
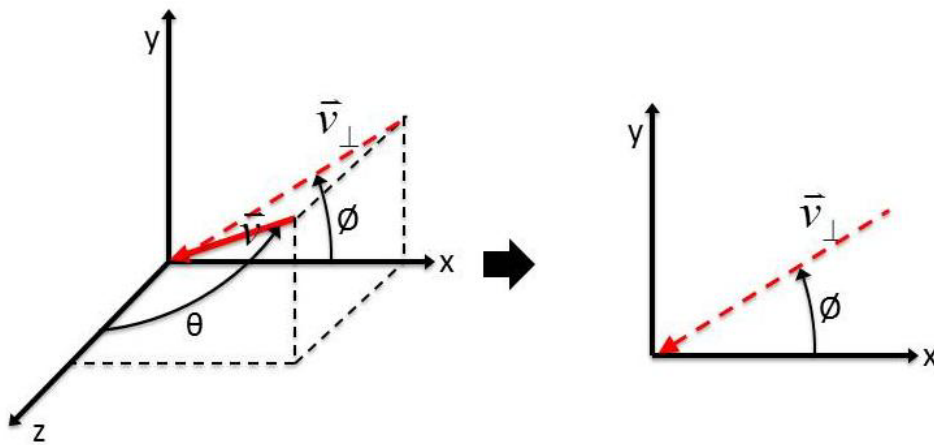
Figure 8.9. Cylinder Model, 3D to 2D Coordinates

As shown above, for a given approach angle θ, we can relate the particle's total velocity to its component which is perpendicular to the magnetic field.

$$v_{\perp} = v \sin \theta \qquad (8.11)$$

Thus, drawing from Equation 8.2, the Larmor radius as a function of the particle's total velocity and approach angle θ is written as:

$$r_L(\theta) = \frac{\gamma m_0 v \sin\theta}{qB}$$

(8.12)

Following the same steps outlined in the quasi-spherical case (using Equations 8.6, 8.7, and 8.12) we can show that the particle's kinetic energy is:

$$T_{KE}(\theta) = \sqrt{\left(\frac{r_L qBc}{\sin\theta}\right)^2 + \left(m_0 c^2\right)^2} - m_0 c^2$$

(8.13)

Since the geometric relation for the particle's critical Larmor radius as a function of energy (Equation 8.5) still applies, we can determine the minimum kinetic energy, or cutoff energy ($T_{C/O}$), which will penetrate point P as a function of angle θ and ϕ, by substituting Equation 8.5 for r_L in Equation 8.13.

$$T_{C/O}(\theta,\phi) = \sqrt{\left(\left(\frac{r_O^2 - r_I^2}{2(r_0 - r_P \cos\phi)}\right)\frac{qBc}{\sin\theta}\right)^2 + \left(m_0 c^2\right)^2} - m_0 c^2$$

(8.14)

8.4.2. Energy Cutoff

One can see from Equation 8.14, that the cutoff energy varies with the approach angle θ as a function of $1/\sin\theta$. When θ is equal to 90°, the approach angle is perpendicular to the magnetic field direction, and thus the motion of any particle approaching from this angle will lie entirely in this plane (i.e. it has no velocity component parallel to the magnetic field). For this case, the results are identical to those derived for the quasi-spherical model, and one can see in Figure 8.10 below that the cutoff energies when θ is equal to 90° are indeed identical to the values given earlier for the quasi-spherical model in Appendix A: Additional Analytical-HZETRN Model Data.

As θ either decreases or increases away from 90° and the approach angle becomes more parallel to the central axis of the cylinder, the cutoff energy increases (rapidly for approach angles of $\theta < 40°$ or $\theta > 140°$) and approaches infinity. Particles which approach the habitat at these "glancing angles" have only a small component of their velocity which lies perpendicular to the magnetic field, and thus these particles have small Larmor radii and are easily bent away from the inner volume. This is of course only theoretical since we are examining an infinitely long cylinder, and as a result the flux entering through the end of the cylinder is almost perfectly shielded. However this provides a good reference point as the lower limit for achievable dose equivalent values utilizing a solenoid design.
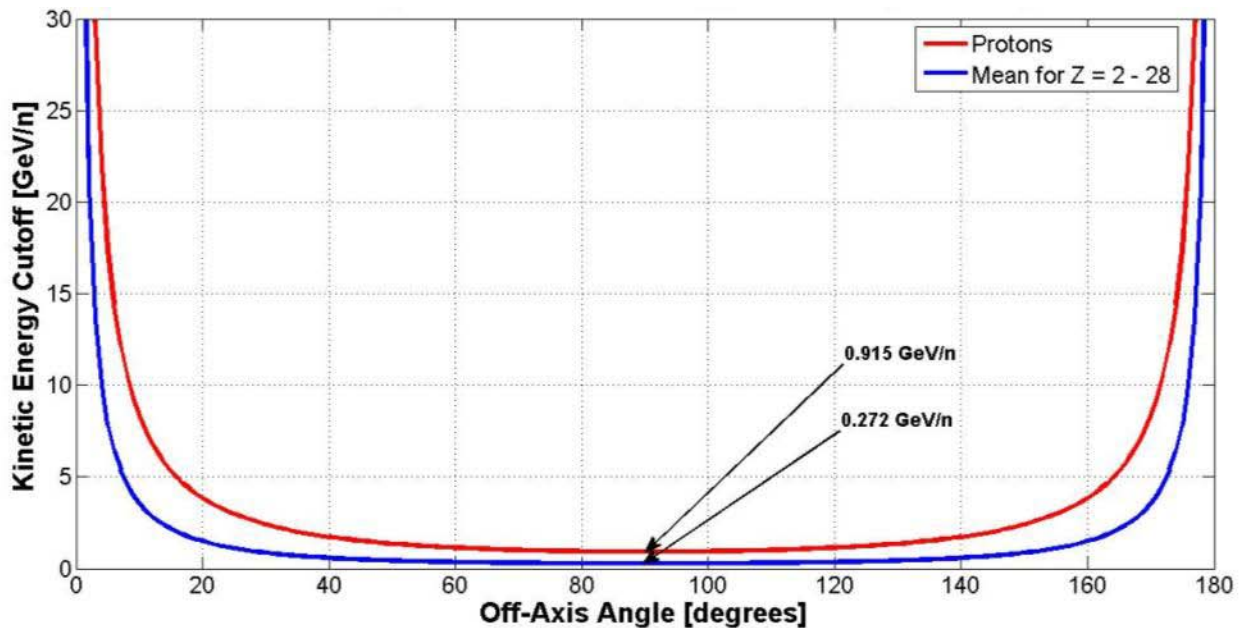
Figure 8.10. Infinite Cylinder Cutoff Energy for 8Tm (r_i = 4m, r_o = 12m, B = 1T)

Tables of the cutoff energy values at the center of the infinite cylinder model for various field strengths and thicknesses can be found in Appendix A: Additional Analytical-HZETRN Model Data.

8.5. Addition of HZETRN

The above analytical model does not account for the effects of structural mass or any passive shielding that may be part of the space habitat. These effects can be significant as this mass can attenuate some of the incident flux. Additionally secondary particle effects that arise from the attenuation of the radiation as it passes through mass can also increase the dose equivalent received inside the shield. For the purposes of this analysis we will assume that all of the mass is confined in the interior of the magnetic field in combination with the habitat structure or passive shielding.

To determine the effects of this mass we make use of the High-Change and Energy (HZE) radiation transport code HZETRN. First the resulting flux inside the magnetic field is determined using the equations outlined above. Then this flux is passed into the HZETRN code where it is transported through a thickness of aluminum (Slaba et. al, 2010a, 2010b). HZETRN then determines the resulting dose equivalent in water, which is assumed to be a good approximation of the dose equivalent in tissue. The quality factors used in HZETRN's calculation of dose equivalent are those recommended in ICRP 60 (1990). The computational run time for a single case is on the order of several seconds and thus an entire trade space of variables may be analyzed in minutes to hours depending on the level of fidelity and range of variables desired.

For this analysis, most results will be presented with 5.1 g/cm2 of shielding. This shielding thickness corresponds to 1.8 cm of aluminum shielding which is considered a reasonable approximation of the

minimum amount of shielding provided by an ISS habitat module, including the hull, walls, racks, conduit, and infrastructure.

8.5.1. Quasi-Spherical Results

8.5.1.1. Flux Determination

We begin by determining the flux inside the magnetic field for the quasi-spherical model. As discussed in Section 8.3.4, the dose equivalent varies a negligible amount as we move away from the center so we will examine the flux resulting at the center of the sphere and assume that this is representative of the dose throughout the magnetic shield environment.

$$\Psi_i(T) = 4\pi \cdot \Phi_i(T > T_{C/O,Center})$$

(8.15a)

$$T_{C/O,Center} = \sqrt{\left(\left(\frac{r_O^2 - r_I^2}{2r_0}\right)qBc\right)^2 + \left(m_0 c^2\right)^2} - m_0 c^2$$

(8.15b)

8.5.1.2. Passive Shielding Effects

We now use HZETRN to determine how the resulting flux and dose equivalent is affected by the shielding material. In Figure 8.11 below we examine the dose equivalent for various B-Field strengths at different thicknesses of shielding.
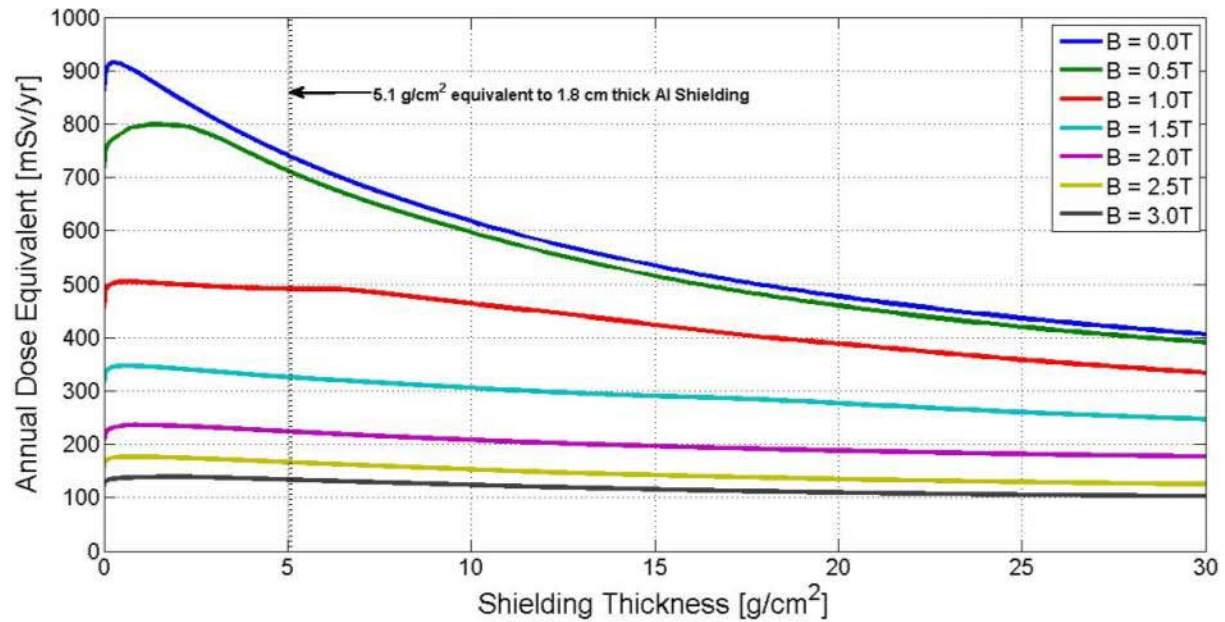
Figure 8.11. Depth vs Dose Equivalent for Various B-Field Strengths (r_i = 4m, r_o = 12m)

Initially the dose equivalent increases as we move through the shielding material. As discussed previously, this is due to secondary particle effects, particularly an increase in proton and alpha particles. As shown in Figure 8.12 below, the dose equivalent contribution of protons and alpha particles initially increases while that of higher Z particles decreases. Neutrons are also generated as secondary particles and, although it is difficult to tell due to the scale of Figure 8.12, do contribute a small amount to the total dose equivalent.
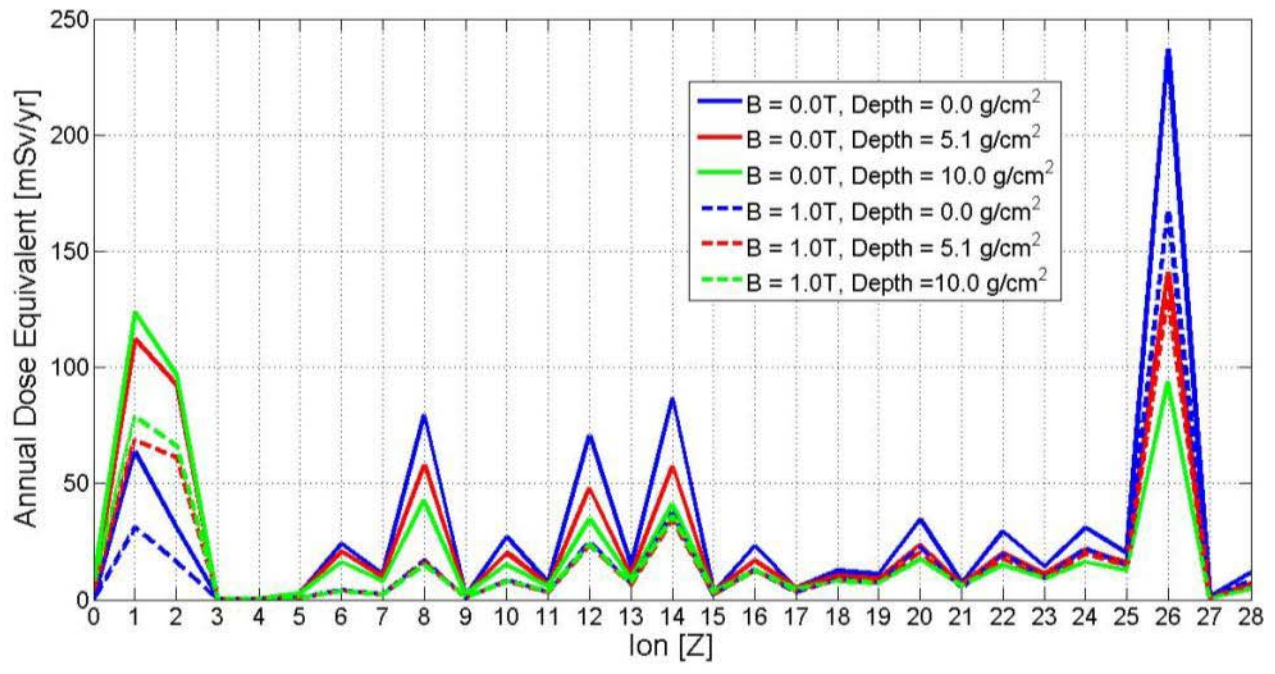
Figure 8.12. Ion Contribution to Total Annual Dose Equivalent (r_i = 4m, r_o = 12m)

8.5.1.3. Trade Space Results

The below trade space plots show the annual dose equivalent for a range of magnetic field strengths and thicknesses. The results shown are for 5.1 g/cm^2 of aluminum shielding (plots for 10.0 and 20.0 g/cm^2 of aluminum shielding are shown in Appendix A). These plots would allow a design team to quickly evaluate this trade space and determine the focus of more detailed analysis based upon various mission constraints such as destination, duration, and astronaut dose equivalent limits. Additionally we have included a derivative of these plots which shows the maximum mission duration achievable for a dose equivalent limit of 150 mSv. This plot is created by dividing the annual dose equivalent by a specified dose limit to determine the maximum number of days which a given configuration would enable before reaching the limit. These plots can be readily modified to utilize any dose limit desired.
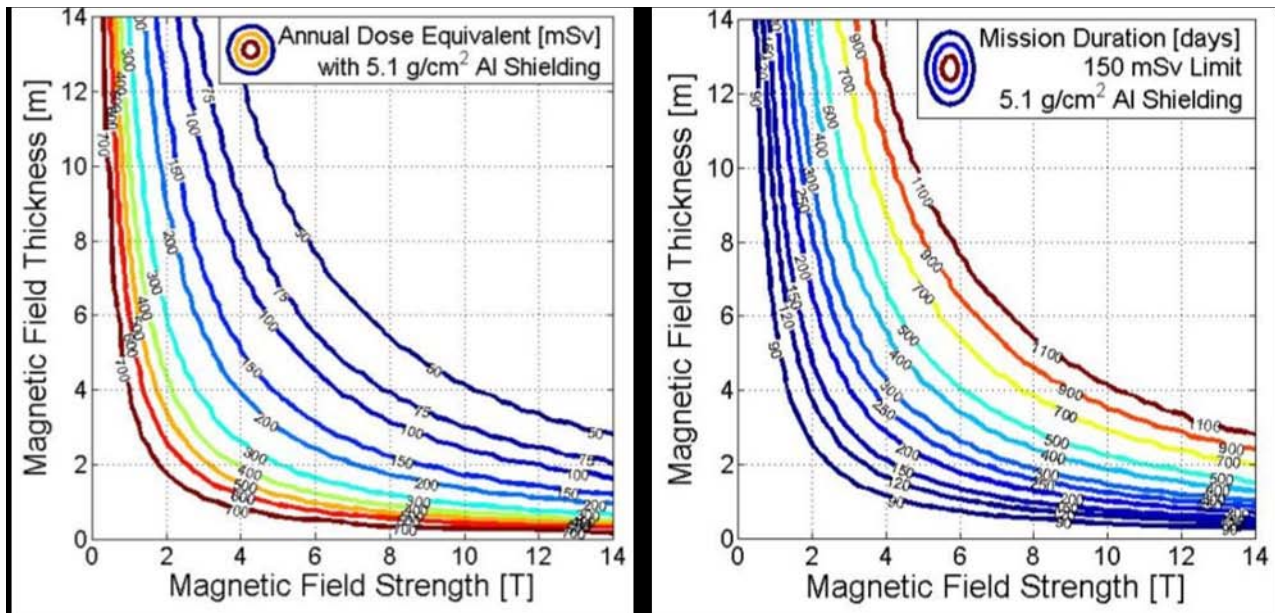
Figure 8.13. Quasi-Spherical Model with 5.1 g/cm2 Al Shielding (ri = 4m)   a) Annual Dose Equivalent
b) Maximum Mission Duration to 150 mSv Limit

We can see in the above plots that they are relatively symmetric. Although a unit increase in field strength is slightly more effective at reducing dose than a unit increase in magnetic shield thickness, the effect is relatively equal. Thus we can plot the "bending power" of the magnetic field, which is equal to the magnetic field strength times its thickness, vs the resulting dose equivalent for various passive shielding thicknesses.
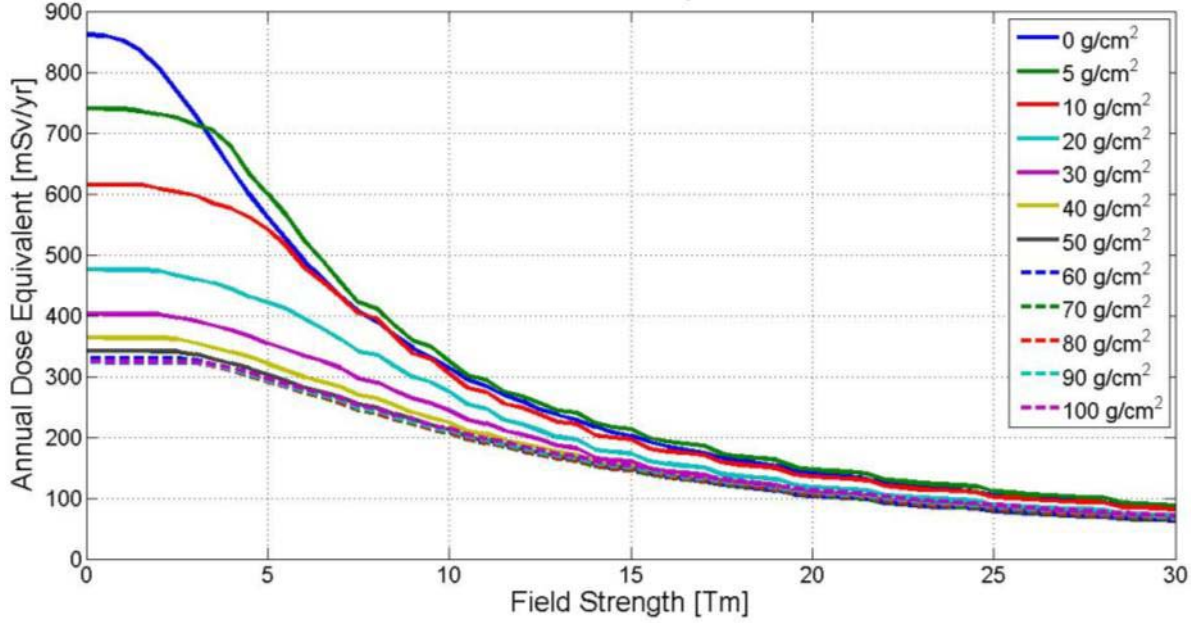
Figure 8.14. Quasi-Spherical Model, Annual Dose Equivalent Limit for Various Shielding Thicknesses ($r_i = 4$m)

We can see that, in general, as the shielding thickness increases, the resulting dose equivalent decreases. However, it is important to note the relative decrease in shielding effectiveness for thicknesses greater than 50 g/cm². This indicates that there is a diminishing rate of return for the benefit provided by increasing shielding thickness and that above a certain threshold the decrease in dose may not be worth the increased cost in mass. We can also see that at approximately 3.5 Tm the 0 g/cm² case actually results in a lower dose equivalent value than the 5 g/cm² case. As discussed earlier, this is due to the contribution of secondary particles, primarily secondary protons and alpha particles, which are generated by the interaction of heavier ions as they pass through the shielding material.

8.5.2. Infinite Cylinder Results

8.5.2.1. Flux Determination

In a similar manner as for the quasi-spherical case, we can determine the flux inside our theoretical infinite cylinder and pass these values into HZETRN for transport through shielding material. As discussed in Section 8.3.4, the dose equivalent varies a negligible amount as we move radially away from the center so we will examine the flux resulting at the center of the cylinder and assume that this is representative of the dose throughout the magnetic shield environment.

$$\Psi_i(T) = 2\pi \cdot \int_{\theta=0}^{\theta=\pi} \Phi_i(T > T_{C/O,Center}(\theta)) \cdot \sin\theta \cdot d\theta$$

(8.16a)

$$T_{C/O,Center}(\theta) = \sqrt{\left(\left(\frac{r_o^2 - r_I^2}{2r_0}\right)\frac{qBc}{\sin\theta}\right)^2 + \left(m_0 c^2\right)^2} - m_0 c^2$$

(8.16b)

114

8.5.2.2.   Passive Shielding Effects

It is important to note that, unlike the quasi-spherical case, the particles which penetrate the interior of the magnetic shield will not pass through a uniform thickness of material. Particles whose trajectories are not perpendicular to the center axis of the cylinder (i.e. $\theta \neq 90°$) will actually pass through a greater thickness of shielding material on their path to point P. As we can see above in Figure 8.11 and Figure 8.14, the dose equivalent results at depths greater than 5.1 g/cm^2 are decreasing. Therefore by assuming that all particles pass through a uniform thickness of material we provide a conservative estimate of the dose.

8.5.2.3.   Trade Space Results

Similar to the quasi-spherical case, the below trade space plots show the annual dose equivalent and maximum mission duration for a range of magnetic field strengths and thicknesses. The results shown are for 5.1 g/cm^2 of aluminum shielding (plots for 10.0 and 20.0 g/cm^2 of aluminum shielding are shown in Appendix A). The infinite cylinder model results presented below provide a limiting case for a real cylindrical design of finite length which is discussed in the following section.

Figure 8.15. Infinite Cylinder Model with 5.1 g/cm^2 Shielding (r_i = 4m) a) Annual Dose Equivalent b) Maximum Mission Duration to 150 mSv Limit

As before with the quasi-spherical model, we can see in the above plots that they are relatively symmetric, and we can plot the "bending power" of the magnetic field, which is equal to the magnetic field strength times its thickness, vs the resulting dose equivalent for various passive shielding thicknesses.
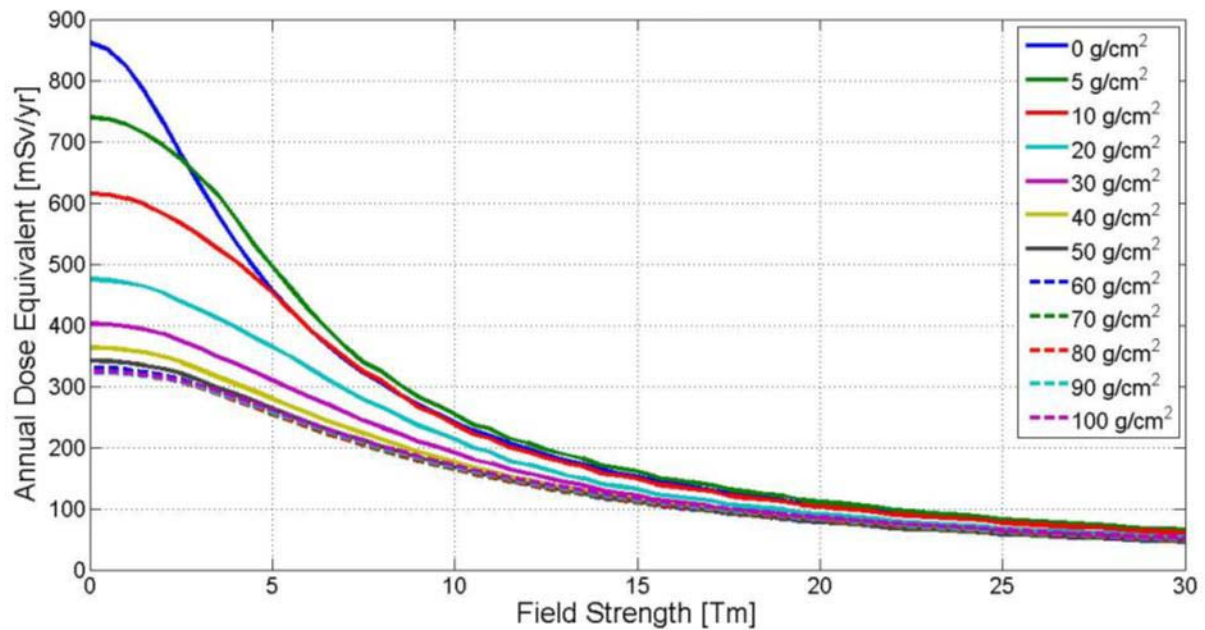
Figure 8.16. Infinite Cylinder Model, Annual Dose Equivalent Limit for Various Shielding Thicknesses (r_i = 4m)

As expected from the quasi-spherical results, there is a relative decrease in shielding effectiveness for thicknesses greater than 50 g/cm². This indicates that there is a diminishing rate of returns for the benefit provided by increasing shielding thickness and that above a certain threshold the decrease in dose may not be worth the increased cost in mass.

8.6.   Solenoid Magnetic Field Model: Open-Ended Cylinder

Up until this point we have only discussed theoretical magnetic field designs. While these designs are not realistic, they provide useful insight into the effects of the magnetic shield and limiting cases for reference. We now turn our attention to a more realistic analysis of a solenoid magnetic shield design: a cylindrical magnetic field of finite length or "open-ended cylinder" design.

Unlike the infinite cylinder, where the flux coming from the end regions is reduced to zero, this magnetic shield is open on the ends. We will term these regions the "End-Cap" regions. Any flux or contribution to the total dose from these End-Cap regions is assumed to be unaffected by the magnetic shield and subject only to passive shielding. Since no magnetic field is present at the ends of the solenoid and if no passive or structural shielding were present, a human inside this shield would be subjected to a partial view of the un-attenuated GCR spectrum entering through these openings. However, this "un-shielded" scenario is unlikely since the habitat itself will afford some protection from the flux entering through the End-Cap region. Additionally the open space in the End-Cap regions makes a likely location for things such as a crew module and service module which would provide significant amounts of additional passive shielding.

We will term the area between the two End-Cap regions the "Barrel" region. Any flux or contribution to the total dose from this region is assumed to have been attenuated by the magnetic shield as detailed previously before passing through the structural and passive shielding of the habitat.
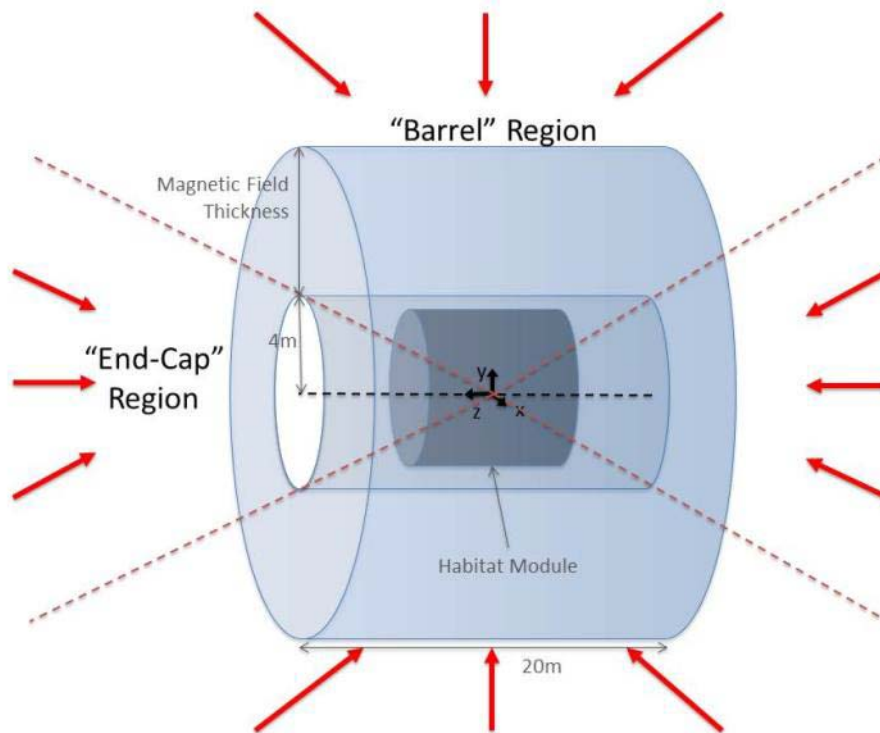
Figure 8.17. Open-Ended Cylinder Model

For the purposes of this analysis we will assume that the length of the magnetic shield is 20m. This length was selected to maximize habitat shadowing and shielding efficiency and could possibly be accommodated by future capacity onboard a heavy lift class launcher such as the Space Launch System (SLS). Additionally we will assume that the inner radius of the magnetic field is 4m. This was selected to allow a 3m radius habitat module plus an additional meter gap to accommodate any equipment or material between it and the interior of the magnetic shield.

8.6.1. Energy Cutoff

As is the case for the infinite cylinder, the cutoff energy at a point on the axial centerline varies with the approach angle θ. Toward the center of the barrel region, where incoming particles pass through the entire thickness of the magnetic field, the cutoff energy is governed by Equation 8.14, the same equation as the infinite cylinder. Thus in this region the cutoff energy varies with the approach angle θ as a function of $1/\sin\theta$. In the end-cap region the energy cutoff is obviously zero since there is no magnetic field present to attenuate the incoming particle flux. In the Open-Ended Cylinder barrel region there also exists a "transition region" where incoming particles enter through the side wall of the

magnetic field and do not pass through the entire thickness of the magnetic field. In this region, Equation 8.14 still holds, however the variable r_o, the outer radius of the magnetic field, is now equal to the radial distance from the axial centerline at which the limiting particle energy penetrates the magnetic field.
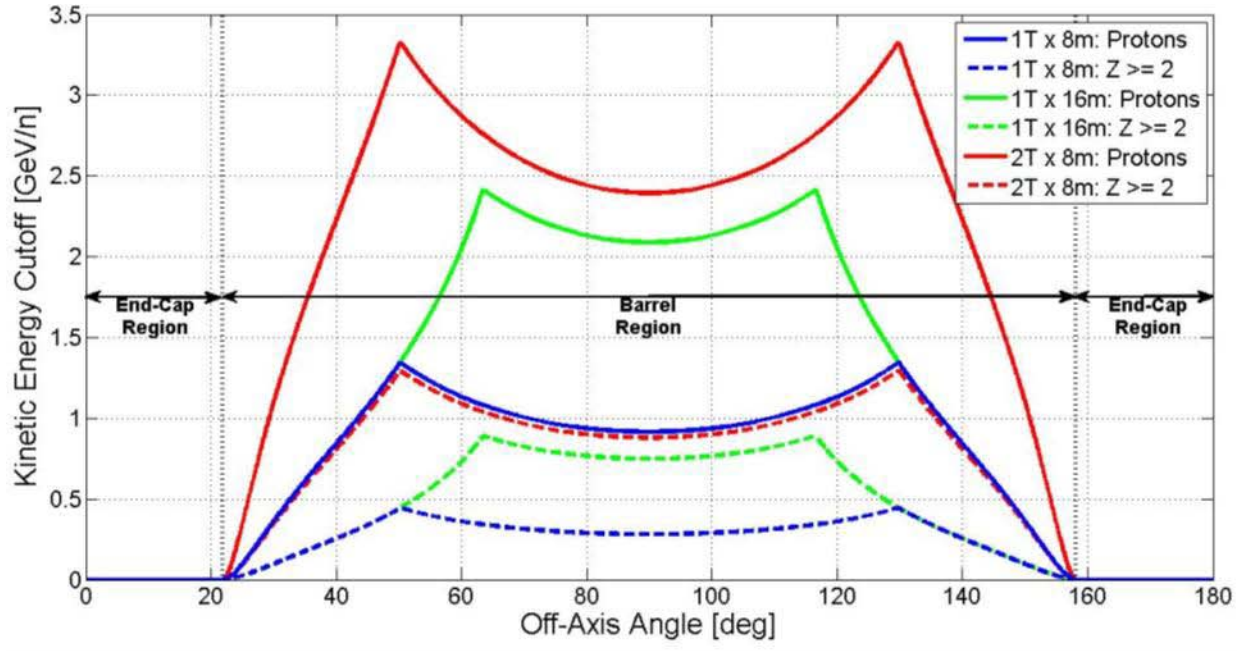
Figure 8.18. Open-Ended Cylinder Cutoff Energy at the Center of the Habitat ($r_i = 4$m)

8.6.2. Dose Equivalent Variation with Axial Distance from Center

We have shown in Section 8.3.4 that the resulting dose equivalent inside the magnetic shield does not significantly depend on the radial distance from the central axis of the shield. We now examine how dose is affected by distance from the absolute center of the shield in the axial direction since moving toward one end of the shield will widen the angular view-factor on that end and narrow it on the other. For the purposes of this analysis, we will assume that the habitat module is only 10m long and thus the greatest axial distance one can be from the absolute center of the module is 5m.
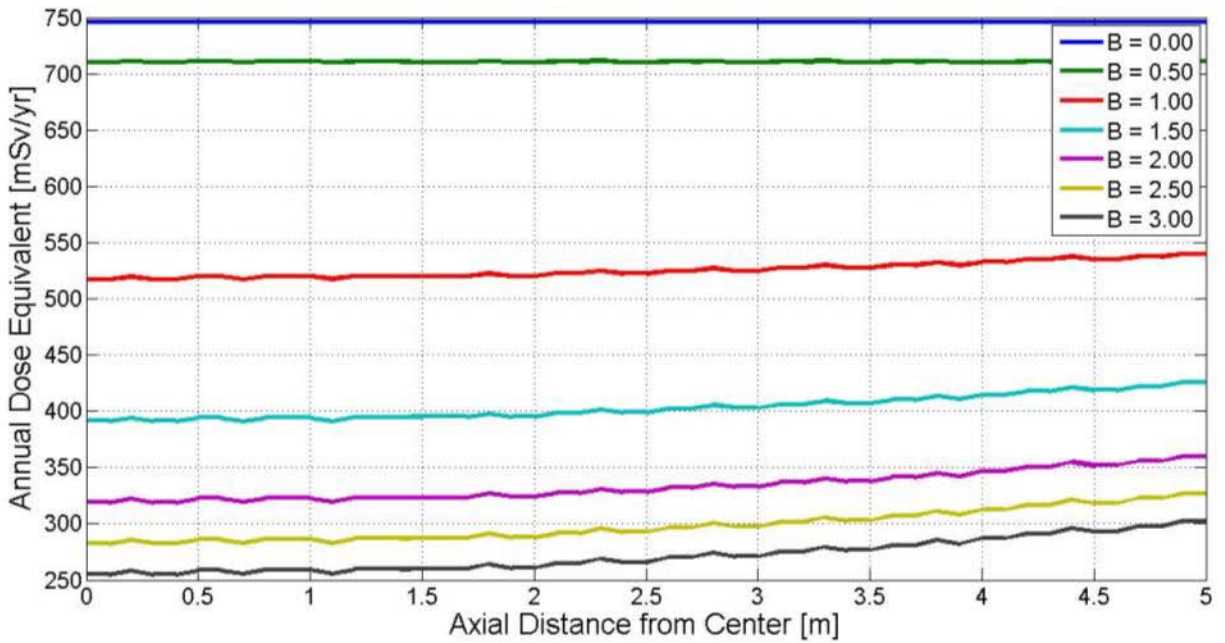
Figure 8.19. Open-Ended Cylinder Dose Equivalent vs Distance from Absolute Center (r_i = 4m, r_o = 12m)

We observe that as our target point P is moved away from the center of the habitat, the resulting dose increases. In order to present the limiting case, the dose values should be evaluated at the edge of the habitat module, away from the absolute center of the shield.

8.6.3. Results

The below trade space plots show the annual dose equivalent and maximum mission duration for a range of magnetic field strengths and thicknesses. The results shown are for 5.1 g/cm^2 of aluminum shielding (plots for 10.0 and 20.0 g/cm^2 of aluminum shielding are shown in Appendix A). The following figures show the highest possible dose equivalent value for the Open-Ended Cylinder Model, i.e. at the edge of the habitat, 5m from the absolute center along the axial centerline.
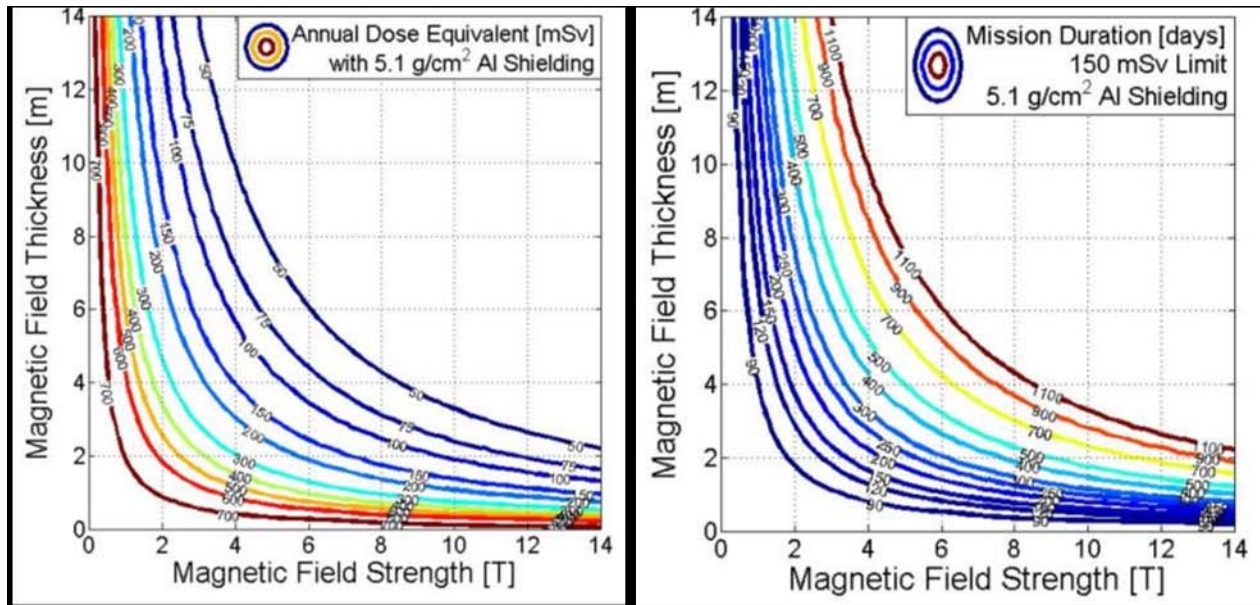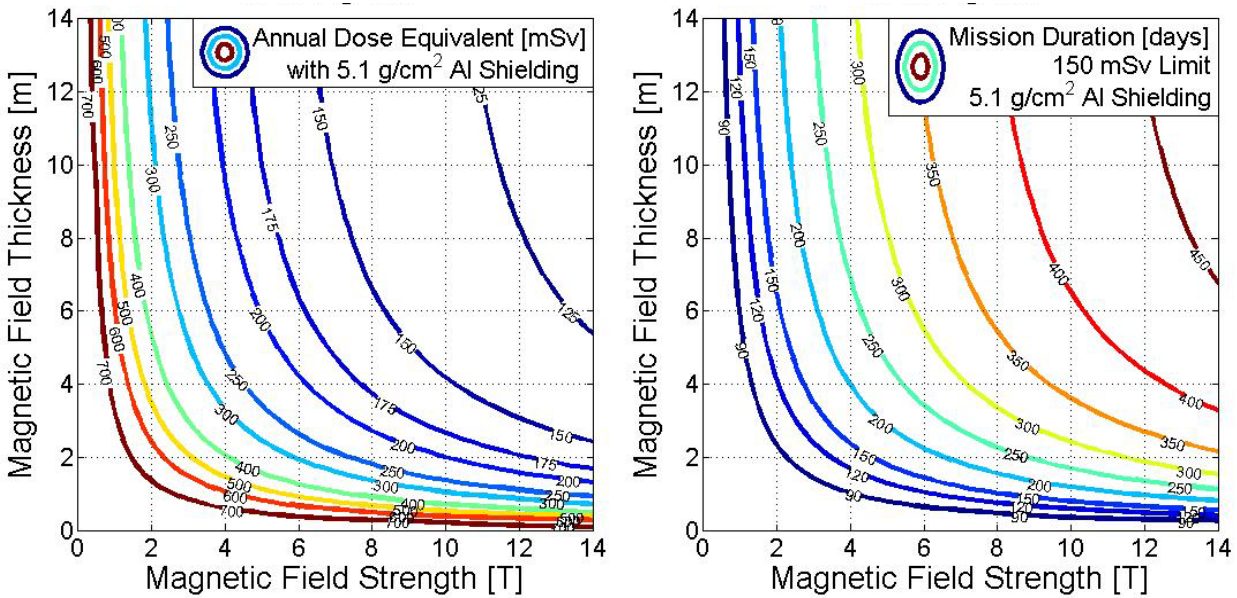
Figure 8.20. Open-Ended Cylinder Model with 5.1 g/cm^2 Al Shielding ($r_i = 4m$) a) Annual Dose Equivalent, b) Maximum Mission Duration to 150 mSv Limit

Unlike the quasi-spherical and infinite cylinder models, we can see that the above plots are not symmetric. A unit increase in field strength is significantly more effective at reducing dose than a unit increase in magnetic shield thickness.

8.6.4.   Variation with End-Cap Shielding

As discussed previously, the open space in the End-Cap regions makes a likely location for items such as a crew module and service module which would provide significant amounts of additional passive shielding. As such, it is useful to analyze the dose equivalent contribution from the Barrel region and End-Cap region separately so that different amounts of passive shielding at the End-Caps can be accounted for. The total dose equivalent can be determined by simply adding the individual contribution from each region (a Table containing values for the barrel region with 20 g/cm^2 is included in Appendix A).

The following tables allow for the computation of the resulting Annual dose equivalent for a variety of magnetic shielding configurations as well as different Barrel and End-Cap passive shielding thicknesses. These results are for the worst-case flux in the habitat (i.e. at the end of the habitat module, 5m from the axial center) and this method assumes that each End-Cap region has the same amount of passive shielding. Additionally, as discussed previously, these values provide a conservative estimate of the dose equivalent since most particles will actually pass through a thicker amount of shielding. Only particles which enter perpendicular to the axial centerline will pass through this minimum thickness for the Barrel Region, and only particles which enter parallel to the axial centerline will pass through this minimum thickness for the End-Cap Region.

As an example, we will determine the annual dose equivalent of a magnetic shield configuration which has a bending power of 8 Tm (1T x 8m) and a habitat module which has 10 g/cm^2 of shielding around the cylindrical portion (Barrel Region) and 25 g/cm^2 of shielding on each end (End-Cap Region). Since the

120

Barrel Region has 10 g/cm^2 of shielding we start by looking at Table 8.2 which gives the Barrel Region contribution for configurations with 10 g/cm^2 of shielding in the Barrel Region (if in our example we had 5.1 g/cm^2 of shielding we would then obtain values from Table 8.1). In Table 8.2 we find the value corresponding to a 1T x 8m magnetic shielding configuration, which is 402.4 mSv/yr. We then look at Table 8.3 to determine the contribution from the End-Cap Region for our given End-Cap shielding thickness of 25 g/cm^2. This results in a contribution of 54.8 mSv/yr. Finally, to determine the total Annual dose equivalent for this configuration we simply add the Barrel Region contribution (402.4 mSv/yr) and the End-Cap Region contribution (54.8 mSv/yr) for a total of 457.2 mSv/yr. Using this value we can easily determine that for a mission dose equivalent limit of 150 mSv, this configuration would enable a mission of 119.8 days.

Table 8.1. Barrel Region Annual Dose Equivalent, 5.1 g/cm^2 Shielding (r$_i$ = 4m) [mSv/yr]

Magnetic Field Strength [T]	Magnetic Field Thickness [m]									
	1	2	3	4	5	6	7	8	9	10
1	644.2	633.0	612.6	588.4	548.4	508.5	473.7	444.3	418.3	397.8
2	627.3	554.2	446.7	369.1	318.4	284.4	259.8	241.8	227.6	216.4
3	589.8	416.6	305.3	247.0	211.7	188.0	171.8	159.9	150.7	143.9
4	522.7	313.0	224.9	180.5	154.3	137.2	125.5	117.2	110.8	106.0
5	443.8	247.0	174.9	139.7	119.3	106.5	97.6	91.2	86.6	83.1
6	376.3	201.0	140.9	112.4	96.1	85.9	79.1	74.2	70.5	67.9
7	319.9	167.4	116.8	93.2	79.8	71.6	66.1	62.2	59.3	57.2
8	277.5	142.3	98.9	79.1	67.8	61.0	56.6	53.3	51.0	49.2
9	242.7	122.9	85.3	68.2	58.8	53.1	49.2	46.5	44.6	43.1
10	215.9	107.4	74.6	59.7	51.7	46.8	43.6	41.3	39.6	38.4

Table 8.2. Barrel Region Annual Dose Equivalent, 10.0 g/cm^2 Shielding (r$_i$ = 4m) [mSv/yr]

Magnetic Field Strength [T]	Magnetic Field Thickness [m]									
	1	2	3	4	5	6	7	8	9	10
1	537.6	529.1	516.0	497.8	479.7	454.3	426.9	402.4	381.5	363.8
2	525.0	478.7	407.1	342.9	295.2	261.6	237.9	220.8	207.6	197.1
3	499.2	382.9	285.3	227.9	194.6	172.3	157.2	146.2	137.7	131.3
4	462.3	294.5	207.9	166.3	141.8	125.9	115.0	107.3	101.3	96.8
5	405.8	229.7	161.4	128.6	109.6	97.7	89.5	83.5	79.2	75.9
6	350.2	186.2	129.8	103.4	88.3	78.8	72.5	67.9	64.5	62.0
7	302.4	154.7	107.7	85.8	73.3	65.6	60.5	56.9	54.1	52.2
8	260.9	131.7	91.3	72.7	62.3	55.9	51.7	48.7	46.6	44.9
9	226.5	113.6	78.6	62.7	54.0	48.6	45.0	42.5	40.7	39.3
10	200.7	99.3	68.7	54.8	47.3	42.7	39.7	37.6	36.0	34.9

Table 8.3. End-Cap Region Annual Dose Equivalent

End-Cap Shielding Thickness [g/cm^2]	End-Cap Annual DE Contribution [mSv/yr]
0	108.9
5	93.5
10	77.8
15	67.3
20	60.0
25	54.8
30	50.9
35	48.0
40	45.9
45	44.4
50	43.2

8.7. Comparison with Monte-Carlo results

Work is currently underway to make an accurate comparison between the Analytical-HZETRN results presented here and the Monte-Carlo results in section 6.5. Preliminary analysis shows that the results are reasonably close, however more work is needed to eliminate differences between the two model types and methods. Comparison with Monte-Carlo results will also allow validation of the assumptions made in the Analytical-HZETRN model, particularly the assumption that all of the structural and passive shielding mass can be lumped together inside the magnetic field with the habitat module.

The primary differences between the two models are:

1. Mass Location:
    a. Analytical-HZETRN model: assumes that all of the structural mass is lumped inside the magnetic field together with the habitat module
    b. Monte-Carlo model: utilizes a more realistic structural geometry
2. Mass Material:
    a. Analytical-HZETRN model: currently uses only an equivalent thickness of aluminum to represent the structure
    b. Monte-Carlo model: multiple materials used to approximate the structure and the shielding
3. Field Geometry:

a. Analytical-HZETRN model: assumes a uniform cylindrical field around the habitat (i.e. no gaps between the coils)

b. Monte-Carlo model: assumes that the field is confined to the solenoid coils

4. GCR Model:
    a. Analytical-HZETRN model: BO'10
    b. Monte-Carlo model: CREME09

5. Dose Equivalent Determination Method:
    a. Analytical-HZETRN model: 24 cm diameter water sphere
    b. Monte-Carlo model: 24 cm diameter by 180 cm long water cylinder

6. Flux source:
    a. Analytical-HZETRN flux source developed uniformly over a spherical surface X meters away from the architecture
    b. Monte-Carlo flux source developed uniformly over a cube surface 5 meters away from the architecture.

In order to make a preliminary comparison between these two models the Analytical-HZETRN model was run using the same CREME09 GCR flux as the Monte-Carlo analysis. Skin and BFO dose equivalent values were determined for the Analytical-HZETRN model by determining dose equivalent using a 24 cm diameter water sphere at the surface and at a depth of 5cm respectively. Initially the "free-space" dose equivalent values were compared to determine differences only in the dose equivalent determination method. These values are shown below in Table 8.4 and we can see that the Analytical-HZETRN model yields lower results than the Mont-Carlo results but are within 22%.

Table 8.4 "Free-Space" Model Comparison

	DE Type [mSv/yr]	Analytic/HZETRN	Monte-Carlo	Delta (% difference)
"Free Space" GCR = CREME09 B = 0T Shielding = 0.0 g/cm^2	Point DE	1320	-	-
	Skin DE	921	1177	256 (22%)
	BFO DE	521	624	103 (17%)

The Analytical-HZETRN model was then run using a shielding thickness of 7.5 g/cm^2 aluminum. The structural mass associated with the shield used in the Monte-Carlo analysis was estimated to be equivalent to 2.4 g/cm^2 of aluminum if this mass was smeared across the surface of the habitat. Assuming a habitat thickness of 5.1 g/cm^2 this resulted in a total thickness of 7.5 g/cm^2.

Table 8.5 Shielding Model Comparison

	DE Type [mSv/yr]	Analytic/HZETRN	Monte-Carlo	Delta (% difference)
GCR = CREME09 B = 1T Shielding = 7.5 g/cm^2	Skin DE	435	604	169 (28%
	BFO DE	343	403	60 (15%)

Again we see that the Analytical-HZETRN results are lower, but the percent difference between the models is relatively the same as for the "free-space" calculations which only showed differences in the dose equivalent calculation method. One could assume that this comprises a majority of the differences between the models, however more work is needed to valid this and determine the exact variances caused by differences in mass location, mass materials, and field geometry as detailed above.

9. Mission Concept

S. Westover - Johnson Space Center, NASA

9.1. Launch, Assembly and Deployment

Launch packaging was analyzed with an objective to minimize launches as well as extravehicular activity (EVA) count for the assembly of a 6 around 1 coil array radiation protection system. With the coil expansion concept, it's conceived that 3 of the 6 coils could fit in a 6 meter diameter fairing for a single launch. Evaluating the fairing size options for the Space Launch System (SLS) under concept development at MSFC, it's plausible to fit all 6 expandable coils in a single 10 meter diameter launch fairing with coils 15 to 20 meters in length by orienting the starfish shaped strongback fingers together in a gear-like fashion, as seen in Figure 9.1 and Figure 9.2. This 6 coil array launch payload mass is estimated at ~50 metric tons which includes the coil, coil strongback, coil blanket and structure with 35% contingency added (see Table 9.1 for mass estimates).

If all 6 coils were launched from a single fairing as suggested above, the habitat and compensator coil with thermal system could be inserted into space on a second launch vehicle as shown in Figure 9.3. Assuming an estimated mass of about 25 metric tons using other reference studies (NASA DRA 5.0, 2009; Drake B.G, NASA Exploration Blueprint, 2007) for a 6 m diameter by 10 meter length cylindrical habitat, the payload mass is estimated at 27.7 metric tons including the compensator coil. Quoted masses did not include radiators and solar arrays as these systems would need to be integrated with other system needs based on mission requirements. Although not included in the phase 1 analysis, a propulsion bus attached to the habitat would likely fit within the same SLS launch fairing and could be attached to the habitat pre-launch during payload processing. The habitat-compensator assembly would dock with the coil array followed with an EVA(s) to connect helium vapor cooling flexlines to the compensator coil. Propulsion capability will be needed to deliver the stack to a deep space location such as GEO or HEO for charging and coil expansion.
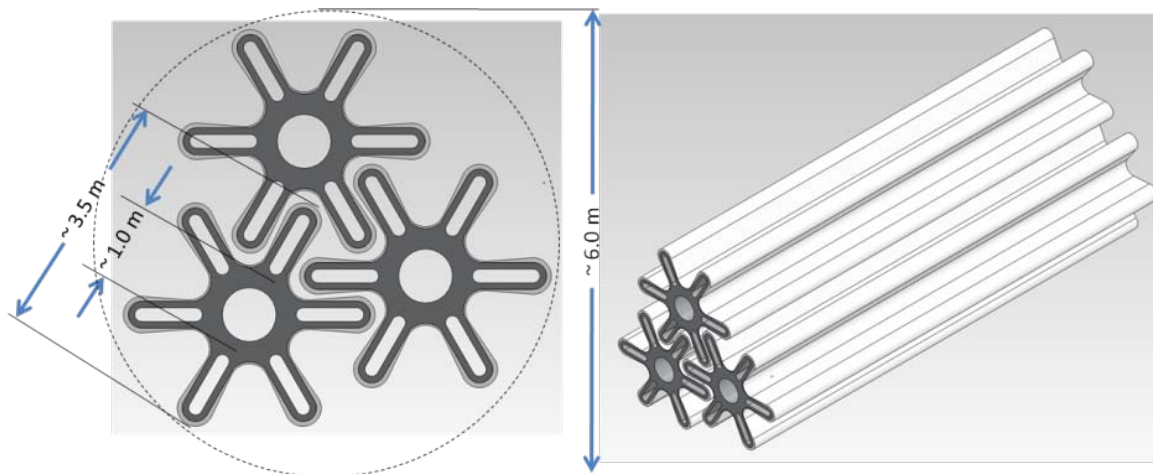
Figure 9.1. Three of six 8 meter diameter coils fit within a 6 meter diameter fairing in their contracted state (reference section 2.2.3 A 6+1 Configuration).
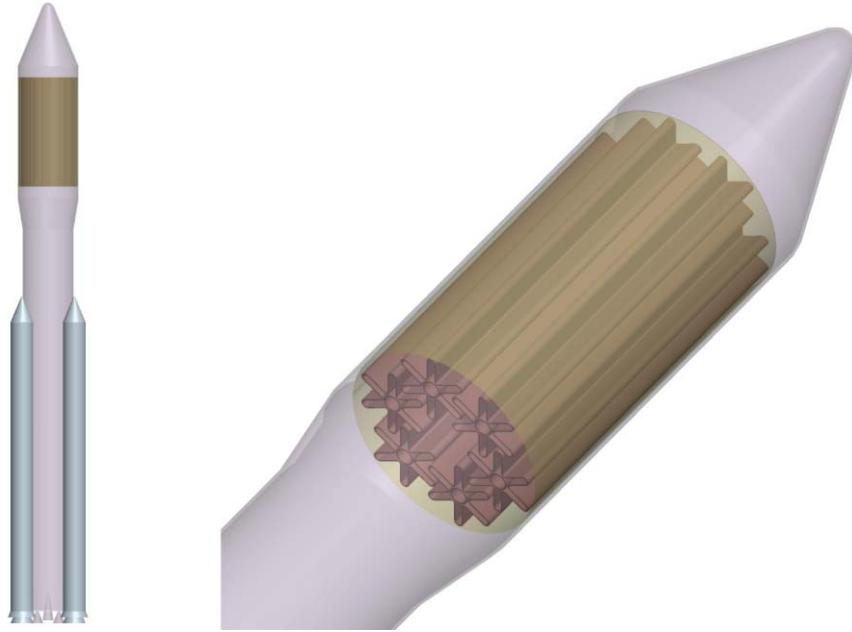
Figure 9.2. The full six coil array with individual coils of 8 meters diameter by 18 meters in length, in their contracted state, are packaged conceptually in a 10 meter diameter fairing.
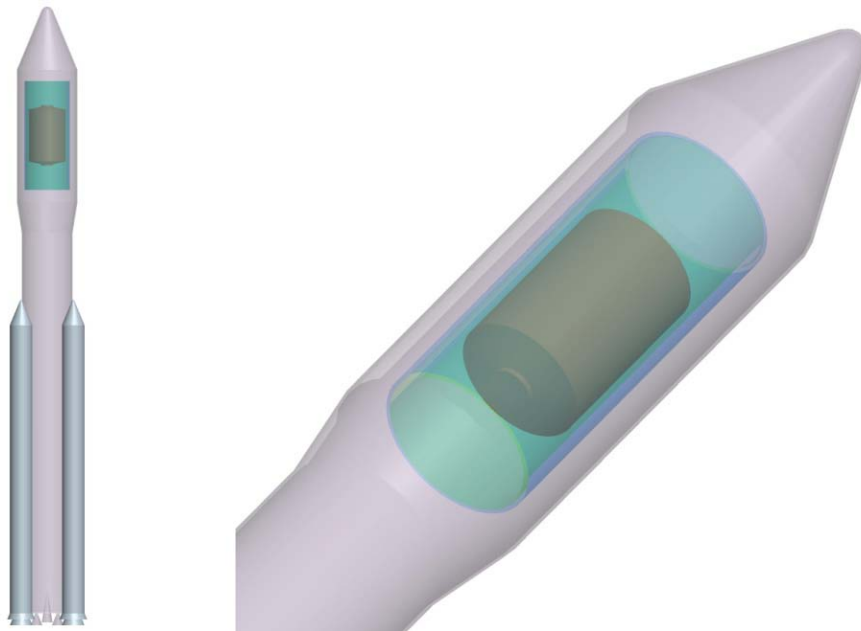
Figure 9.3. The 6 meter diameter habitat and compensator coil with integrated coil cryocooling thermal system launched separately for later assembly with the coil array. This constitutes the two-launch habitat and radiation protection system.

The thermal design concept considered local deep space environment temperatures similar to EML1. The thermal concept addresses solar heat at this location as well as radiant heat from the habitat. In light of this approach, the coil charging and expansion would need to occur in a similar environment

beyond LEO away from the Earth's radiant heat. This was a trade made to minimize the power requirements of the thermal system.

Coil charging and expansion would occur at HEO or maybe one of the local Lagrangian points. The system would be charged with flux pumps over a period of days or possibly weeks depending on power reserves. Expansion of the coils would, in concept, lock in place once fully deployed to provide some level of rigidity for complete power-up of the superconducting coils and stabilizing the magnetic field. The superconducting coils operate in a persistent mode to provide radiation protection for the crew.
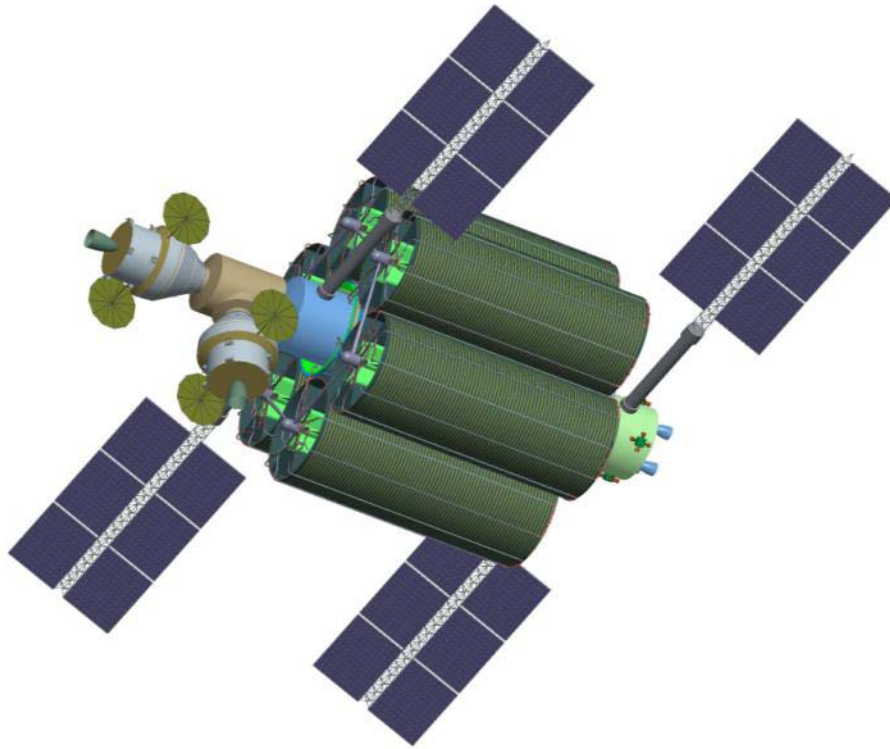
Figure 9.4. The 6 expandable coils and 1 compensator coil are wrapped around the crew module for radiation protection with the exploration propulsion module and logistics module peaking out the end caps. A docking module with two Orion capsules are linked to the logistic module serving as parasitic radiation shielding.

On one end cap, it is envisioned that a propulsion transfer module would provide attitude control and translation propulsion designed for the mission at hand. It might include both chemical and electric propulsion for both high efficiency and high thrust modes. The propellant tanks and their propellant commodities would provide some level of radiation protection on the end cap that would need to be determined in phase II.

On the other end cap of the habitat, phase II might consider a logistics module for food and water stores and other typical luggage for the trip. It would also include a crew transport capsule such as Orion as well as an airlock pressure chamber for EVA. All of this infrastructure will have an effect on the total radiation dose for the crew, which is considered for phase II study. This architecture is visualized as a first iteration in Figure 9.4.

Operational concepts such as quench protection sequences or power down sequences for potential repair operations will need to be considered. A risk evaluation of a coil system such as this could be evaluated in a phase 2 study.

9.2.   Mass and Power Requirements Summarized

The mass and power requirements are summarized in Table 9.1 below using information provided in section 2.5 and section 3.4 from the coil concept and the thermal concept, respectively. Contingency of 35% mass is added to account for the early concept and lack of development to date. As for the structure and blanket mass, it's conceivable that this material weight could be 20% less than estimated depending on advanced material capability and availability, however, 35% contingency was added for a more conservative approach in the total mass. In a similar fashion, since the Brayton-cycle cryocooler is yet to be fully developed, the sterling cycle thermal system mass estimate is used here. Radiator sizing has not been performed at this time and the mass is unaccounted for.

The total mass for the 6 coils is estimated to be ~50 metric tons for a single launch, while an additional launch could feasible take a 25 mT 6 m diameter, 10 m length cylindrical habitat assembled with a 2 mT compensator coil prior to launch.

Table 9.1. Total Mass and Power Requirements for Expandable Coil System

Coil System	Mass (kg)	Power (kW)
Strongback, 20 m carbon	2714	
Conductor, 20 m coil	503	~330 W/coil (~ 2 kW) (assumes 2 weeks flux pumped)
Blanket - for coil & structural support	2895	
Coil, Strongback, & Blanket subtotal	6112	
Contingency, -20% to +35%	-1222 to 2139	
Total 6 (1) Coils with Contingency	**49,507 (8251)**	
Thermal system - Brayton (Sterling)	420 (1216)	19
Contingency, +35% mass ,25% pwr (sterling)	147 (426)	5
Total Thermal & Contingency (sterling)	**567 (1642)**	
Compensator coil	**2126**	Included above
Radiators	TBD	TBD
Launch #1 - 6 Coils Total	**49500**	-
Launch #2 - Habitat & Compensator Coil	**25,000 + 2126**	**26 kW**

10.   Conclusions

The NIAC one year study evaluated multiple coil geometries including the Double Helix from AML and toroid designs. The Double Helix and other toroid concepts have a constant, no gap transverse field for turning ionized radiation, however significant loads on the habitat and between the coils result in significant structural design architecture and mass. Most toroid configurations result in a large field within the habitat requiring complex shielding from the magnetic field for the crew and electronics. The down-selected 6+1 solenoid coil array and compensator coil configuration minimizes both mass and in the cabin fringe field technical issues. The concept of coil expansion using the Lorentz force with high temperature superconductors enables very large coil diameters to increase the integral BdL of the system for improved dose efficiency while keeping to a reasonable launch mass and simplified assembly. Not only does the compensator coil tune to minimize fringe fields entering the habitat, but also simplifies the coil thermal management system by capturing the radiant heat from the habitat with cryocoolers.

As a protection from SPE, analysis was completed for a 6m diameter by 10m length cylindrical habitat that resulted in 141 metric tons of 75 cm thick polyethylene providing similar protection as that from a 6+1 expanding coil array at 8 Tm with a simulated mass of 36 metric tons.   The Blood Forming Organ (BFO) dose was ~50 mSv for a 180 hour SPE from October of 1989. This comparison maintained a constant habitable volume vice filling the volume with polyethylene for individual crew protection such as a storm shelter.

Dose equivalent results for the 8 Tm configuration are comparable with annual dose equivalents for a spacecraft in LEO with "barrel-only" BFO results at 309 mSv and total results with nearly "naked" end caps with an empty habitable volume at 451 mSv.   For comparison with the 150 mSv career limit, the body dose equivalent is 232 mSv for the 8 Tm barrel region only and up to 363 mSv if one includes the dose received through the end caps with missing architectural mass. Real GCR reduction has been achieved however, the reduction is not significant enough to provide significantly greater mission duration so more work is needed.

Phase 2 intends to refine the vehicle configuration with added spacecraft architecture such as the propulsion system, logistics module, and a crew transfer capsule on the end caps of the habitat, all which is expected to contribute to the overall shielding efficiency of the 8 Tm 6+1 coil configuration. The technology will be considered along with the potential scalability of the 8 Tm coils. External fringe fields will be evaluated and the compensator coil integration with the solenoid array loads analyzed. The magnetic loads and structural design concept will also be considered for engineering feasibility and refinement of the system shielding mass.

11. References

Agostinelli, S. et al., Nucl. Instr. and Methods A, 506 (2003) 250.

Aguilar, M. et al., Phys. Reports, 366 (2002) 331.

Battiston, R., Burger, W.J. et al., ESA ARSSEM report, http://arxiv.org/abs/1209.1907

Battiston, R., Burger, W.J. et al., An Active Radiation Screen Design Based on Superconduction Double-Helix Solendoids, Proceedings of the 5th IAASS Conference "A Safer Space for a Safer World", Versailles, France 17-19 October 2011 (ESA SP-699, January 2012)

Brun, R., et al., GEANT -Detector description and simulator tool, CERN Program Library Long Write-up W5013, CERN, Geneva (1993).

Choutko, V., Hofer, H. and Ting, S.C.C., The AMS Experiment and Magnet Faraday Cage for Human Space Exploration, presented at the NASA Active Radiation Shielding Workshop, Ann Arbor, MI, August 17-18, 2004.

Cosmic Rays Effects on Micro Electronics (CREME), https://creme.isde.vanderbilt.edu/CREME-MC

Drake, B.G., "Exploration Blueprint Data Book", NASA, July 2007. NASA/TM-2007-214763 and JSC 63724.

Durante, M., Cucinotta, F., Rev. Mod. Phys., Volume 83 (2011) 1245.

Fass`o, A., Ferrari, A., Ranft, J. and Sala, P.R. FLUKA: present status and future developments, proceedings of 4th International Conference on Calorimetry in High Energy Physics, La Bidola (Italy) 21-26 September 1993, World Scientific, pp. 493-502.

HTS4 Fusion Workshop, May 26-27, 2011, Karlsruhe, Germany

https://oltaris.nasa.gov/ as viewed on 13 November, 2012. All calculations used Version 3.1.

Hurlbert, K., Bagdigian, B., Carroll, C., Jeevarajan, A., Kliss, M., Singh, B., "DRAFT Human Health, Life Support and Habitation Systems, Technology Area 06," NASA, November, 2010. Found at http://www.nasa.gov/offices/oct/home/roadmaps/ as viewed on 13-Nov-2012.

International Commission on Radiological Protection, Recommendations of the International Commission on Radiological Protection. ICRP Publication 60, Pergamon Press, New York, 1990.

Kate, H.J. ten, et al., A Thermally Switched 9 kA Superconducting Rectifier Flux Pump, IEEE Transactions on Magnetics, Vol. Mag-17, No.5, Sept. 198

National Aeronautics and Space Administration (NASA), "Constellation Program, Human-System Integration Requirements," CxP 70024, Revision C, March 6, 2009.

National Aeronautics and Space Administration (NASA), "Human Exploration of Mars, Design Reference Architecture 5.0," NASA-SP-2009-566, July 2009.

National Aeronautics and Space Administration (NASA), "NASA Space Flight Human System Standard, Volume 1: Crew Health," NASA-STD-3001, March 2007.

"National Aeronautical and Space Administration Authorization Act of 2010," S.3729, Sec. 302(c)(1)(B), January 2010.

National Council on Radiation Protection and Measurements (NCRP), "Radiation Protection Guidance for Activities in Low-Earth Orbit," NCRP Report 132, 2000.

NISTWEB-HTS Database

O'Neill, P.M., "Badhwar–O'Neill 2010 Galactic Cosmic Ray Flux Model - Revised". IEEE Transactions on Nuclear Science 57 (6), 3148–3153, 2010.

O'Neill, P.M., "Badhwar-O'Neill "Galactic Cosmic Ray Model Update Based on Advanced Composition Explorer (ACE) Energy Spectra from 1977 to Present," Advances in Space Research, 37 (2006) 1727-1733.

Rapp, D., "Human Missions to Mars: Enabling Technologies for Exploring the Red Planet," Springer/Praxis Books, Table 3.14, 2008.

Rapp, D., Radiation Effects and Shielding Requirements in Human Missions to the Moon and Mars, Mars Volume 2, 46-71 (2006); doi:10.1555/mars.2006.0004

Singleterry, R.C. Jr., Blattnig, S.R., Clowdsley, M.S., et al., "OLTARIS: On-Line Tool for the Assessment of Radiation In Space", Acta Astronautica, 68 (2011) 1086-1097.

Singleterry, R.C. Jr., Blattnig, S.R., Clowdsley, M.S. et al., "OLTARIS: On-Line Tool for the Assessment of Radiation In Space", NASA Technical Paper 2010-216722, July 2010.

Slaba, T.C., Blattnig, S.R., Badavi, F.F. Faster et al., "Accurate Transport Procedures for HZETRN." Journal of Computational Physics 229, 9397-9417, 2010a.

Slaba, T.C., Blattnig, S.R., Aghara, S.K., Townsend, L.W., Handler, T., Gabriel, T.A., Pinsky, L.S., Reddell, B. "Coupled Neutron Transport for HZETRN." Radiation Measurements 45, 173-182, 2010b.

Sorge, H., Physical Review C, Volume 52, number 6 (1995) 3291.

Iwasa, Y., "Stability and Protection of SC Magnets – A Discussion", IEEE Transactions on Applied Superconductivity, p. 1615, June 2005.

12. Acronyms

Acronym	Definition
A	Ampere
AML	Advanced Magnet Lab
AMS	Alpha Magnetic Spectrometer
BdL	Magnetic field times the change in length
BFO	Blood forming organ
CERN	European Organization for Nuclear Research
CREME	Cosmic Rays Effects on Micro Electronics
CU	University of Colorado
DE	Dose Equivalent
DESY	German Electron Synchrotron
DH	Double Helix
DRM	Design Reference Mission
ED	Effective dose
EML1	Earth-Moon Lagrangian Point 1
ESA	European Space Agency
EVA	Extravehicular Activity
FLUKA	FLUktuierende KAskade
FSU	Florida State University
GCR	Galactic Cosmic Radiation
GEANT	GEometry ANd Tracking
GEO	Geostationary Earth Orbit

MAARSS

Acronym	Definition
GeV	Gigaelectron volt
GJ	Gigajoule
GPa	Gigapascal
GV	Gigavolt
HEO	High Energy Orbit
HERA	Hadron-Electron Ring Accelerator
HTS	high temperature superconducting
HTSC	High temperature superconducting
HZE	High charge and energy
HZETRN	High charge and energy transport computer program
IAASS	International Association for the Advancement of Space Safety
ICRP	International Commission on Radiological Protection
IEEE	Institute of Electrical and Electronics Engineers
INFN	National Institute for Nuclear Physics
ISS	International Space Station
JSC	Johnson Space Center
LaRC	Langley Research Center
LEO	Low Earth Orbit
LTS	Low Temperature Superconductors
MAARSS	Magnet Architectures and Active Radiation Shielding Study
MeV/n	Mega electron volt per nucleon
MgB2	Magnesium-boride
MJ	Megajoule

Acronym	Definition
MN	Meganewton
MRI	Magnetic Resonance Imaging
MSFC	Marshall Space Flight Center
mSv	Millisievert
NASA	National Aeronautics And Space Administration
Nb$_3$Sn	Niobium-tin
NbTi	Niobium-titanium
NCRP	National Council on Radiation Protection and Measurements
NIAC	NASA Innovative Advanced Concepts
OLTARIS	On-Line Tool for the Assessment of Radiation in Space
R&D	Research And Development
RQMD	Relativistic Quantum Molecular
SEP	Solar energetic particle
SLS	Space Launch System
SMES	superconducting magnetic energy storage
SOA	state of the art
SPE	solar proton event
TBD	To Be Determined
TC/O	Energy cutoff
TLI	Trans-lunar injection
TMI	Trans-Mars Injection
W	Watt
YBCO	Yttrium-barium-copper-oxide

Appendix A: Additional Analytical-HZETRN Model Data

Quasi-Spherical Energy Cutoff

The tables below give the cutoff energy per nucleon at the center of the quasi-spherical model for various magnetic field strengths and thicknesses. Table A.1 gives the cutoff energy for protons. Table A.2 gives the average cutoff energy for Z > 2. The "average" cutoff value is given since the cutoff energy of a specific ion is dependent both on the mass and charge of the ion. It is important to note the significantly higher cutoff energy for protons due to their higher charge to mass ratio.

Table A.1 Proton Cutoff Energy [GeV/nucleon]

Magnetic Field Strength [T]	Magnetic Field Thickness [m]									
	1	2	3	4	5	6	7	8	9	10
0	0.000	0.000	0.000	0.000	0.000	0.000	0.000	0.000	0.000	0.000
1	0.038	0.125	0.236	0.361	0.494	0.632	0.773	0.915	1.060	1.205
2	0.144	0.432	0.758	1.090	1.421	1.749	2.073	2.394	2.712	3.028
3	0.301	0.830	1.380	1.918	2.442	2.954	3.455	3.949	4.436	4.918
4	0.492	1.269	2.040	2.779	3.492	4.184	4.861	5.525	6.180	6.827
5	0.705	1.730	2.717	3.655	4.555	5.426	6.276	7.110	7.931	8.742
6	0.933	2.203	3.404	4.538	5.624	6.674	7.697	8.700	9.687	10.662
7	1.170	2.683	4.096	5.426	6.697	7.924	9.120	10.292	11.445	12.583
8	1.415	3.167	4.792	6.317	7.772	9.177	10.545	11.886	13.205	14.506
9	1.665	3.655	5.490	7.209	8.849	10.431	11.972	13.481	14.965	16.430
10	1.918	4.145	6.190	8.103	9.927	11.687	13.399	15.076	16.726	18.355

Table A.2 $Z \geq 2$ Average Cutoff Energy [GeV/nucleon]

Magnetic Field Strength [T]	Magnetic Field Thickness [m]									
	1	2	3	4	5	6	7	8	9	10
0	0.000	0.000	0.000	0.000	0.000	0.000	0.000	0.000	0.000	0.000
1	0.009	0.030	0.059	0.094	0.133	0.176	0.223	0.272	0.323	0.376
2	0.035	0.115	0.218	0.334	0.458	0.587	0.719	0.853	0.989	1.126
3	0.077	0.242	0.442	0.655	0.874	1.094	1.314	1.534	1.754	1.974
4	0.132	0.400	0.705	1.018	1.330	1.640	1.947	2.252	2.554	2.854
5	0.200	0.579	0.991	1.403	1.808	2.206	2.599	2.986	3.369	3.748
6	0.278	0.773	1.291	1.801	2.297	2.783	3.259	3.728	4.191	4.650
7	0.363	0.976	1.601	2.206	2.793	3.365	3.925	4.476	5.019	5.556
8	0.456	1.187	1.916	2.617	3.294	3.952	4.595	5.227	5.849	6.464
9	0.553	1.403	2.236	3.032	3.798	4.541	5.267	5.980	6.681	7.375
10	0.655	1.623	2.558	3.449	4.304	5.133	5.941	6.734	7.515	8.287

Annual Dose Equivalent Tables:

Table A.3 Quasi-Spherical Model, Annual Dose Equivalent with 5.1 g/cm^2 Shielding (r_i = 4m) [mSv/yr]

Magnetic Field Strength [T]	Magnetic Field Thickness [m]									
	1	2	3	4	5	6	7	8	9	10
0	737.4	737.4	737.4	737.4	737.4	737.4	737.4	737.4	737.4	737.4
1	737.4	730.2	717.2	700.6	655.9	592.8	548.7	488.3	445.5	390.8
2	728.8	681.7	552.3	421.8	355.1	297.5	255.5	220.3	197.6	175.0
3	707.9	524.9	358.2	272.3	218.4	187.0	151.7	130.7	119.4	103.5
4	656.7	385.6	264.9	193.1	150.9	124.1	104.4	87.6	74.6	68.1
5	555.2	298.2	197.2	145.4	110.4	90.0	73.8	60.8	55.1	46.5
6	485.7	243.3	156.1	110.6	86.8	69.7	56.3	46.7	41.7	34.9
7	414.2	199.1	125.7	90.0	69.5	55.1	44.1	36.2	32.2	26.8
8	355.6	168.9	105.3	73.4	55.9	43.8	35.3	28.1	25.4	20.7
9	308.1	145.4	88.7	60.2	45.9	35.8	28.0	24.9	20.1	18.1
10	272.3	124.8	74.5	53.8	37.6	30.9	25.0	20.0	17.4	14.4

One may note that the "free-space" dose equivalent values shown (i.e. for B = 0T, where no magnetic shielding is present) are significantly lower than similar values presented in previous literature. As discussed in greater detail in Section 8.2, this is due to the use of the BO'10 GCR model instead of older models commonly used in previous literature.

Table A.4 Infinite Cylinder Model, Annual Dose Equivalent with 5.1 g/cm^2 Shielding (r_i = 4m) [mSv/yr]

Magnetic Field Strength [T]	Magnetic Field Thickness [m]									
	1	2	3	4	5	6	7	8	9	10
0	737.4	737.4	737.4	737.4	737.4	737.4	737.4	737.4	737.4	737.4
1	726.1	695.8	654.7	608.2	547.0	483.6	436.1	389.4	350.3	312.3
2	689.1	576.4	442.2	338.3	277.3	231.6	196.6	170.3	150.2	133.3
3	630.8	418.0	282.5	211.4	167.8	139.3	114.9	98.3	87.4	76.0
4	548.1	304.0	201.8	147.1	113.9	92.7	77.0	65.0	55.4	49.3
5	455.1	233.2	149.9	109.1	82.7	66.4	54.4	45.2	39.7	33.8
6	385.3	186.9	117.0	83.0	63.8	50.7	41.2	34.0	29.1	25.1
7	324.7	151.8	94.5	66.4	50.4	39.7	32.0	26.3	22.4	19.3
8	278.2	127.8	78.3	54.0	40.7	31.8	25.4	20.7	18.0	15.0
9	239.6	109.1	65.4	44.5	33.3	25.9	20.5	17.3	14.4	12.3
10	211.4	93.6	55.2	38.3	27.4	21.6	17.5	14.3	11.9	10.1

Table A.5 Open-Ended Cylinder Model, range of Annual Dose Equivalent Values in Habitat with 5.1 g/cm^2 Shielding (r_i = 4m) [mSv/yr]

Magnetic Field Strength [T]	Magnetic Field Thickness [m]									
	1	2	3	4	5	6	7	8	9	10
0	737.4	737.4	737.4	737.4	737.4	737.4	737.4	737.4	737.4	737.4
1	736.1-736.1	725.4-724.9	705.4-704.5	677.1-680.1	632.6-640.3	588.6-600.6	549.5-566.0	516.2-536.2	487.1-510.5	464.0-489.9
2	719.7-719.2	634.0-645.9	513.9-538.8	428.2-461.2	371.9-410.5	333.9-376.6	306.2-351.8	285.6-333.7	270.0-319.6	257.8-308.3
3	674.9-681.7	481.1-508.4	359.8-397.4	295.5-339.2	256.1-303.9	229.8-280.0	211.4-263.8	198.1-251.8	187.9-242.8	180.2-236.0
4	598.2-614.7	370.3-405.2	274.1-317.2	225.1-272.7	195.8-246.3	176.7-229.3	163.6-217.6	154.2-209.2	147.2-202.7	141.8-198.0
5	513.1-536.7	300.3-339.1	221.8-267.2	182.8-231.7	160.2-211.4	145.7-198.4	135.9-189.5	128.8-183.1	123.5-178.6	119.7-174.9
6	440.7-468.9	251.8-293.0	186.5-233.0	155.1-204.0	136.9-188.2	125.5-178.0	117.8-171.1	112.5-166.1	108.4-162.5	105.5-159.8
7	381.1-412.8	216.9-259.7	161.8-208.9	135.8-158.3	120.9-171.9	111.7-163.6	105.4-158.0	101.2-154.1	97.9-151.2	95.7-149.1
8	336.0-369.8	190.9-234.5	143.7-191.0	121.7-171.0	109.3-159.9	101.6-153.0	96.7-148.4	93.0-145.2	90.5-142.9	88.5-141.2
9	300.0-335.6	170.8-214.9	130.0-177.3	111.2-160.2	100.7-150.7	94.3-145.0	90.0-141.1	87.0-138.4	84.9-136.5	83.2-135.0
10	271.1-308.0	155.0-199.5	119.3-166.7	102.9-151.7	94.0-143.6	88.4-138.7	84.8-135.5	82.4-133.2	80.5-131.5	79.1-130.3

Since the dose equivalent can vary over the distance from the center of the cylinder, the table above gives the range of calculated dose equivalent values. The first number listed gives the dose equivalent at the absolute center of the cylinder. The second value gives the dose equivalent at the edge of the habitat along the centerline axis, 5m from the absolute center.
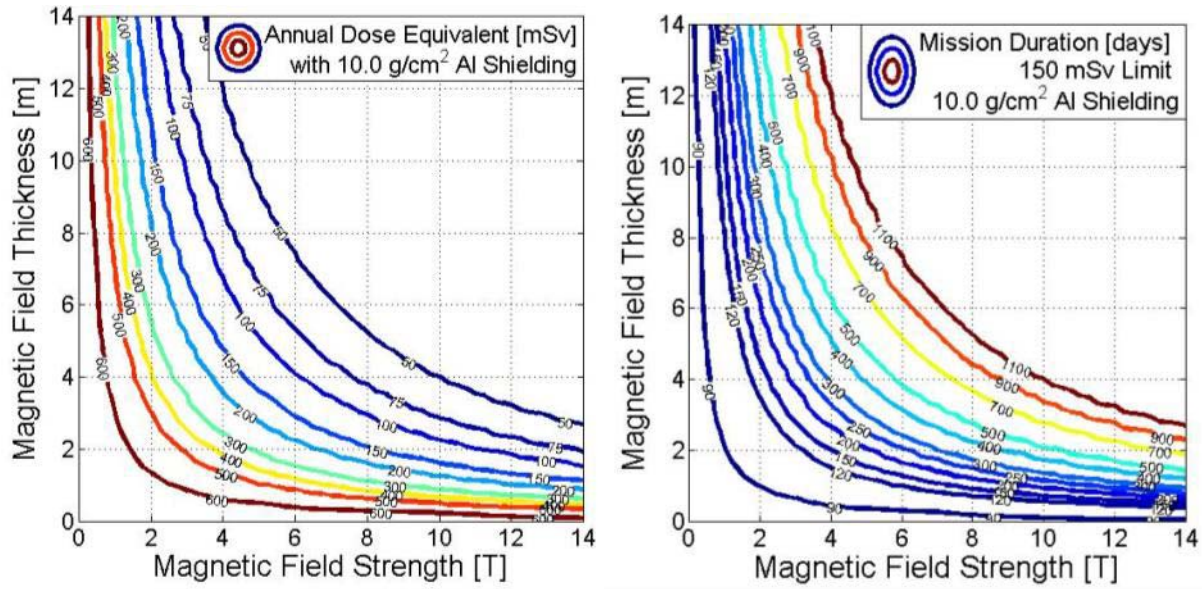
Trade Space Plots: Quasi-Spherical Model

Figure A.1 Quasi-Spherical Model with 10.0 g/cm^2 Al Shielding (r_i = 4m) a) Annual Dose Equivalent, b) Maximum Mission Duration to 150 mSv Limit
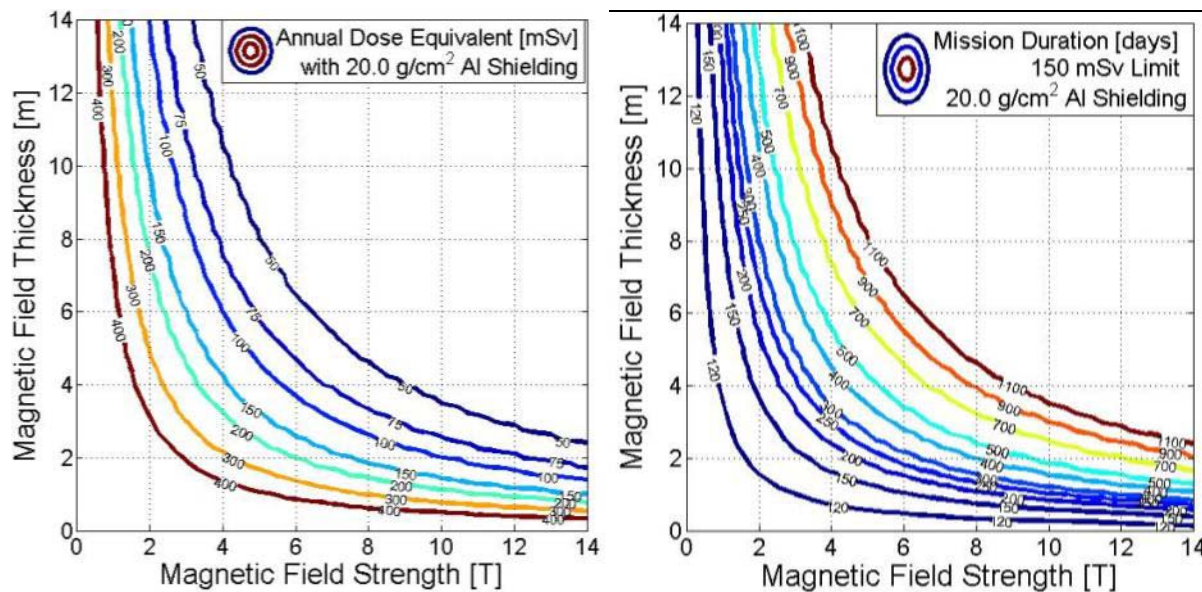

Figure A.2 Quasi-Spherical Model with 20.0 g/cm^2 Al Shielding (r_i = 4m) a) Annual Dose Equivalent, b) Maximum Mission Duration to 150 mSv Limit
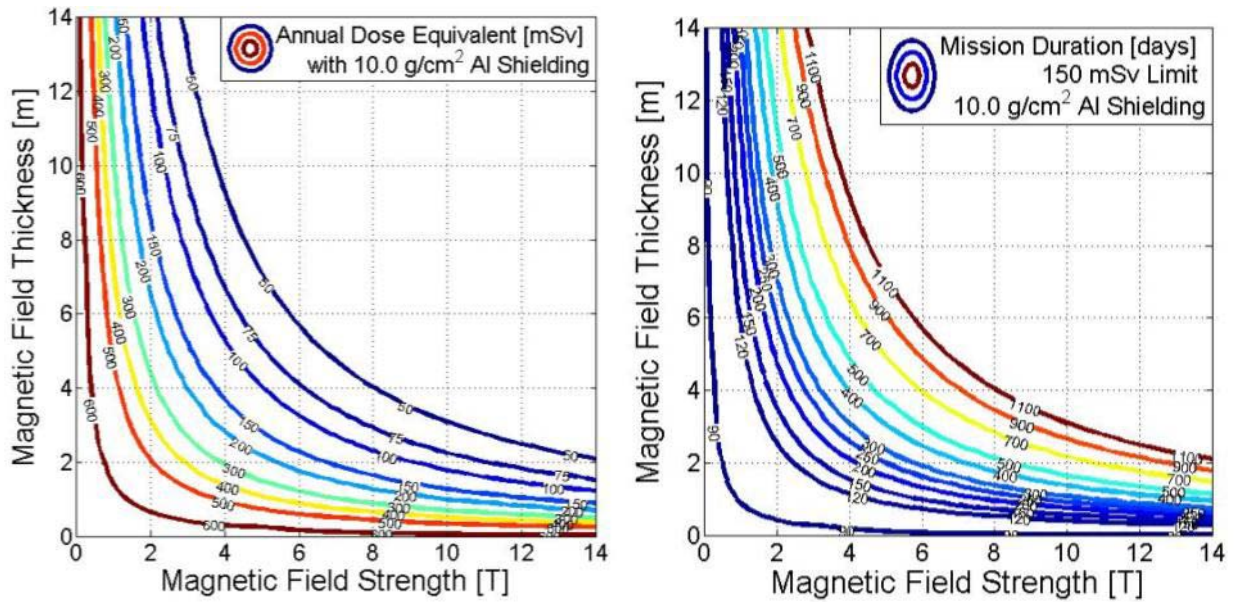
Trade Space Plots: Infinite Cylinder Model

Figure A.3 Infinite Cylinder Model with 10.0 g/cm^2 Shielding (r_i = 4m) a) Annual Dose Equivalent, b) Maximum Mission Duration to 150 mSv Limit
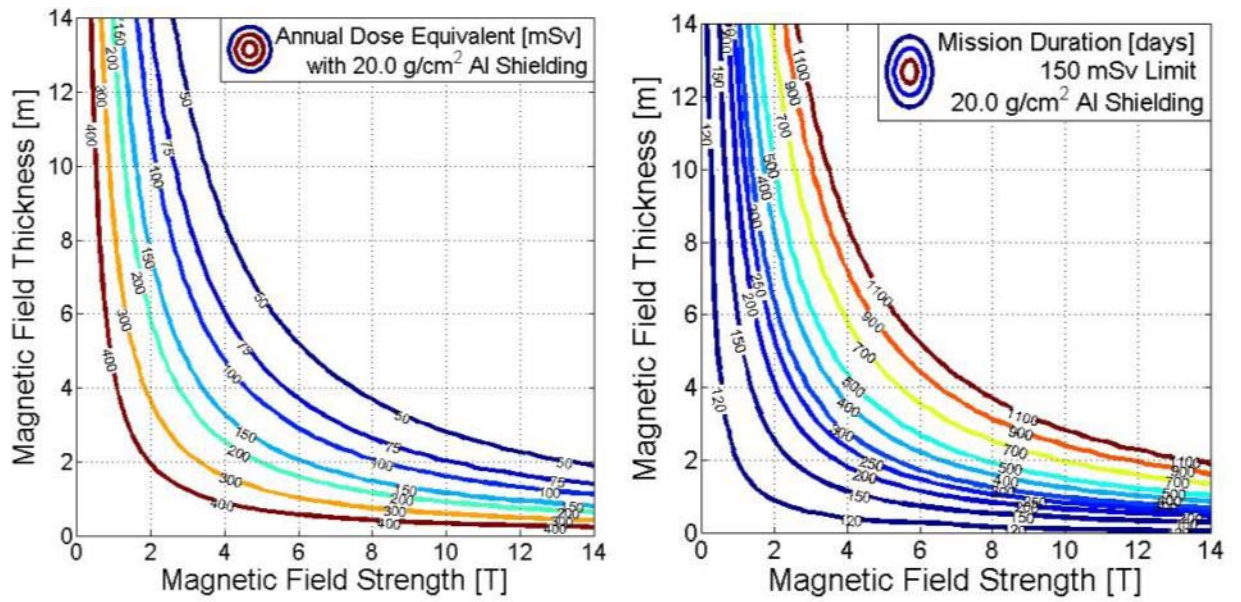

Figure A.4 Infinite Cylinder Model with 20.0 g/cm^2 Shielding (r_i = 4m) a) Annual Dose Equivalent, b) Maximum Mission Duration to 150 mSv Limit
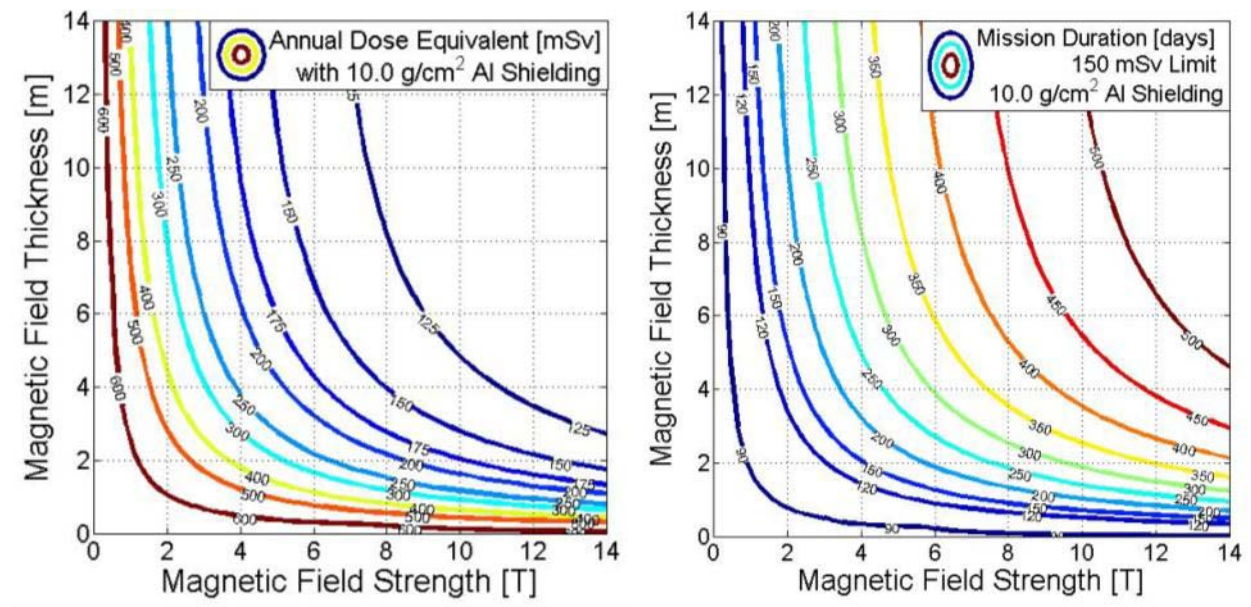
Trade Space Plots: Open-Ended Cylinder Model

Figure A.5 Infinite Cylinder Model with 10.0 g/cm^2 Al Shielding (r_i = 4m) a) Annual Dose Equivalent, b) Maximum Mission Duration to 150 mSv Limit
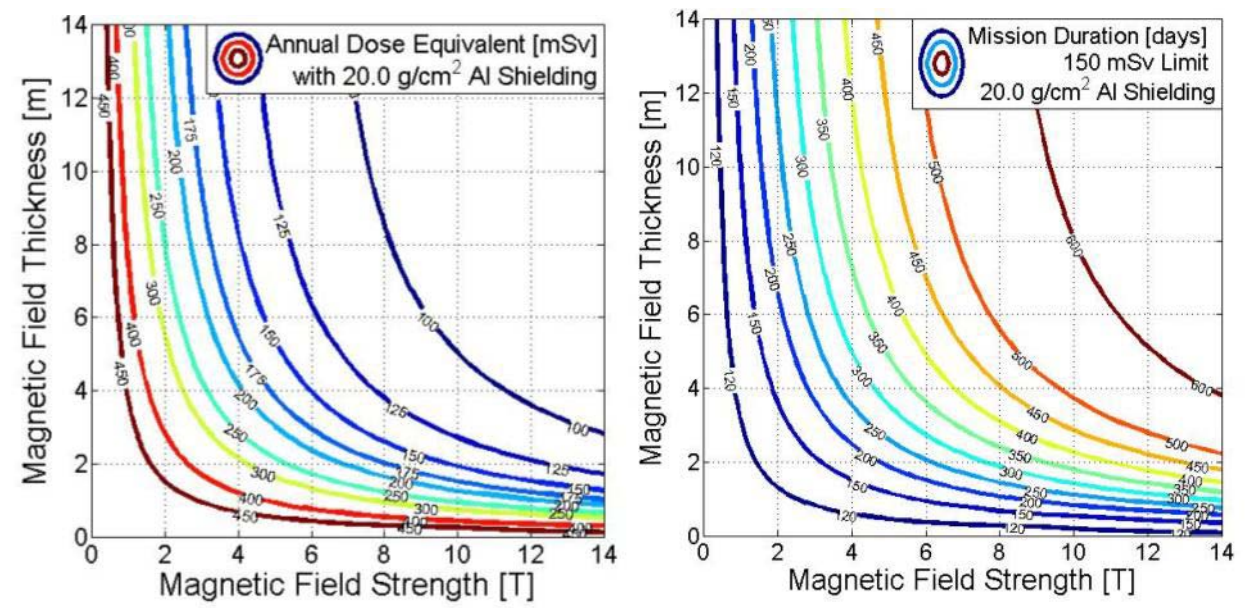

Figure A.6 Infinite Cylinder Model with 20.0 g/cm^2 Al Shielding (r_i = 4m) a) Annual Dose Equivalent, b) Maximum Mission Duration to 150 mSv Limit

Open-Ended Cylinder Barrel Only Data: 20g/cm² Al Shielding

Table A.5 Barrel Region Annual Dose Equivalent with 20.0 g/cm2 Shielding (ri = 4m) [mSv/yr]

Magnetic Field Strength [T]	Magnetic Field Thickness [m]									
	1	2	3	4	5	6	7	8	9	10
1	415.1	410.3	398.5	386.7	372.3	359.1	345.5	329.7	314.8	301.8
2	406.8	372.3	332.5	288.1	252.6	226.4	205.0	189.2	177.3	167.9
3	386.9	316.9	245.6	199.2	168.7	148.7	135.2	125.4	118.0	112.3
4	360.4	252.6	182.5	144.5	122.6	108.7	99.0	92.2	86.9	82.9
5	331.0	203.0	140.9	111.8	94.9	84.4	77.1	71.8	68.0	65.1
6	294.2	163.8	113.2	89.8	76.6	68.1	62.5	58.4	55.3	53.2
7	258.9	135.6	93.9	74.6	63.5	56.7	52.1	48.9	46.4	44.7
8	228.1	115.3	79.6	63.2	53.9	48.3	44.5	41.8	39.9	38.4
9	201.4	99.5	68.6	54.4	46.7	41.9	38.7	36.4	34.8	33.6
10	178.4	86.9	59.9	47.6	40.9	36.8	34.1	32.2	30.8	29.8